Design and Development of Earthquake Resistant 3D Printed Concrete Walls

A thesis submitted

in partial fulfilment of the requirements

for the degree of

Doctor of Philosophy

by

Syed Bustan Fatima Warsi
Roll No.- 216156105

Under the supervision of

Dr. Biranchi Panda

and

Prof. Pankaj Biswas

Centre for Intelligent Cyber Physical Systems

Indian Institute of Technology Guwahati

Guwahati-781039, India

March 2026

Declaration

I, hereby declare that the content embodied in this thesis entitled ***"Design and Development of Earthquake Resistant 3D Printed Concrete Walls"*** is the result of investigations carried out by myself at the Centre for Intelligent Cyber Physical Systems, Indian Institute of Technology Guwahati, Guwahati, India.

In keeping with the general practice of reporting scientific observations, due acknowledgements have been made wherever the work described is based on the findings of other investigators.

Date: 24.03.2026

Place: IIT Guwahati

Syed Bustan Fatima Warsi

Dedicated to

Almighty, My parents and family

Certificate

This is to certify that the thesis entitled ***"Design and Development of Earthquake Resistant 3D Printed Concrete Walls"*** by Syed Bustan Fatima Warsi (Roll No: 216156105), at the Centre for Intelligent Cyber Physical Systems (CICPS), Indian Institute of Technology Guwahati, Guwahati, India, for the award of Doctor of Philosophy, is a record of bonafide research work carried out by her under our guidance and supervision. The work embodied in this thesis has not been submitted for any other degree or diploma. In our opinion, the thesis is up to the standard of fulfilling the requirements of the doctoral degree as prescribed by the regulations of this Institute.

Date: 24.03.2026
Place: IIT Guwahati

Dr. Biranchi Panda

Assistant Professor
Department of Mechanical Engineering
Associate Faculty, CICPS
Indian Institute of Technology Guwahati
Guwahati-781039, Assam, India

Prof. Pankaj Biswas

Professor
Department of Mechanical Engineering
Associate Faculty, CICPS
Indian Institute of Technology Guwahati
Guwahati-781039, Assam, India

Acknowledgements

This thesis represents the culmination of the guidance, support, and encouragement of numerous individuals whose contributions have been invaluable throughout my PhD journey. The challenges encountered during this process have imparted lessons in perseverance, resilience, and dedication. Without the assistance of these individuals, the completion of this work would not have been possible, and I am profoundly grateful to all who have supported me, both directly and indirectly.

First and foremost, I express my heartfelt gratitude to my advisors, Dr. Biranchi Panda and Prof. Pankaj Biswas, for their unwavering belief in my capabilities and their continuous guidance. Their insightful feedback, constructive suggestions, and steadfast encouragement have been instrumental in shaping this research. Their pursuit of excellence and extensive expertise in 3D concrete printing have profoundly influenced my work and will continue to guide my future endeavours. Collaborating with them has been an intellectually enriching and rewarding experience.

Special thanks are extended to Dr. Arun Chandra Borsaikia, Department of Civil Engineering (Structural Engineering), whose insightful guidance and constructive feedback greatly strengthened the quality and direction of this research. I extend my sincere thanks to the members of my PMRF and Doctoral Committee—Prof. Santosha Kumar Dwivedy, Prof. Bulu Pradhan, Dr. Rinku Kumar Mittal, and Dr. Poonam Kumari—for their valuable suggestions, timely feedback, and unwavering support throughout the various stages of my research.

I am also deeply grateful to the former and current heads of the Centre for Intelligent Cyber-Physical Systems (CICPS), the project director of the Technology Innovation Hub (TIH), and the faculty and staff of TIH and CICPS for providing essential resources that facilitated the successful completion of this work. My appreciation extends to the faculty in charge of the Structural Engineering Laboratory, the Material Science Laboratory, and the Strength of Materials Laboratory, as well as to staff members Mr. Biswajit Debnath, Mr. Saurabh Mudoi, Mr. Pranab Hazarika, Mr. Saifuddin Ahmed, and Mr. Sanjib Sarma for their technical assistance. I also acknowledge the support of Mr. Bijoy Orang and Mr. Sujit Rajbhar, whose dedication was invaluable during the extensive experimental work. Furthermore, I appreciate the assistance provided by the Central Instruments Facility (CIF), CICPS, the Department of Mechanical Engineering, and the Department of Civil Engineering, IIT Guwahati.

I also extend my gratitude to my lab mates, colleagues, friends, and seniors. I give special thanks to Dr. Dodda Srinivas and Dr. Dhrutiman Dey for their invaluable assistance with 3D printing and throughout the experimental work. I am also grateful to Mr. Akshay Sahu and Mr. Shubham Maurya for their support during the testing and research activities. I further acknowledge Mr. Srajan Prakash, Mr. Boda Ramalingaiah, and Dr. Boddepalli Uday for their insightful discussions, collaborative efforts, and encouragement. I sincerely thank all those who, directly or indirectly, have contributed to shaping this work and supported its successful completion.

Finally, I owe my deepest gratitude to my parents and family for their unconditional love, encouragement, and sacrifices. Their unwavering support and belief in me have been the foundation of my achievements. I dedicate this thesis to them with profound respect and heartfelt appreciation.

Syed Bustan Fatima Warsi

Abstract

Three-dimensional (3D) extrusion-based concrete printing is transforming construction by enabling complex geometries with reduced material use, shorter construction times, and lower labor demands compared to conventional methods. Despite these advantages, widespread adoption is limited by challenges in material formulation, structural design, computational modeling, and process optimization. In seismic regions, the demand for resilient and sustainable systems drives increased interest in 3D printed concrete (3DPC). Achieving sufficient ductility, energy dissipation, and effective reinforcement integration, while ensuring constructability and cost-efficiency, remains a critical challenge. Existing studies predominantly emphasize static performance, with limited focus on cyclic behavior, leaving significant knowledge gaps in understanding the seismic response of 3DPC systems. This research addresses these challenges by developing earthquake-resistant 3DPC walls through an integrated approach combining material-level innovation, codal design adaptation, advanced numerical modeling, and full-scale experimental validation.

In the first stage, the material development process commences with a systematic investigation of constituent integration strategies. Preliminary trials incorporate coarse aggregate within the interlayer regions during printing, resulting in an increase of up to 32% in direct tensile strength. Subsequently, a range of fibers, including PVA, glass, and steel, are evaluated at dosages of 0.25–1.0% for their effect on buildability, extrudability, and mechanical properties. Steel fibers demonstrate superior performance, enhancing interlayer bonding and tensile behavior. To mitigate extrusion challenges, aggregates are incorporated during mixing and steel fibers are used at critical fiber volume determined through tensile and pull-out tests, while printing auger modifications ensure smooth aggregate passage. The optimized composite developed through this process exhibits distinctive strain-hardening behavior, with a yield point, strain-hardening factor of 1.62, ductility factor of 10.86, and energy absorption capacity of +105 kJ/m^3, confirming its suitability for seismic-resistant applications.

Subsequently, a robust numerical modeling framework is established to simulate the in-plane cyclic behavior of 3DPC walls. A composite interface micro-model, combining Concrete Damage Plasticity (CDP) and cohesive zone modeling, is developed to account for interlayer effects and localized failure mechanisms. Model validation against benchmark experimental data demonstrates high accuracy in predicting hysteresis response, stiffness degradation, and energy dissipation. Results of parametric studies suggest that seismic performance of the 3DPC

wall can be considerably enhanced by reducing height–width ratio and by inclusion of solid edge columns and continuous reinforcement throughout the wall. Incorporating the strain-hardening 3DPC material further improves wall performance, with lattice shear walls exhibiting a 108% increase in deformability and flexural walls achieving a 59% strength gain relative to control walls.

The third stage investigates the applicability of codal provisions (ACI 318-19, Eurocode 8, IS 13920:2016) for 3DPC wall design. Comparative analysis of single- and double-layer reinforcement systems under quasi-static cyclic loading shows that the double-layer configuration achieves 30.6% higher lateral load capacity (465.72 kN vs. 356 kN), 9.8% greater failure displacement, a higher ductility factor (4.36 vs. 4.01), and superior energy dissipation. The single-layer reinforcement, while lower in strength, maintains, reduces, and offers easier integration in 3DPC construction. To further enhance seismic performance, self-centering reinforcement and confined boundary elements are incorporated following codal guidelines, resulting in lateral strength gains of 54.08% and 46.89%, along with improved stability and damage tolerance.

In the final stage of the research, following the development of the optimized material and the selection of wall geometry and reinforcement configuration based on simulation and design outcomes, it is observed that conventional infill geometries are unsuitable for the proposed reinforcement layout. Hence, a modified infill pattern with hollow side regions is developed to facilitate reinforcement placement and reduce material usage by ~20%. Numerical simulations confirm a ~20% increase in lateral load capacity and slower stiffness degradation. Subsequently, full-scale quasi-static cyclic tests are performed on three 3DPC wall systems: (i) a plain mortar wall (3DPM), (ii) a 3DPC wall with strain-hardening ductile mix (3DPC-CF), and (iii) a modularly reinforced wall incorporating prefabricated steel cages within the 3DPC-CF matrix (3DPC-CFR). The experimental results demonstrate a clear progression in seismic performance, with 3DPC-CFR exhibiting the highest lateral strength (197%), delayed stiffness degradation, enhanced ductility (80%), and stable post-peak load retention compared to 3DPM. This research presents an integrated framework encompassing material-level innovation, codal design adaptation, advanced numerical modeling, and full-scale experimental validation of 3DPC structural walls. The findings advance the feasibility of deploying 3DPC for earthquake-resistant applications, contributing critical insights toward safe, economical, and scalable adoption in large-scale construction.

Table of Contents

List of Figures

List of Tables

Nomenclature

A_{cv}	Gross cross-sectional area of 3DPC wall
A_{st}	Total area of vertical reinforcement
c	Factor for neutral axis depth determination
d	Effective flexural depth
D	Dead load or self load of the 3DPC wall
d_c , d_t	Compressive and tensile damage parameter
d_{ult} , d_{yield}	Ultimate and yield displacement
D_0^{el}	Initial (undamaged) elastic stiffness
f_{cm}	Ultimate compressive stress of 3DPC
F_d	Flexural demand
f_y	Yield stress of reinforcement bar
E	Seismic load
E_c	Young modulus of 3DPC
E_i	Energy dissipated during each cycle
E_{in}	Elastic modulus of the layer interface
G_c	Shear modulus of 3DPC
G_{in}	Shear modulus of the layer interface
G_{IC}, G_{IIC}, G_{IIIC}	Specific fracture toughness for Mode I, Mode II, Mode III
h_w	Hight of the 3DPC wall
K	Ratio between second stress invarient on the tensile meridian and that on the compressive meridian,
K_n ,$K_s = K_t$	Normal and Tangential interface elastic stiffness
K_R	Rate of stiffness degradation
K_{si}, K_o	Secant and initial stiffness

l_w	Length of the 3DPC wall
M_d	Design flexural strength
M_n	Nominal flexural strength
P_O	Axial compressive strength
P_d	Design axial compressive strength
P_{max}	Maximum load under load–displacement curve
P_{yield}	Yield load under load–displacement curve
P_n	Nominal axial compressive strength
s	Reinforcement spacing
S_d	Shear demand
T	Total tensile component of force couple during bending
t_c	layer thickness
t_w	Thickness of the 3DPC wall
V_d	Design in-plane shear strength
V_n	Nominal in-plane shear strength
α, β, ω	Neutral axis determination factor
α_c	Coefficient defining the relative contribution of concrete strength
ϕ	Nominal flexural strength determination factor
ϕ_v	Strength reduction factor for shear
ϕ_c	Strength reduction factor for compression
ϑ	Poisson ratio
μ	Displacement ductility
ε_1	Strain at peak stress
ε_{c1}	Strain at peak stress
ε_{cu1}	Ultimate strain
ε_c^{in}	Inelastic (crushing) strain
ε_{oc}^{el}	Elastic strain corresponding to the undamaged material
ε_c^{pl}	Plastic compressive strain tensor

ε_t^{pl}	Plastic tensile strain tensor
ε_{nom}	Nominal strain tensor
ε_{true}^{pl}	True plastic strain
σ_c	Compressive stress tensor
σ_{c0}	Compressive yield stress of 3DPC
σ_{true}	True plastic stress
$\delta_{max,i}$	Maximum displacement during the i^{th} load cycle
ρ_l, ρ_t	Vertical and horizontal reinforcement check
λ	Factor accounting for aspect ratio
ζ_{eq}	Equivalent viscous damping ratio

Chapter 1

Introduction

This chapter outlines the overall structure of the thesis and introduces the potential of digital construction technologies, particularly 3D concrete printing, in advancing structural and seismic applications.

1.1. Background and motivation

In recent years, 3D printed concrete (3DPC) has emerged as a groundbreaking technology, offering unprecedented flexibility and efficiency for constructing complex forms with reduced material and labour demands [1]. The 3D printing techniques, specifically extrusion-based 3DPC, the emergence of 3DPC technologies has introduced new paradigms in structural construction, offering automation, geometric flexibility, and material efficiency [2–4]. Despite rapid progress in 3DPC extrusion systems, and printable cementitious materials [5,6], the application of 3DPC to seismically resilient structural components remains in its infancy. As the main vertical structural component, walls deserve to be studied thoroughly in terms of their mechanical performance since they easily can be automatically constructed on site. Some researchers have recently performed simple loading tests of 3DPC walls, such as axial compressive or eccentric compression, and the failure modes and mechanical performance are determined. To the best of our knowledge, only a limited number of studies have experimentally investigated the seismic behavior of 3DPC walls [6–9]. However, these investigations are mostly confined to specific reinforcement systems or isolated wall configurations, while aspects such as material design, reinforcement detailing with standard design provisions, and failure mechanisms under realistic cyclic loading remain largely unexplored. This leaves significant gaps in developing a comprehensive understanding of the seismic performance of large-scale 3DPC walls. In 3DPC, steel reinforcement remains the most widely adopted approach, similar to conventional construction. However, its integration must be carefully managed to avoid disrupting the printing process, while ensuring adequate bond with the printed matrix, since this interface is critical to structural performance [10]. Another critical limitation is the lack of standard design provisions specific to 3DPC systems, particularly for reinforcement detailing, ductility, and energy dissipation—essential parameters in earthquake-resistant design.

In conventional reinforced concrete construction, performance under seismic loading is governed by material ductility, well-detailed reinforcement. Transferring these principles, directly to additive manufacturing is non-trivial, due to geometric constraints and the difficulty of integrating reinforcement during or after printing. Moreover, while advanced strain-hardening cementitious composites have been shown to enhance tensile behavior at the material level, their integration within reinforced and dynamically loaded 3D printed structures has not been adequately explored in full-scale systems. Furthermore, in most existing studies, 3D printed walls are often used as formwork rather than primary load-bearing components, and

the baseline mechanical behavior of plain 3D printed mortar walls is not comprehensively documented—making it difficult to predict their actual structural response. To address these gaps, the present research systematically investigates the progressive enhancement of 3D printed wall systems through large-scale cyclic testing. A plain mortar wall is first evaluated as a reference specimen. Subsequently, a specially engineered strain-hardening ductile composite is introduced, and finally, an optimized modular reinforcement layout is integrated within the enhanced material system. The reinforcement is configured using a prefabricated cage and designed infill pattern, enabling compatibility with the 3D printing process. This practical and scalable approach is aimed at facilitating real-world deployment of 3DPC in seismic regions, thereby advancing its structural applicability and accelerating the global adoption of this emerging construction technology.

1.2. Objectives and scope

The main objectives of this research work are as follows:

1. To develop a novel ultra-ductile strain-hardening 3D printed concrete composite by utilizing critical fibre volume and coarse aggregate.
2. To evaluate the structural performance of 3DPC walls under cyclic loading using advanced numerical analysis, through:
    a. Development and validation of a numerical modelling framework for 3DPC walls using experimental data from the literature
    b. Assessment of the influence of key design parameters and material properties on the cyclic behaviour of 3DPC walls
3. To characterize the structural behaviour of 3DPC walls under cyclic in-plane loading by
    a. Designing structural 3DPC wall systems in accordance with codal provisions
    b. Optimizing reinforcement strategies and structural parameters through parametric numerical analysis to achieve improved strength, ductility, and efficiencyprovisions
4. To experimentally evaluate the in-plane cyclic behavior of a full-scale 3DPC walls through quasi-static testing, focusing on the interaction between material properties, reinforcement configuration, and overall structural performance.

1.3. Thesis organization

This thesis is organized into seven chapters, each focusing on a specific aspect of the research:

Chapter 1: Introduces the overall research problem, emphasizing challenges in material design, reinforcement integration, numerical modeling, and seismic performance of 3DPC systems. The motivation, research objectives, and the overall structure of the thesis is also defined.

Chapter 2: Reviews state-of-the-art literature on 3DPC materials, reinforcement approaches, and structural performance under static and cyclic loading, identifying key research gaps.

Chapter 3: Development of strain-hardening 3DPC composite for seismic applications addresses Objective 1, focusing on the formulation of an ultra-ductile strain-hardening composite incorporating critical fiber volume and coarse aggregate, with detailed mechanical characterization.

Chapter 4: Numerical framework for cyclic behavior corresponds to Objective 2 and develops a composite interface-based numerical modeling framework for 3DPC walls. Validation against benchmark data and parametric studies are performed to assess the influence of design parameters and material innovation.

Chapter 5: Codal provisions and reinforcement optimization addresses Objective 3 by evaluating codal design frameworks and optimizing reinforcement strategies through parametric numerical simulations, aiming to achieve robust and lightweight 3DPC walls.

Chapter 6: Experimental investigation of full-scale 3DPC walls addresses Objective 4 by conducting quasi-static cyclic tests on full-scale walls to evaluate in-plane behavior, strength, ductility, material and reinforcement performance.

Chapter 7: Conclusions and future work summarises the major findings of the research and provides recommendations for further studies on earthquake-resistant 3DPC structures.

Chapter 2

Literature Review

*This chapter critically examines the current state of research in 3DPC with a focus on material development, reinforcement strategies, structural performance, and seismic behavior. It reviews studies on extrusion-based 3DPC composites, including fiber-reinforced and aggregate-integrated mixes, highlighting advances in ductility, energy dissipation, and interlayer bonding. The chapter also surveys numerical modeling approaches for cyclic and seismic performance assessment of 3DPC walls, as well as codal design adaptations and experimental investigations of full-scale walls. Key research gaps are identified, particularly regarding integrated approaches that combine material innovation, reinforcement optimization, and seismic resilience in large-scale 3DPC structures, which forms the motivation for the present research.

*A portion of this chapter has been published in:

1. **Warsi SBF**, Panda B, Biswas P. Exploring fibre addition methods and mechanical properties of fibre-reinforced 3D printed concrete: A review. Developments in the Built Environment 2023;16:100295. https://doi.org/https://doi.org/10.1016/j.dibe.2023.100295.
2. **Warsi SBF**, Srinivas D, Panda B, Biswas P. Investigating the impact of coarse aggregate dosage on the mechanical performance of 3D printable concrete. Innovative Infrastructure Solutions 2023;9:5. https://doi.org/10.1007/s41062-023-01317-0.

2.1. 3D concrete printing

The majority of the literature classifies additive manufacturing of cementitious materials, or 3DPC, into two categories: binder jetting [14] and extrusion-based 3DPC [15]. The underlying concept behind these two techniques is to build a three-dimensional structure layer by layer until it is finished. These techniques also require a 3D model that has been divided into 2D layers for printing, much like other 3D printing techniques. The detailed description of these methods is presented below.

2.1.1. Binder jetting

Enrico Dini recommended binder jetting method for creating complex 3D structures [16]. The idea behind binder jetting in construction is similar to that of inkjet 3D printing [26]. In this method, a printing head is used to spray a liquid binder over the thin layer of material. According to the slice geometry, the head follows the contour. By utilising this technique, it is simple to print a structure's overhanging feature without the use of a support structure. In 3D printing, the slice height of material deposition affects the surface quality and construction time of the component. Large slice height will shorten build time but will make inclined and freeform structures' surfaces rougher, and vice versa. When using a binder jet, the height of the slice is determined by the capacity of the binder to penetrate. Because the capacity of the binder to penetrate is so limited, the slice height is likewise much lower than with other AM processes utilised in construction. Minimal slice (5mm) height of binder jetting produces fairly acceptable surface quality (Fig. 2.1) [16].

Fig. 2. 1 Structures created by binder jetting [16].

2.1.2. Extrusion based 3D concrete printing

Extrusion-based 3D printing (3DPC) is a digital fabrication technique which combines extrusion process with 3D printing [17]. The component shown at the bottom of Fig. 2.2 shows the finish that is possible right out of the factory. 3DPC can create highly specialised structural components [18] and Contrary to D-Shape, it uses a single nozzle, ensuring that the structure contains only the necessary volume of material. However, a single nozzle technique eventually limits the deposition speed because the nozzle must circulate throughout the structure. The earliest work of using the technology in the construction industry was by Pegna, and later it was popularized by Khoshnevis who invented the contour crafting technique.

Fig. 2. 2 3D printed concrete bench [17].

2.2. Material development in 3D printed concrete

2.2.1. Extrusion based 3D printing of fibre reinforced concrete

A key issue in 3DPC is the difficulty of placing traditional reinforcement, which has led to the adoption of fibers as an alternative method to enhance structural performance without complicating the printing process [19,20]. 3D printed fibre reinforced concrete is useful in many construction projects as they can reduce shrinkage and deformation in the plastic stage [21]. Fibres can be added in extrusion-based concrete printing before and during the printing (see Fig. 2). Different kinds of short fibres added in the past by the researchers (before printing) are carbon and basalt fibres [22], [23], green tow flax [24], glass fibres [25], Polyethylene (PE) fibres [26], Polypropylene (PP) and hooked-end steel fibres [27], Polyvinyl alcohol (PVA) fibres [28,29], steel fibres [30,31], and wollastonite microfibres [32]. However, very few fibres such as carbon, basalt, glass, and steel fibres [33–35] are found to be added during the printing process via following methods.

- Methods of fibre addition before 3D printing:
    a. Pre-mixed fibres: Fibres are thoroughly mixed with the printing material before the printing process begins.
    b. Fibre impregnation: Fibres are soaked or impregnated with a binding agent or resin prior to printing.
    c. Fibre suspension: Fibres are suspended in a liquid solution and then mixed with the printing material.
- Methods of fibre addition during 3D printing:
    a. Inline fibre dosing: Fibres are added directly to the printing nozzle or extruder during the printing process.
    b. Layer-wise fibre deposition: Fibres are deposited layer by layer onto the freshly printed concrete layer.
    c. Fibre spraying: Fibres are sprayed onto the printed layers using specialized equipment.
    d. Fibre insertion: Fibres are manually or automatically inserted into specific regions of the printed object.
    e. Fibre weaving: Fibres are interlaced or woven into the printed structure as it is being built.

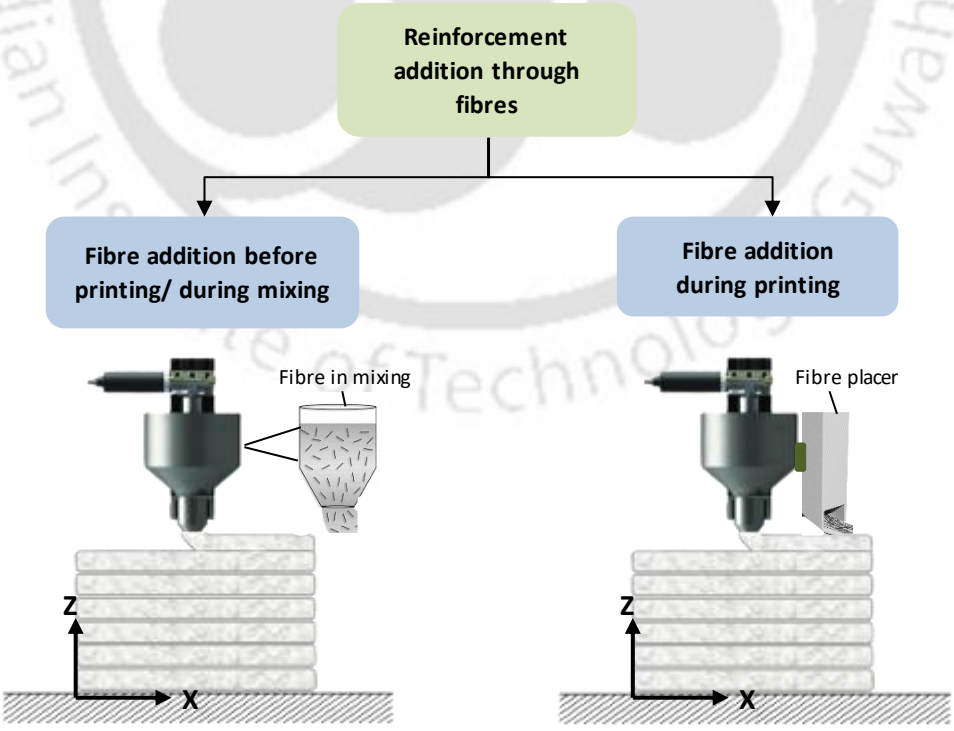

Fig. 2. 3. Schematic representation of classification of fibre addition during 3D concrete printing (schematic developed for illustration purposes)

The quantity of fibres introduced into a concrete mixture is denoted as a proportion of the overall volume of the composite, known as the "volume fraction" (V_f). This V_f typically falls within the range of 0.1% to 3%, In case of fibre reinforced 3D printed concrete. The aspect ratio (l/d) is determined by dividing the length (l) of the fibre by its diameter (d). For non-circular cross-section fibres, an equivalent diameter is employed to compute the aspect ratio. Certain companies have integrated reinforcement methods that are pre-installed or post-installed [36]. These approaches eliminate the necessity of integrating the reinforcement system during the printing process, affording greater flexibility in reinforcement placement.

2.2.1.1. The effect of fibre addition before printing

Fig. 2.4 presents a comprehensive analysis of the mechanical properties of various fibre-reinforced 3D printed concrete composites at different fibre volume fractions (ranging from 0% to 2%) with uniform fibre length of 6 mm. The data collected from different research studies revealed noteworthy variations in strengths even at the same fibre content. For instance, at 1% carbon fibre content, Korniejenko et al. [24] reported a compressive strength of 40.33 MPa and a flexural strength of 8.1 MPa, whereas Hambach et al. [37] achieved a higher compressive strength of 60 MPa and a flexural strength ranging from 10 to 30 MPa (depending on print path). Similar discrepancies were observed for 1% glass fibre content, with Panda et al. [38] obtaining a compressive strength of 22.74 MPa and a flexural strength of 5.82 MPa, while Hambach et al. [37] achieved a significantly higher compressive strength of 60 MPa and a flexural strength of 13 MPa. These variations suggest that the strength of fibre-reinforced 3D printed concrete not only depends on the fibre content but also on other factors such as the use of engineered cementitious composites (ECC) or strain-hardening cementitious composites (SHCCs) [39,40] [41] can significantly improve the mechanical properties of the material compared to conventional concrete due to their ductile nature. The results, as depicted in both Fig. 2.4 and Table 2.1, illuminate discernible trends in the mechanical properties of fibre-reinforced 3D printed concrete.

Table 2. 1. Strength increment (+) or decrement (-) with respect to non-fibrous element (%)

Fibre type	Fibre dosage (%)	Strength increment (+) or decrement (-) with respect to non-fibrous element (%)			Remark	Cross Ref
		Compressive strength	Flexural strength	Tensile strength		
Steel	0.25-1	-1.82 to +10.95	+10 to +22.05	-	Influenced by layer bonding strength	[31]
	1-2	-	-	+113.29 to +165.03		[42]
Carbon	1	-15.68	+9.02	-	Strength decrement due to void between layers	[24]

Glass	0.25-1	-6.67 to -14.01	+9.18 to +44.42	+11.27 to +85.92	Performance influenced due to density variation	[38]
HDPE	1-1.5	-	-	+6.39	Strain-hardening behaviour	[41]
Basalt	0.22-0.86	-0.02 to -18.1	-1.62 to -17.75	-	Changes in the interfacial transition	[43]
PVA	0.25-1.5	-2.38 to -22.37	-4.61 to -9.41	-	Higher percentage of porosity	[44]
PP	0.25-1	-29.89 to +15.11	-1.29 to -2.59	-	Fibre-induced increase in entrapped air	[45]
PE	1-2	-2.64 to +3.87	-	-	Interfacial interactions between PE fibres and the matrix	[39]
	0.25-2	-	+88.19 to +250.55	+32 to +328		[46]

For instance, the introduction of steel fibres exhibits noteworthy outcomes. A clear trend emerges wherein the compressive strength attains a peak of 101.33 MPa at a 0.75% fibre content. However, when the steel fibre content is raised from 0.75% to 1%, a corresponding 11.51% reduction in compressive strength is observed (Fig. 2.4 (a)). Conversely, the presence of steel fibres positively impacts flexural strengths, primarily influenced by the bond strength between layers [31].

Moving on to glass and PP fibres, their compressive and flexural strengths exhibit relatively less variance with varying fibre content (Fig. 2.4 (b)). Nevertheless, when compared to specimens containing 0.25% glass fibres and without PP fibres, both glass and PP fibres contribute to a reduction in compressive strength by 14.01% in the case of glass fibres and by 29.89% for PP fibres. However, the flexural strength behaves distinctively. For glass fibres, it increases by 44.42% at a 1% fibre dosage compared to specimens containing 0.25% fibre dosages. This effect can be attributed to the closer packing of material due to the high pumping pressure exerted during mortar extrusion [38]. It is important to note that the extruder's shape partly influences performance by causing density variations in the printed part. In the case of PP fibres, a decrease of 2.59% in strength is observed at a 1% fibre dosage when compared to specimens without fibres. This variation may be due to a fibre-induced increase in entrapped air, resulting in higher porosity within the mixture [45].

Further examination of basalt and PVA fibres reveals a reduction in both compressive and flexural strength. For basalt fibres, increasing the fibre dosage from 0.22% to 0.86% leads to an 18.1% decrement in compressive strength and a 17.75% decrease in flexural strength. In the case of PVA fibres, a 22.37% reduction in compressive strength and a 9.41% drop in flexural strength are recorded at a 1.5% fibre dosage when compared to specimens without fibres. This decline can be primarily attributed to changes in the interfacial transition zone (ITZ) between the fibres and the bulk matrix of paste [44]. An increased quantity of PVA fibres results in

greater total surface area, necessitating more paste matrix for nucleation, consequently leading to a higher percentage of porosity. In the case of basalt fibres, the strength reduction is attributed to the presence of entrapped air bubbles in the interlayer zone between consecutive layers [43].

The carbon and PE fibres exhibit some positive results, particularly in flexural strength. An increment of 9.02% in flexural strength is observed at a 1% carbon fibre content when compared to specimens without fibres. The PE fibres demonstrate even more pronounced results, displaying a significant increase in flexural strength, specifically 250.55%, at a 1.4% fibre dosage when compared to specimens without fibres. This is indicative of the significant positive effect of increased PE fibre content on the flexural strength of the printed material, primarily due to interfacial interactions between PE fibres and the matrix [46] (Fig. 2.4 (a, b)). Conversely, both carbon and PE fibres display reduced compressive strength, with decrements of 15.68% and 2.64% observed at 1% and 2% fibre dosages, compared to specimens without fibres and with 1% fibre dosages, respectively. This reduction results from the introduction of small pores between the printed layers due to the nature of the 3D printing process [39].

In the context of tensile strength (Fig. 2.4 (c)), all fibres exhibit an increment in tensile strength as fibre content increases. Notably, the steel and PE fibres demonstrate substantial improvements, with a remarkable increase of 165.03% and 328% at 2% fibre content compared to specimens without fibres. The well-documented crack-bridging effect of steel and PE fibres contributes to this considerable enhancement [47]. Furthermore, although the hydrophobic nature of PE and HDPE fibres reduces fibre–matrix chemical bonding, it promotes controlled debonding and frictional pull-out, thereby significantly enhancing the complementary energy of fibre bridging [48], [41].

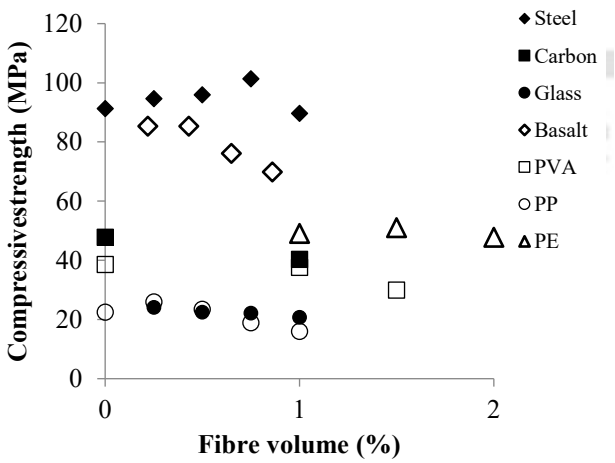

(a) Compressive stength versus fibre content

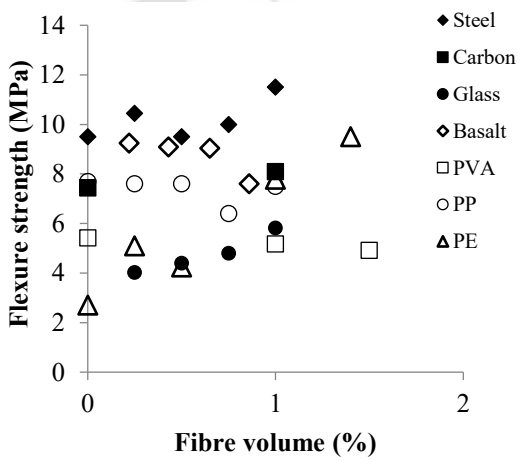

(b) Flexure strength versus fibre content

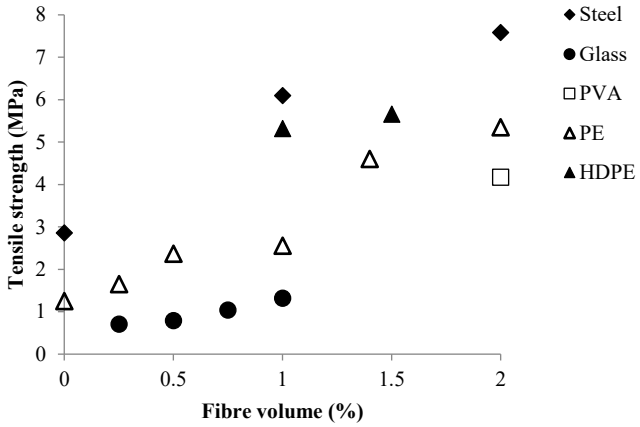

(c) Tensile strength versus fibre content

Fig. 2. 4. Strength of various fibre composites at different fibre content [31], [24], [38], [46], [39], [41], [45], [42], [43], [44]

In conclusion, it is essential to view the data in the table as part of a broader framework that considers the myriad variables influencing the behaviour of fibre-reinforced concrete. By taking these factors into account, we can better comprehend and interpret the observed variations in mechanical properties across different studies. These results emphasize the significance of optimizing fibre content in 3D printed fibre-reinforced concrete to achieve a balanced combination of mechanical properties. Attentive calibration of fibre ratios is essential to produce structurally robust materials, while averting potential vulnerabilities stemming from excessive fibre content. This delicate equilibrium is vital to attaining the desired mechanical properties in 3D printed concrete.

2.2.1.2. The effect of fibre addition during printing

The entrainment of reinforcement directly into the 3D printing process can be achieved by different mechanism or process such as (i) stationary impregnation process (Fig. 2.5), where fibre can be supplied to the print head in three different ways, (a) supply from a spool (two-step process), (b) supply from a continuous, stationary impregnation line (one-step process), (c) supply from a mobile impregnating device (one-step process) [49], (ii) Flow-Based Pultrusion (FBP) and (iii) Extrusion Moulding (EM) technique for continuous fibres in additive manufacturing [34,50], (iv) repetitive sequential process (fibres are added in between the layers of deposited cementitious filament) [51], (v) un-bonded post-tensioning and conventional bonded passive fibre reinforcement technique [33]. Herein, we discuss the effect of different fibre addition during the printing process on mechanical performance of 3D printed concrete.

(a) Supply from a spool

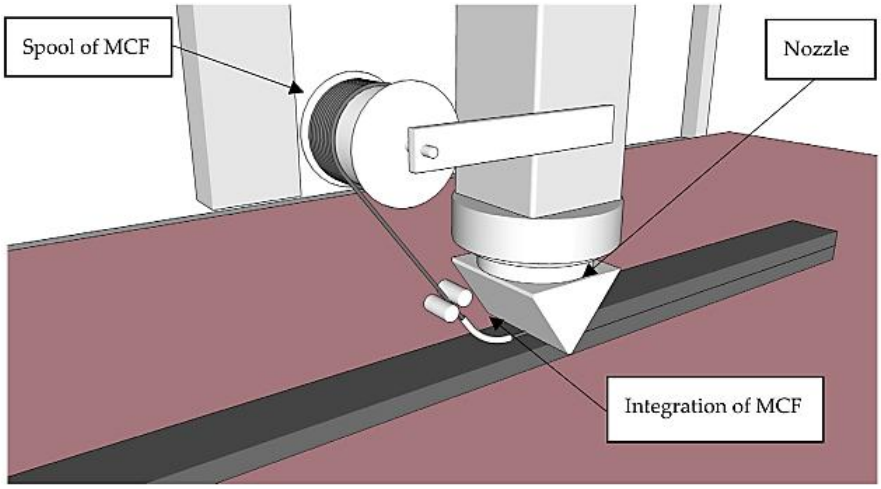

(b) Supply from a continuous impregnation line (c) Supply from a mobile impregnating device

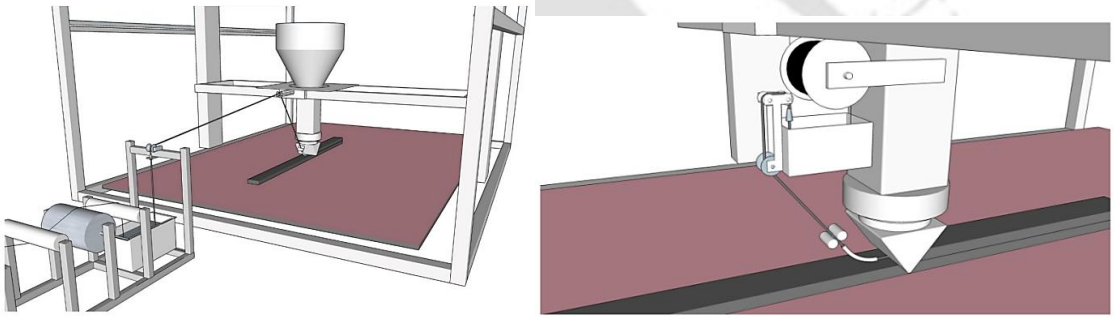

Fig. 2. 5. 3D concrete printing with mineral-impregnated CF [49]

Mechanical properties of fibre reinforced 3DPC when fibres are added during printing have investigated by few researchers, where compressive, flexure and tensile strength of 3D printed specimens containing steel fibre have been examined [33,51,52]. The strength of 3D printed specimens containing steel fibre with respect to different fibre content (0%-1.2%) has been plotted in Fig. 2.6. As reported by Ahmed et al. [51], the influence of steel fibres on compressive strength does not follow a consistent monotonic trend, with an initial increase at lower fibre contents followed by a reduction at higher dosages. In contrast, flexural strength exhibits a clear increasing trend with increasing fibre content, which is consistent with general observations in fibre reinforced concrete (FRC) [51]. Similarly, tensile performance shows improvement at higher fibre dosages, primarily due to fibre bridging mechanisms. It is important to note that, in fibre reinforced concrete systems, the primary benefit of fibre incorporation lies not only in strength enhancement but in improved post-cracking behaviour and toughness. The inclusion of fibres enhances energy absorption capacity and crack resistance through bridging action, even when the increase in compressive strength is limited or inconsistent.

However, in the context of 3D printing, the addition of fibres during the extrusion process may introduce filament disruption and interlayer defects, which can adversely affect interfacial bonding between printed layers [51]. This process-induced heterogeneity can explain the variation and occasional reduction in compressive strength at higher fibre contents.

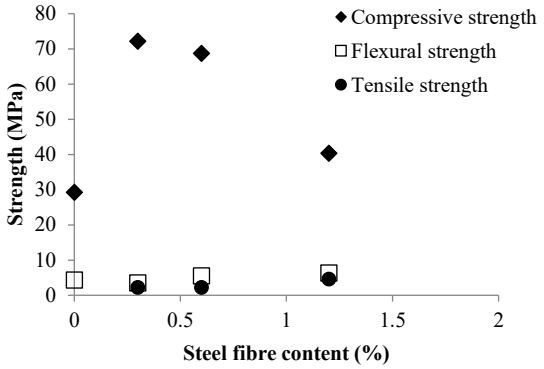

Fig. 2. 6. Strength of steel fibre reinforced 3DPC at different fibre content [51]

Additional investigations [51,52] have also corroborated this observed trend. In the absence of steel fibres, the compressive strength and flexural strength are quantified at 29.2 MPa and 4.3 MPa, respectively [52]. However, at a steel fibre content of 1.2%, the compressive strength experiences a notable augmentation to 40.3 MPa, accompanied by an increase in flexural strength to 6.3 MPa [51]. These results indicate that moderate fibre addition can enhance strength, whereas excessive fibre content may lead to reduced compressive performance due to poor dispersion and weak interfacial zones. Furthermore, increasing fibre content significantly improves toughness and post-peak behaviour, which are critical for structural performance under loading, particularly in applications requiring energy dissipation. The enhanced toughness is attributed to increased fibre bridging, pull-out resistance, and crack arresting mechanisms.

Nevertheless, excessive fibre content can lead to fibre clustering, poor workability, and inadequate bonding, resulting in localized weak zones. Therefore, an optimal fibre dosage is essential to achieve a balance between strength, toughness, and printability. The integration of fibres during the printing process significantly influences the mechanical response of 3D printed concrete and requires careful control to ensure optimal structural performance.

2.2.2. Incorporation of coarse aggregates into 3DPC

2.2.1.1. Background

3DPC is an innovative additive manufacturing technique although the material used in 3DPC is commonly referred to as concrete, the majority of them are primarily mortar with no coarse

aggregate [53–58]. There is limited research on the utilization of coarse aggregate in 3D printed concrete mixtures [59–62]. One study by Yu et al. 2022 [63] is conducted on 3DPC with coarse aggregate, which differed from extrusion-based concrete printing in which coarse aggregates were incorporated into the printing process and served as the supporting material (Fig. 2.8). However, a very interesting property of these specimens, such as split tensile behaviour, was not investigated in their research [63].

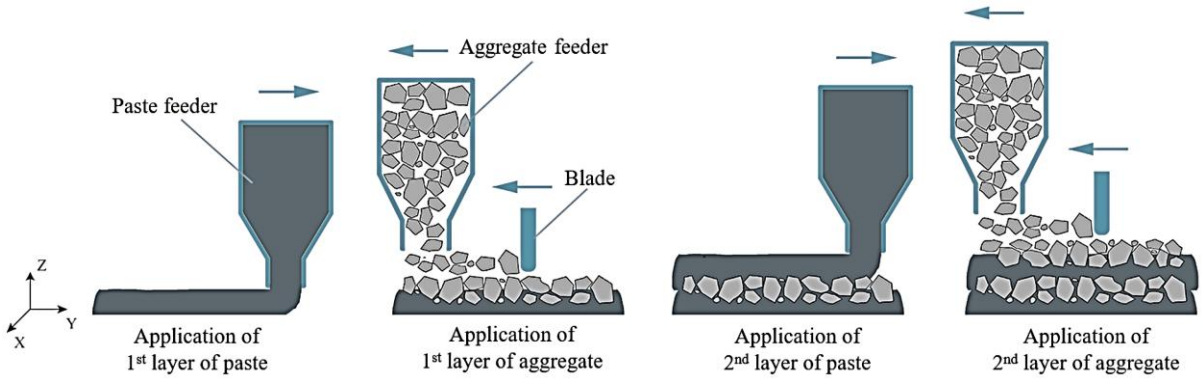

Fig. 2. 7. Aggregated-bed 3D concrete printing process [63]

When compared to traditional construction methods, 3D printing has enormous potential, including greater architectural freedom, faster construction, lower labor costs, fewer work-related injuries, and less waste material [64]. As evident from the literature, 3DPC has witnessed significant advancements in recent years. Notably, various large-scale structures [65–67]] have been successfully printed, including multistoried buildings and the world's first 3D-printed five-story building in China [68]. However, some researchers believe that the current low average strength of mortar may limit the availability of 3DPC to lightweight or art buildings rather than large, heavy buildings [69], and that the sensitivity of mortar to construction sites may influence the on-site applications of 3DPC [70]. Despite the fact that 3DPC mortars are becoming leaner, featuring lower cement content and higher volumes of supplementary cementitious materials (SCMs), and grow in their respective field's application (for example, architectural elements, furniture, and urban elements), the transition from mortar to concrete is a sensible approach not only from the standpoint of sustainability but also in terms of cost. This is because large aggregates are the least expensive (in terms of cost and CO_2 emissions) components in concrete. Specifically, the CO_2 emissions associated with large aggregates correspond to around 1/100 to 1/150 of that from CEM I [71]; which is a typical ordinary Portland cement (OPC).

Coarse aggregates have been observed to penetrate interlayers and improve interlayer bonding [72,73], thereby enhancing the structural robustness and practical applicability of 3DPC. Their

inclusion offers significant advantages by improving load transfer and reducing material consumption, contributing to the overall efficiency of the system. However, the integration of coarse aggregates also presents challenges. As shown in Fig. 2.9, inadequate compaction in the 3D printing process—where consolidation depends solely on extrusion pressure and the weight of subsequent layers—can lead to weak interfacial bonding between the matrix and aggregate. This imperfect bonding promotes localized porosity, which ultimately compromises the strength and uniformity of the printed material. This interfacial behaviour is particularly relevant to the present study, as the mechanical performance and failure characteristics of 3DPC walls are strongly governed by interlayer bonding and the integrity of the aggregate–matrix interface.

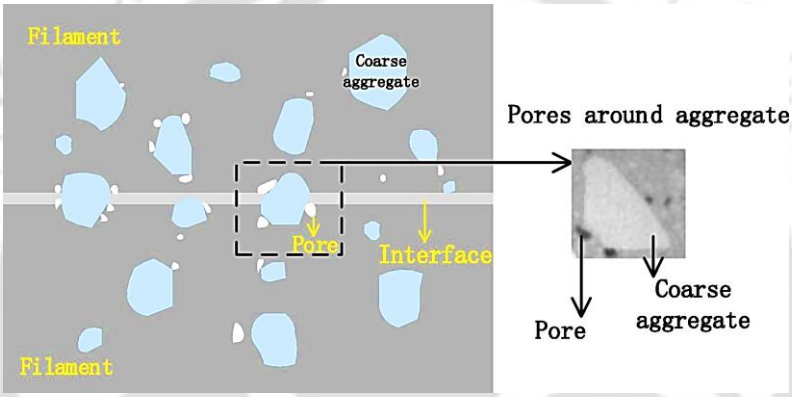

Fig. 2. 8. The pores around aggregate in 3DPC [74]

2.2.1.2. Hardened state properties

Research into the hardened state mechanical performance of 3D printed concrete (3DPC) with coarse aggregate (CA) is growing, though findings highlight both benefits and limitations.

Compressive strength

Studies show that adding coarse aggregates generally reduces compressive strength compared to printed mortar (3DPM) or cast concrete, mainly due to increased porosity and weaker interfacial transition zones (ITZ) (Fig. 2.10) [73]. Fig. 2.10 further highlights the influence of loading direction and material composition on compressive strength, emphasizing the anisotropic nature of 3D printed systems, which is a critical consideration for structural applications. For example, in Extrusion-based 3DPC with coarse aggregate, a specimen with coarse aggregate up to 20 mm had lower compressive strength than comparable cast specimens; strength reductions are attributed to voids and non-uniform matrix-aggregate bonding [2]. Similarly, 3D printed recycled coarse aggregate concrete (3DPRAC) showed that as the recycled aggregate content increased, compressive strength decreased, especially at higher

replacement ratios [75] (Fig. 2.11). The inclusion of coarse aggregate (CA) changes the degree of anisotropy. In 3DPRAC, for example, mechanical tests revealed notable anisotropy in both compressive and flexural strengths, with lower strengths when loading across layers versus along layers. Some Ultra-High-Performance Fiber Reinforced Concrete studies with coarse aggregate show over 100 MPa compressive strength even with CA, but still some anisotropy remains [76].

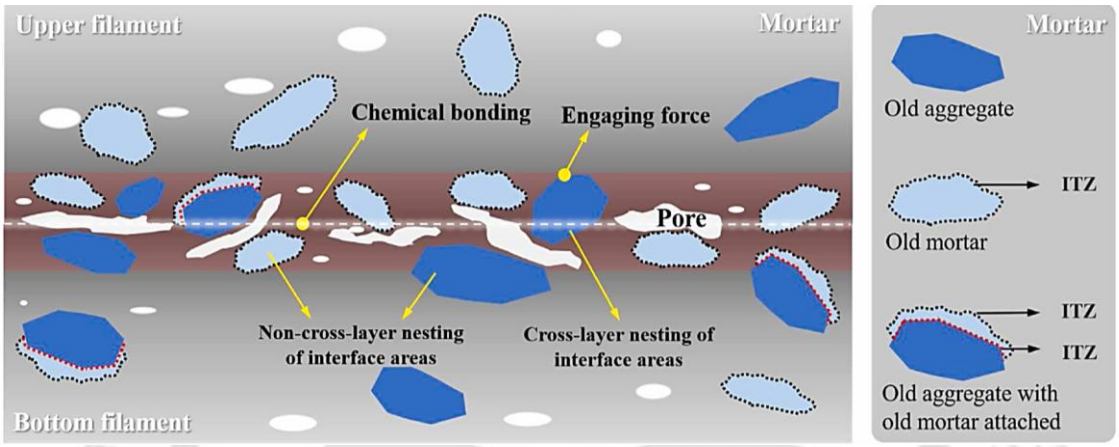

Fig. 2. 9. Schematic presentation of the 3DPRAC filament interface composition [73]

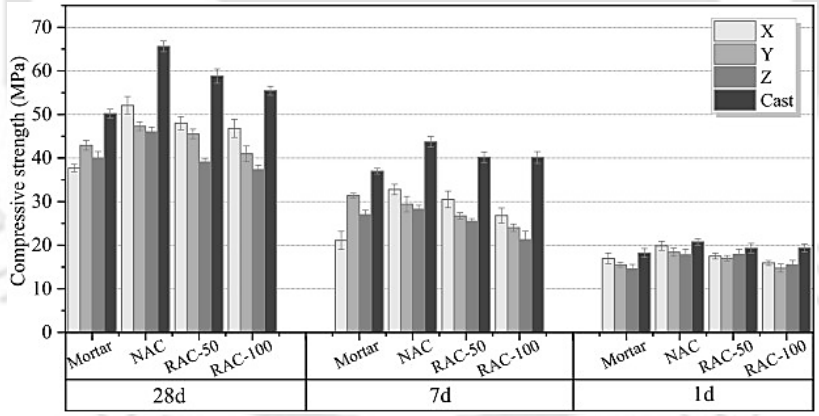

RAC-100: recycled coarse aggregate concrete with a 100 % replacement ratio)
NAC: Natural coarse aggregate

Fig. 2. 10. Test results in compressive strength for different ages, replacement ratios, and loading directions [75]

Flexural, tensile strength and interlayer bonding

Flexural strength tends to show stronger dependence on printing direction when coarse aggregates are used [2]. Flexural strength perpendicular to the printing direction decreased significantly more (≈20-25 %) relative to parallel direction than compressive strength (≈5 %) when compared to cast specimens [77]. Also, with recycled coarse aggregate (RCA), interlayer bond strength deteriorates with increasing RCA content and longer time intervals between layer

deposition due to the weak mechanical properties of old mortar and ITZs [73]. However, even with a 100% replacement ratio, the interlayer bond strength remained substantially greater than that of 3DPM. This is mainly because the RCA across the layers embedded at the interlayer interface widens the bond area and force transfer path at the 3DPRAC interlayer interface, enhancing the interlayer bond performance of 3DPRAC overall (Fig. 2.12(c)).

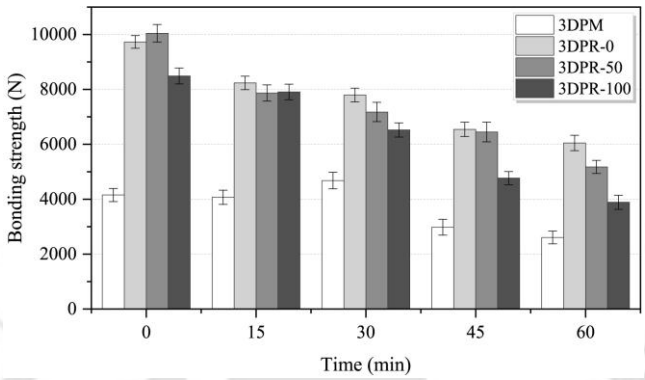

Fig. 2. 11. The variation in bond strength with printing time interval [73]

2.2.1.3. Porosity, microstructure and other properties

Coarse aggregate tends to increase macroscopic voids, especially around interlayers. For RCA mixes, the pore geometry becomes more elongated (ellipsoidal), more oriented along the printing direction, and interfilament and interlayer voids grow larger [73]. The microstructure near the interfaces between aggregate and matrix often shows weak bonding, which acts as crack initiation sites (Fig. 2.23). SEM and X-CT studies confirm that total porosity, pore volume and size distribution increase with higher CA content, and that interlayer pores are especially critical [77].

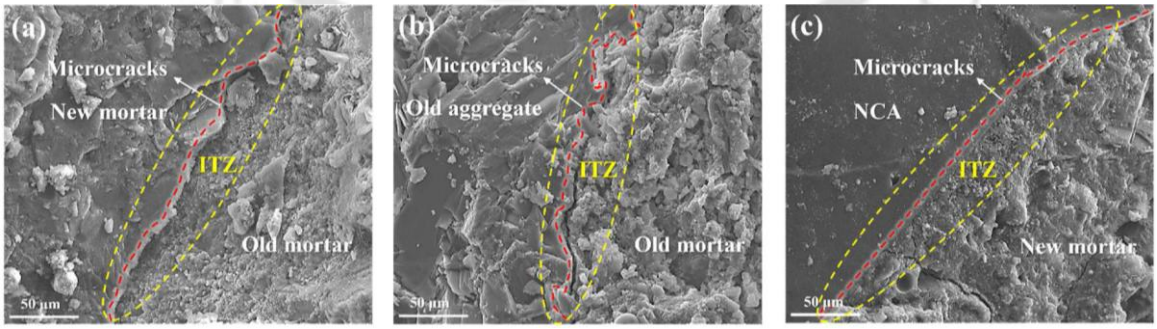

Fig. 2. 12. Microscopic morphology of old mortar and new mortar [73]

On durability and other hardened properties there are few studies so far, but there is evidence that CA inclusion can affect shrinkage, cracking behaviour, and possibly long-term durability [78]. However, many durability tests are with mortar mixes; CA-based 3DPC durability data are more limited. The benefits of coarse aggregate (lower binder content, potential for higher

strength, cost and carbon savings) come at the cost of reduced flowability, increased risk of nozzle blockage, issues in layer deposition, and weaker interlayer bonding. Also, field-scale implementation is scarce; most experiments are lab-scale, small specimens. The inability to compact and reliance on extrusion pressure / overlying layer weight limits how well CA mixes can eliminate voids and ensure strong bonding.

2.2.3. Material Innovations and research gaps

There is a need for more sustainable mix designs in 3DPC which also exhibit superior structural performance such as ECC [79], particularly noting that many existing mixes exclude coarse aggregates, leading to concerns about the material's long-term performance. While significant research has focused on the fresh-state properties of 3D printed ECC [80–82], a gap exists in understanding its hardened-state properties, which are crucial for ensuring structural integrity over time [83,84]. Addressing this gap is essential for expanding the practical use of 3D printed strain-hardening ECC in construction.

One of the challenges in enhancing the performance of 3DPC involves the interaction between fibers and aggregates in the hardened state. For example, Chen et al. [85] noted that increasing steel fiber volume in 3DPC can result in poor fiber orientation due to the presence of coarse aggregates, leading to material anisotropy. Zhu et al. [86] compared traditional ECC with 3D printed ECC and found that the latter exhibited more uniform fiber dispersion, resulting in higher tensile strength and strain capacity. Further research by Pham et al. [87] and Yang et al. [88] highlighted the importance of fiber size and directional alignment in optimizing mechanical properties, particularly tensile and flexural strength. Although these studies have provided valuable insights into fiber performance [87–90], they largely neglect the role of coarse aggregates and their interaction with fibers. Coarse aggregates are critical not only for improving fiber distribution but also for enhancing interfacial bonding, both of which significantly impact the mechanical properties of 3DPC structures [85]. Additionally, there is limited research on determining the optimal fiber volume required to maximize the performance of 3DPC [85–88,91]. Unlike conventional concrete, where higher fiber volume often correlates with increased strength, in 3DPC, excessive fiber volume can lead to clogging and reduced material performance. Therefore, establishing the critical fiber volume rather than an arbitrary fiber volume is essential for developing ultra-ductile, strain-hardening 3DPC, particularly in applications like seismic-resistant structures where ductility and energy absorption are vital.

2.3. Mechanical and Structural Performance of 3DPC

The mechanical and structural performance of 3DPC defines its applicability in real-scale load-bearing components. Unlike conventional cast concrete, 3DPC exhibits unique mechanical characteristics influenced by its layered deposition process, printing parameters, and reinforcement configuration. The anisotropic nature of the printed material, resulting from directional deposition, weak interlayer bonding, and heterogeneous stress transfer mechanisms, plays a decisive role in determining its load-bearing capacity and long-term structural reliability. A comprehensive understanding of both static and dynamic mechanical behavior, as well as the efficacy of different reinforcement strategies, is therefore fundamental for structural-grade applications and seismic design.

2.3.1. Static and dynamic mechanical behavior

In recent decades, significant strides in automatic construction techniques and additive manufacturing technologies have sparked a wave of innovative architectural endeavours. These advancements have led to the successful realization of diverse creative projects such as 3D printed concrete military shelter built in just 36 hours [92]. While 3D printing has experienced rapid development in both the research [93–96] and construction sectors [5,97,98], its application in construction remains in the experimental and exploratory phases. Extensive research has focused on examining the fresh state characteristics [99–102] and static performance of 3D printed components, primarily through experimental [95,103,104] and numerical investigations [105–110] (presented in Table 1). Despite the limitations imposed by the weak tensile, shear, and flexural capabilities of 3DPC [6] its engineering applications are still underexplored particularly the behaviour of printed structures under cyclic loading or extreme events like earthquakes [6,111]. Given the susceptibility of our communities to natural disasters, a comprehensive evaluation and safety enhancement of these structures are imperative. To the best of authors knowledge, only a limited number of studies have experimentally investigated the seismic behavior of 3DPC walls [6–9] (see Table 2.2). However, these investigations are mostly confined to specific reinforcement systems or isolated wall configurations, while aspects such as material design, reinforcement detailing with standard design provisions, and failure mechanisms under realistic cyclic loading remain largely unexplored. This leaves significant gaps in developing a comprehensive understanding of the seismic performance of large-scale 3DPC walls.

Table 2. 2. Overview of 3DPC wall elements under mechanical loading conditions in the literature

Reference	Year	Specimen	Specimen dimension (H: height, L: length, W: width, T: thickness)	Loading condition	Mode of study
Patiphat et al. [103]	2020	Eight walls with different section forms and material strengths	H 1300 mm * W 900 mm * T 125 mm	Axial compression	Experimental
Daungwilailuk et al. [105]	2021	Two patterns of walls	H 970 mm * W 1320 mm * T 120 mm	Axial compression	Experimental and numerical
Ganchai et al. [106]	2022	Three walls with different infill patterns	H 900 mm * W 1300 mm * T (75-125) mm	Axial compression	Experimental and numerical
Han et al. [95]	2022	Eight walls with different height to thickness	H (720–2400) mm * W 710 mm * T 240 mm	Axial compression	Experimental
Zhang et al. [104]	2022	Twelve core-column walls	H 1200 mm * W 1040 mm * T 240 mm	Axial compression	Experimental
Paudel et al. [108]	2023	Single wall with single infill patterns	H 1100 mm * W 900 mm * T 125 mm	Axial compression	Experimental and numerical
Zhang et al. [6]	2023	Three walls with different height to width	H 1500 mm * W (1000-1500) mm * T 150 mm	Quasi-static cyclic loading	Experimental
Delavar et al. [110]	2024	reinforced concrete framed 3DPC wall	H 3000 mm * 2000 mm * 300 mm	Quasi-static loading	Analytical and numerical
Giulivo et al. [7]	2024	Single wall with fixed base anchorage	H 2100 mm * 1350 mm * 330 mm	Quasi-static cyclic loading	Experimental
Liu et al. [8]	2025	Wall with different rebar configuration	H 1600 mm * 1200 mm * 240 mm	Quasi-static cyclic loading	Experimental and numerical
Mercimek et al. [9]	2025	Five walls with different loading and joint conditions	H 1100 mm * 1500 mm * 250 mm	Monotonic and cyclic loading	Experimental

The dynamic response of 3DPC under cyclic or impact loading is less explored but critically important for structural applications in seismic zones. Preliminary investigations have reported that the damping and energy absorption capacity of unreinforced 3DPC is limited due to its brittle fracture mode and interfacial delamination. Hence, to enable ductile performance under cyclic or seismic conditions, appropriate reinforcement integration is essential.

2.3.2. Reinforcement strategies in 3D printed concrete

2.3.2.1. Fiber reinforcement

The integration of discrete fibers into 3DPC mixtures has proven effective in enhancing tensile strength, ductility, and crack control. Fibers act as micro-reinforcement bridges that transfer stresses across cracks and delay their propagation (detailed in Section 2.2.1). When optimally dispersed, fibers can induce strain-hardening behavior, characterized by multiple cracking and sustained load-carrying capacity beyond the initial crack formation. This behavior is vital for improving energy absorption and deformation capacity, particularly under seismic or cyclic loads. However, the performance of fiber-reinforced 3DPC is highly dependent on factors such as fiber orientation, volume fraction, and dispersion uniformity. The printing process tends to align fibers along the extrusion direction, resulting in directional mechanical properties. This

fiber alignment can be advantageous in tension-dominant regions but may reduce transverse strength. Moreover, achieving the critical fiber dosage necessary for uniform strain hardening is often constrained by printability limitations—excessive fiber content can increase mix viscosity and cause nozzle blockages.

At large scales, the application of fiber-reinforced 3DPC faces additional challenges in ensuring consistent fiber distribution throughout the structure. Therefore, while fibers enhance local ductility and post-cracking behavior, their scalability in field applications remains limited. The optimization of fiber geometry (e.g., corrugated or hooked-end) and matrix compatibility remains an ongoing area of research.

2.3.2.2. Conventional reinforcement integration

The incorporation of conventional steel reinforcement in 3D printed elements poses significant technical and automation challenges. Unlike cast concrete, 3DPC is fabricated without formwork, making it difficult to position and secure reinforcement bars or meshes during the printing process. Embedding reinforcement manually interrupts the continuous automated process, defeating the purpose of full-scale digital construction.

Moreover, the layered nature of 3DPC restricts proper encapsulation of reinforcement, resulting in insufficient bond and anchorage between the steel and the printed matrix. The interlayer interfaces further complicate stress transfer and may lead to premature debonding under load. The mismatch between the rheological properties of fresh 3DPC and the rigidity of reinforcement also contributes to void formation around bars, reducing composite action.

Automating the placement of reinforcement remains a major obstacle. Research has explored robotic or co-extrusion systems capable of laying reinforcement concurrently with printing, but such techniques are still confined to laboratory environments. Consequently, compatibility between conventional reinforcement and extrusion-based 3D printing systems is a key barrier to practical application.

2.3.2.3. Hybrid reinforcement and emerging techniques

Given the potential for innovation, fibre composites are being used in more and more technical goods, particularly in the aerospace and wind energy sectors. This increased utilisation is being driven by new automated processing methods like Automated Fibre Placement (AFP) or winding procedures (Fig. 2.14). Quality improvement and fully automated geometrically difficult components are promised by combining AFP with 3DPC [112].

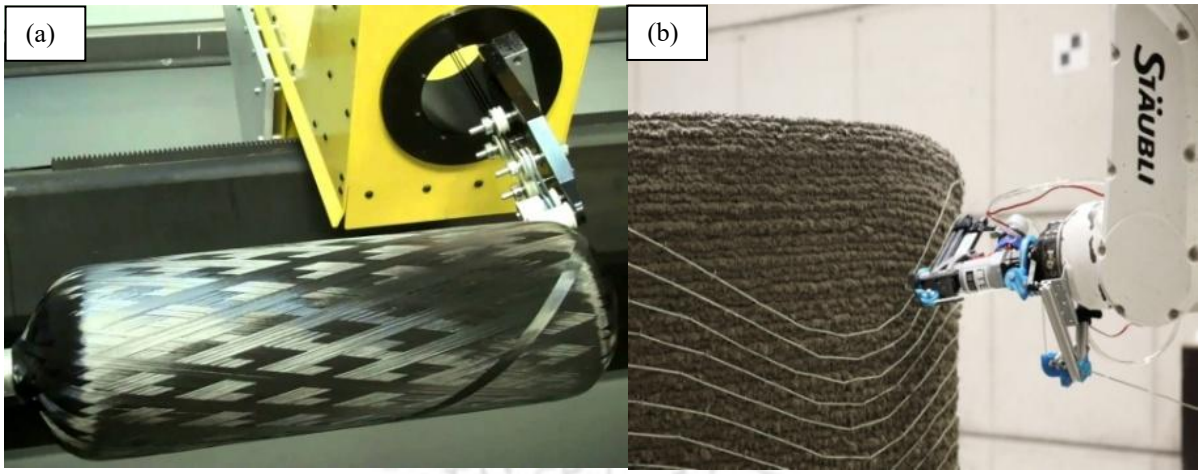

Fig. 2. 13. (a) Fibre wraps on mandrel; (b) prototype wall with robotic fibre deposition end-effector featuring integrated staple device for reinforcement configuration [112]

Hence, a potential avenue toward achieving a fully automated printing process, encompassing the simultaneous incorporation of continuous and rigid reinforcement along both vertical and horizontal orientations, envisions a groundbreaking printing system where multiple robots operate autonomously to execute concrete printing and reinforcement placement concurrently. In this domain, a recent study [113] emphasizes the potential of a novel device to automate the reinforcement of printed elements in all directions during the printing process. However, as it currently addresses small-scale applications, further development is necessary, focusing on upscaling the device for large-scale concrete 3D-printed elements and industrial applications.

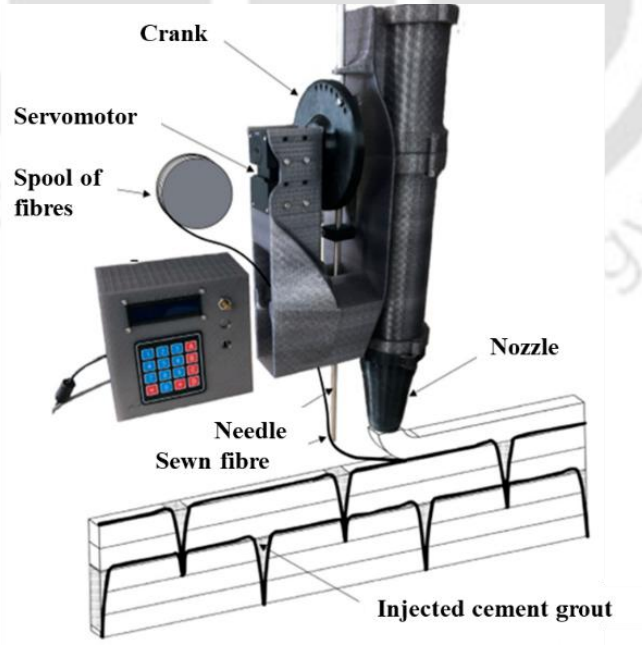

Fig. 2. 14. Sewing concrete device to control needle oscillation along the printing path [113]

Furthermore, integrating various reinforcement techniques is better for higher strengthening levels than using only one reinforcement strategy. Additionally, the reinforcing technique needs to be in line with the respective load scenarios. In order to automate the entire construction process, it will be necessary to investigate how printing styles can change.

2.3.2.4. Limitations, challenges and opportunities for structural reinforcement integration

The use of fibres for reinforcement in 3DPC offers various benefits, such as improved load-carrying capacity, deflection hardening behaviour, and reduced brittle failure in specific directions. Steel and PE fibres, in particular, exhibit superior strain hardening behaviour, higher tensile strength, and increased ductility under tensile load, due to the fibre bridging effect [31,114]. However, some unfavourable characteristics of fibre-reinforced 3DPC have been observed, including fibre discontinuity, reduced design freedom, and challenging fibre orientation optimization. Despite demonstrating significant potential to enhance the mechanical properties of printed concrete, widespread application of reinforcement techniques is hindered by certain limitations. Incorporating both vertical and horizontal reinforcement is essential to address these limitations and ensure the structural integrity of large-scale constructions. While some fibres might not be sufficiently strong on their own for large-scale applications, their high ductility, affordability, stiffness, and exceptional durability make them suitable for specific use cases durability [31]. Table 2.3 provides details on current fibre reinforcement techniques and the failure modes of various fibres under different loading conditions. Overcoming these challenges is crucial in developing a fully automatic printing system for more widespread and efficient use of fibre-reinforced 3D concrete printing technology.

Although many researchers have looked into the integration of reinforcement in 3DPC, the main issue with reinforced concrete manufacturing is how to incorporate reinforcement in both vertical and horizontal direction into printed concrete with the least amount of interference to the concrete printing process. The use of traditional reinforcement techniques is not only inappropriate for digital fabrication; it also runs counter to one of its primary goals, automation. As a result, a reinforcement strategy, which can be incorporate in 3DPC automatically such as fibre, is required but as mentioned above fibres are not strong on their own for large-scale application.

Table 2. 3. Details of existing fibre reinforcement technique

Fibre addition	Used fibre	Direction & Location	Failure mode	Key findings
Before printing or during mixing	Carbon, Glass and Basalt fibre [22,25,37,38,43]	Horizontal & inner the filaments	Carbon fibre-reinforced specimens do not exhibit post-cracking attributes, while conversely, samples reinforced with glass and basalt fibres display post-cracking behaviour.	The proper choice of various fibre types significantly impacts the flexural strength of the tested samples.
	HDPE, PE and PP fibre [41,114,115]	Horizontal & inner the filaments	Well-distributed, fine cracks with 1-1.5% fibre content of HDPE fibres but with lesser fibre content i.e., 0.25%, shows brittle type failure	Pronounced strain-hardening behaviour has been seen under uniaxial tensile loading for fibre concentrations as low as 1%.
	PVA and, steel fibres [29,44,116–118]	Horizontal & inner the filaments	PVA and steel fibres bridged cracks to reduce concrete explosion& showing non explosive brittle type failure under bending	Steel fibre exhibits the maximum tensile strength than other fibres due its highly ductile property and well-known crack bridging effect and able to prevent catastrophic failure.
	Wollastonite microfibres [32]	inner the filaments	Fibre pull-out	It is less expensive and has a smaller environmental footprint than synthetic/metallic fibres.
During printing or in-process	Glass and basalt fibre, [34,50]	Horizontal & inner the filaments between the layers	Specimens with low yield stress exhibit a brittle failure mode devoid of pseudo strain-hardening, a consequence of the robust fibre/matrix bond where fibres fracture directly depend upon crack propagation.	The considerable tensile strength inherent in the fresh lace (fibre roving) undoubtedly presents opportunities for novel applications in concrete printing.
	Carbon and PVA fibre [49], [119]	Horizontal & inner the filaments between the layers	Delamination and spalling of the concrete cover, which was accompanied by fibre pull-out and concrete splitting	These fibres showcase exceptional mechanical attributes and durability, while simultaneously offering the advantage of effortless processing and shaping during the fresh state.
	Steel fibre [118], [33], [51], [120,121]	Horizontal, vertical, inner the filaments between the layers	Less brittle than that of the printed specimens without fibres, showing pseudo-elasto-plastic failure behaviour	i. Reinforces the layer interface, ii. Insufficient bonding iii. Voids exist

Fibre reinforced 3DPC still restricted to a few specific uses such facades, industrial floors, or tunnel linings that predominantly conduct compression. There are several limited applications of fibre reinforced 3DPC because of lot of uncertainty in the design process since the fibres are spread throughout the matrix in an unknown location and orientation. Second, at practical fibre doses, 3DPC reinforced with common fibre exhibits strain-softening behaviour. Another

limitation is the use of short fibres i.e., lack of continuous reinforcement, somehow reinforcement in horizontal direction can be achievable but to provide vertical continuous reinforcement is a difficult task, in a recent study [122], an attempt was made to introduce vertical reinforcement using lap joint reinforcement. However, a key aspect that remains essential is the comprehension of the minimal lap length required in the context of 3DPC specifications. Another issue encountered in integrating bars within the 3DPC process is the increase in void area (as depicted in Fig. 2.7), leading to suboptimal bonding between the reinforcement bar and the matrix. Consequently, this results in reduced overall strength. Notably, this challenge can be successfully mitigated across all the examined scenarios by modifying the toolpath, adjusting process parameters, and optimizing rebar joint geometry. This underscores the immense potential inherent in leveraging digital modelling techniques to overcome such obstacles.

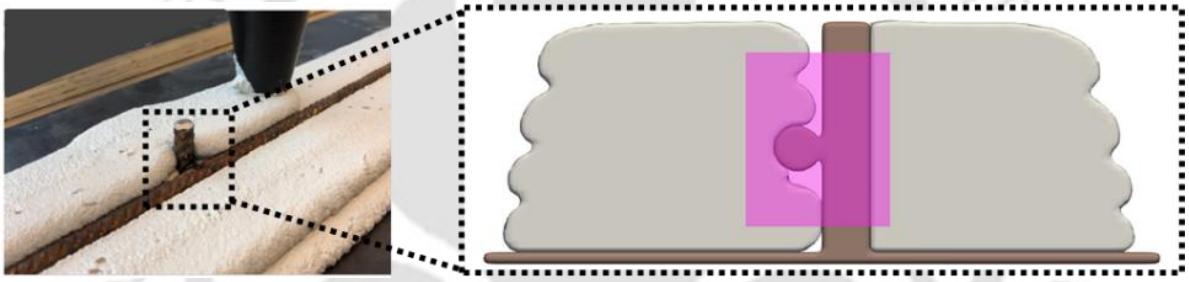

Fig. 2. 15. Presence of air voids around the vertical rebars and their schematic [123]

Although fiber reinforcement enhances the tensile behavior and crack control of 3D printed concrete, relying solely on fibers remains insufficient for achieving higher structural strength, especially under complex load scenarios. The effectiveness of any reinforcement strategy must align with the specific loading conditions to ensure structural reliability. However, integrating conventional reinforcement within the 3D printing process poses significant challenges related to automation, printing path continuity, and bonding performance. While several novel reinforcement methods have been explored at the laboratory scale, their application in large-scale or on-site construction remains impractical due to limited compatibility with existing printing systems. Therefore, instead of developing entirely new reinforcement approaches, greater emphasis should be placed on optimizing the interaction and bond characteristics of conventional reinforcement within 3D printed concrete to enable feasible and structurally efficient large-scale implementation.

2.4. Numerical modeling and simulation approaches in 3DPC

The numerical modeling of 3D printed concrete (3DPC) structures plays a key role in understanding and predicting performance under various conditions—fresh state, curing / early age, mature state, and under cyclic / seismic loads. Because of the complex, anisotropic, layer-wise deposition and interfacial behavior, simulation is challenging. This section reviews current modeling approaches, constitutive laws used, boundary conditions, limitations, and potential for future development.

2.4.1. Different numerical modelling approaches

A number of studies have used finite element modelling (FEM) to simulate both fresh and hardened behavior of 3DPC, including: a multi-surface anisotropic continuum macro-modelling strategy [107,124], micro-modelling approach or Interface-based model [107], 2D plane stress model [107], concrete damage plasticity (CDP) model [125], [126], [127], and cohesive zone model (CZM) [128].

2.4.1.1. Macro-modelling approach or Continuum model

The filament layers and interfacial regions are not distinguished in this model. An anisotropic Rankine-Hill cap plasticity continuum crack model (Fig. 2.16a) is chosen by Heever et al. (2022) [129] for its ability to capture the anisotropic inelastic response of layered structures [130] with separate softening in tension (Rankine) and compressive hardening-softening (Hill). The presented material model is implemented in the DIANA FEA simulation package and requires two Isotropic elastic parameters (E, μ), seven orthotropic strength parameters (f_{tx}, f_{ty}, f_{cx}, f_{cy}, α, β, and γ), and five orthotropic inelastic parameters (G_{fx}, G_{fy}, G_{fcx}, G_{fcy}, and κ_p) to define the yield criteria shown in Fig. 2.16a. The orthotropic directions depicted in Fig. 2.16b are denoted by the subscripts (x, y). Heever et al. [129] use the experimental approach described in [131] to get these parameters.

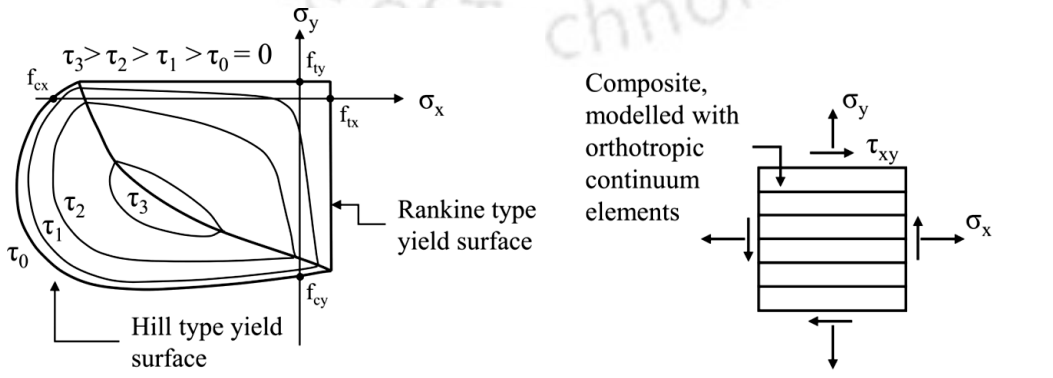

(a) Continuum material model [132] (b) Macro-modelling approach [129]

Fig. 2. 16. Simulation frameworks for 3D concrete printed elements

2.4.1.2. Micro-modelling approach or Interface-based model

Interface-based model is based on Lourenco and Rots' [133] interface elastoplastic constitutive model (Fig. 22a) for unreinforced masonry structures, which has been extended to incorporate isotropic continuum elements that represent the intralayer matrix. To specify the interface regions (Irs) in the 3DPC composite, Heever et al. [129] used the combined-cracking-shearing-crushing (CCSC) interface model from DIANA FEA. It is observed that the cohesion is the interface's pure shear strength (i.e., with no normal stress) [134]. Because there is a shortage of experimental data specifically relevant to 3D printed cementitious composites, the parameters that cannot be determined through physical experiments are based on [135].

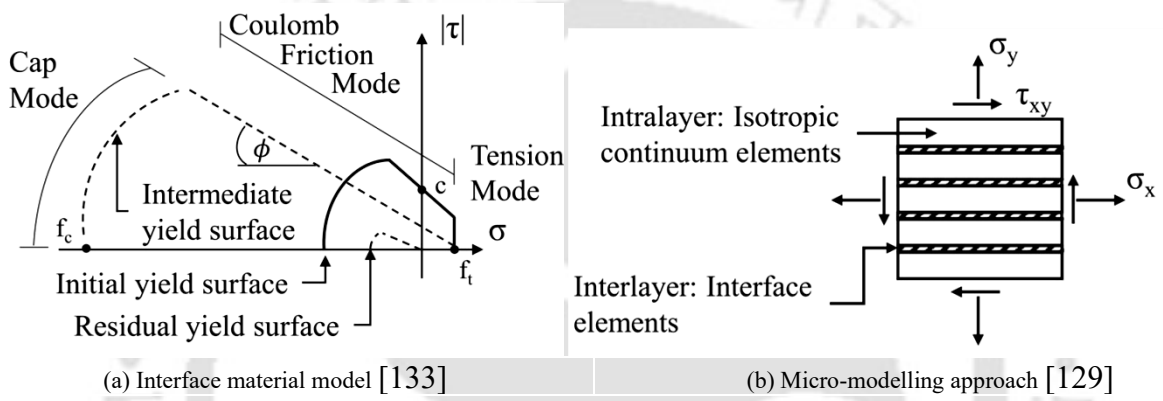

(a) Interface material model [133] (b) Micro-modelling approach [129]

Fig. 2. 17. Simulation frameworks for 3D concrete printed elements

2.4.1.3. 2D Plane stress (2D) model

The justification for 2D plane stress simplification of 3DPC hollow sections, with biaxially symmetric cellular infill patterns, is discussed by Heever et al. [129]. Such modification allows 3DPC elements' cellular form to be transformed to a relevant thickness exhibiting identical mechanical characteristics, decreasing the analytical and simulation work required to analyze the behaviour of such components under different loading scenarios. Here three parameters need to be considered a representative rectangular thickness (t_r) effective contact area ($A_{secA\text{-}A}$) and contact factor (Δ_{CF}). Because the contact area of a rounded filament is smaller than that of its square counterpart (as shown in Fig. 2.18), a contact factor is used to compensate for such lower contact efficiency associated with various layer geometries.

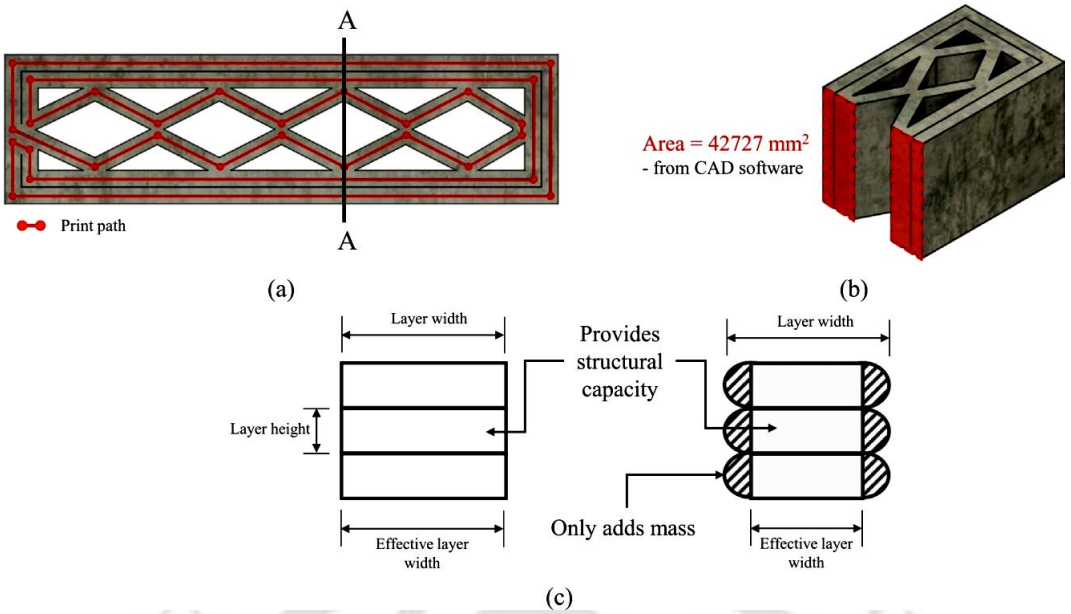

Fig. 2. 18. The explanation for the 2D simplification is demonstrated in (a) a plan view of a section within the cellular portion of the printed object, (b) the load resisting area derived from the infill geometry, and (c) the difference between rounded and square filaments and their effect on the effective contact area [129]

2.4.1.4. Concrete Damage Plasticity (CDP) material model

It has been observed in several studies [125], [126], [127] that numerical modelling of the test using Abaqus' CDP material model, with a Thorenfeldt-based constitutive law [136] in compression (Fig. 2.19) and a customised constitutive law in tension [137] (Fig. 2.20), provides a close approximation to the experimental observations. It is also observed in the study by Bos et al. (2019) [125] that CDP material model is capable enough to simulate the flexural behavior of 3DPC beams with close agreement. The constitutive relation of concrete under compression proposed by Thorenfeldt et al. [136] is used and compared with CDP model in Abaqus by Bos et al. [125] and Wang et al. [127] which is given by Fig. 2.19.

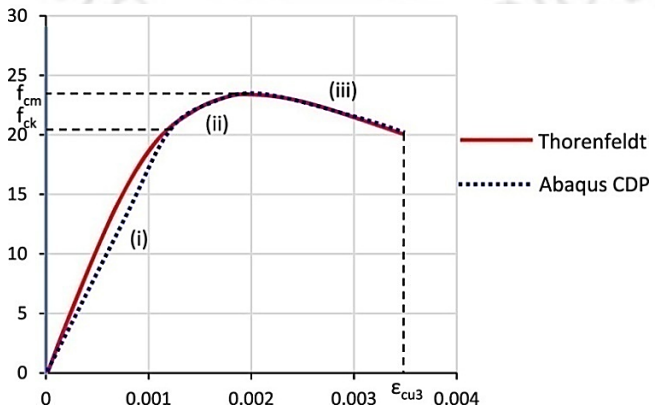

Fig. 2. 19. Thorenfeldt compression material model versus CDP model in Abaqus (i) linear elastic stage; (ii) hardening stage; (iii) softening stage after reaching peak stress

Several studies [138,139] have developed distinct governing equations for the behaviour of concrete under tension, however these constitutive relations essentially require two quantities, i.e., the fracture energy G_f and the strain softening curve. Rots et al. [138] observed out that the fracture energy must be delivered within a specific crack width, that is, G_f is constant and independent of the mesh size, in place to evade discretization of the data. As a result, in the CDP the crack development width is set as a fixed value. For the strain softening curve, the constitutive relation of plain concrete adopts the uniaxial tensile stress-strain curve proposed by Hordijk et al. [137] as shown in Fig. 26.

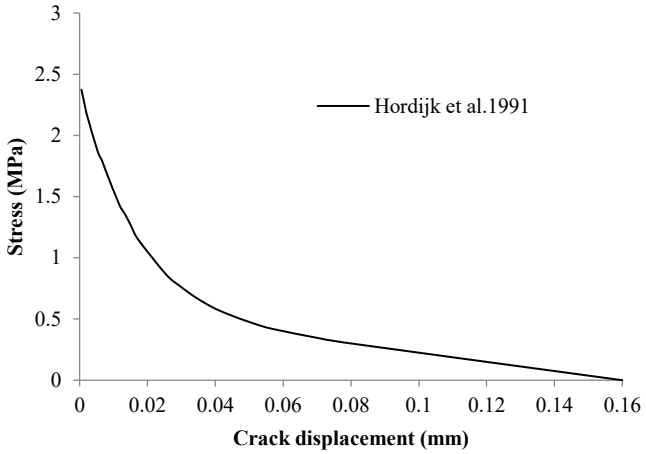

Fig. 2. 20. stress strain curve of concrete under uniaxial tension

2.4.1.5. Concrete Smeared Cracking (CSC) model

There is another model called concrete smeared cracking (CSC), which is a type of Concrete Damage models (CDM) and based on continuum damage mechanics theory (CDMS). CSC model in Abaqus, developed for monotonic loading conditions, is cracking-based and also it can adopt cracking as distributed effect with directionality. This model isn't well-developed enough to anticipate concrete's cyclic reaction or the resultant drop in elastic stiffness due to inelastic straining. CSC models, on the other hand, require data on tension stiffening. According to Liu et al. [140], a zero inelastic/plastic strain must match to the very first value of the yield stresses. As a result, total compressive strain values (ε_c) should be transformed to inelastic ($\varepsilon^{in,h}$) or plastic strains as needed. The uniaxial response of the incorporated model in the compression and tension phases is shown in Fig. 2.21.

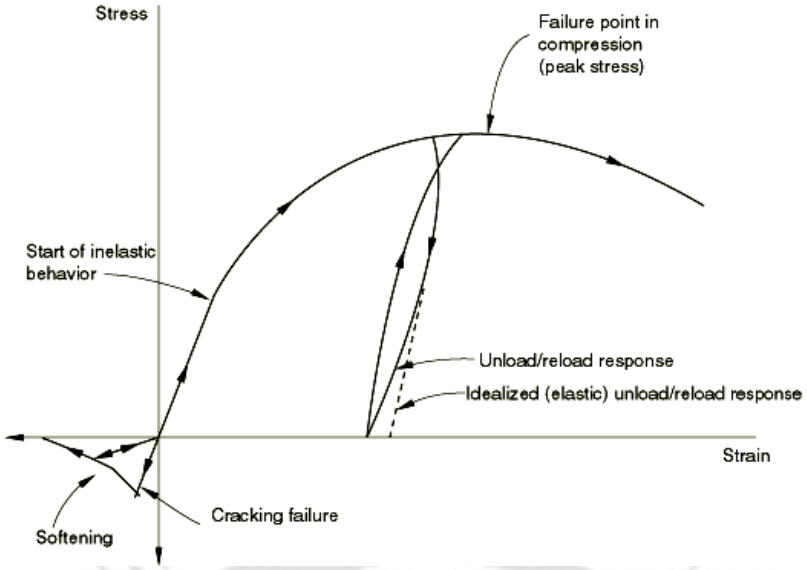

Fig. 2. 21. Uniaxial behavior of plain concrete (available in commercial FE numerical software)[140]

2.4.1.6. Cohesive zone model

Cohesive Zone Modeling (CZM) is a viable numerical modelling technique for verifying the mesoscale tensile interfacial transition zone (ITZ) response of 3DPC elements. Heever et al. [128] used cohessive zone model to simulate the PP fibre reinforced 3DPC. Heever et al. [128] also use mechanical characterisation procedures including as direct tension tests (DTT), Iosipescu shear tests (IST), and orthogonal compression tests to investigate the differential interlayer capacity of 3DPC specimens.

2.4.2. Comparison of numerical simulation result through different modelling approaches

The load versus displacement curve by using all above-mentioned approach is produced to see the validity of experimental results with numerical simulation (shown in Fig. 2.22). IFM, CM, CZM, CSC, and CDP stand for interface-based model, continuum model, cohesive zone modelling, concrete smeared cracking, and concrete damage plasticity, respectively. In Fig. 2.22, a plot is made between validation ratio (F_{num}/F_{exp}) and numerical model approaches present by different researchers (Bos et al. [125], Heever et al. [129], Heever et al., Heever et al. [128], Liu et al. [140]). The concrete smeared cracking (CSC) model, which is shown in the plot, has a somewhat higher disparity between numerical simulation results and experimental data, notably 8.89%, and CDP model is showing very less difference i.e. 0.29%. All other model i.e., IFM, CM and CZM are also showing acceptable limits i.e. 1.82%, 3.61% and 0.58%. CDP material model provides a close approximation to the experimental observations, some other researchers also supports this statement [125], [126], [127].

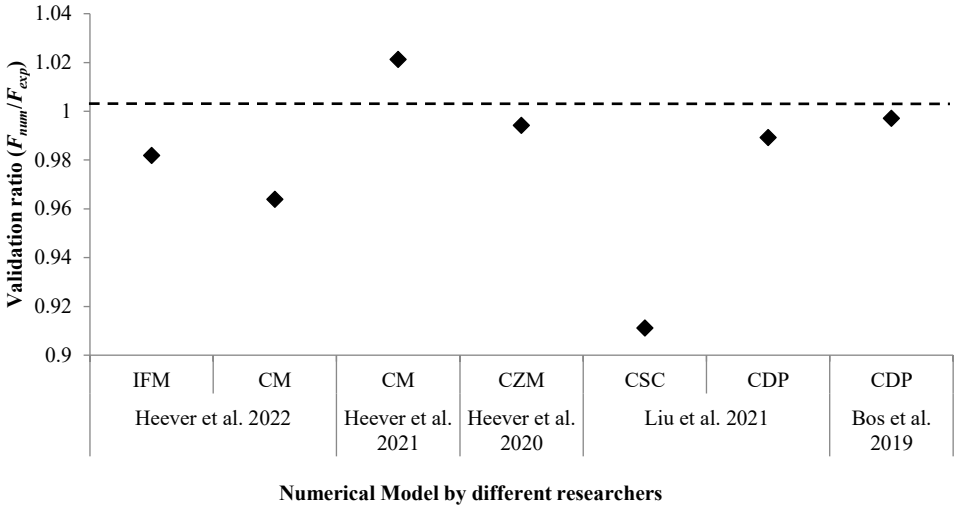

Fig. 2. 22. Validation ratio (i.e. Numerical results/experimental results) by adopting different modeling approaches

Numerical modeling and simulation approaches for 3DPC have advanced significantly capturing fresh and early age behavior, layer deposition effects, material aging, and basic failure modes. However, for earthquake-resistant design and cyclic structural performance, gaps remain—especially in simulating mature reinforced specimens under real load histories, modeling reinforcement integration, coarse aggregate effects, and interlayer bond deterioration. Addressing these will be essential for reliable design and code compliance of earthquake-resistant 3DPC walls.

2.5. Design considerations and codal provisions for 3DPC structures

The rapid development of 3DPC has exposed the limitations of conventional reinforced concrete (RC) design rules when applied to additively manufactured elements. Key differences—layered deposition, direction-dependent material properties, variable interlayer bond quality, and novel reinforcement placement methods—necessitate a re-examination of codal assumptions and the development of tailored design guidance for 3DPC. This section reviews existing standards and guidance efforts, identifies the principal technical issues for design, discusses proposed adaptations of conventional codal provisions to 3DPC, and highlights outstanding research gaps for seismic design of 3DPC elements.

2.5.1 Existing standards and standardization efforts

Recent international standardization initiatives recognize the need for specific guidance on additive construction. The joint ISO/ASTM standard ISO/ASTM 52939:2023 provides high-level requirements for additive manufacturing in construction and lays foundations for production and quality assurance of additively manufactured structures, but it does not yet provide structural-engineering level design rules for concrete elements under seismic loads.

RILEM Technical Committee activities (notably RILEM TC 304-ADC / 304 series) and interlaboratory studies are producing recommended test methods and data for printable and printed concrete (mechanical testing, shrinkage/creep, durability, and reinforcement bond) [141]. These efforts aim to generate harmonized test methods that will underpin future design recommendations. National and model-code level work is also underway. Draft guidance and preliminary standards have been produced, such as the ICC draft standard for automated construction technology for 3D printing walls [142], which attempts to translate model code intent into prescriptive requirements for 3D printed walls (application, materials, reinforcement, and connections).

Finally, technical reviews and primers produced by practice-oriented organisations (HUD, Home Innovation Research Labs, ACI webinars) provide design proposals and performance-based frameworks to bridge the gap between industry practice and formal codification. Delavar et al. [110] proposes adapting the Equivalent Lateral Force (ELF) method for 3DPC walls while accounting for 3DPC-specific failure modes and response modification factors.

2.5.2 Key design issues specific to 3DPC

2.5.2.1 Material anisotropy and interlayer bonding

The layer-by-layer deposition inherent to extrusion printing produces anisotropic mechanical properties and potential cold joints between successive layers. Interlayer interfaces commonly exhibit reduced tensile and shear capacity compared to bulk material, and these interfaces often control cracking and failure modes in printed elements. Consequently, design must explicitly account for anisotropic strength and stiffness, and for reduced bond strength at the layer interfaces rather than assuming homogeneous isotropic behavior used in conventional RC codes. RILEM interlaboratory results and multiple reviews emphasize that interlayer bond characterization and standardized testing are prerequisites for reliable design [143,144].

2.5.2.2 Reinforcement placement and bonding

Conventional reinforcement detailing (bar spacing, development length, anchorage) assumes full encapsulation in cast concrete and well-defined bond conditions (e.g., cover, compaction). In extrusion-based 3DPC, embedding bars or meshes during printing creates discontinuities, voids around bars, and inconsistent bond conditions because compaction is absent or limited to the extrusion/overburden effect. Automated placement of reinforcement is still largely experimental (robotic insertion, co-extrusion of wires), and the interaction between conventional steel reinforcement and printed layers—including bond-slip behavior—remains under-characterized. Published interlaboratory work demonstrates that manually placed

reinforcement between printed layers can result in widely varying bond behavior depending on printing setup and timing. These uncertainties imply that conventional code formulas for development length and lap splices cannot be applied directly without calibration [144,145].

2.5.2.3 Connections, openings and detailing

Connections (e.g., wall-to-foundation, wall-to-wall and wall-to-floor) are critical for seismic performance. 3D printed wall systems lack established methods for connection detailing compatible with printing workflows. Connections often require hybrid solutions—integrated post-cast joints, mechanical anchors, or prefabricated connection plates—and must be designed to transfer shear, moments, and ductility demands reliably.

2.5.2.4 Quality control, production variability and durability

Design provisions must assume realistic variability in printed material properties, layer bond strength, and as-built geometry. Quality control and inspection methods (non-destructive testing, sampling regimes) are less mature for 3DPC than for conventional cast concrete. Durability aspects—protective cover for embedded reinforcement, permeability at layer interfaces, freeze-thaw and carbonation performance—must be considered in codal development, particularly for seismic zones where long-term reliability after cyclic loading matters. RILEM and ASTM working groups emphasize measurement protocols for shrinkage/creep and durability to inform safe design.

In summary, current design and codal frameworks for 3DPC remain in an early stage, lacking specific provisions for anisotropy, interlayer bonding, and reinforcement detailing. While emerging standards such as ISO/ASTM 52939:2023 and RILEM recommendations mark progress, they do not yet address structural and seismic performance requirements. 2.6. Seismic performance of 3DPC elements.

2.6. Seismic performance of 3DPC structures

Despite rapid progress in 3DPC extrusion systems, and printable cementitious materials [5,6], the application of 3DPC to seismically resilient structural components remain in its infancy. As the main vertical structural component, walls deserve to be studied thoroughly in terms of their mechanical performance since they easily can be automatically constructed on site. Some researchers have recently performed simple axial compressive or eccentric compression loading for full-size 3DPC walls, and the failure modes and mechanical performance are determined. To the best of authors knowledge, only a limited number of studies have experimentally investigated the seismic behavior of 3DPC walls [6–9] (see Table 2.1). However, these investigations are mostly confined to specific reinforcement systems or

isolated wall configurations, while aspects such as material design, reinforcement detailing with standard design provisions, and failure mechanisms under realistic cyclic loading remain largely unexplored.

Zhang et al. [6] examined the performance of 3D printed walls reinforced with flexible FRP textiles, where the layer-by-layer integration of FRP within the printed matrix enhanced energy dissipation and deformation capacity under cyclic loading. However, the reinforcement strategy is limited to textile systems and did not incorporate conventional steel reinforcement, restricting its relevance to real seismic design practices. Giulivo and Menna [7] explored the in-plane cyclic response of an unreinforced 3D printed wall with fixed base anchorage, identifying brittle shear failure and delamination at interlayer interfaces, thereby emphasizing the weakness of layer bonding under cyclic actions. Similarly, Liu et al. [8] conducted a combined experimental and numerical study on steel-reinforced 3D printed concrete walls, demonstrating that while embedded steel bars improved strength and ductility, interfacial bond loss between steel and printed concrete led to premature cracking and stiffness degradation under repeated loading. More recently, Mercimek et al. [9] investigated the structural performance of prefabricated 3D printed concrete walls under various axial and lateral loading conditions, highlighting that cold joints and print discontinuities significantly affected lateral load resistance and crack propagation.

These investigations collectively reveal that, although 3DPC has shown promising results in automation and material development, its seismic performance is still constrained by limited ductility, weak interlayer bonding, reinforcement incompatibility, and lack of standardized design approaches. Further large-scale cyclic testing, along with the development of reliable reinforcement integration methods and codal validation, is essential to ensure the structural reliability of 3D printed concrete systems in seismic applications.

2.7. Potential structural application of 3DPC structures

After a decade of research on 3D printing in various domains, the interest of 3D printing in construction has drastically increased in the recent years [146]. About 10 years ago, Lim et al. [147] described full-scale concrete printing with limited size (5.4 × 4.4 × 5.4 m) of building elements such as walls and facades. In 2014, WinSun Company in China successfully printed a number of houses in less than 24 h [148].

Despite the challenges of 3DPC, as discussed earlier, with the development of technologies and large-size 3D printers, the world has now witnessed many printed structures ranging from houses, offices, bridges, pavilions, shelters and many more [149]. The coastline protection

structure is also proposed by [150] which can adapt its shape to its natural surroundings rearranging locations for marine plants and will setting up a new habitat defending the original ecosystem. Fig. 2.23 presents some innovative 3D-printed construction projects around the world that demonstrate the future potential for large-scale adoption of 3D printing in the construction industry.

Fig. 2. 23. 3D-printed construction projects around the world

2.8. Overview/ Research gaps

Despite notable progress in advancing 3DPC technologies, the literature collectively highlights that the transition from material-scale innovation to full-scale, earthquake-resistant structural applications remains incomplete. Most existing studies have focused on optimizing printability, mechanical anisotropy, and buildability of mortar-based mixes, while the structural-scale implications—particularly under cyclic or seismic loading—remain underexplored. The following critical research gaps have been identified through the review of material, structural, and design perspectives.

i. **Material design and heterogeneity control**: Current 3DPC mixes are predominantly mortar-based, with limited integration of coarse aggregates due to extrusion constraints.

Although coarse aggregate incorporation has shown potential to enhance interlayer bonding and reduce material cost and carbon footprint, its influence on pore formation, interfacial transition zones, and global mechanical uniformity remains inadequately understood. The absence of systematic studies examining how aggregate gradation, content, and shape interact with fiber distribution and extrusion pressure represents a major limitation in optimizing printable concrete suitable for seismic applications.

ii. **Reinforcement strategies and structural compatibility**: Reinforcement integration in 3DPC remains one of the most critical and unresolved challenges. Fiber reinforcement has improved ductility and crack resistance; however, issues of orientation, dispersion, and critical volume control limit its scalability and reproducibility. Meanwhile, embedding conventional steel reinforcement or mesh during printing is hindered by automation barriers and weak bonding at interfaces. Hybrid or textile-based reinforcement techniques have shown potential in controlled environments but are yet to demonstrate reliability under cyclic or in-plane loading at the structural level. Consequently, a gap persists in developing reinforcement strategies that balance automation compatibility with adequate ductility and load transfer efficiency.

iii. **Numerical Modeling and Validation**: Although several numerical models have been developed to simulate fresh-state printing, layer activation, and interfacial mechanics, only a few studies address cyclic or seismic behavior of 3DPC walls. Existing models often lack coupling between process-induced heterogeneity, material anisotropy, reinforcement interaction, and interlayer shear strength. Furthermore, limited experimental datasets for cyclic testing hinder the calibration and validation of numerical frameworks. A robust simulation methodology that captures multi-scale material behavior, including interface degradation and materials effect under cyclic loading, remains absent.

iv. **Design frameworks and codal limitations**: Existing reinforced concrete design provisions, which assume isotropy, full compaction, and conventional reinforcement anchorage, are not directly applicable to 3DPC. Although some studies have incorporated reinforcement within printed elements, these are implemented without reference to standard design provisions, relying instead on empirical arrangements with uncertain structural reliability. While emerging standards such as ISO/ASTM 52939:2023 address production and quality control, no codified framework currently accounts for the anisotropy, weak interlayer bonding, or distinct failure modes of 3DPC. The absence of performance-based seismic design guidelines further limits its safe use in structural and load-bearing applications.

v. **Seismic performance and full-scale validation**: Experimental studies investigating the in-plane cyclic response of 3DPC walls are extremely limited. Most available work focuses on monotonic compression or small-scale specimens, which cannot fully represent seismic demands. The few existing cyclic studies report early stiffness degradation, brittle interlayer failures, and inadequate energy dissipation, emphasizing the need for material systems with enhanced ductility and bonding. Moreover, the lack of full-scale quasi-static cyclic testing of reinforced 3DPC walls with realistic boundary conditions and axial load ratios creates a significant knowledge gap in assessing the true seismic resilience of 3D printed structures.

vi. **Integrated multi-domain framework for earthquake-resistant 3DPC**: The literature reveals a fragmented research landscape—where material innovations, reinforcement strategies, and structural analyses are developed in isolation. There is an evident need for an integrated approach that unifies material design (fiber–aggregate synergy), structural modeling (interface and cyclic response), and design adaptation (codal compliance and reinforcement detailing). Such a framework is essential for developing performance-based, reliable, and sustainable 3D printed concrete systems suitable for seismic regions.

In summary, while advancements in printable materials, reinforcement strategies, and simulation methods have demonstrated the feasibility of 3DPC in structural applications, its adoption in earthquake-resistant construction is limited by the absence of ductile, scale-compatible materials, validated cyclic models, and design frameworks. Addressing these gaps—through the development of an application-oriented 3D printed composite, numerical modeling of cyclic behavior, and full-scale experimental validation—constitutes the foundation and novelty of the present research.

Chapter 3

Development of ultra-ductile strain hardening 3D printed concrete composite utilizing critical fiber volume and coarse aggregate

[*] This chapter focuses on the material development of an ultra-ductile strain-hardening 3DPC composite incorporating critical fiber volume and coarse aggregate. It presents the mix design methodology, optimization of constituent proportions, and evaluation of fresh and hardened properties. The chapter also investigates the strain-hardening response and ductility enhancement mechanisms, establishing the material's suitability for structural and seismic applications.

*A portion of this chapter has been published in:
Warsi SBF, Panda B, Biswas P. Development of ultra-ductile strain hardening 3D printed concrete composite utilizing critical fiber volume and coarse aggregate. Additive Manufacturing 2024, p. 104541. https://doi.org/10.1016/j.addma.2024.104541

3.1. Introduction

Civil engineering structures are increasingly exposed to multi-hazard events such as earthquakes, high winds, and blast loads, driving the need for advanced materials and construction technologies to enhance resilience and durability. Among these, engineered cementitious composites (ECC), also known as strain-hardening cementitious composites (SHCC), have emerged as high-performance materials with exceptional ductility and tensile strain-hardening behavior [151]. However, as Li et al. [79] noted, most existing 3D printed ECC mixes are mortar-based and exclude coarse aggregates, which can limit long-term performance and sustainability. Incorporating coarse aggregates introduces additional challenges due to the interaction between fibers and aggregates in the hardened state, which significantly influences mechanical performance. For instance, Chen et al. [85] observed that increasing steel fiber content in 3DPC can result in poor fiber orientation in the presence of coarse aggregates, leading to material anisotropy, while Zhu et al. [86] reported that 3D printed ECC exhibited more uniform fiber dispersion than traditional ECC, enhancing tensile strength and strain capacity. Further studies by Pham et al. [87] and Yang et al. [88] highlighted the critical role of fiber size and alignment in optimizing tensile and flexural behavior. Although these investigations provide valuable insights into fiber performance [87–90], they largely overlook the synergistic effect of coarse aggregates on fiber distribution and interfacial bonding, both of which are essential for the mechanical robustness of 3DPC [85].

To address these gaps, this chapter presents a detailed analysis of the synergistic interactions between coarse aggregates and steel fibers—both smooth and corrugated—on the strain-hardening behavior, ductility, and energy absorption capacity of 3DPC. An ultra-ductile strain-hardening 3DPC mix is developed incorporating coarse aggregates (up to 10 mm) and steel fibers (15 mm and 30 mm), and its mechanical properties—including compressive, flexural, split tensile, and uniaxial tensile strength are evaluated. The results indicate synergistic effect of corrugated fibers and coarse aggregates on the tensile properties and unlike straight smooth fiber, corrugated long fibers significantly contribute to excellent strain hardening behaviour. The new 3DPC composite developed in this chapter exhibited distinctive yield point with high strain hardening factor (1.62), ductile factor (10.86), and enhanced energy absorption capability (+105 kJ/m³). These enhanced properties make the material particularly suitable for applications in seismic-resistant structures and other load-bearing applications where ductility and energy absorption are critical.

The inclusion of coarse aggregates poses challenges such as mechanical occlusion and extrusion difficulties [2]; to overcome this, modifications are made to the printing system to enable smooth extrusion of aggregate-containing mixes (Section 2.2). A large-scale extrusion-based 3D printer auger system is designed to handle aggregates up to 20 mm, although this chapter strategically limits aggregate size to 10 mm to avoid excessive stress concentrations that can lead to brittle behavior [152]. Prior to finalizing the material composition, preliminary trials are conducted in which coarse aggregates are incorporated within the interlayer regions during printing. These trials demonstrated up to a 32% increase in direct tensile strength, confirming the beneficial effect of aggregates on interlayer bonding and mechanical interlocking. To enhance the overall strength, subsequently, multiple fiber types—including PVA, glass, and steel—are evaluated at dosages of 0.25–1.0% for their influence on buildability, extrudability, and mechanical performance. Steel fibers are identified as the optimal choice, providing superior tensile strength and interlayer cohesion. Based on these findings, steel fibers (15 mm and 30 mm) and coarse aggregates (≤10 mm) are selected for the final composite formulation.

3.2. Materials and methods

3.2.1. Materials and mix preparation

Table 3.1 presents mixture proportions of the 3D-printable mortar (3DPM) and concrete (3DPC). Total four type of mixes are taken into consideration i.e., 3DPM, 3DPC, 3DPC-SF (3DPC with straight smooth steel fiber (SF)), and 3DPC-CF (3DPC with corrugated steel fiber (CF)). All the mixes comprised of 43-grade ordinary Portland cement (OPC) confirming to IS 269:2015 [153], natural fine river sand confirming to IS 383:2016 [154] with maximum particle size of 2.36 mm and specific gravity of 2.65. Methyl cellulose-based viscosity modifying admixture (VMA) is added (0.2 wt. % of binder) to tailor the rheology of the mixes along with PCE-based superplasticizer (SP).

These concrete mixtures (i.e., 3DPC, 3DPC-SF, 3DPC-CF) (see Table 1) are designed to meet guidelines mentioned in IS 10262: 2009 [155] and IS 456:2000 [156]. This approach is adopted due to the inclusion of coarse aggregates and the objective of developing a structurally relevant concrete comparable to conventional M30 grade concrete, unlike typical 3D printed mortar-based systems which do not follow standard codal mix design procedures. 3DPM is taken as reference mix to compare the effect of coarse aggregate and combined effect of coarse aggregate and fibers. The compositions of 3DPC-SF and 3DPC-CF are same as that of 3DPC, except the addition of straight smooth fibers (SF) and corrugated fibers (CF) at their critical

fiber volume fraction ($V_{f,cr}$) percentages by volume of the mix. It is important to note that the fiber volumes are based on the critical fiber volume as detailed in Section 3. The 3DPC property confirms to standard grade M30 specifications.

Table 3. 1. Mixture compositions

Mix ID	OPC	Sand	Water	VMA	SP	Steel Fiber	Coarse aggregate
3DPM	740	1209	296	1.9	3.7	…	…
3DPC	541	851	221	2.2	9.9	…	625
3DPC-SF	541	851	221	2.2	9.9	$V_{f,cr}$ **(SF)**	625
3DPC-CF	541	851	221	2.2	9.9	$V_{f,cr}$ **(CF)**	625

All mixtures are prepared using tap water, and locally available coarse aggregate with sieve analysis of 10 mm. This choice is made with an aim for sustainable, cost-effectiveness, and regional suitability. The grading curves for both fine and coarse aggregates are provided in Fig. 3.1. These curves are crucial for determining the particle size distribution, which significantly impacts the packing density and, in turn, the material properties. In 3D printing, mix needs to be workable enough to extrude through the nozzle but stiff enough to hold its shape after printing. Well-graded aggregates, both fine and coarse, enhance the packing density of the mix, minimizing voids between particles. This improved packing not only enhances the mix's workability but also ensures a more consistent flow through the nozzle, reducing the chances of clogging and resulting in a smoother extrusion process. The detailed sieve analysis performed for the coarse and fine aggregates adhered to IS 383:2016 [154], and their physical properties are measured in accordance with ASTM C125 [157] and ASTM C127 [158], as shown in Table 3.2.

Table 3. 2. Physical properties of aggregate

Aggregate	Bulk specific gravity-Dry*	Bulk specific gravity-SSD*	Apparent specific gravity*	Water absorption (%) *	Fineness modulus**
Basalt	2.47	2.49	2.52	1.7	3.5

Abbreviations: SSD – Density at the saturated surface dry condition

*- ASTM C127[158]; **- ASTM C125[157]

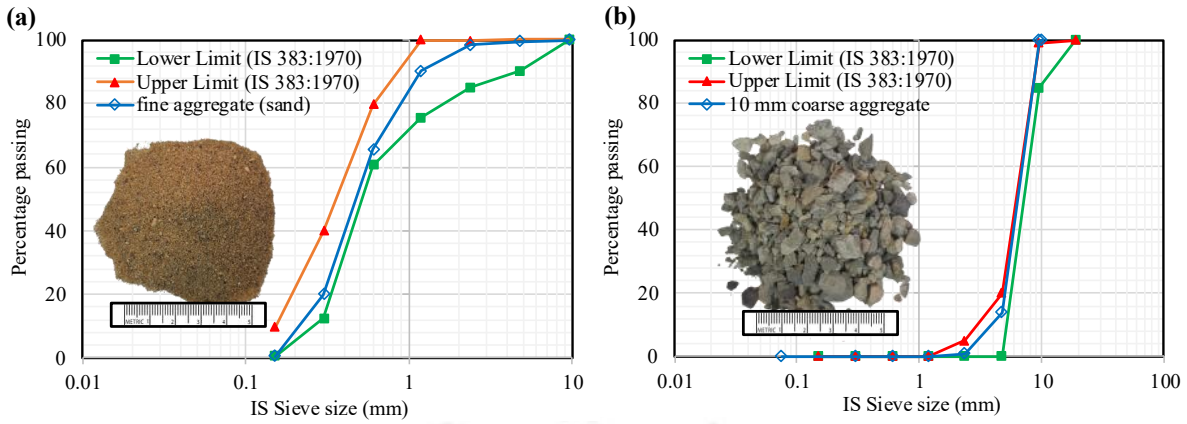

Fig. 3. 1. Grading curve of (a) fine aggregate (sand) (b) coarse aggregate (10 mm)

In this chapter, corrugated (CF) and smooth straight (SF) fibers are utilized as reinforcement. The geometrical and mechanical properties of these steel fibers are summarized in Fig. 3.2 and Table 3.3. The Hobart planetary mixer is employed to prepare the 3D printed concrete mixes. Initially, all dry ingredients, including coarse aggregates, are combined in an 80 L-capacity pan mixer and mixed at 100 rpm for 3 minutes to create a homogeneous dry mixture. Subsequently, 75% of the required water, along with the combined superplasticizer (SP), is added to the dry mixture. This initial water addition ensures proper coating of the dry ingredients, promoting better dispersion and preventing clumping. The mixture is then mixed for 5 minutes to achieve a uniform consistency. Following this, steel fibers are incorporated into the mixture, and mixing continued for an additional 1 minute at 360 rpm to ensure thorough integration of the fibers. The remaining water is added step-by-step to refine the mixture's workability, as suggested by [159,160]. This staged approach allows for precise adjustments to achieve the desired consistency and homogeneity. Finally, the mixing process continued for an additional 2 minutes at 198 rpm to ensure a well-blended final mixture. The detailed process of the mixing procedure is illustrated in Fig. 3.3.

Table 3. 3. Properties of steel fibers

Type	Density (g/cm^3)	Length (mm)	Diameter (mm)	Ultimate tensile strength (GPa)	Elastic modulus (GPa)	Aspect ratio
Corrugated (CF)	7.85	30±2	0.5	2.15	190	64
Smooth straight (SF)	7.85	15±1	0.3	2.65	200	43.33

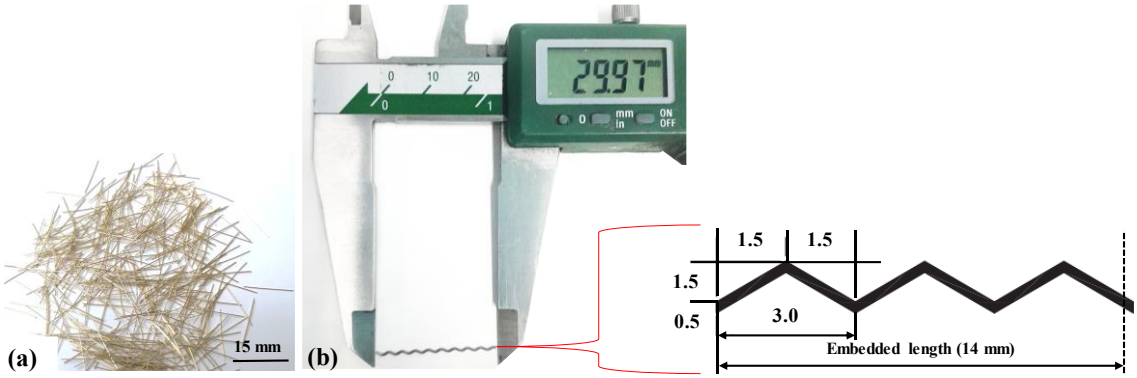

Fig. 3. 2. Steel fiber used in the tests (units in mm) (a) straight smooth fiber (b) corrugated fiber

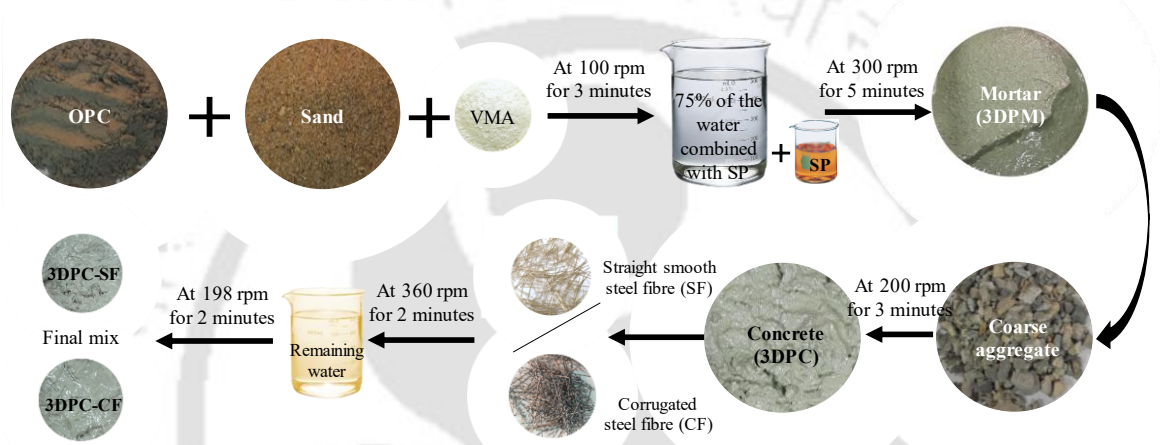

Fig. 3. 3. Mixing process of fiber reinforced 3DPC

3.2.2. 3D printing process

A steel frame gantry-type 3D printer is employed in this current investigation, featuring a printable area measuring 1.0 m in length, 1.0 m in width, and 1.0 m in height (Fig. 3.4). The 3D printer utilized in this work is a specially designed auger-type extruder that effectively incorporates coarse aggregates and macro fibers longer than 30 mm into the printing process. A key modification to the extruder system involved creating an extra gap between the auger and the extruder wall, which facilitates a smooth flow of material and minimizes the risk of obstruction during extrusion (Fig. 3.4b). This design enables the continuous feeding of concrete mixtures containing coarse aggregates and log fibers, ensuring that they are uniformly distributed throughout the printed layers (Fig. 3.5). The auger's rotation speed can be precisely controlled to optimize the extrusion rate, allowing for consistent material deposition while accommodating larger aggregate sizes. This careful engineering of the extruder, combined with the controlled material formulation, enhances the overall performance of the printed structures by ensuring that the coarse aggregates and fibers are effectively integrated and homogeneously

distributed into the matrix. Fig. 3.4 is presented to show the different printed beams and the printing system.

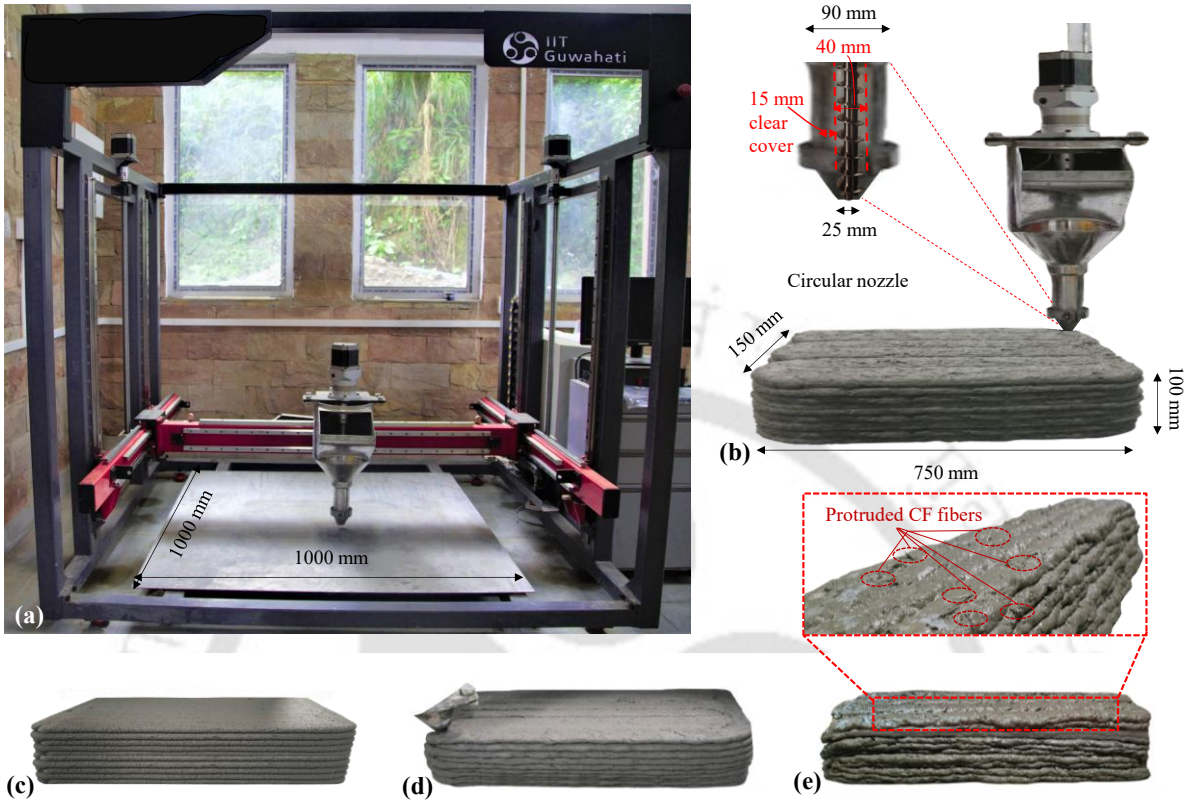

Fig. 3. 4. 3D printing system (a) concrete 3D printer (b) enlarge view of nozzle with printed 3DPC-SF beam (c) 3DPM beam (d) 3DPC beam (e) 3DPC-CF beam

The 25 mm diameter circular nozzle is engineered to accommodate larger aggregate sizes and longer fibers (Fig. 3.4b). This larger opening minimizes blockages and allows the extruder to push the composite material through the nozzle without compromising structural integrity. The 25 mm diameter circular nozzle is deliberately chosen to accommodate larger aggregate sizes and longer fibers. This diameter is selected to be slightly less than the length of the macro fibers (30 mm) i.e., CF used in the mix, a decision that led to an interesting phenomenon during extrusion. Due to the longer fiber length relative to the nozzle diameter, the fibers become slightly curved as they are extruded, causing some to protrude from the filament layers (as shown in Fig. 3.5). This curving effect results in fibers crossing between the layers, acting as natural interlayer reinforcement. As subsequent layers are printed, these protruding fibers enhance the bond between layers, leading to a stronger, more cohesive structure. This phenomenon can also be observed in the load vs. deflection curve of the corrugated fibers (Fig. 3.9), where the interlayer bonding contributes to increased structural performance. This unique reinforcement mechanism does not occur with smooth straight steel fibers (SF), which have

less bonding strength compared to corrugated fibers and do not exhibit the same level of interlayer interaction.

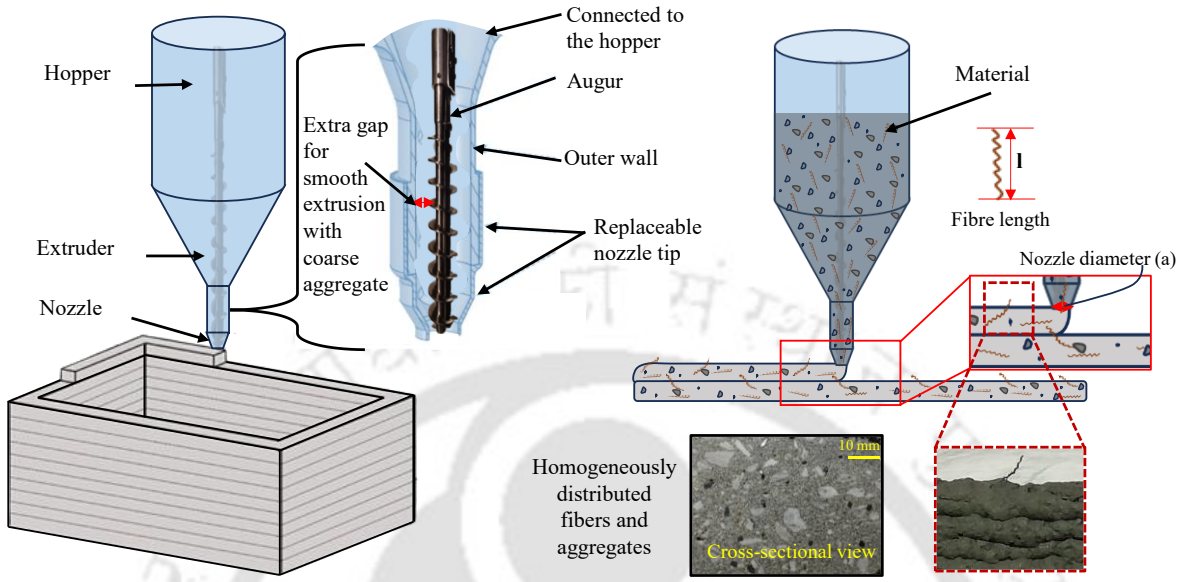

Fig. 3. 5. Schematic representation of extrusion-based 3D printing for fiber-reinforced strain-hardening concrete (**3DPC-CF**) and its reinforcement mechanism

To evaluate the workability of the 3DPC mixtures, a mini slump cone with an inside diameter of 70 mm at the top, 100 mm at the bottom, and a height of 60 mm is used to test the slump and flowability of the mix designs (Table 3.4). Here, slump refers to the vertical reduction in height of the material after lifting the cone, while flowability represents the lateral spread (diameter) of the mix, reflecting its ability to deform and flow. The spread diameter of fresh mortar mixtures is measured after 25 drops of the flow table according to ASTM C1437-20 [161]. A 3D printed cylindrical mold is used to measure the slump and diameter of the sample after demolding to estimate the density and yield stress [162]. It's important to emphasize that the slump value of the selected mix in this current investigation, within the range for smooth extrusion and desired buildability [163].

Table 3. 4. Fresh state properties of mix

Mix	Slump (mm)	Flowability (mm)	Density (kg/m^3)	Yield stress (Pa)
3DPM	11	138	2200	1381
3DPC	8	131	2249	1442
3DPC-SF	7	128	2291	1466
3DPC-CF	6	112	2352	1491

In this chapter, solid beams having 150 mm×100 mm cross-section area and 750 mm in length (for all specimen) is 3D printed (refer to Fig. 3.4b, Fig. 3.7a) with 10 layer height, where a single concrete layer height is 10 mm and width is 25 mm. The selection of a 10 mm layer height was made deliberately to ensure compatibility with the maximum particle size of the coarse aggregates used. The extrusion rate, set at 40 mm/s print speed, is adjusted by controlling the augur's rotation speed. To ensure uniformity, all samples are left undisturbed for 24 hours post-printing. Subsequently, the beams are delicately removed from the printing platform and immersed in water for curing until the 28-day testing period. For each specific test, a total of 6 sample are extracted from each beam along the Z-direction. This direction is chosen for testing as it aligns with real-world loading conditions expected in large-scale applications of 3DPC structures.

3.2.3. Test methods

After formulating the mixes, the initial mechanical properties of concrete are evaluated. Final testing is conducted following critical fiber volume analysis to achieve simultaneous strain hardening and ductility. Single fiber pull-out testing is performed for the critical fiber volume. Fig. 3.6 illustrates the testing framework developed in this research to achieve ultra-ductile strain-hardening 3DPC.

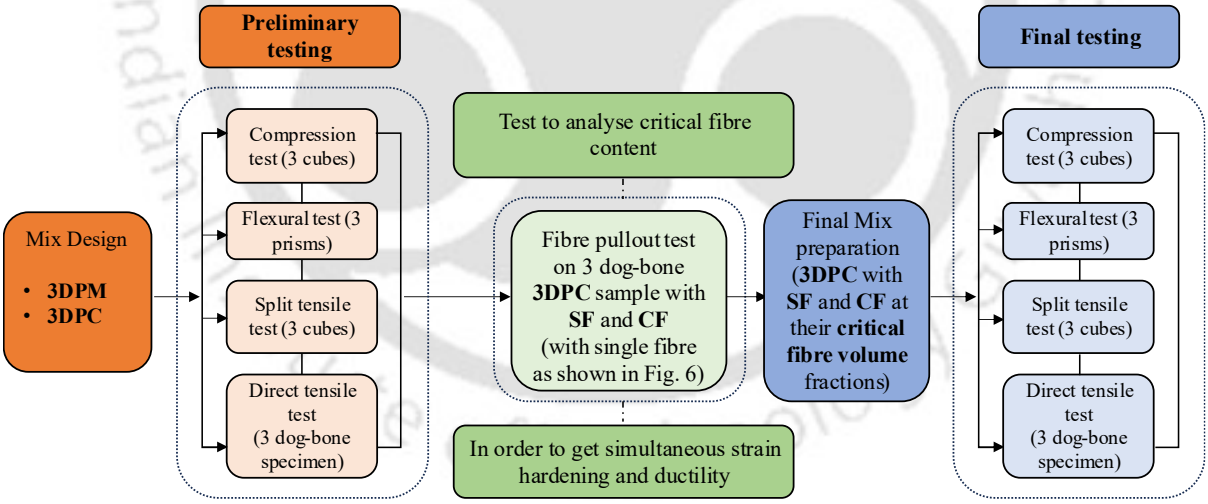

Fig. 3. 6. Testing flowchart to achieve the ultra-ductile strain hardening 3DPC

3.2.3.1. Compression, flexure, and split tensile test

After 28 days of curing period, the printed beams are cut into 50 mm cubes for compressive, split tensile (3 cubes along Z-direction) and 40×40×160 mm prisms for flexural strength tests (3 prisms along Z-direction) (Fig. 3.7b,c). This selection of specimen size is also applied to the 3DPC samples containing coarse aggregates to maintain consistency and facilitate effective comparisons with the referenced mortar samples (3DPM). The cut specimens are subjected to

compression, split tensile, and flexure loads. The compressive and split tensile strengths are measured using universal testing machines (UTM) with constant displacement control rate of 1 mm/min. The flexural behaviour is investigated using a three-point bending test with load control rate of 2.5 kN/min. All specimens are tested under 250 kN load along Z- direction and the loading orientation of 3D printed specimens are depicted in Fig. 3.7.

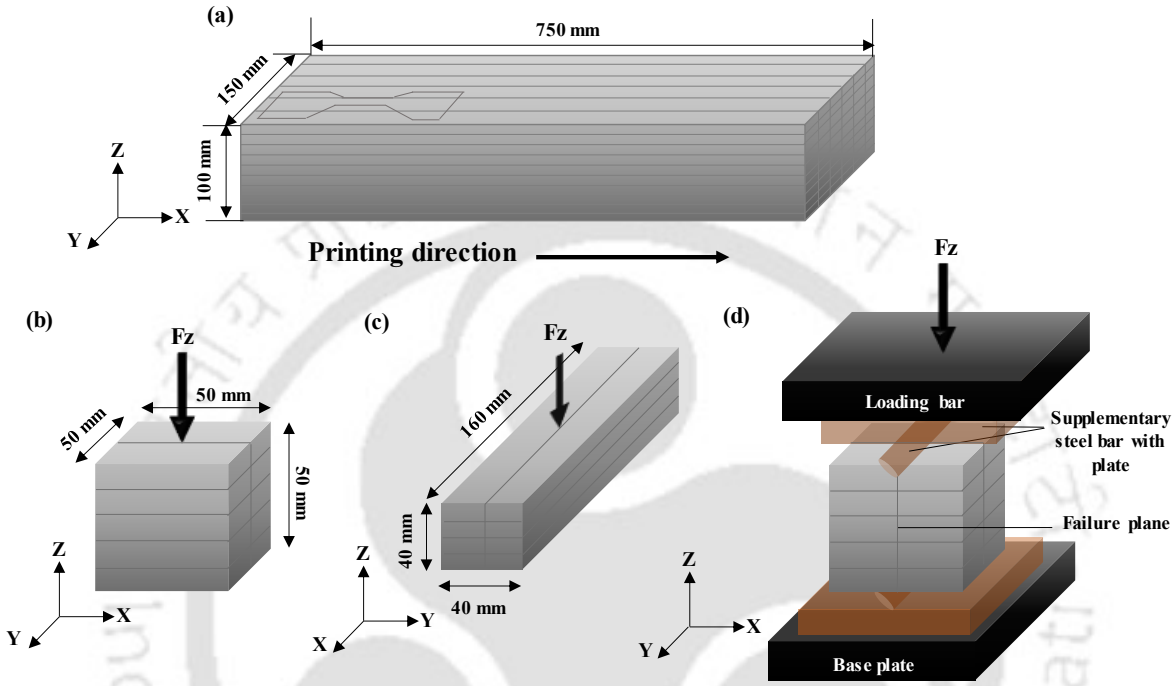

Fig. 3. 7. Schematic Illustration for loading orientation of (a) printed beam; (b)cubes (compression and split tensile); (c) prism (flexural), and (d) split tensile test setup

3.2.3.2. Direct tensile test and single fiber pull-out test

Two different servo-controlled UTMs are utilized for the fiber pull-out and direct tensile test. The test setup and geometry for fiber pull-out and direct tensile test specimen is shown in Fig. 3.8a, b. All specimens were manufactured via 3D printing process. The dog-bone mold is precisely aligned on the printing bed to ensure that the entire specimen, particularly the gauge length the central portion of the dog-bone mold. A layer width of 30 mm and a layer height of 20 mm are employed to match the specified mold dimensions, ensuring accurate fabrication. In order to quantify the critical fiber volume, bond strength between steel fiber and matrix is measured through single fiber pull out test. Dog-bone shape mold with dimension of 330 mm × 60 mm × 20 mm is adopted for the fiber pull out test. A slot with 1 mm width is located in the middle of mold (as shown in Fig. 3.8b), and a PVC (Polyvinyl Chloride) slice with a single fiber passing through the centre is inserted into the slot [164]. The embedded lengths of the single fiber on both sides of slice are half of the fiber length. The pull-out specimens are

inserted into the steel grip jig and pulled vertically with loading rate of 0.018 mm/s [165]. The fiber pull-out load is measured using a load cell with maximum capacity of 3 kN. A 'fixed-fixed' boundary condition is applied for the fiber pull-out test.

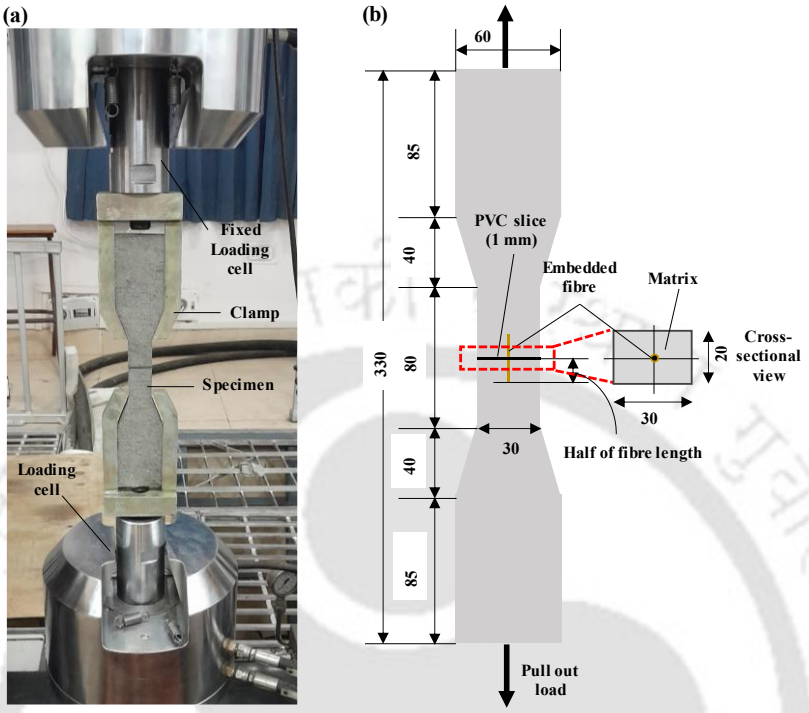

Fig. 3. 8. Direct tensile and fiber pull-out test (a) fiber pull-out test setup; (b) schematic of dog-bone specimen (all dimensions are in mm)

In order to design fiber reinforced 3D printed strain hardening concrete by considering critical fiber volume, fiber-matrix bond strength (τ) is considered. The value of τ can be determined from Eq. (3.1) [166,167]. The detailed bonding and pull-out behavior of the different fibers is illustrated in Fig. 3.9. It can be observed that the SF fiber having lower bonding strength compared to the CF fiber, experiences a sudden failure after reaching its peak load. This abrupt failure is due to the brittle nature of the SF fiber's bond at the interface. In contrast, the CF fiber exhibits a stronger bond and a more favorable bond-slip behavior, with a gradual decrease in load after the peak. This improved performance of the CF fiber can be attributed to its ability to sustain bond integrity and better distribute stress, resulting in enhanced slip and ductility.

$$\tau = \frac{P_{max}}{\pi . d_f . L_e} \tag{3.1}$$

where P_{max} is the maximum pull out load (Table 3.5), d_f is the fiber diameter, L_e is the initial embedment length.

3.2.3.3. Single fiber pull-out behaviour

The pull-out load-slip curves, depicted in Fig. 3.9a illustrate the debonding characteristics of both steel fibers within the 3DPC matrix. As shown in Fig. 3.9a, the steel fibers are pulled out from the matrix, revealing two distinct stages in the curves: 1) rapid debonding stage and 2) gradual frictional one. Notably, the latter stage tends to be as a horizontal line, particularly evident in the case of corrugated steel fiber. Considering the limited embedded length over which adhesive bonding strength operates, it is presumed that SF are solely held in the matrix by adhesive strength, lacking frictional bonding strength. The magnitude of frictional bonding strength is contingent upon the average height value within the gradual stage of the curves [168]. As indicated in Table 3.5 and Fig. 3.9b, it's important to highlight that lower bonding strength of straight smooth steel fibers in 3DPC is observed, since the plastic deformation of SF is relatively weak due to their smooth surface and short embedment length. However, the frictional bonding strength of CF surpasses that of SF, which is attributed to mechanical deformation accompanying the pull-out response of CF.

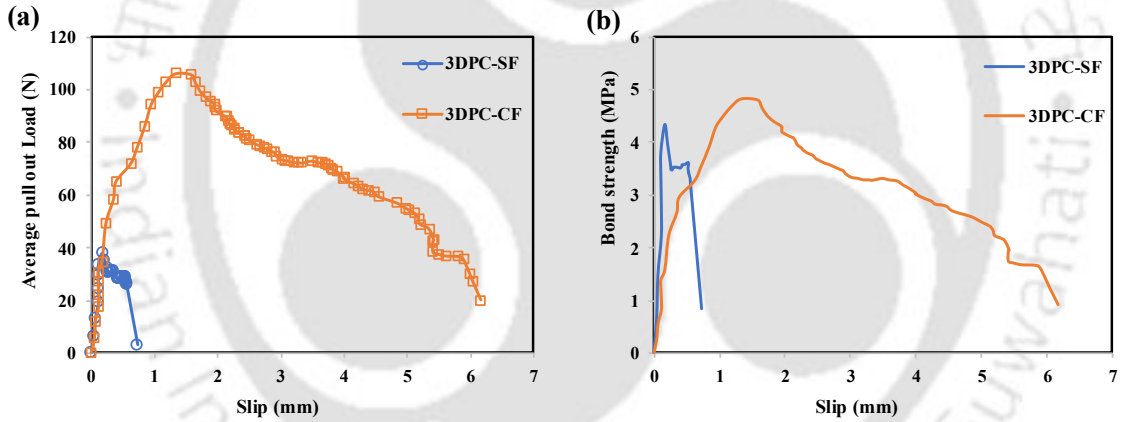

Fig. 3. 9. Experimental load-slip displacement (pull-out tests curves) for steel fibers embedded in 3DPC

Table 3. 5. The bonding strength of steel fibers

Mix	P_{max} (N)	P_{drop} (N)	Max slip (mm)	d_f (mm)	L_e (mm)	τ (MPa)
3DPC-SF	38.03	2.99	0.72	0.3±1	7	4.33
3DPC-CF	105.98	20.01	6.16	0.6±1	14	4.82

3.3. Engineering design of fiber reinforced 3D printed strain hardening concrete

In this section, we delve into the primary aspects of designing fiber-reinforced 3D printed strain hardening concrete, with a focus on the mechanisms of strain hardening and multi-cracking behavior. Strain hardening is a critical property that enhances the tensile strength and ductility

of concrete, making it suitable for engineering applications that demand high energy absorption and deformation capacity, such as seismic-resistant structures and large-scale infrastructure.

Strain hardening refers to the ability of a material to continue carrying increasing loads after initial cracking, without experiencing catastrophic failure. In fiber-reinforced 3DPC, strain hardening results in the formation of multiple fine cracks, as opposed to a single large crack. This behavior is primarily governed by the fiber-matrix interaction, where the fibers bridge cracks, redistribute stresses, and prevent further crack propagation. The process enhances the material's energy absorption capacity and ensures it can undergo significant deformations before failure, thus improving both strength and toughness.

Based on established theories outlined in [169–171], analytical models are presented using principles from the rule of mixtures and fracture mechanics to explain the characteristics of this composite material. The discussion is grounded in the following assumptions:

- Both the matrix and fibers exhibit linear elastic–perfectly brittle tensile response.
- The fibers are arranged parallel to each other and uniformly dispersed throughout the matrix, and does not affect the porosity of the matrix; thus, the volumetric proportions of the matrix (V_m) and fiber (V_f) constituents are related as $V_m = 1 - V_f$.
- Forces are applied parallel to the fiber direction in case of direct tensile testing, meaning the fiber reinforcement solely bears load along the loading axis.
- The composite begins in a stress-free state, and Poisson's effects are negligible.
- In the pre-crack state, perfect bonding exists between the fibers and matrix. This results in equal strains on both components, while stresses are proportional to each constituent's elastic modulus.
- Upon the development of a crack in the matrix, it extends to the fibers causing debonding at the fiber–matrix interface.

Prior to strain hardening concrete design, it is crucial to establish a concrete performance level. Fig. 3.10 illustrates the performance classification and behaviour of 3DPM as a reference material (Level 1), which places the 3DPC composite into the following categories of behavior: (Level 2) strain softening or crack controlling with little enhancement in mechanical properties, (Level 3) mild strain hardening, (Level 4) high tensile strain hardening with mild ductility enhancement, (Level 5) mild tensile strain hardening with mild ductility and energy absorbtion capacity, and (Level 6) high tensile strain hardening with high ductility and high energy

absorbing capacity. Fig. 3.10 include the following parameters: first cracking stress σ_{cc} which can also consider as the yield point corresponds to the first significant deviation from linearity in the curve, marking the onset of plastic deformation and associated first cracking strain ε_{cc}, coressponding elastic modulus E_{cc}, and post-cracking strength σ_{pc}, which denotes the peak load-bearing capacity before strain hardening initiates. It is worth noticing that the stress versus strain relationship is only valid prior to matrix cracking. The material softening behavior is characterized by stress versus crack opening relationship. During the multiple cracking phase (i.e., strain hardening segment), the material can be characterized by stress versus strain values assuming a smeared cracking approach. In Fig. 3.10 (level 1) has been added to the performance classification to illustrate the behavior of non-fiber printed mortar (3DPM) as a reference material. The material developed in this research aims for the sixth and highest performance level that is a strain-hardening material with ductility and a high energy absorbing capacity.

To evaluate and quantify this ultra ductile strain hardening 3DPC behavior, we introduce three key parameters: strain hardening factor (φ), ductility factor (μ), and energy absorption capacity (G_{pc}) (Fig. 3.10 (Level 6)). The ductility factor (ratio of ultimate to yield deformation) correlates with the material's ability to withstand significant deformations without failure [172], which is vital in seismic applications. In 3DPC, high ductility ensures both safety and longevity, enabling structures to endure seismic shocks. While specific data on the ductility factor for strain-hardening 3DPC is limited, cementitious strain-hardening materials generally exhibit values between 0.1% and 6% [89]. G_{pc} represents the amount of energy absorbed by the material before failure, calculated from the area under the stress-strain curve. It is a measure of the material's ability to dissipate energy through cracking and deformation. In large-scale and seismic-resistant structures, materials with high energy absorption capacity are essential to mitigate the effects of dynamic and impact loads. High G_{pc} ensures that 3DPC can absorb shocks and prevent catastrophic failure, enhancing the overall resilience of the structure. For strain hardening ultra high performance fiber reinforced concrete, the target G_{pc} values range from 55 to 94 kJ/m^3, depending on the fiber volume fraction (typically 2.5%) [173].

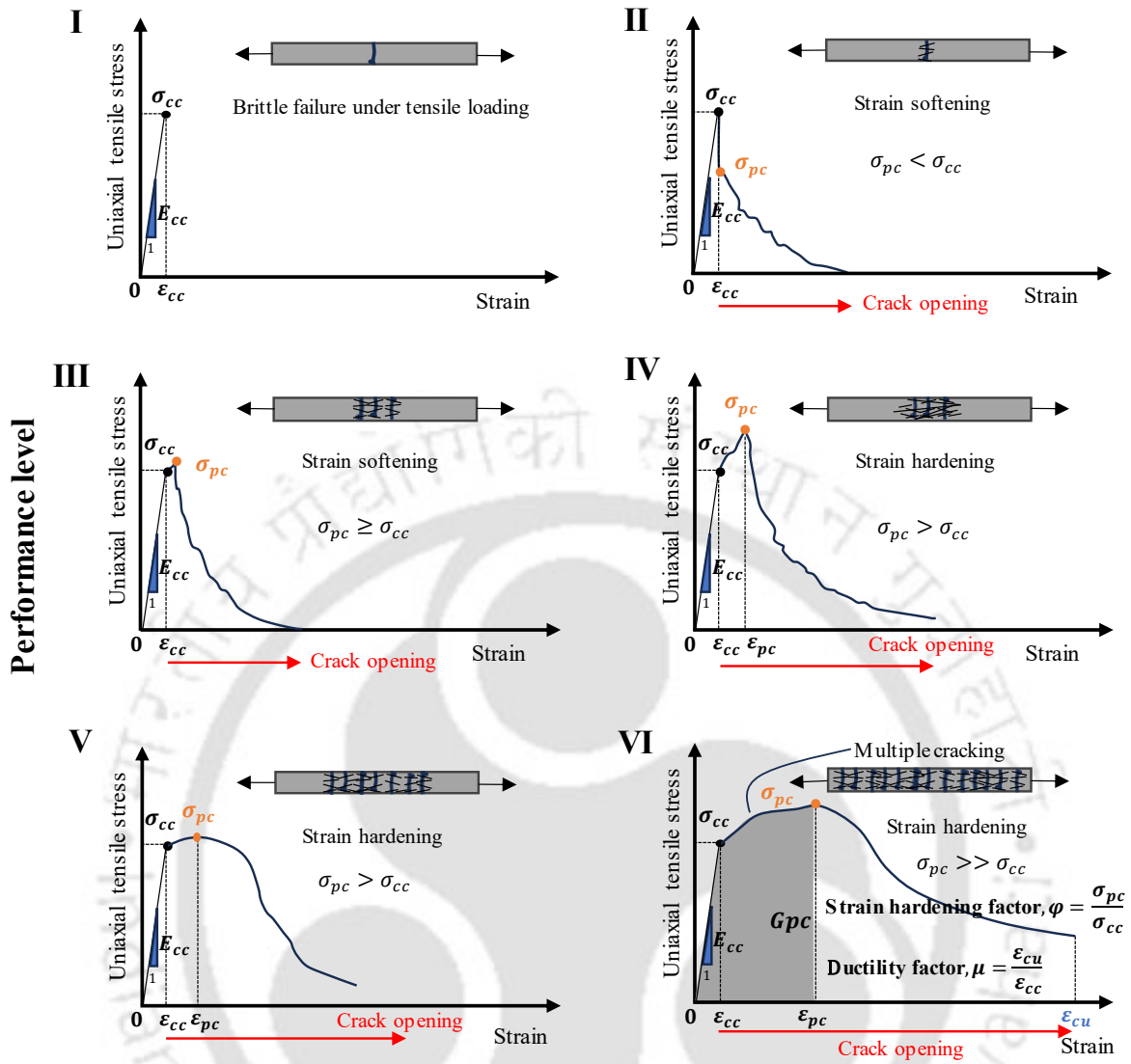

Fig. 3. 10. Performance level illustration of fiber reinforced strain hardening concrete

3.3.2. Critical fiber volume fraction to achieve strain hardening behaviour in tension

In fiber reinforced 3DPC, the failure strain of the matrix is typically much lower than the failure strain of fibers ($\varepsilon_m << \varepsilon_f$) and therefore, the first crack occurs when tensile capacity of the matrix (σ_m) is reached. Based on the assumption of elastic stress distribution up to crack formation, the tensile stress in composite at onset of first percolation cracking (just before the cracking) of the matrix can be expressed by Eq. (3.2):

$$\sigma_{cc} = \sigma_m.(1 - V_f) + \alpha.\tau.V_f.\frac{l}{d} \quad (3.2)$$

where τ *is* fiber-matrix bond strength, $\frac{l}{d}$ is the fiber aspect ratio, α is bonding coefficient, given by Eq. (3.3):

$$\alpha = \alpha_1 . \alpha_2 . \alpha_3 \quad (3.3)$$

where α_1 is coefficient describing the average contribution of bond at onset of matrix cracking i.e., P_{drop}/P_{max} (given in Table 3.5 and 3.6), α_2 is the efficiency factor of fiber orientation in uncracked state of composite, which is 1 in case of unidirectional fiber i.e., fibers aligned in the direction of loading. α_3 is coefficient describing the reduction in bond strength at matrix fiber interface due to applied external stress either radial or normal to the interface, and it is also 1 for unidirectional fiber, hence in this case, $\alpha = \alpha_1$.

Maximum post cracking stress, σ_{pc} mainly depends on fiber reinforcement parameter and bond at the fiber-matrix interface. In case of a tensile prismatic member with unidirectional fiber, it is assumed that critical planer crack exists across the entire section of tensile member (Fig. 3.11), which is normal to the axis of fiber. For circular fiber, the post cracking strength is given by Eq. (3.4):

$$\sigma_{pc} = \lambda . \tau . V_f . \frac{l}{d} \tag{3.4}$$

where λ is tension stiffening coefficient, which is the product of several coefficients (Eq. (3.5)):

$$\lambda = \lambda_1 . \lambda_2 . \lambda_3 . \lambda_5 ; \ \lambda_2 = 4\alpha_2 . \lambda_4 \tag{3.5}$$

where λ_1 is average or expected value of the ratio of embedded distance of fiber from a forming crack to the length of the fiber. The shorter embedded length is assumed to be the one that will be pulled out under load. The value of λ_1 is ¼ as derived from probability theory consideration (Fig. 3.11), λ_3 is the group reduction coefficient for bond and is 1 for single fibre pull out, λ_4 is also 1 for fiber with longitudinal axis oriented in the direction of loading, λ_5 is 1 for aligned fibers and hence $\lambda = 1$.

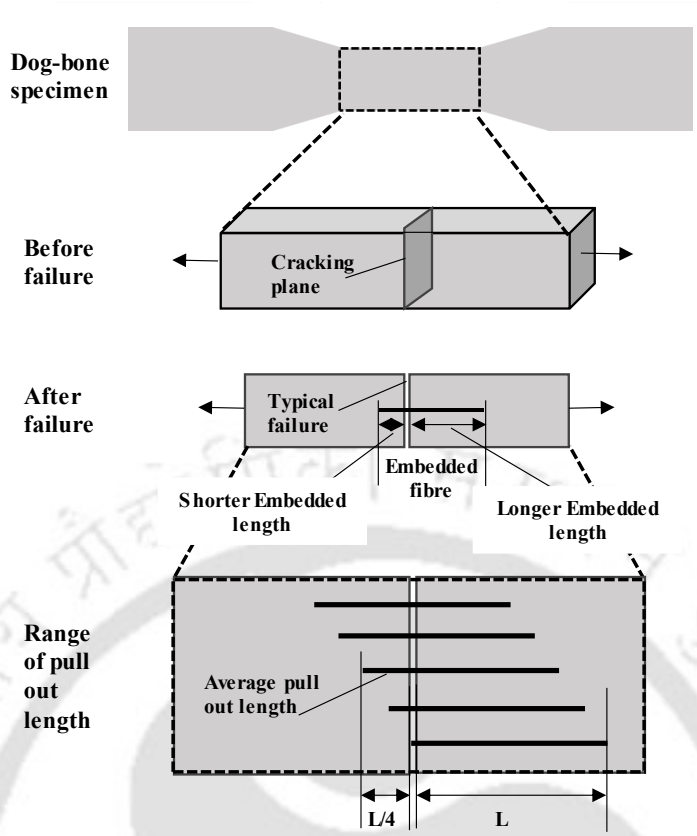

Fig. 3. 11. Assumed model for general pull out after matrix cracking

In order to achieve strain hardening behaviour in tension, through critical fiber volume fraction the post cracking strength should be greater than strength at first cracking i.e., $\sigma_{pc} \geq \sigma_{cc}$ (given by Eq. (3.6)-(3.10)).

From Eq. (3.2) and Eq. (3.4):

$$\lambda.\tau.V_f.\frac{l}{d} \geq \sigma_m.(1-V_f) + \alpha.\tau.V_f.\frac{l}{d} \tag{3.6}$$

$$(\lambda-\alpha)\tau.V_f.\frac{l}{d} \geq \sigma_m - \sigma_m.V_f \tag{3.7}$$

$$\left(\sigma_m + \left[(\lambda-\alpha)\tau.\frac{l}{d}\right]\right)V_f \geq \sigma_m \tag{3.8}$$

$$V_f \geq \frac{\sigma_m}{\left(\sigma_m + \left[(\lambda-\alpha)\tau.\frac{l}{d}\right]\right)} \tag{3.9}$$

here, V_f becomes critical fiber volume fraction i.e., $V_{f,cr}$ (Table 5) and the simplified form of Eq. (3.9) can be found through Eq. (3.10):

$$V_{f,cr} \geq \frac{1}{\left(1 + \left[(\lambda - \alpha)\frac{\tau}{\sigma_m} \cdot \frac{l}{d}\right]\right)} \quad (3.10)$$

Average bond strength τ, and all other parameters such as σ_m, L/D, λ, α can be obtained from Fig. 3.9 and Table 3.6.

Table 3. 6. Critical fiber volume for varying steel fibers

Mix	τ (MPa)	σ_m (MPa)	L/D	λ	α	$V_{f,cr}$ (%)
3DPC-SF	4.33	3.01	50	1	0.08	**1.48**
3DPC-CF	4.82	3.01	64	1	0.19	**1.18**

From the above table, the critical fiber volume of different fibers are obtained to achieve strain hardening behaviour in 3DPC.

3.3.3. Ductility enhancement mechanism through coarse aggregate

Ductility is a crucial property that enables structures to withstand extreme loads, such as significant pressure fluctuations, earthquakes, and hurricanes, without sudden failure or collapse. The ductility index, defined as the ratio of ultimate deformation to yield deformation, measures the material's capacity for substantial deformation before failure [172]. This index is particularly important in seismic applications, where high ductility is vital for energy dissipation and preventing catastrophic failure. Past studies [152] have shown that incorporating 10 mm coarse aggregates effectively improves ductility, but similar improvement is not seen while using 20 mm coarse aggregates [152]. The larger aggregates cause more severe stress concentrations, thus leading to more brittle behaviour in the concrete specimen.

Fig. 3.12 illustrates the mechanism of ductility enhancement in high-strength 3DPC. In plain concrete, the mechanisms involved in the fracture process include (see Fig. 3.12): (I) crack shielding, (II) crack deflection, (III) aggregate bridging. It has been observed that a higher probability of active voids leads to more frequent multiple cracking phenomena [151]. Active voids are those that contribute to multiple cracking and sometimes it's large enough to initiate the crack extension at tensile stresses below the capacity of bridging fibers. In high-strength 3DPC with coarse aggregate, the coarse aggregate not only forms good bond with the cementitious matrix but also acts as "additional voids" in the high-strength matrix. By incorporating coarse aggregate, the fraction of active voids increases, thus resulting more saturated multiple cracking and higher tensile ductility without debonding at the aggregate/matrix ITZ. Furthermore, in this chapter it is observed that cracks propagate through

the aggregate rather than bypassing it. This behavior can be linked to the enhanced ITZ formed by the aggregates used in our mix, leading to a relatively high bond strength between the matrix and aggregate, which makes the aggregate more susceptible to cracking (Fig. 3.12). This interaction contributes to a more uniform stress distribution, facilitating crack propagation through the aggregate.

In this work, coarse aggregate is used to tailor the void distribution, ultimately affecting the toughening mechanism and enhancing ductility in 3DPC.

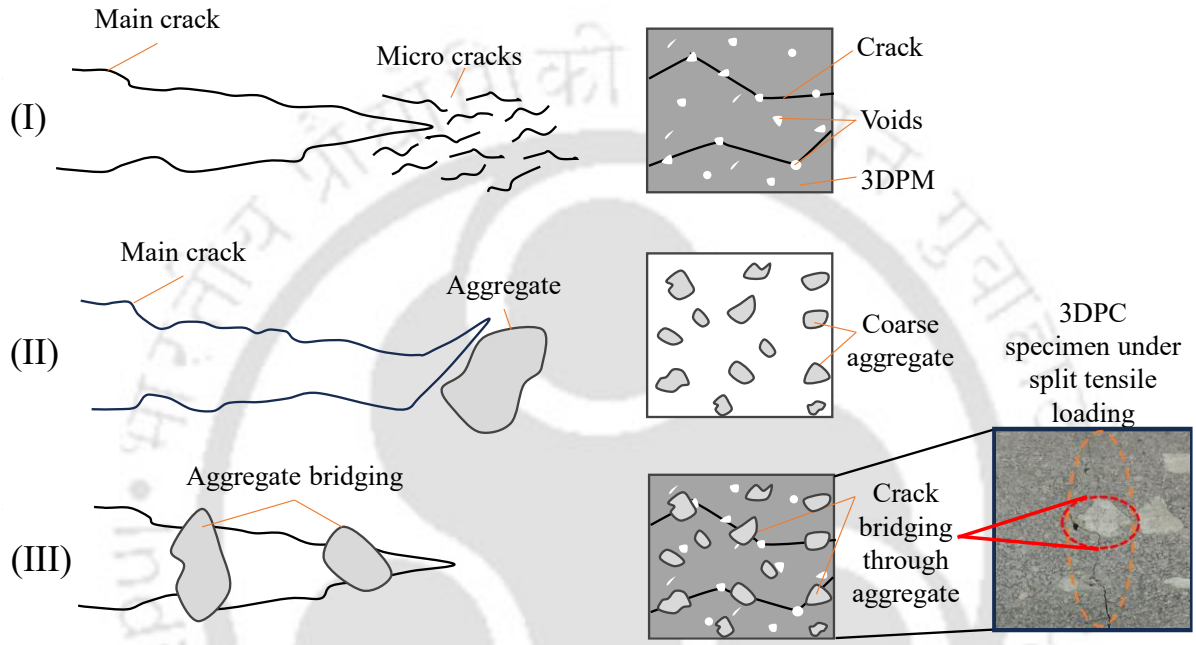

Fig. 3. 12. Illustration of toughening and ductility mechanisms in concrete using coarse aggregate

3.4. Results and discussion

3.4.1. Sigle fiber pull-out mechanism of steel fibers

This section explores the mechanisms behind pull-out behaviour of the SF and CF. The process of gradual interfacial degradation is characterized by combination of bond-slip deterioration and frictional contact. Constitutive law for fiber-interface load transfer is proposed to accurately model the bond-slip behaviour and predict the overall performance of fiber-reinforced 3DPC.

3.4.1.1. Characterizing the fiber-matrix interface bond

The relationship between bond stress and slip at the fiber-matrix interface is considered as constitutive property for predicting mechanical and fracture properties of the fiber-reinforced concrete (Fig. 3.13a). However, characterizing this bond is a challenging task. The

physicochemical characterization involves both debonding of the surrounding interface and frictional slip of the fiber [174].

Fig. 3.13b illustrates pull-out behaviour of the SF, which involves two primary mechanisms: 1) debonding and 2) frictional pull-out: Initially, debonding occurs due to cracking within and along the ITZ followed by fiber pull-out under frictional resistance. In post-peak phase, the load decreases as the extracted length increases, thus reducing the available frictional area and surface roughness of the channel. Fig. 3.13a shows the average bond-slip curve and the schematic of straight fibers (Fig. 3.13b) embedded in a concrete matrix up to half the fiber length (7 mm).

For CF, the initial mechanisms are similar to those for SF, with an additional contribution from mechanical anchorage (Fig. 3.13c). The corrugated shape of CF enables significant plastic deformation with curvatures straightening within plastic hinges (PH), leading to a substantial increase in the maximum pull-out load (Fig. 3.13a). This sequence is diagrammatically shown in Fig. 3.13c. Beyond the maximum load, pull-out load decreases due to progressive mobilization and entry of PH1 into the same corrugated groves of the fiber channel. As PH1 straightens, the fiber moves further, followed by the straightening of PH2 (as shown in Fig. 3.13c), which enters in the opposite groove of the debonded channel causing the mechanical anchorage. This results in higher debonding stress (τ_d) which leads to slower slip rate instead of direct fall into the frictional state. Once several PH's are fully deformed and straightened, the pull-out load only needs to overcome kinetic frictional resistance, similar to a straight fiber, until the fiber is completely removed from the matrix.

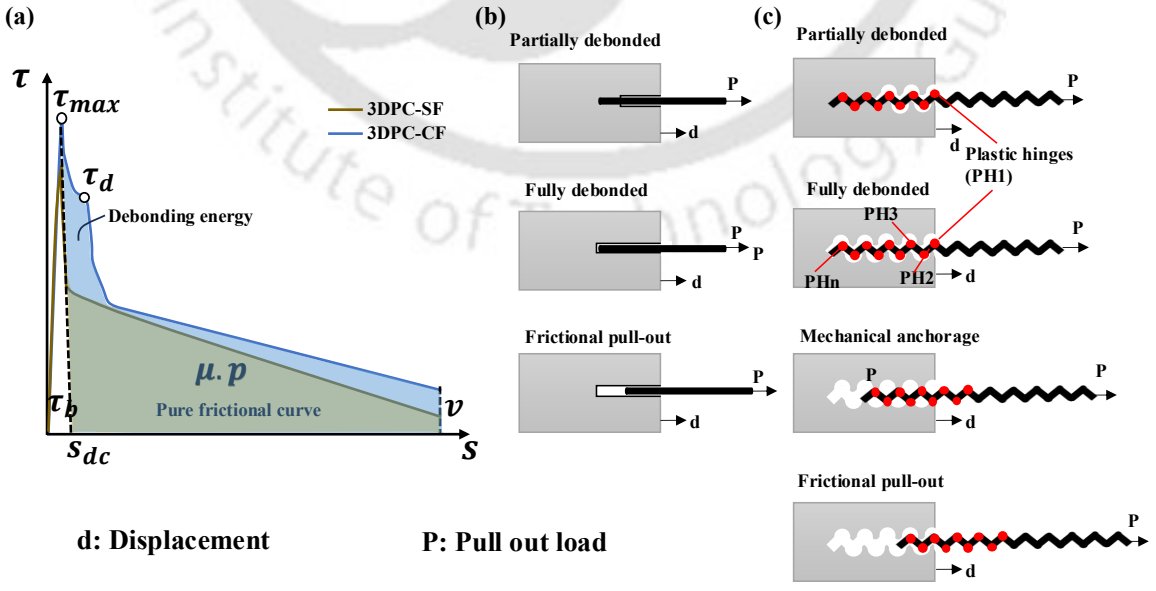

Fig. 3. 13. (a) Bond-slip at the interphase; schematic diagram of pull-out mechanism of (b) SF (c) CF

3.4.1.2. Constitutive law for CF-interface load transfer

From this analysis it is evident that in case of CF, the load transfer at the interface occurs first through adhesive bond stress and debonding stress followed by frictional stress. Consequently, a generic constitutive law with three components can be proposed to reflect the gradual deterioration at the interface. The first component, $\tau b(s)$, represents the interfacial bond relation due to physical and chemical cohesion [175]. The shear stress at the interface can be decomposed accordingly (given by Eq. (3.11)) to accurately model the bond-slip behaviour and predict the overall performance of fiber-reinforced 3DPC.

$$\tau(s, v) = \tau_b(s) + \mu(v).p + n_{PH}.\tau_d(v) \tag{3.11}$$

where $\tau_d(v)$ is the debonding stress as a function of the slip rate, and given by [176] Eq. (3.12):

$$\tau_d(v) = \frac{F_d}{2\pi r L_e} \tag{3.12}$$

where $\tau_b(s)$ represents the interfacial bond stress as a function of the local slip displacement, s. The second term, v is the slip rate accounts for the frictional contact, μ is the Coulomb's friction coefficient, and p is the contact pressure. Additionally, n_{PH} denotes the number of plastic hinges passes through debonded region at the interface, F_d is the external load at the onset of interfacial debonding, r is the fiber radius, and L_e is the embedded fiber length. It is important to note that p is automatically determined during the calculations, while $\mu(v)$ must be specified as part of the constitutive relationship.

Assuming a linear-decreasing bond-slip relationship for $\tau_b(s)$, the bond is totally depleted in case of SF (as per Eq. (3.13) and only the frictional component remains once a critical slip displacement, s_{dc}, is achieved [175].

$$\tau_b(s) = \tau_{max}(s)\left[1 - \frac{s}{s_{dc}}\right]; 0 \leq s < s_{dc} \tag{3.13}$$

where $\tau_{max}(s)$ is the maximum shear stress resisted at the interface.

3.4.2. Effect of coarse aggregate on tensile properties of 3DPC

The tensile fracture of concrete is complex phenomena and not yet fully understood. Generally, it is known that under tensile stress concrete crack bridging results from the coalescence of microcracks in the matrix, development of bond cracks between aggregates and matrix, and frictional pull-out of the aggregates [177]. The uniaxial tensile behaviour can be explained as shown in Fig. 3.14.

The microcracks are present in the concrete due to internal restraint caused by the aggregate, shrinkage and thermal deformations. When stress is applied, these microcracks begin to grow from the interface between the cement paste and aggregates (A), and eventually propagate into the mortar (B). Upon reaching the peak tensile stress (σ_m), also known as the post-cracking stress (σ_{pc}) (C), microcracks propagate unstably, leading to crack localization and propagation, thus resulting in a stress drop (D). Crack bridging and branching are the main mechanisms responsible for the long softening tail (D-E) observed in experiments.

However, since the fracture process largely depends on aggregates and their bond to the matrix, it varies between high-strength concrete and lightweight aggregate concrete. For large-size lightweight coarse aggregates, the aggregates may act as weak link, causing aggregate rupture, which reduces the bridging effect and further leads to brittle fracture process [178].

From Fig. 3.14 and Table 3.7, we have observed that the ultimate tensile strength of 3DPC is 3.01 MPa, with an ultimate strain of 0.0304. The strain hardening factor (φ) is 1.19, and ductility factor (μ) is 3.01. In contrast, 3DPM has an ultimate tensile strength of 2.48 MPa and ultimate strain of 0.0115, exhibiting no strain hardening or ductility behaviour. Furthermore, 21.37% strength improvement and 159.11% ductility improvement has been observed in 3DPC compared to 3DPM.

The significant improvement in ductility and strain hardening behaviour in 3DPC can be attributed to inclusion of the coarse aggregate. The coarse aggregates provide effective crack bridging during the initial cracking phase and create an optimized bond with the matrix. The synergy between coarse aggregates and cementitious matrix allows the 3DPC to withstand higher tensile stresses and undergo greater deformation without sudden failure, unlike plain mortar (3DPM) which lacks these beneficial interactions and fails abruptly.

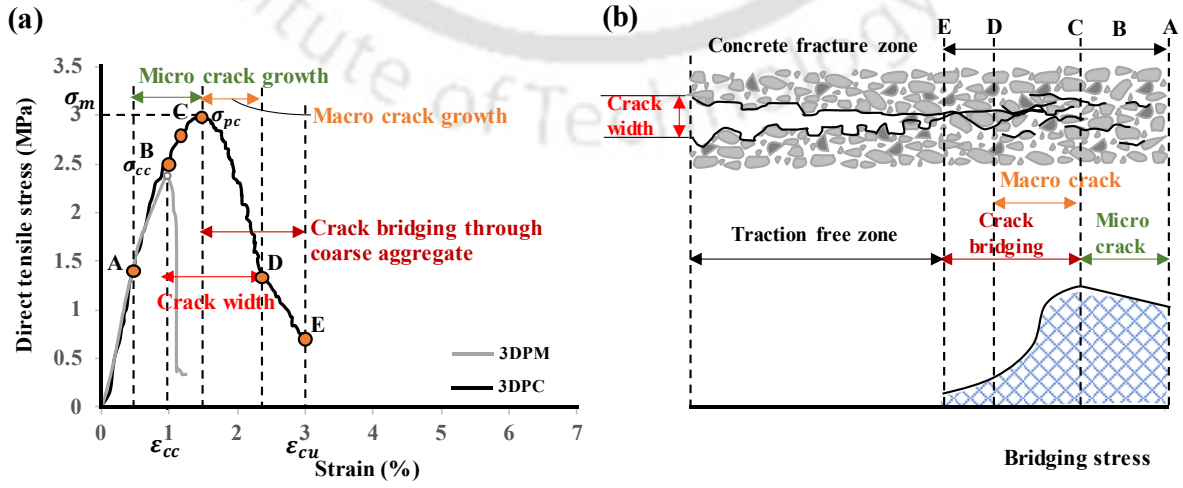

Fig. 3. 14. Direct tensile stress-crack opening relationship (a) direct tension plot of plain concrete (3DPC); (b) schematic description of crack mechanism in under uniaxial tension

The presence of coarse aggregates in 3DPC enhances its tensile properties by preventing the rapid propagation of cracks, thereby increasing its toughness under tensile loading. This comparison highlights the crucial role of coarse aggregates in improving the mechanical performance of 3DPC compared to 3DPM. The detailed comparison of these results is discussed in the below sections.

3.4.3. Effect of critical fiber volume on strain hardening behaviour of 3DPC

In accordance with Naaman and Reinhardt's definition [179], the tensile strength (σ_{pc}) of material exhibiting strain hardening behaviour surpasses its cracking stress (σ_{cc}). This section explores the effect of SF and CF fibers on tensile strain hardening capacity at their critical volume fractions of 1.48% and 1.18% (by the total volume of the mix), respectively. The reinforcement of steel fibers typically relies on geometric and mechanical characteristics, volume of the fiber, and fiber-to-matrix bond strength [178]. To assess the influence of these fibers on the strain hardening capacity of 3DPC, reinforcing factor (η) [178] and strain hardening factor (φ) [180] are introduced as described in Eq. (3.14) and (3.15) (see Fig. 3.15).

$$\eta = \frac{\sigma_{3DCP-SF/CF}}{\sigma_{3DCP}} \tag{3.14}$$

$$\varphi = \frac{\sigma_{pc}}{\sigma_{cc}} \tag{3.15}$$

The strength properties of 3DPC with and without steel fibers are denoted as $\sigma_{3DCP-SF/CF}$ and σ_{3DCP} respectively. Fig. 3.15 presents the reinforcing factors concerning first crack strength (η_{cc}) and peak strength (η_{pc}). The reinforcing factor related to first crack strength (η_{cc}) exhibits minimal variation ranging between 1.31 and 1.37. This suggests that the initial crack stress is not significantly influenced by the type of fiber, instead it is predominantly governed by the 3DPC matrix. Conversely, the reinforcing factor for peak strength (η_{pc}) notably exceeds that of first crack strength (η_{cc}) for identical 3DPC compositions, indicating a more substantial contribution of steel fibers to peak strength rather than initial crack strength. During strain hardening phase, the fiber-to-matrix bonding force reaches to its maximum, thus yielding a larger reinforcing factor (η_{pc}).

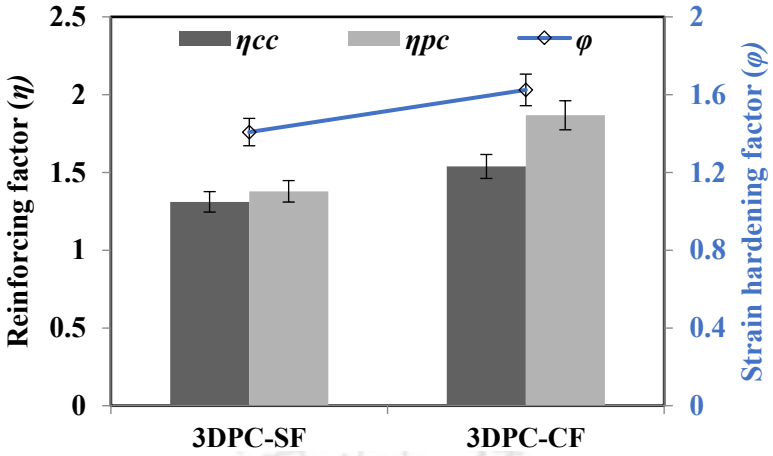

Fig. 3. 15. Reinforcing factor and strain hardening factor of 3DPC-SF and 3DPC-CF compared to 3DPC

When steel fibers induce strain hardening phenomenon (Fig. 3.15), the strain hardening factor exceeds 1.0 which indicates a more robust strain hardening behaviour. In 3DPC-SF, a subtle strain hardening behaviour is observed, characterized by φ factor of approximately 1.4. In contrast, CF with its longer length and unique shape exhibits greater strain hardening capacity (φ = 1.62) by augmenting the peak pull-out load and corresponding slip. This enhancement is attributed to increased effective bonding area of fibers at the crack surfaces (Fig. 3.13, Fig. 3.16 and Fig.17).

3.4.4. Combined effect of coarse aggregate and fiber for simultaneous improvement of strain hardening and ductility

The fiber-reinforced 3DPC benefits from fibers acting as an additional bridging mechanism compared to plain 3DPC, which significantly increases the critical crack opening (the stress-free) by a factor greater than 10, along with corresponding increase in energy absorption capacity. While post-cracking tensile stress (σ_{pc}) is less affected by the fibers, the maximum fiber bridging stress depends on bond strength between the fiber and matrix and effects of unidirectional fiber orientation. Consequently, there is a combined effect of aggregate and fiber bridging, in case of fiber-reinforced concrete, with aggregate bridging having relatively shorter range compared to fiber bridging (see Fig. 3.16 andFig. 3.17).

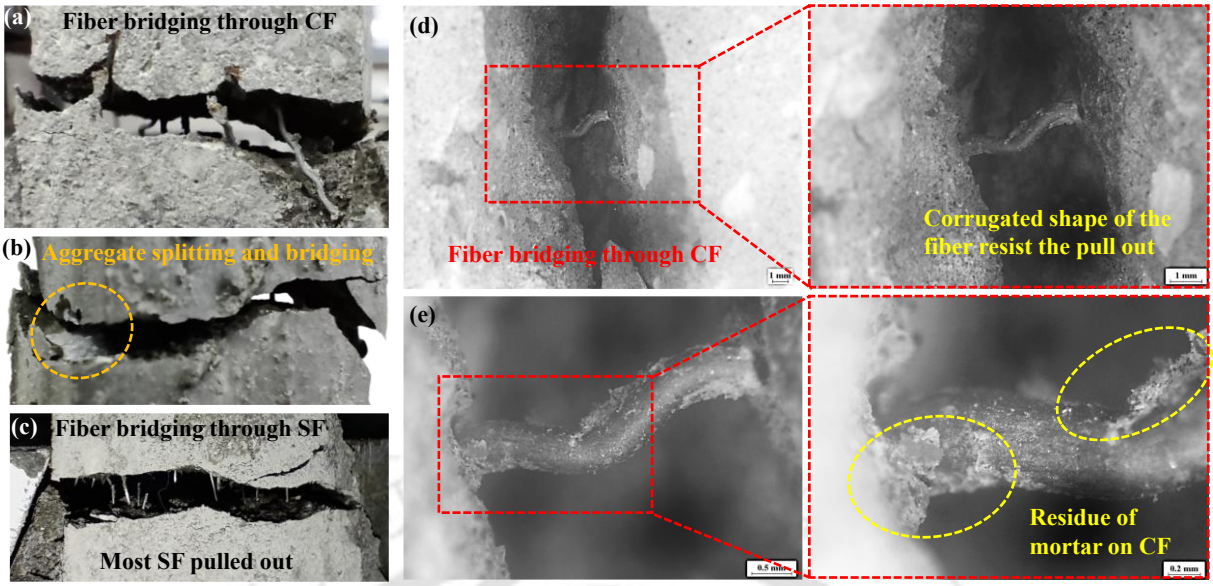

Fig. 3. 16. Fiber bridging under uniaxial tensile loading (a-c) experimental failure; (d,e) optical microscopic images

In Fig. 3.17, three distinct zones are identified: (i) traction-free zone for relatively large crack openings; (ii) bridging zone where stress is transferred by fiber pull-out and aggregate bridging; and (iii) zone of microcracking and microcrack growth. The stress-crack opening relationship in Fig. 3.17 depends on fracture properties of the concrete, typically starting with a steep descending part (C-D) for small crack openings. The contribution from fiber bridging gradually becomes significant. Depending on fiber characteristics, the curve levels out and slowly decrease with increasing fiber slip (or crack opening) until it becomes zero (D-E). For corrugated fibers, the curve enters into an ascending phase where stress increases as the fiber deforms during loading, eventually it decreases to zero.

Fig. 3.17a illustrates that the stress-strain curves of 3DPC-CF show greater strain-hardening behaviour (strain-hardening factor is 1.62) and higher ductility (ductility factor is 10.86) (Table 3.7). These values represent 15.41% and 193.84% increase respectively, compared to 3DPC-SF. Additionally, the strain-hardening factor of 3DPC-CF is 35.44% higher and ductility factor is 260.79% higher compared to 3DPC (Table 3.7). This indicates that smooth straight steel fiber is less effective in improving the tensile behaviour of 3DPC compared to corrugated fibers.

From Fig. 3.17 and Fig. 3.18, it's evident that incorporating CF into 3DPC significantly improves tensile performance as indicated by strain-hardening response with lower critical fiber volume of 1.18% compared to 1.48% for SF. This improvement can be attributed to the superior bond strength of CF compared to SF, as the corrugated surface of CF fibers provides

better mechanical interlocking with the matrix as shown in optical microscopic images (Make: Nikon SMZ25) (Fig. 3.16 and Fig. 3.18a,b). In contrast, SF fibers have an ITZ, often accompanied by voids near the fiber-matrix interface due to their smooth surface, which hinders bonding (Fig. 3.18e,f). These voids reduce the efficiency of load transfer and compromise tensile strength. On the other hand, the stronger bond strength of CF, combined with its ability to avoid these void formations, results in more effective load transfer, better crack bridging, and enhanced tensile properties (Fig. 3.16 and Fig. 3.18b,c). Both the peak tensile strength and tensile strain of 3DPC-CF are higher than those of 3DPC-SF (Fig. 3.17). Initially, both SF and CF engage to provide bridging action and crack deflection. As the crack expands and crack width increases, short steel fibers are pulled out of the matrix and cease to contribute, while long steel fibers (CF) continue to slow down crack expansion, thereby increasing tensile strength of the specimen (Fig. 3.17b).

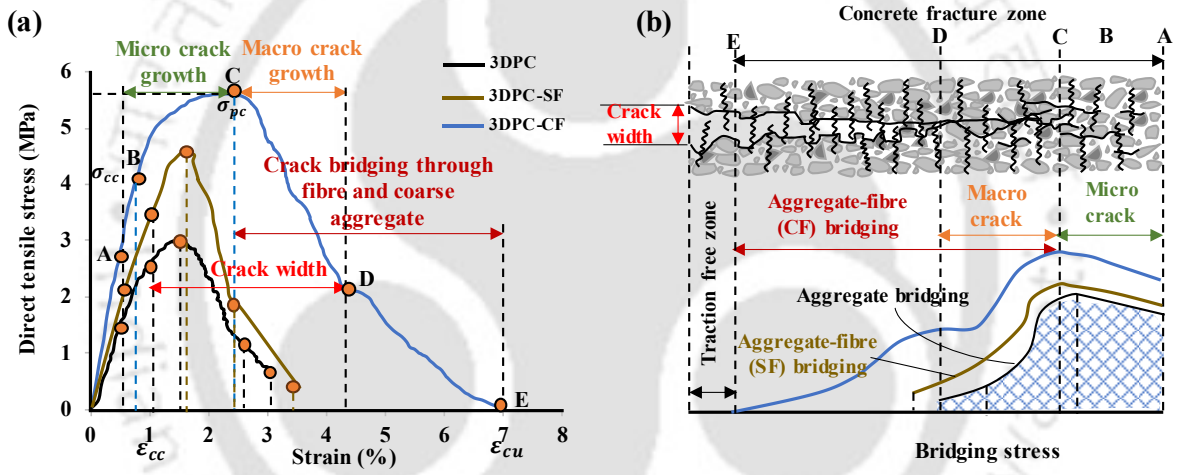

Fig. 3. 17. Direct tensile stress-crack opening relationship (a) direct tension plot of fiber reinforced 3DPC; (b) schematic description of crack mechanism in under uniaxial tension

It is clear from the experiments that the size of fibers relative to aggregates and microcracks (both load-induced and pre-existing) significantly influences the fracture process. For instance, straight fibers have weaker bond compared to corrugated fibers, which led to gripping effect on the surface (Fig. 3.16c). Additionally, short fibers cannot fully cover large aggregates, resulting in limited fiber-bridging interlock stress.

Apart from fibers, aggregates also play a crucial role in improving performance. They positively affect fiber distribution by adjusting between CF fibers (Fig. 3.18g), enhancing dispersion, and strengthening interfacial bonding, which reinforces the ITZ (Fig. 3.18c). This improved bonding boosts fiber utilization efficiency (Fig. 3.15) and enhances the bridging effect between the matrix and fibers (Fig. 3.16d,e), contributing to superior tensile properties

(Fig. 3.17). However, if coarse aggregates are too large relative to fiber length, the distribution of fibers in the matrix can be significantly disrupted [178]. Moreover, CF better cover the coarse aggregates, as shown in X-ray micro-computed tomography (X-CT) images (Fig. 3.18g), improving interlock and further enhancing tensile performance (Fig. 3.17). The X-CT device used for measurement is the Xradia 520 Versa from ZEISS, Germany. By scanning a target specimen (of 20 mm^3, with a voxel size of 32 µm [181]) with X-rays, a series of reconstructed images were obtained, allowing for microstructural investigation.

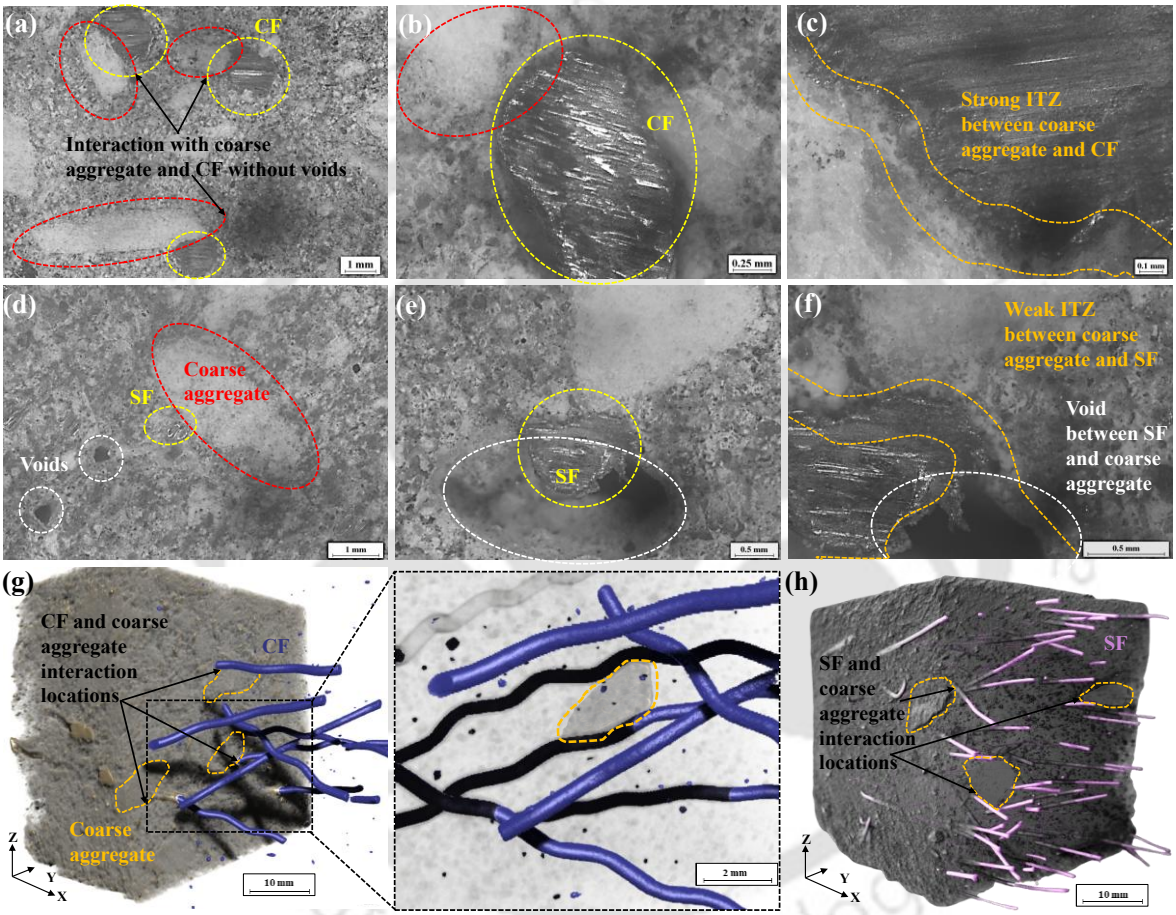

Fig. 3. 18. Interaction between coarse aggregates and fibers in 3DPC (a-f) optical microscopic images; (g,h) X-CT images of the fiber distribution

However, limiting the corrugated size to half the fiber length is recommended for better workability [182], which also reduces the likelihood of the "fiber balling" phenomenon. Based on current results and past studies [178,183], the length of steel fibers should be in between 2 to 5 times the maximum aggregate size for ultra-high performance 3DPC systems. Optimal synergistic effects are observed between aggregates with maximum size of 10 mm and 30 mm corrugated steel fibers.

Table 3. 7. Strain hardening factor (φ) and ductility factor (μ) of the printable mixes

Mix	σ_{pc} (MPa)	σ_{cc} (MPa)	ε_{cu} (%)	ε_{cc} (%)	$\varphi = \sigma_{pc}/\sigma_{cc}$	$\mu = \varepsilon_{cu}/\varepsilon_{cc}$
3DPM	2.48	…	1.15	0.99	…	1.16
3DPC	3.01	2.51	3.04	1.01	1.19	3.01
3DPC-SF	4.63	3.29	3.4	0.92	1.41	3.69
3DP-CF	5.62	3.46	6.95	0.64	1.62	10.86

3.4.5. Effect of ultra-ductile strain hardening on mechanical properties of 3DPC

3.4.5.1. Compressive strength

Fig. 3.19 shows the compressive strength of ultra-ductile strain-hardening 3DPC after 28 days. The compressive strength increases significantly from 22.11 MPa (3DPM) to 31.72 MPa (3DPC) due to the inclusion of coarse aggregates. Also, the use of coarser basalt aggregates reduces the binder demand i.e., the 3DPC mix with coarse basalt aggregates requires less binder (541.2 kg/m^3) compared to the 3DPM mix (739.47 kg/m^3) (see Table 3.1), which helps in improving the compressive strength due to more efficient particle packing [178]. However, this strength is lower than the characteristic strength expected for M30 grade concrete (38 MPa). This reduction can be partly attributed to adjustments made to maintain the required workability for 3D printing, where changes in water content or admixture dosage may have had a modest impact on the mix's overall compressive strength. Adding steel fibers in the conventionally designed concrete mix (3DPC) at their critical volume fraction ($V_{f,cr}$) enhances compressive strength, ranging from 70.28% (3DPC-SF) to 94.3% (3DPC-CF) (Fig. 3.19). The 30 mm corrugated steel fibers provide the best reinforcement, resulting in slightly higher compressive strength than the 15 mm smooth straight fibers. The increased strength from the longer fibers is likely due to their better crack bridging and load transfer (Fig. 3.19), which enhances the overall toughness and load-bearing capacity of the concrete. Their greater anchorage within the matrix also contributes to higher strength improvement.

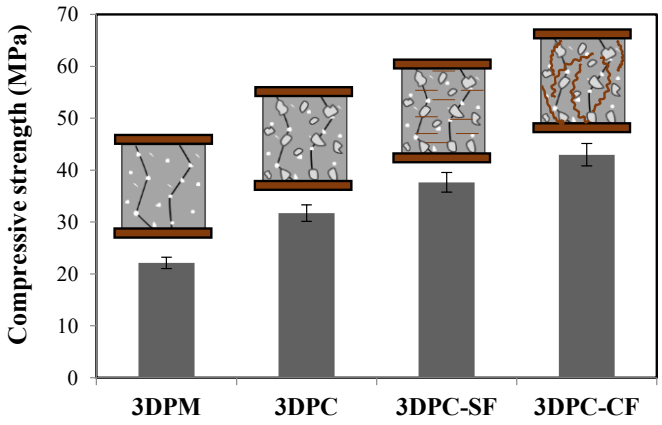

Fig. 3. 19. Compressive strength of 3D printed specimens

To quantify the relationship between the compressive strength of the various material types (3DPM, 3DPC, 3DPC-SF, and 3DPC-CF), a simple linear model (given by Eq. (3.16)) is also developed based on the results:

$$Compressive\ strength\ (MPa) = 22.11 + 9.61 * X_{3DPC} + 15.54 * X_{3DPC-SF} + 20.85 * X_{3DPC-CF} \quad (3.16)$$

where $X_{3DPC}, X_{3DPC-SF}, X_{3DPC-CF}$ are variables representing the different material types:

- For 3DPM (baseline): $X_{3DPC} = 0, X_{3DPC-SF} = 0, X_{3DPC-CF} = 0$
- For 3DPC: $X_{3DPC} = 1,\ X_{3DPC-SF} = 0,\ X_{3DPC-CF} = 0$
- For 3DPC-SF: $X_{3DPC} = 0,\ X_{3DPC-SF} = 1,\ X_{3DPC-CF} = 0$
- For 3DPC-CF: $X_{3DPC} = 0,\ X_{3DPC-SF} = 0,\ X_{3DPC-CF} = 1$

This model quantitatively represents the increase in compressive strength due to the introduction of coarse aggregates, steel fibers, and corrugated fibers in 3DPM. It provides a clear relationship between material composition and compressive strength gains, confirming that the inclusion of corrugated fibers results in the highest strength improvement due to their anchorage within the matrix.

3.4.5.2. Flexural and split tensile strength

Flexural and splitting tests are commonly used to indirectly measure the tensile strength of specimens. The flexural and splitting strengths of various mixes are shown in Fig. 3.20a,b. Both strength value increases when transitioning from 3DPM to 3DPC by 11.16% and 44.08%, respectively. The use of concrete instead of mortar enhances both flexural and tensile strengths due to the inclusion of aggregates and further addition of steel fibers at their critical volume fraction ($V_{f,cr}$) enhances the flexural strength by 69.37% (3DPC-SF) to 128.19% (3DPC-CF) (Fig. 3.20a) and split tensile strength by 110.43% (3DPC-SF) to 178.67% (3DPC-CF) (Fig.

3.20b). The corrugated fibers provide a positive anchoring effect compared to straight smooth fibers, while longer fibers improve flexural, split tensile strength and energy absorption capacity by increasing the peak pull-out load and corresponding slip. This enhancement is due to increased effective bonding area of fibers at the crack surfaces [184].

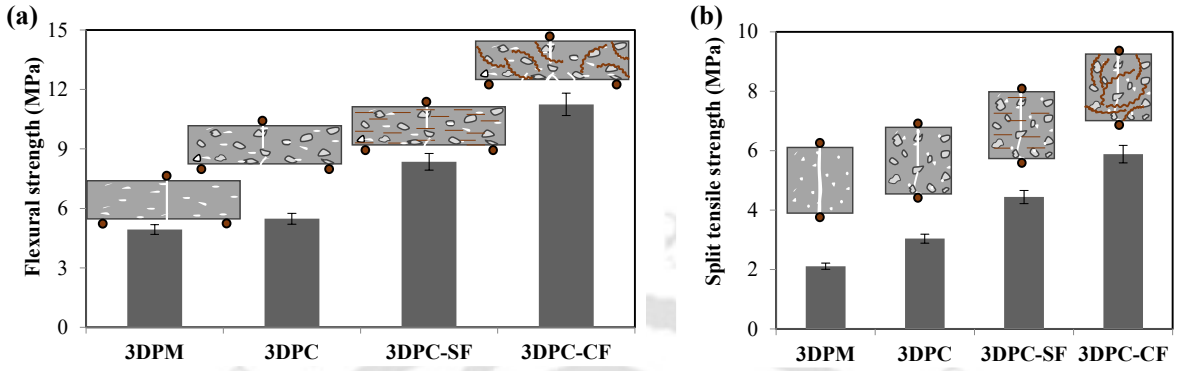

Fig. 3. 20. (a) Flexural strength; (b) split tensile strength of 3D printed specimens

To quantify the relationship between the flexural strength and split tensile strength of the various material types (3DPM, 3DPC, 3DPC-SF, and 3DPC-CF), a simple linear model is also developed (given by Eq. (3.17 & 3.18)) based on the results:

$$Flexural\ strength\ (MPa) = 4.93 + 0.55 * X_{3DPC} + 3.42 * X_{3DPC-SF} + 6.32 * X_{3DPC-CF} \quad (3.17)$$

$$Split\ tensile\ strength\ (MPa) = 2.11 + 0.93 * X_{3DPC} + 1.77 * X_{3DPC-SF} + 3.77 * X_{3DPC-CF} \quad (3.18)$$

where $X_{3DPC}, X_{3DPC-SF}, X_{3DPC-CF}$ are variables representing the different material types as discussed above. This model effectively demonstrates how different material types influence flexural strength. It provides a quantitative approach to highlight the effect of fiber content and material composition on the flexural properties of the 3DPC. While the optimal fiber content was pre-analysed in this research work, the established mathematical model may serve as a foundation for future studies investigating the effects of varying fiber dosages and coarse aggregate content in more detail.

Overall, the mechanical properties of 3DPC demonstrate significant enhancements through strategic modifications in the mix and inclusion of critical fiber volume. The transition from mortar to concrete improves overall strengths, while the addition of steel fibers, particularly those with corrugated shapes and longer lengths, further amplifies the strength. These findings highlight the potential of concrete mix optimization with fiber reinforcement to achieve superior mechanical performance in the domain of 3D concrete printing.

3.4.5.3. Ductility and energy absorption capability

The experimental results provide critical insights into the correlation between energy absorption capacity and ductility factor in strain-hardening 3DPC (Fig. 3.21). The effects of different fiber types and their integration with coarse aggregates on these properties are thoroughly evaluated. The 3DPC-CF demonstrated energy absorption capacity of 105 kJ/m³, which is a stark contrast to the 49 kJ/m³ observed in case of 3DPC-SF (Fig. 3.21). This represents 114% increase in energy absorption capacity with the use of CF compared to SF. In comparison, 3DPM and 3DPC exhibited energy absorption capacities of 12 kJ/m³ and 28 kJ/m³, respectively. The addition of coarse aggregates and fibers, especially CF, significantly improved energy absorption. The superior energy absorption capacity of CF can be attributed to its enhanced mechanical interlock and better stress distribution within the concrete matrix (Fig. 3.13c), which effectively dissipates energy under load.

On the other hand, 3DPM exhibited the lowest performance with an energy absorption capacity (G_{pc}) of 12 kJ/m³ and ductility factor (μ) of 1.19 (Fig. 3.21). This limited performance is expected, given the absence of coarse aggregates and fibers, which play a critical role in enhancing these properties. When coarse aggregates are added to develop 3DPC, there is a notable improvement in both energy absorption capacity and ductility. The addition of coarse aggregates contributes to a better stress distribution and improved load-bearing capacity, resulting in enhanced performance under diverse loading conditions. Additionally, a correlation equation has alo been presented in the Fig. 3.21 to quantify the relationship between energy absorption and ductility across different mixes.

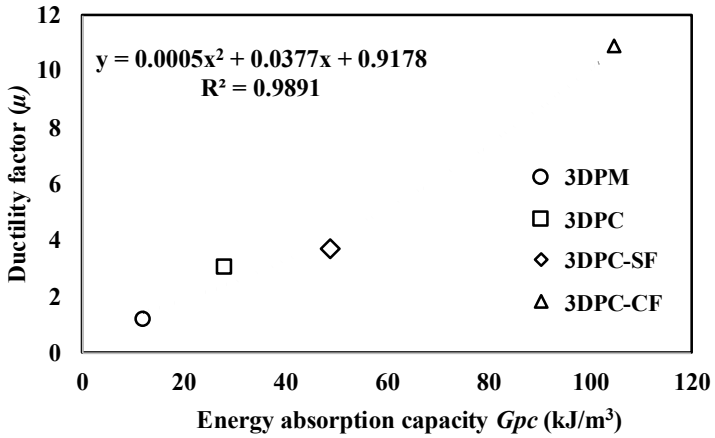

Fig. 3. 21. Correlation between energy absorption capacity and ductility factor of 3D printed specimens

It is shown in Fig. 3.21 that 3DPC-CF has a ductility factor (μ) of 10.86, compared to 3.7 for 3DPC-SF. This indicates 194% increase in ductility factor when using CF over SF (Fig. 3.21).

The enhanced ductility in 3DPC-CF is due to the longer length and special shape of the fibers, which provide better mechanical interlock and more effective stress transfer across cracks. This leads to more pronounced energy absorption capacity and higher ductility. In contrast, 3DPC-SF, while providing some improvement, do not achieve the same level of performance due to their smoother surface and shorter length, which results in less effective bonding and lower friction (Fig. 3.13c).

In summary, the transition from 3DPM to concrete 3DPC with coarse aggregates significantly enhances the material's energy absorption capacity and ductility. The subsequent addition of fibers, especially CF, further amplifies these benefits, demonstrating the importance of a well-designed mix that incorporates both coarse aggregates and optimized fiber to achieve superior mechanical properties in strain-hardening 3DPC.

3.5. Comparison of the developed 3DPC material with existing cast and 3D-printed UHPC

Building on this enhanced performance, it is also crucial to compare the developed 3DPC material with existing cast and 3D-printed ultra-high-performance concrete (UHPC) to evaluate its overall value. While UHPC is recognized for its high compressive strength and durability, it often comes with significant costs due to dense binder use and fine particle gradations [85,87,160,185–190]. In contrast, the 3DPC mix presented here employs a more conventional mix design with coarse aggregates, reducing binder demand and offering a more cost-effective solution. While there is a substantial body of literature on UHPFRC (Table 3.8), some studies could not be included due to the unavailability of binder content values [159,173,188,191–193]. Furthermore, other research employed different types of fibers in the formulation of strain-hardening 3DPC [89,194–196], which limits the potential for direct performance comparisons.

Table 3. 8. Performance level of different cast and printed ultra high-performance concrete

	Material	Fiber volume (%)	Binder (kg/m^3)	Performance indicator	Performance level
Cast	**UHP-FRC** [190]	2.5	Premix (2355)	G_{pc} (25-54 kJ/m^3)	**IV**
	UHP-SHCC [189]	1.5	1338.6	Strain capacity (2.8%)	**IV**
	UHP-FRC [187]	2	Premix (2195)	Strain capacity (0.58%)	**III**
	UHP-FRC [186]	2	1200	Tensile strength (6 MPa)	**IV**
	UHPFRC [185]	6	1051	Tensile strength (10.8 MPa) with strain capacity (0.25%)	**IV**
Printed	**SFR-3DPC** [87]	1	1073	Flexural strength (13 MPa) with strain capacity (1.67%)	**IV**
	3DP-UHPFRC [160]	2	~1145	Strain capacity (2.9%)	**III**

	3DP-SFRC [85]	2	~850	Flexural strength (8.71MPa) with strain capacity (5%)	**IV**
(Current work)	**3DPC-SF**	1.48	541.2	Tensile strength (4.63 MPa) with strain capacity (3.4%) G_{pc} (49 kJ/m^3)	**V**
	3DPC-CF	1.18	541.2	Tensile strength (5.61 MPa) with strain capacity (6.95%) G_{pc} (105 kJ/m^3)	**VI**

Abbreviation: UHP-FRC:- Ultra high-performance fiber reinforced concrete; UHP-SHCC:- Ultra high-performance strain hardening cementitious composite; SFR-3DPC:- Steel fiber reinforced 3DPC.

In terms of mechanical behavior, while UHPC typically exhibits exceptional compressive and flexural strength, the 3DPC developed here offers competitive strength with the added benefits of improved ductility and energy absorption, particularly with corrugated fibers. The stress-strain behavior of the 3DPC-CF mix aligns with sixth-level performance benchmarks and the performance levels of the compared literatures (shown in Table 3.8) is based on earlier studies and design codes for HPFRC [173,197,198]. This balance between strength and ductility renders the 3DPC-CF mix particularly suitable for seismic and dynamic load applications, thus expanding its potential from indoor architectural use to large-scale applications [199].

This blend of economic efficiency and robust mechanical performance makes the 3DPC a compelling alternative to traditional UHPC materials, especially for applications where both cost constraints and material resilience are critical considerations.

3.6. Summary

This chapter develops an ultra-ductile strain-hardening 3D printed concrete composite by systematically integrating coarse aggregates and steel fibers at critical volumes. The resulting Level VI type 3DPC exhibits significantly enhanced ductility and energy absorption (G_{pc} up to 105 kJ/m³). Key findings include:

i. **Fiber type dominance:** Strain-hardening behavior, ductility, and energy absorption are highly sensitive to steel fiber type, while first-crack strength is primarily influenced by coarse aggregates.

ii. **Critical fiber volume effect:** Incorporating steel fibers at critical volumes substantially improves tensile performance, achieving a ductility factor (μ) of 10.86, strain-hardening factor (φ) of 1.62, and energy absorption (G_{pc}) of 105 kJ/m³.

iii. **Performance comparison:** Compared to mixes with standard steel fibers (3DPC-SF) or no fibers (3DPC/3DPM), the 3DPC-CF mix demonstrates superior performance, with ductility, strain-hardening, and energy absorption increased by 193%, 15%, and 114%, respectively.

iv. **Synergistic role of aggregates and fibers:** The combination of coarse aggregates and steel fibers enhances interfacial bonding, crack control, and mechanical performance, enabling the achievement of ultra-ductile behavior suitable for reinforced 3DPC applications.

These findings provide a systematic framework for designing high-performance 3DPC composites, offering guidance for engineers to optimize structural performance and material efficiency. Also lay the groundwork for future investigations into tensile behavior and scalability for practical applications.

Chapter 4

Composite micro-modeling and seismic performance evaluation of 3D printed concrete walls

*This chapter develops a numerical modeling framework to simulate the in-plane cyclic behavior of 3DPC walls using a composite interface micro-model that integrates concrete damage plasticity (CDP) and cohesive zone modeling (CZM). The model accurately predicts hysteresis response, stiffness degradation, and energy dissipation under cyclic loading. Parametric studies indicate that reducing the height–width ratio, adding solid edge columns, and ensuring continuous reinforcement significantly enhance seismic performance. Incorporation of strain-hardening 3DPC further improves deformability and strength compared to conventional walls. This numerical approach allows systematic exploration of multiple influencing parameters, reducing the need for extensive costly experiments and guiding targeted large-scale testing for optimized seismic performance.

*A portion of this chapter has been published in:

1. **Warsi SBF**, Panda B, Biswas P. Structural analysis of 3D printed concrete wall under quasi-static cyclic loading using composite micro model. Progress in Additive Manufacturing **2024,** p. 1-21. https://doi.org/10.1007/s40964-024-00874-9.
2. **Warsi SBF**, Srinivas D, Panda B, Biswas P. Investigating the impact of coarse aggregate dosage on the mechanical performance of 3D printable concrete. Innovative Infrastructure Solutions **2023**;9:5. https://doi.org/10.1007/s41062-023-01317-0.
3. **Warsi SBF**, Panda B, Biswas P. Effect of strain hardening material on seismic performance of 3D printed concrete wall: a numerical study. **4th RILEM International Conference on Concrete and Digital Fabrication**, 2024, p. 1–8. https://doi.org/10.24355/dbbs.084-202408191226-0.

4.1. Introduction

The growing emphasis on performance-based seismic design has underscored the importance of evaluating the cyclic and failure behavior of emerging construction systems like 3D printed concrete walls. 3DPC walls, though promising for rapid and automated construction, still lack comprehensive understanding of their structural performance under lateral cyclic loading. Experimental studies on 3DPC walls remain limited, with only a few investigations addressing quasi-static cyclic behavior [6–9]. Consequently, numerical analysis serves as a crucial tool to evaluate and predict their performance prior to large-scale experimental validation.

In this chapter, a robust finite element-based composite interface micro-model is developed to simulate the in-plane cyclic behavior of 3DPC walls. The model integrates CDP to represent cracking and crushing mechanisms, and a cohesive zone formulation to capture the interlayer debonding and localized failure typical of printed structures. Unlike conventional macro-models (Fig. 4.1a), which treat 3DPC as a homogeneous material, the proposed micro-model explicitly incorporates layer interfaces using zero-thickness cohesive elements (Fig. 4.1b), enabling realistic representation of nonlinear damage and energy dissipation under cyclic loads.

Model validation against benchmark experimental data [6] demonstrates the accuracy of the proposed framework in predicting hysteresis response, stiffness degradation, and energy dissipation of printed walls. Parametric studies are subsequently conducted to assess the influence of design and material parameters—including wall aspect ratio, edge column configuration, reinforcement continuity, and material type—on seismic performance. Results indicate that reducing the height-to-width ratio, incorporating continuous reinforcement, and using strain-hardening 3DPC material substantially improve strength, deformability, and energy absorption. Specifically, lattice shear walls exhibit up to 108% enhancement in deformability, while flexural walls demonstrate a 59% gain in peak strength compared to control specimens (3DPM).

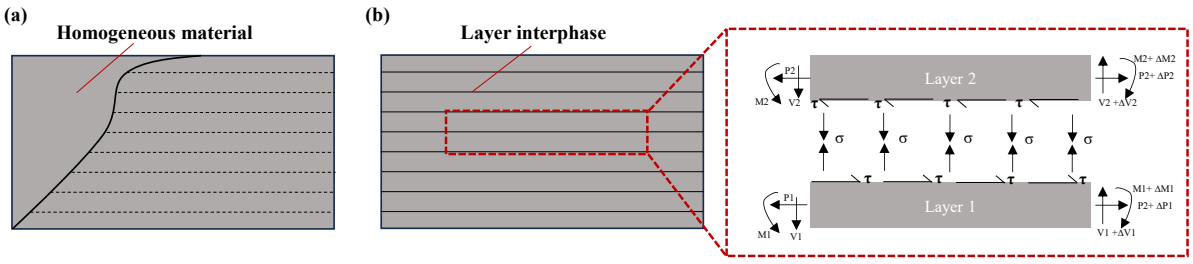

Fig. 4. 1. Finite element modelling approaches: (a) Macro-model; (b) Micro-model (based on [106])

Overall, this chapter establishes a validated numerical modeling framework that provides a fundamental basis for performance-based seismic evaluation and design optimization of 3D printed concrete systems, bridging the current gap between material-level advancements and full-scale structural applications. Given that the cyclic response of 3D printed concrete walls is influenced by numerous interdependent parameters—such as geometry, reinforcement continuity, interlayer bonding, and material heterogeneity—experimental investigation of each influencing factor becomes highly time-consuming and economically impractical. Therefore, a robust numerical simulation approach is adopted to systematically analyze the impact of these parameters, enabling efficient exploration of the seismic performance and failure mechanisms prior to large-scale experimental validation. This is made possible through the development of a composite micro-model that realistically captures the in-plane cyclic response and localized failure mechanisms of 3D printed concrete walls.

4.2. Numerical modelling approach

This section outlines the proposed numerical modelling framework and pertinent theoretical considerations. Given the anisotropic mechanical properties of 3D printable material [124], it becomes evident to consider the orthotropic constitutive relationship, orthotropic damage and plasticity to comprehensively characterize the intricate nonlinear behaviour of 3DPC elements. A composite interface micro-modelling strategy is proposed here for performance evaluation of 3DPC walls under quasi-static cyclic loading.

4.2.1. Micro-modelling: A composite interface model for 3DPC to define layer interface

A comprehensive micro-model should encompass all fundamental failure mechanisms that define the holistic structural behaviour of 3DPC, including it's layer interfaces. These mechanisms are cracking at the interface (depicted in Fig. 4.2a) [200] sliding along the layer interface at low levels of normal stress—known as shear slip (depicted in Fig. 4.2b, c), cracking due to direct tension within layers (intralayer cracking, Fig. 4.2d), diagonal tensile cracking resulting from combined compression and shear at normal stress levels sufficient to generate friction in the layer interface (Fig. 4.2e), and concrete crushing (Fig. 4.2f), commonly recognized as splitting of 3DPC under tension owing to mortar dilatancy at elevated normal stress levels, as illustrated in Fig. 4.2d. The described phenomena (in Fig. 4.2a-c) represent interlayer mechanisms, while Fig. 4.2d portrays an intra-layer mechanism. The Fig. 4.2d,e showcases combined mechanisms entailing both interlayer and intra-layer interactions. Furthermore, the micro-model should capture the linear and fracture behaviour of the

interface, which is based on traction separation behaviour between the printed layers (as depicted in Fig. 4.3).

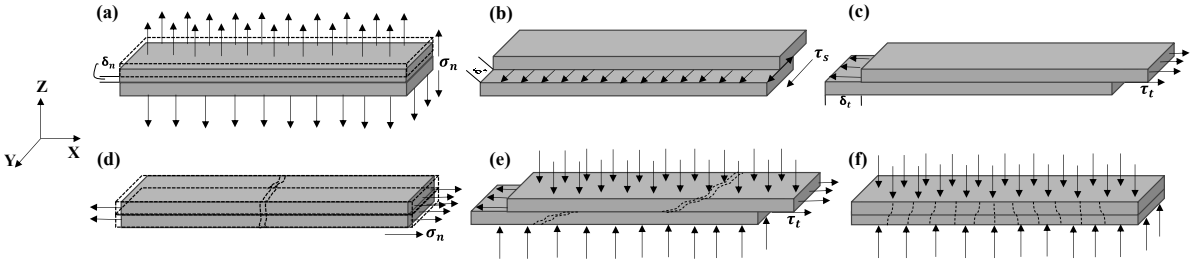

Fig. 4. 2. Probable failure modes in 3DPC: (a) layer interface tensile cracking (Mode I); (b) shear sliding (layer slipping along lateral direction) (Mode II); (c) shear sliding (layer slipping along longitudinal direction) (Mode III); (d) direct tensile cracking; (e) diagonal crushing; (f) crushing (reproduced from [201])

4.2.1.1. Elastic behaviour of the layer interfaces

The suggested cohesive model relies on eight essential parameters and this section delves into the discussion of effective methods for precise determination of the parameters. These interface elements allow for disruptions in the displacement field and articulate their response through the correlation between tractions (σ) and relative displacements (δ) across the interface. Typically, the linear elastic relationship between these generalized stresses and strains is represented by a standard form, expressed in Eq. (4.1):

$$\sigma = D.\varepsilon \tag{4.1}$$

where for a 3D configuration, $\sigma = \{\sigma_n, \tau_s, \tau_t\}^T, D = diag\{K_n, K_s, K_t\}^T$, and $\varepsilon = \{\delta_n, \delta_s, \delta_t\}^T$, with n, s and t denoting the normal and two tangential directions of the interface, respectively.

The elastic stiffness matrix D can be derived based on the characteristics of 3D printed mortar and interphase thickness (considered zero in thickness). The elastic behaviour described in Eq. (4.1) can manifest in a manner represented by Eq. (4.2).

$$\sigma = \begin{bmatrix} \sigma_n \\ \tau_s \\ \tau_t \end{bmatrix} = \begin{bmatrix} K_n & 0 & 0 \\ 0 & K_s & 0 \\ 0 & 0 & K_t \end{bmatrix} . \begin{bmatrix} \delta_n \\ \delta_s \\ \delta_t \end{bmatrix} = K\,\delta \tag{4.2}$$

where K and δ represent the initial stiffness matrix and the relative displacement vector, respectively.

The interface elastic stiffness of bonding [202] is expressed in Eq. (4.3):

$$K_n = \frac{E_{in}}{t_{in}};\ K_s = \ K_t = \frac{G_{in}}{t_{in}} \tag{4.3}$$

where E_{in} and G_{in} are the elastic and shear modulus of the layer interface, respectively; and t_{in} is the thickness of the interface region.

The given formulas provide a direct way to determine interface stiffness based on the interlayer bonding characteristics. Nevertheless, this strategy is not feasible since the stiffness value tends towards infinity as the contact thickness approaches to zero. Based on theories of contact or damage cracking mechanism [203], the initial tensile stiffness is assumed to be infinite and because of the high elastic stiffness, applying such trial (high) stress may cause possible convergence issues [204]. As a result, here we offer a modified version of the homogenised notion Eq. (4.4), which is frequently used in masonry modelling [201,205]

$$K_n = \frac{E_{in}E_c}{E_{in}t_c - E_c t_{in}};\ K_s = \ K_t = \frac{G_{in}G_c}{G_{in}t_c - G_c t_{in}} \tag{4.4}$$

Since we have considered zero-interface thickness concept, Eq. (4.4) can be directly written as Eq. (4.5):

$$K_n = \frac{E_c}{t_c};\ K_s = \ K_t = \frac{G_c}{t_c} \tag{4.5}$$

where E_c and G_c are the elastic and shear modulus of the concrete filament, respectively; and t_c is the filament layer thickness i.e. t_c=15 mm.

4.2.1.2. Plastic behaviour of the layer interfaces

The initiation of damage occurs upon reaching a predefined criterion based on user-defined tractions encompassing both shear and tensile strength of the interface. The quadratic stress criterion is employed to identify damage initiation, whereby the criterion is satisfied for quadratic stress ratio (of layer interfaces) is equal to one. This criterion is chosen for its effectiveness in predicting damage initiation under mixed-mode loadings [205,206]. The expression for this criterion is presented in Eq. (4.6) as follows:

$$\textit{Damage initiation:}\ \left[\frac{\langle\sigma_n\rangle}{\sigma_n^0}\right]^2 + \left[\frac{\langle\tau_s\rangle}{\tau_s^0}\right]^2 + \left[\frac{\langle\tau_t\rangle}{\tau_t^0}\right]^2 = 1 \tag{4.6}$$

Once the damage initiation criterion is reached, the propagation of cracks in the layer interphase causes stiffness degradation and failure of interphase (see Fig. 4.3). Thus, Eq. (4.2) can be rewritten as Eq. (4.7):

$$\sigma = (1 - d)K\delta \tag{4.7}$$

where *d* is the damage evolution variable, the value increases from 0 to 1 as per continuity of traction stresses after the damage initiation criterion met [205].

The region beneath the traction-separation curve (refer to Fig. 3) represents the specific fracture toughness for Mode I, II, or III (denoted as G_{IC}, G_{IIC} and G_{IIIC}, respectively). It determines the ultimate relative displacements $(\delta_n^f, \delta_s^f, \delta_t^f)$ that correspond to complete decohesion, as outlined in Eq. (4.8). Subsequently, the final displacements can be derived using the following expression [207]:

$$\delta_n^f = \frac{2G_{IC}}{\sigma_n};\ \delta_s^f = \frac{2G_{IIC}}{\sigma_s};\ \delta_t^f = \frac{2G_{IIIC}}{\sigma_t} \tag{4.8}$$

The effective separation d_{eff} and effective separation at complete failure d_{eff}^f, is also expressed as (Eq. (4.9)) [205]:

$$\delta_{eff} = \sqrt{\langle\delta_n\rangle^2 + \langle\delta_s\rangle^2 + \langle\delta_t\rangle^2};\ d_{eff}^f = \frac{2G_{TC}}{\sigma_{eff}^0} \tag{4.9}$$

where σ_{eff}^0 is effective traction stress at damage initiation under combinations of normal and shear tractions in the interface and the critical fracture energy in mixed-mode, denoted as G_{TC}, can be determined using the Benzeggagh-Kenane (BK) law [208], especially suitable when the critical fracture energies for both shear directions (mode II and mode III) are identical, as often observed in masonry joints. The exponent η in the BK law is set at *2*, assuming the brittle behaviour of the mortar [208]. The critical fracture energy G_{TC} under mixed-mode (G_{II}/G_T) conditions in the BK law is expressed as shown in Eq. (4.10):

$$G_{TC} = G_{TC} + (G_{IIC} - G_{IC})\left\{\frac{G_{II}}{G_T}\right\}^{\eta} \tag{4.10}$$

An accurate constitutive equation for formulating the de-cohesion surface is crucial for precisely simulating the interface cracking process. It is assumed that there exist a process zone or cohesive zone preceding the delamination tip. In Fig. 4.3, the cohesive zone is depicted in specimens subjected to Mode II or Mode III loading.

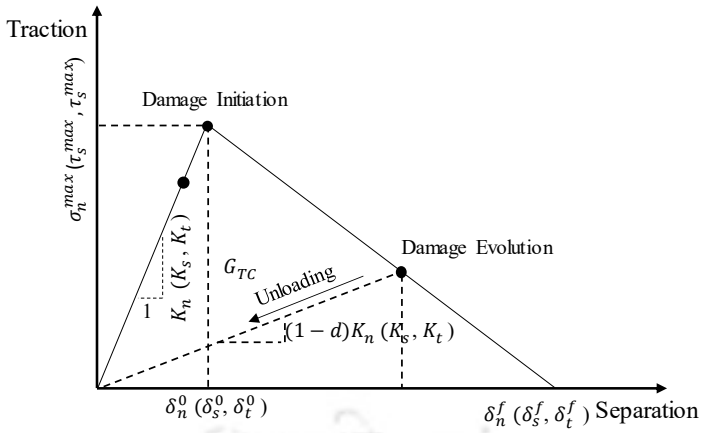

Fig. 4. 3. Traction separation response of 3DPC layer interfaces in tension and shear

4.2.2. Concrete Damage Plasticity model

The Concrete Damage Plasticity concept is a widely employed method for modelling brittle materials [209–211] and it relies on two primary damage criteria—tensile cracking and compressive crushing [212]. The stress–strain response of the material under uniaxial compression is regulated by a damage parameter, denoted as "d " constrained within $0 < d < 1$ limit.

4.2.2.1. Modelling of concrete under compression

Herein, three parameters such as compressive stresses (σ_c), inelastic strains (ε_c^{in}), compressive damage parameter (d_c) are obtained to model the concrete behaviour. Eq. (4.11) is utilized to derive the inelastic strain ε_c^{in} which is related to total compressive strain ε_c and the elastic strain ε_{oc}^{el} corresponding to the undamaged material.

$$\varepsilon_c^{in} = \varepsilon_c - \varepsilon_{oc}^{el} = \varepsilon_c - \frac{\sigma_c}{E_0} \tag{4.11}$$

While performing the numerical modelling using Abaqus finite element package, the post peak strength related to material degradation can be considered via a damage parameter (d_c) as shown in Fig. 4.4a, b.

It is important to note that necessary corrective measure is taken to ensure the plastic strain values ε_c^{pl} (see Eq. (4.12)) are neither negative nor decreasing with increasing stresses.

$$\varepsilon_c^{pl} = \varepsilon_c^{in} - \frac{d_c}{1-d_c}\frac{\sigma_c}{E_0} \tag{4.12}$$

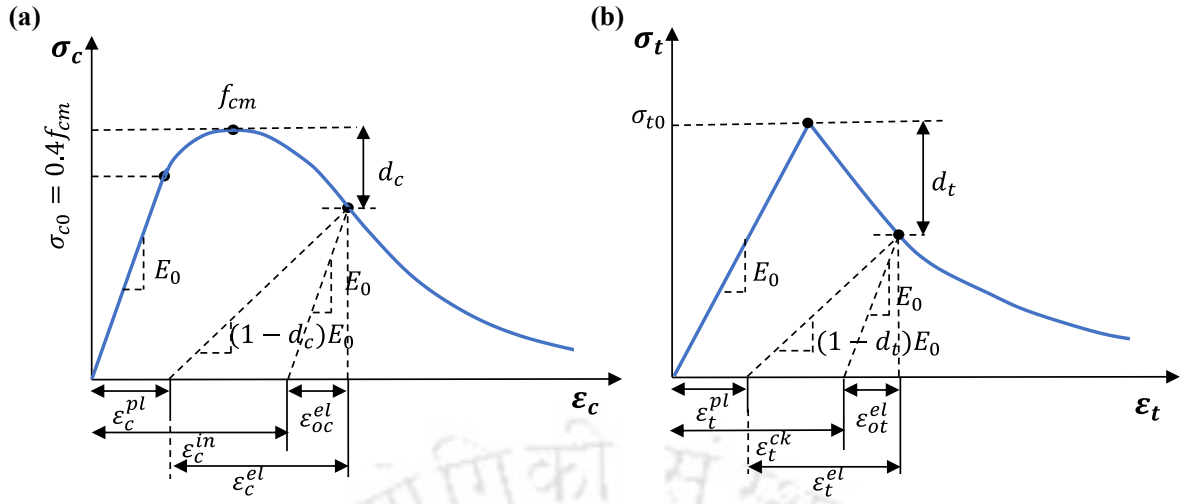

Fig. 4. 4. Concrete Damage Plasticity model to define simplified analytical stress–strain curve for concrete under (a) compression; (b) tension

Stress-strain relationships for concrete in compression and post-failure relationship in tension are used to model the concrete behaviour in compression. To model the complete σ-ε_c response, Eurocode 2 [213] is utilized, which suggests the following expression (Eq. (4.13), (4.14)):

$$\sigma_c = \frac{k\eta - \eta^2}{1+(k-2)\eta} f_{cm}; \quad \eta = \frac{\varepsilon_c}{\varepsilon_{c1}}; \quad k = 1.05E_0 \frac{\varepsilon_{c1}}{f_{cm}} \tag{4.13}$$

$$\varepsilon_{c1}(\%_0) = 0.7(f_{cm})^{0.31} \leq 2.8; \quad E_0 = 22(0.1f_{cm})^{0.3} \tag{4.14}$$

where E_0 is elastic modulus of concrete; and f_{cm} is the ultimate compressive strength of concrete.

As per Eurocode 2, the response of concrete under uniaxial compression is shown in Fig. 4.5 with the ultimate compressive stress f_{cm}, strain at peak stress ε_{c1}, and ultimate strain ε_{cu1} which is taken as 0.0035.

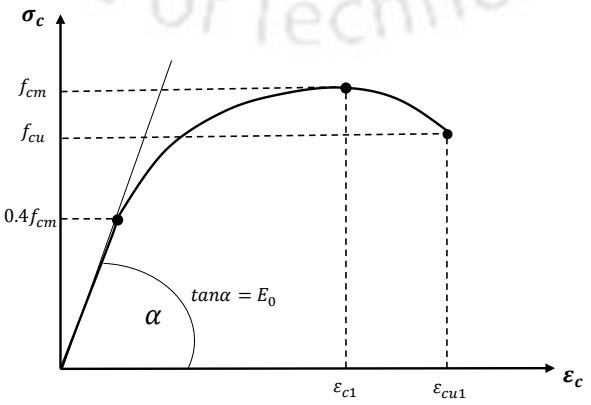

Fig. 4. 5. Stress-strain diagram of concrete in compression according to Eurocode 2 [213]

At each inelastic strain level, the compressive damage parameter d_c is defined. The descending branch of stress-strain response of concrete in compression is utilized to obtain values of damage parameter d_c as follows (Eq. (4.15), (4.16)):

$$d_c = 0; \quad \varepsilon_c < \varepsilon_{c1} \tag{4.15}$$

$$d_c = 1 - \frac{\sigma_c}{f_{cm}}; \quad \varepsilon_c \geq \varepsilon_{c1} \tag{4.16}$$

where strain at peak stress ε_{c1} is given by Eq. 4.14 and Fig. 4.5. While the plastic strains are calculated using Eq. (4.17):

$$\varepsilon_c^{pl} = \varepsilon_c^{in} - \frac{d_c}{1 - d_c}\frac{\sigma_{c0}}{E_0} \tag{4.17}$$

where σ_{c0} is compressive yield stress.

4.2.2.2. Modelling of concrete under tension

The post-cracking behaviour of reinforced concrete structures is governed by stress-strain relationship of the concrete under tension. A typical stress-strain curve under tension is illustrated in Fig. 4(b), which shows the parameters used in the numerical model. The cracking strain (ε_t^{ck}) can be calculated from Eq. (4.18) using total strain (ε_t), tensile stress (σ_t) and the Young's modulus (E_0).

$$\varepsilon_t^{ck} = \varepsilon_t - \varepsilon_{ot}^{el} = \varepsilon_t - \frac{\sigma_t}{E_0} \tag{4.18}$$

The tensile damage parameter d_t is selected in such a way that no negative and/or decreasing tensile plastic strain values, ε_t^{pl}, are recorded. Eq. (4.19) can be used to calculate the tensile plastic strain.

$$\varepsilon_t^{pl} = \varepsilon_t^{ck} - \frac{d_t}{1 - d_t}\frac{\sigma_t}{E_0} \tag{4.19}$$

The ascending and descending branches of stress–strain curve of concrete in tension are given by Eq. (4.20), (4.21) as [214]:

$$\sigma_t = E_c \varepsilon_c; \quad \varepsilon_t < \varepsilon_{cr} \tag{4.20}$$

$$\sigma_t = f_{cm}\left(\frac{\varepsilon_{cr}}{\varepsilon_t}\right)^{0.4}; \quad \varepsilon_t \geq \varepsilon_{cr} \tag{4.21}$$

and ultimate tensile strength of the concrete can be estimated by Eq. (4.22) [215]:

$$\sigma_{t0} = 0.33(f_{cm})^{0.66} \quad (4.22)$$

Plastic strain ε_t^{pl} is calculated similarly as in the case of compression after defining degradation parameter d_t. The value d_t is obtained only for the descending branch of the stress-strain curve of concrete in tension as follows (Eq. (23), (24)):

$$d_t = 0; \quad \varepsilon_t < \varepsilon_{cr} \quad (4.23)$$

$$d_c = 1 - \frac{\sigma_t}{\sigma_{t0}}; \quad \varepsilon_t \geq \varepsilon_{cr} \quad (4.24)$$

while, the plastic strains are calculated using Eq. (4.25)

$$\varepsilon_t^{pl} = \varepsilon_t^{ck} - \frac{d_t}{1 - d_t}\frac{\sigma_{t0}}{E_0} \quad (4.25)$$

where σ_{c0} is tensile yield stress

4.2.2.3. Modelling of GFRP bars

The ultimate value of stress and strains for Glass Fiber-Reinforced Polymer (GFRP) bars are obtained from [6] to replicate complete stress-strain response (see Fig. 4.6c).

The true plastic stress (σ_{true}) and plastic strain (ε_{true}^{pl}) are calculated as per Eq. (4.26), (4.27):

$$\sigma_{true} = \sigma_{nom}(1 + \varepsilon_{nom}) \quad (4.26)$$

$$\varepsilon_{true}^{pl} = \ln(1 + \varepsilon_{nom}) - \frac{\sigma_{true}}{E} \quad (4.27)$$

4.2.3. Calibration of material models

Considering that concrete in the wall experiences both compressive and tensile stresses, the Concrete Damage Plasticity model is employed incorporating damage characteristics. The comprehensive stress-strain response of 3D printed Engineered Cementitious Composite (ECC) under compression and tension, and GFRP bars is depicted in Fig. 4.6. All other parameters including textile properties, detailed in Table 4.1, serves as input in ABAQUS FEM package to accurately capture the behaviour of 3DPC wall reinforced with flexible FRP textile under quasi-static cyclic loading.

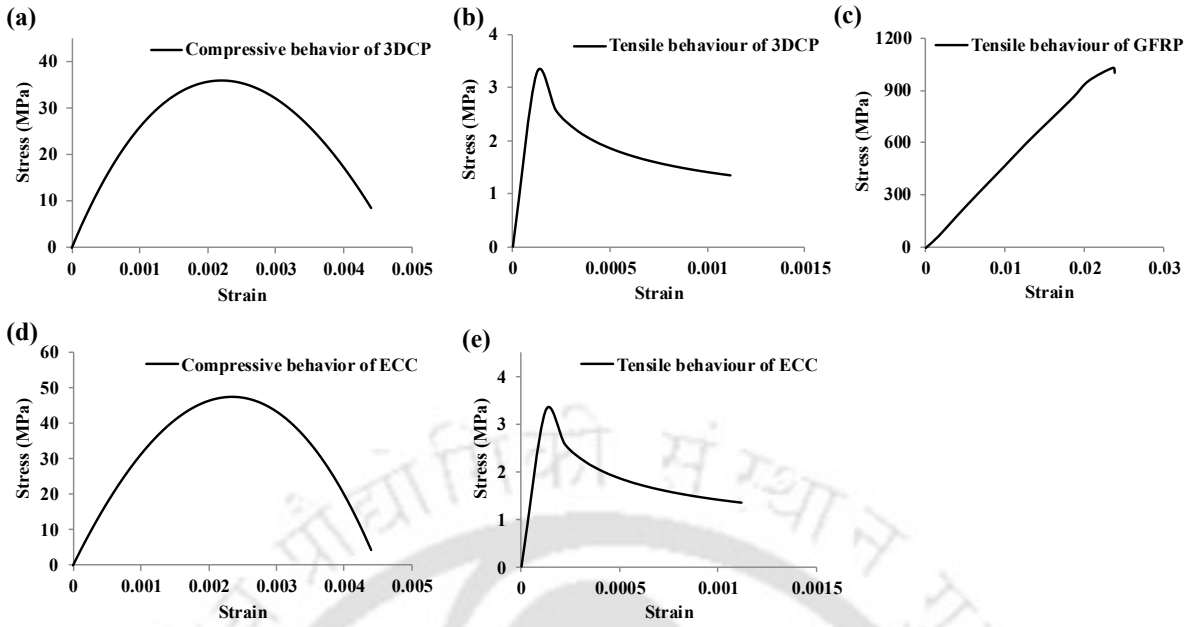

Fig. 4. 6. Stress-strain properties specified in Concrete Damage Plasticity Model for: (a)-(b) 3DPC; (c) GFRP bars; (d)-(e) ECC

Table 4. 1. Properties of flexible CFRP textile [20]

Textile	Grid space (mm×mm)	Mass (g/cm^3)	Cross section of each yarn (mm^2)	Width of mesh (mm)	Width of single rib (mm)
Carbon	20×20	160	0.85	20 ± 5	3 ± 1

The inputs for numerical models are partly obtained from experimental data reported in [6]. Based on these data a complete stress strain response have been produced (detailed in Section 4.2) and some values are assumed based on pertinent information available in the literature (Table 4.2). The average cubic compressive strength of 3DPC and ECC tested at 28 days is 45.0 MPa and 59.2 MPa, respectively [6]. However, design codes often rely on compressive strength of the Φ150 cylinders and therefore, as per Eurocode 2 [213], a constant value of 0.80 has been adopted here to determine the cylindrical compressive strength of the material [216,217].

The elastic modulus, tensile strength, and ultimate strain of a single yarn for the CFRP textile are 211000 N/mm^2, 2300 N/mm^2, and 1.09%, respectively [6]. The Poisson's ratio (ϑ) is presumed to be *0.2*, aligning with prior validation studies [107]. For the layer interface, the cohesion value (c) is established at 0.6 N/mm^2 in line with experimental findings [218]. The shear fracture energy is set at 0.6 N/mm, in accordance with the recommended range provided in [201]. The coefficient of friction is assumed to be 0.75 as mentioned in earlier studies [205]. The material parameters utilized in the validation study are detailed in Table 4.2.

Table 4. 2. Input parameters used for the model validation

Interface-based model		Concrete Damage Plasticity model	
E_c (N/mm^2)	18900 (3DPC), 36754 (ECC) [6]	f_{cm} (N/mm^2)	36 (3DPC), 47.36 (ECC) [6]
ϑ	0.2 [107]	ε_{c1}	0.0022 (3DPC), 0.0023 (ECC) (Calculated from Eq. (4.14))
G_c (N/mm^2)	7875 (Calculated by $E=2G(1+\vartheta)$)	k	2.155 (3DPC), 1.91 (ECC) ((Calculated from Eq. (4.13))
t_c (mm)	15 [6]	σ_{c0}	14.4 (3DPC), 18.94 (ECC) ($0.4f_{cm}$)
K_n (N/mm^3)	1260 (Calculated from Eq. (4.5))	Density (N/mm^3)	21000 [6]
$K_s = K_t$ (N/mm^3)	525, 525(Calculated from Eq. (4.5))	Dilation Angle (degree)	35^0 [211]
G_{IC} (N/mm)	0.29 (Calculated from Eq. (4.8))	Eccentricity	0.1 [204]
G_{IIC}, G_{IIIC} (N/mm)	0.6, 0.6 (Calculated from Eq. (4.8))	Biaxial compressive yield stress/uniaxial compressive yield stress (f_{b0}/f_{c0})	1.16 [211]
μ	0.75 [205]	K	0.67 [204]
		Viscosity parameter	0.00001

4.3. Model validation

4.3.1. Description of the 3DPC wall specimens

The proposed model accuracy is validated with respect to the test data of lateral load performance of 3DPC walls mentioned in [6]. The approach begins with utilization of the Concrete Damage Plasticity model to validate the conventionally cast control wall (CCW). Upon the successful validation of the control wall, the Concrete Damage Plasticity & cohesive interface model is further incorporated to assess the effectiveness of the composite modelling approach in validating the 3DPC reinforced wall (PRW).

Both the PRW and CCW walls shared a height of 1500 mm with a height-to-width ratio of 1.0. Fig. 4.7 illustrates the cross-sectional configurations of these specimens. The PRW is 3D printed with trusses, holes, and an edge column, while the CCW is conventionally cast without any reinforcement in the main body. The outline width in the PRW specimens is limited to 30 mm following typical concrete filament width. Despite variations in structural details, both PRW and CCW specimens have same material properties (Fig. 4.6a, b). To stabilize the walls and facilitate the application of lateral loads, a top beam (250 mm×300 mm cross-section) and a foundation beam (400 mm×500 mm cross-section) are modelled in addition to the main body of the wall. GFRP bars, measuring 250 mm and 570 mm in length, are embedded in all wall specimens to ensure secure connections with wall and the top and bottom beams respectively. Consequently, the solid section of the PRW extends 270 mm above the bottom beam. Fig. 4.7 illustrates the structural configuration of the tested walls. In the PRW, trusses are designed to allow manual insertion of one GFRP bar into each hole, while the edge column section was intentionally left without GFRP bars to avoid interference with the 3D printing process as discussed in [6].

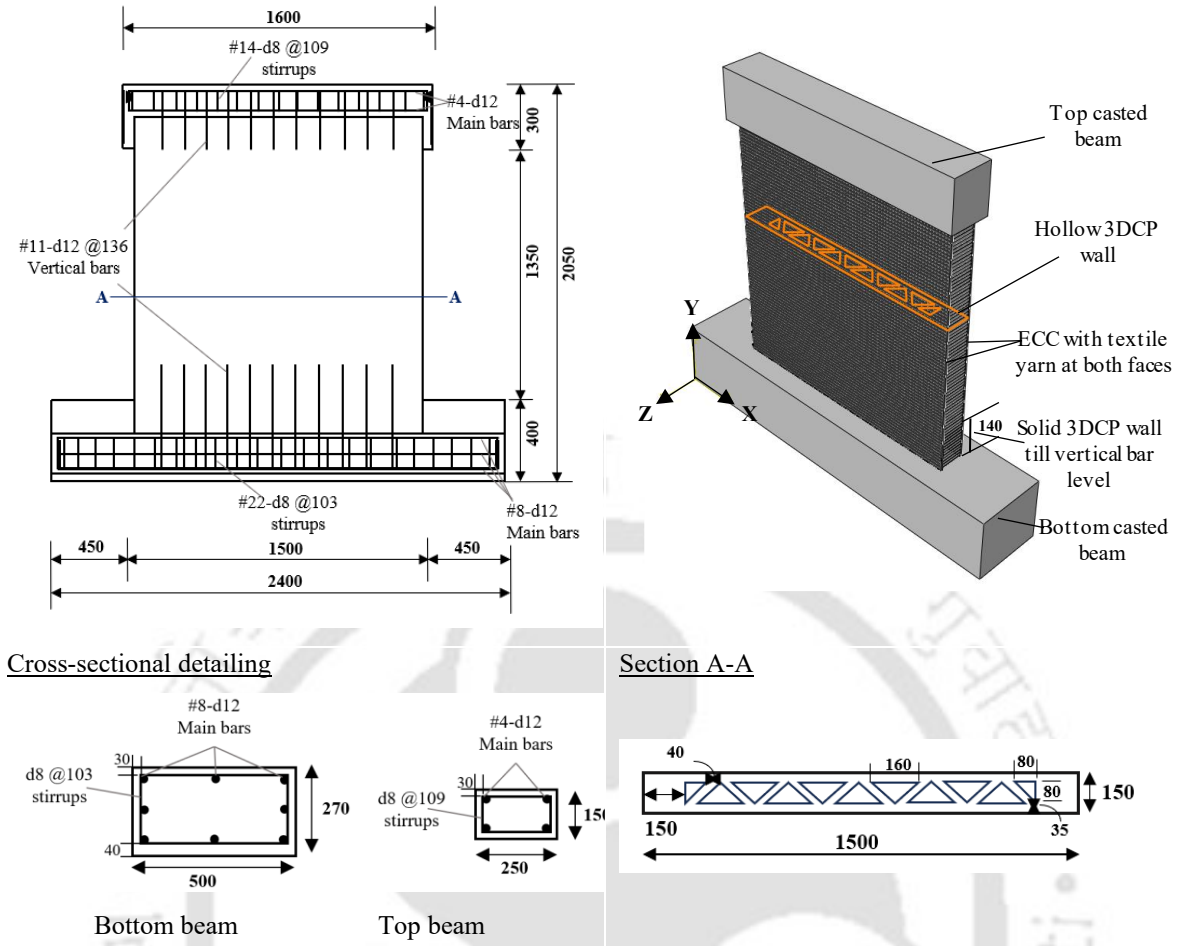

Fig. 4. 7. Elevation and cross-sectional detailing of the 3DPC wall (PRW) (all dimensions are in mm, based on [6])

4.3.2. Description of the numerical model: boundary condition, meshing and loading protocol

In the proposed 3D finite element composite interface model, both the linear and non-linear behaviour of the printed layers and interfaces are explicitly defined. Specifically, 3D hexahedral-shaped eight-node linear brick elements with reduced integration and hourglass control (type C3D8R) are employed to model the printed layers, ECC, and concrete. The GFRP bars and textile-mesh are modelled using 2-noded 3D truss elements (T3D2). Textile mesh is discretized according to its grid size and ECC is also discretized in a similar manner to that of textile mesh for compatibility. Within the PRW, joint interfaces are modelled using surface-based cohesive approach.

For the interfaces between printed layers (interlayer), a surface-to-surface discretization method is applied utilizing finite sliding formulation. The contact behaviour between adjacent surfaces of 3DPC layers (intra-layer) is characterized by hard contact approach using contact pressure-overclosure relationship.

Embedded body constraints are used to support the load transfer mechanism and ensure appropriate bonding between the textile mesh and ECC matrix [219]. Additionally, to simulate the occurrence of de-bonding between the 3DPC substrate and ferro-cement composite interface, surface-to-surface interaction is established. This interaction involved specifying tangential and normal behaviour. The interaction between the densely meshed slave surface (representing the ECC) and coarsely meshed master surface (representing the 3DPC substrate) is characterized by normal hard contact and tangential behaviour with a penalty friction coefficient set at 0.75. The integration of these specifications in the numerical model corroborates realistic simulation of de-bonding mechanisms.

Mesh sensitivity analysis is carried out with varying mesh sizes (Fig. 4.8a and Table 4.3). Based on the findings, 50 mm mesh size is selected for the discretization of 3DPC and casted concrete elements (Fig. 4.8c) and similarly, 15 mm mesh size for ECC and textile as the grid space of yarn is 20×20 mm. The viscosity parameter sensitivity analysis is carried out and 0.00001 viscosity parameter is selected as per the calculation shown in Fig. 4.8b.

After analysing Fig. 4.8a and Table 4.3, it becomes evident that a coarser mesh size results in reduced computational time but also impacts the ultimate load. Specifically, as depicted in Fig. 4.8a, transitioning from mesh size 15 to Mesh size 100 while maintaining a constant viscosity parameter of 0.01 leads to an increase in the stiffness of the PRW. Consequently, after evaluating the load profile, characterized by the stiffness factor, and the ultimate load ratio, i.e., error, mesh size 50 is selected. Despite its longer computational time compared to mesh size 100, Mesh size 50 exhibits lower stiffness in loading profile (Fig. 4.8a). Subsequently, a sensitivity analysis is also performed on the viscosity parameter. As illustrated in Fig. 4.8b, decreasing the viscosity parameter from 0.01 to 0.00001 results in a reduction in the stiffness of the curve, decrease in error rates associated with the ultimate load ratio (Table 4.3) and showing approximately similar loading profile as experimental work (Fig. 4.8b) [6]. Based on this comprehensive examination and to strike a balance between accuracy and computational efficiency, we have set the viscosity parameter at 0.00001 for all subsequent numerical analyses. The selections are made with the need for accurate representation of the physical phenomena under investigation, while balancing computational efficiency.

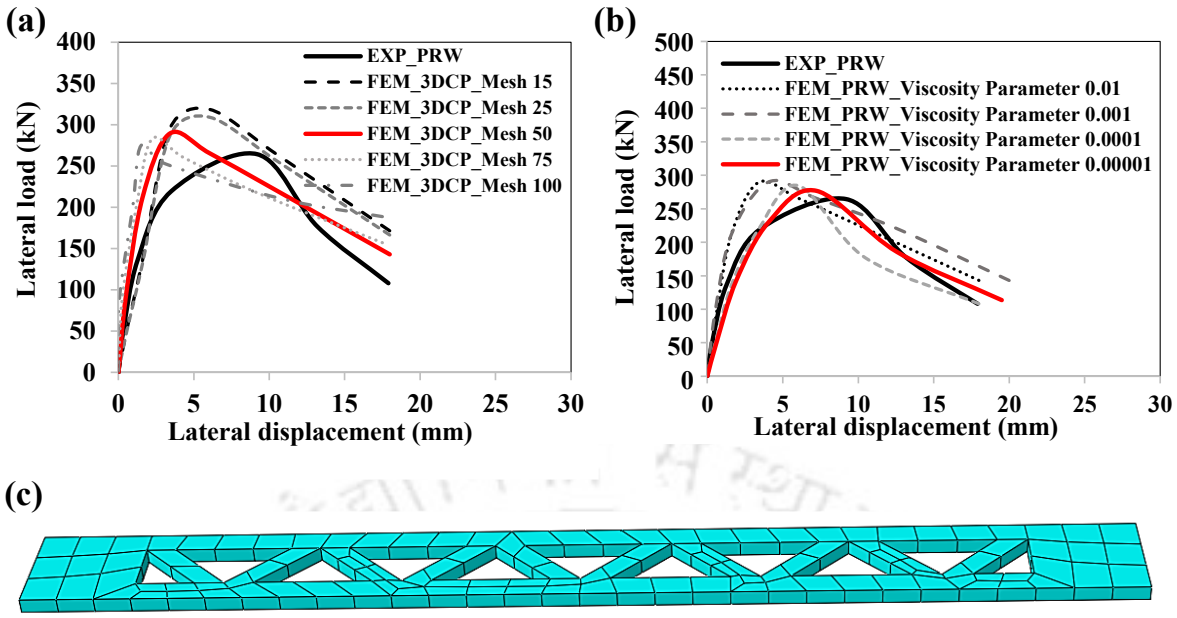

50 mm mesh size with truss type infill pattern

Fig. 4. 8. Sensitivity analysis by varrying (a) mesh size; (b) bviscosity parameter; (c) mesh representation for a 3DPC layer

Table 4. 3. Error of different mesh size and viscosity parameter

Legends	EXP_PRW	Mesh 15	Mesh 25	Mesh 50	Mesh 75	Mesh 100
Ultimate load (N)	264453.96	318709.68	309148.39	289247.31	283462.37	274958.49
Error (FEM/EXP)	…	1.21	1.17	**1.09**	1.07	1.04
Legends	**EXP_PRW**	**Viscosity Parameter 0.01**	**Viscosity Parameter 0.001**	**Viscosity Parameter 0.0001**	**Viscosity Parameter 0.00001**	**Fixed Mesh size**
Ultimate load (N)	264453.96	289247.31	290247.31	284453.96	276676.66	50.00
Error (FEM/EXP)	…	1.09	1.10	1.08	**1.05**	

Surface-to-surface interaction is established to facilitate communication between the adjacent layers and the top and bottom casted beam connected to the 3DPC wall. Where bottom layer top surface served as master surface and top layer bottom surface is served as slave surface; by considering strict master-slave formulation i.e., the slave surface should be the more finely meshed surface; and if the mesh densities are similar, the slave surface should be the surface with the softer underlying material. In contrast, a general contact algorithm is applied to the casted wall, where this contact type encompasses interactions among all adjacent surfaces in the model without specifying specific surface pairs. In the tangential direction, isotropic Coulomb friction—commonly referred to as "penalty friction" in Abaqus (SIMULIA,

2019)—is employed, with a friction coefficient set at $\mu = 0.75$. In the normal direction, hard contact relationship is defined.

To ensure realistic transmission of the forces, contact surfaces between the layers are configured to be parallel. The incorporation of large, flat surfaces on the top and bottom of each layer served to maximize the number of nodes in contact. This strategic design aimed to prevent poorly distributed forces throughout the model, which could elevate the risk of local failure and potentially impact the overall results. An example of layer interaction surfaces is schematically shown in Fig. 4.9.

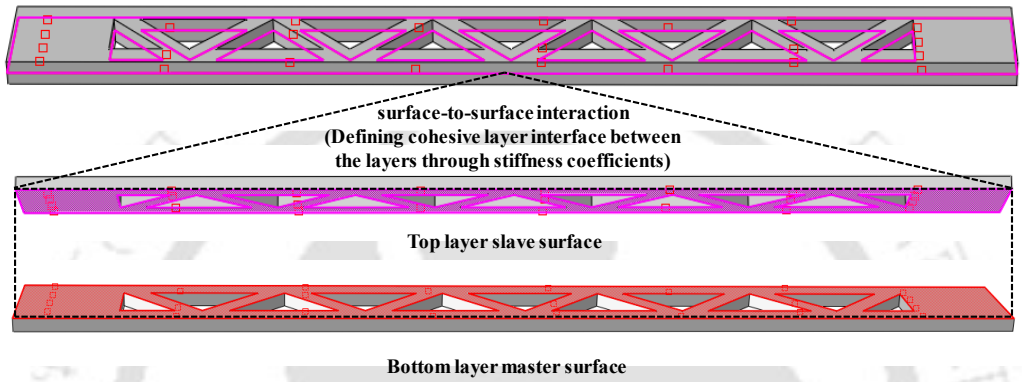

Fig. 4. 9. Interaction between the 3DPC layers

The loads are applied on the 3DPC walls in two stages. Initially, a constant pre-compression vertical stress is applied. The walls are then subjected to horizontal cyclic loads with 21 cycles of loading controlled by displacement. Fig. 4.10a,b shows the cyclic loads applied at the control node and top surface of the top beam. During testing, the specimens are moved in 1 mm increments as shown in the lateral loading history. Each cycle involves two repetitions of push and pull to simulate both positive and negative loads. To stabilize the walls, a pre-compression load of 20 kN is applied equally to both the PRW and CCW specimens as described in [6].

For clarity and comparability, the displacement-controlled loading is characterized by the lateral drift ratio θ, gradually increasing from 0.03% to 2.67% (where $\theta = \Delta/H$, here, Δ represents the lateral displacement at the loading point, and H is the distance between the horizontal loading point and the base of the wall). A non-linear dynamic implicit procedure is followed, thus facilitating the pursuit of quasi-static solution that iteratively resolves equilibrium at each increment.

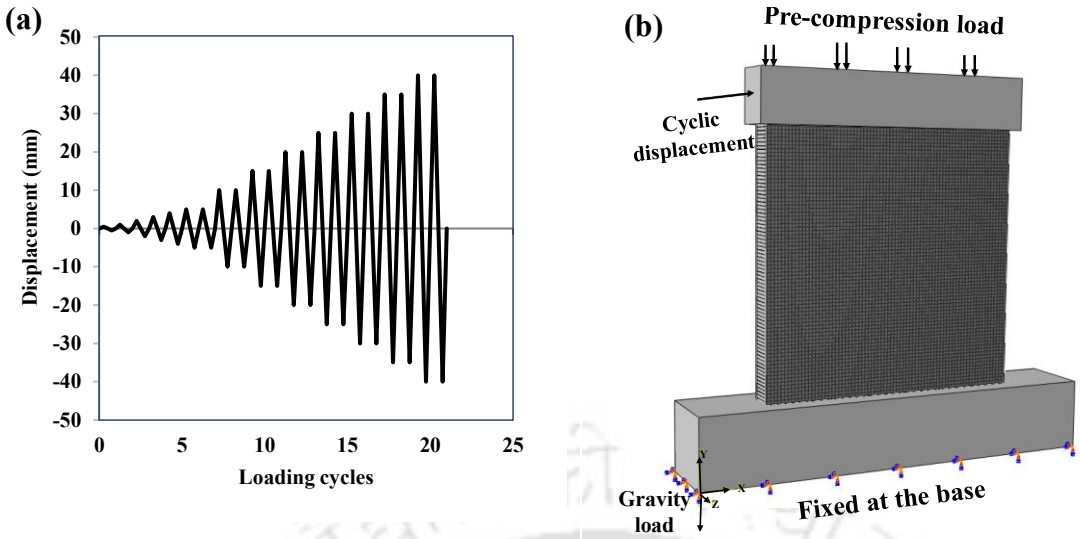

Fig. 4. 10. (a) Cyclic loading protocol [6]; (b) numerical loading setup of 3DPC wall

4.3.3. Validation of the numerical model

Fig. 4.11 illustrates the load–displacement relation and failure modes of the CCW and PRW walls. Notably, the predictions align well with experimental results. It's worth mentioning that the predicted ultimate loads and load profile along with failure modes show almost similar results in line with experimental results. While this phenomenon is significant, it underscores the confidence in adopting the proposed model as a valuable tool in practical designs.

The analysis proceeded in two stages: In the first step under load control, the initial (constant) vertical stress and gravity loads are imposed on top beam of the walls using a rigid body. Subsequently, in second step the wall is subjected to cyclic in-plane loads under displacement control through rigid body with constraints applied to out-of-plane displacement and rotation.

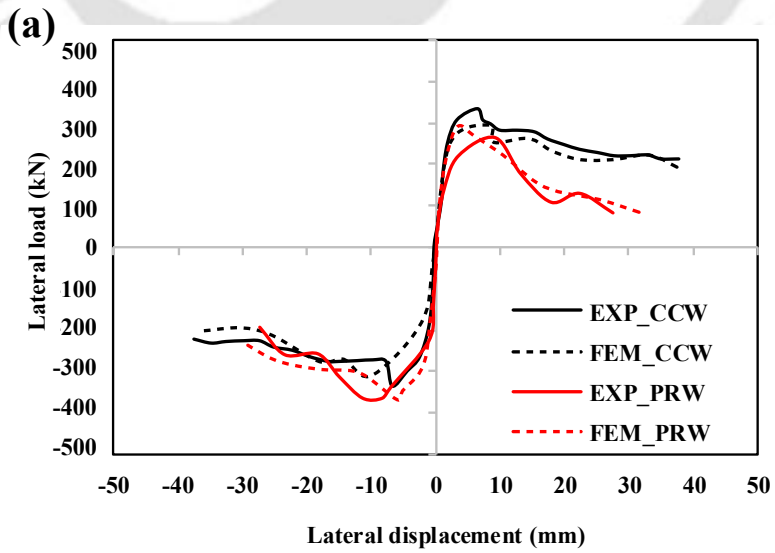

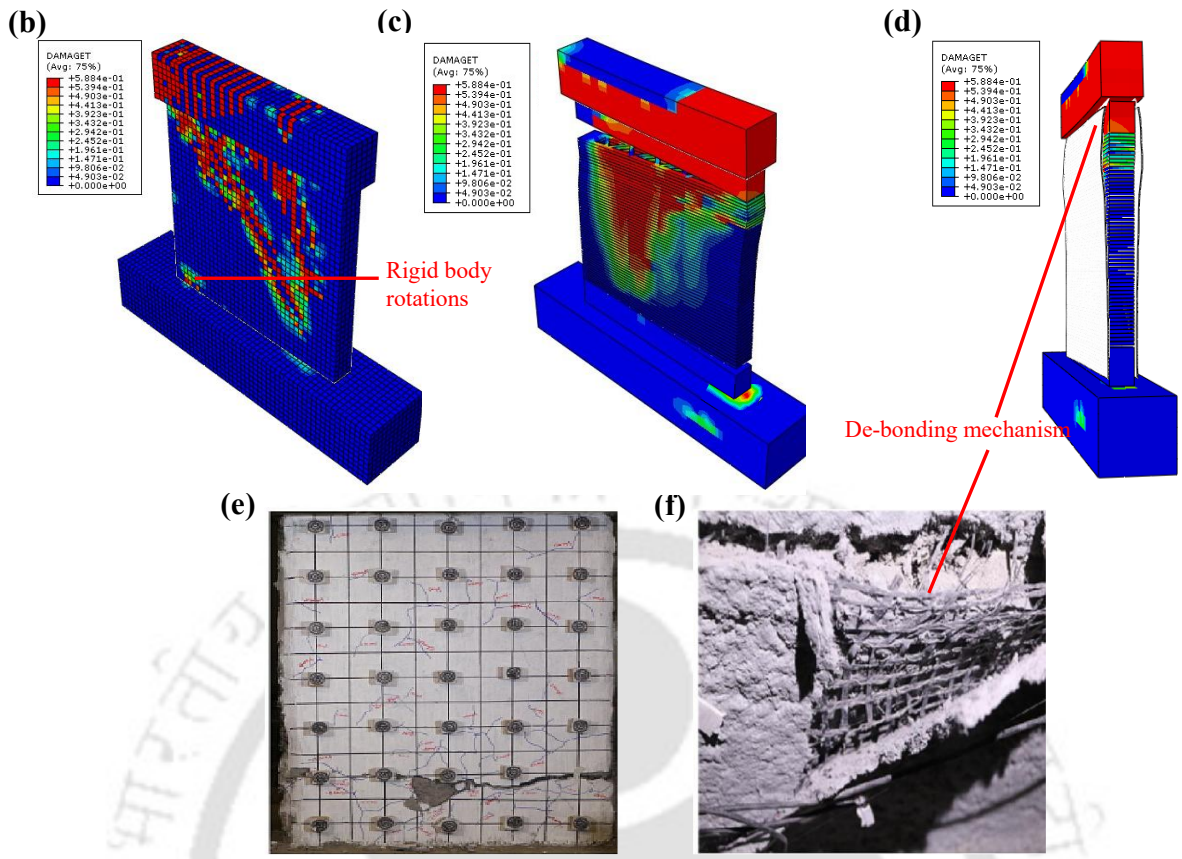

Fig. 4. 11. (a) Experiment vs numerical envelope curves of hysteretic response of walls; numerical failure modes of (b) CCW; (c, d) PRW; (e, f) experimental failure modes of PRW [6]

The wall's quasi-ductile behaviour initiates from energy dissipation at the layer interface. It is worth noting that in the case of PRW, the maximum horizontal load (264.45 kN) reported in experiment is relatively lower than the maximum load predicted by the numerical model (289.25 kN). This difference suggests late occurrence of horizontal crack propagation at the first layer interface in the numerical model than the experiment. This is further supported by the ultimate failure occurring at displacements of 25.58 mm and 31.68 mm in the experiment and numerical results respectively (see Fig. 4.11a). Following propagation of the horizontal crack, the response of model is governed by proportional relationship of coefficient of friction to the normal compressive stresses (at interaction surface of 'bottom beam' and 'first layer interface of 3DPC wall').

In case of CCW, nearly rigid body rotations are observed (Fig. 4.11b), centering on the edge toes of the walls. It is important to note that some cracks in the CCW appeared at about a 45-degree angle. This suggests that the forces applied are causing diagonal cracks rather than crushing. In contrast, vertical cracks and separation between the 3DPC substrate and the ECC-

textile composite are observed in PRW due to the cyclic sliding movements of the upper part of the wall (Fig. 4.11c,d). Similar failure modes are observed in the experimental results (Fig. 4.11e).

In comparison to CCW, the PRW exhibited approximately 36% lower lateral strength than the casted wall (see Fig. 4.11a). This can be primarily ascribed to the hollow cross-section of 3DPC wall, resulting in smaller section area in contrast to the casted wall [6]. In the absence of vertical rebars, the yield and peak loads of the casted wall are predominantly influenced by the section area, adhering to the shear-friction theory. As a result, specimen CCW exhibited higher yield and peak load than PRW. Notably, the PRW demonstrated comparable mechanical capability with less concrete material probably due to the FRP reinforcement and inclusion of an edge column in the specimen.

4.4. Parametric analysis of numerical results

A parametric analysis is conducted to assess the sensitivity of the validated model by varying edge column size, aspect ratio, reinforcement bar length, material (mortar) strength and pre-compression load. The material properties outlined in Table 4.2 serves as baseline model, while both geometric and material parameters are systematically adjusted to examine the performance metrics detailed in Table 4.4 and Fig. 4.12. The rebar area and arrangements are considered similar to PRW (Fig. 4.7) in the baseline model, except for the replacement of top and bottom vertical GFRP bars with continuous GFRP bar within the wall. Following successful validation of the PRW, textile reinforcement along with the ECC overlay (as ferro-cement) are omitted from all parametric model to assess the behaviour of the control 3DPC wall. The findings from the parametric analysis are discussed in the subsequent sections.

Table 4. 4. Details of specimen used in parametric analysis

Sr. No.	Parameter selected for parametric analysis	Specimen Id	Ultimate lateral load (N)	Maximum lateral deflection (mm)	Remark
1	Effect of edge column size	FEM_PRW_150×150	188010.75	31.68	As the size of the edge column increases from 150×150 to 250×250, both the ultimate lateral load and maximum lateral deflection increase consistently
2		FEM_PRW_175×175	248644.22	32	
3		FEM_PRW_200×200	270276.27	33.27	
4		FEM_PRW_250×250	293790.3	34.85	
9	Effect of vertical GFRP bar length	FEM_PRW_140	188010.75	31.68	The ultimate lateral load increases with the increase in GFRP bar length from 140 to 1350 mm, but there is no significant change in maximum lateral deflection have observed
10		FEM_PRW_375	211225	31.4	
11		FEM_PRW_750	320609.38	29	
12		FEM_PRW_1350	400761.72	31.39	
5		FEM_PRW_C40	188010.75	31.68	

6	Effect of printed mortar's compressive strength	FEM_PRW_C45	269548.13	32.56	As the printed mortars strength increases maximum lateral deflection increases slightly but an enormous rise in ultimate strength has been noted i.e., 122.14%.
7		FEM_PRW_C50	313235.29	33.12	
8		FEM_PRW_C55	417647.06	33.72	
13	Effect of walls aspect ratio	FEM_PRW_AR1	188010.75	31.68	Increasing the aspect ratio of walls leads to a decrease in ultimate lateral load but increase in maximum lateral deflection
14		FEM_PRW_AR1.25	144430.34	31.94	
15		FEM_PRW_AR1.5	100393.28	33.34	
16		FEM_PRW_AR2	54005.87	35.34	
17	Effect of pre-compression load	FEM_PRW_P20	188010.75	31.68	Higher pre-compression loads result in a very slight increase in ultimate lateral load, but significant increase in maximum lateral deflection of 35.59%.
18		FEM_PRW_P40	194105.95	34.91	
19		FEM_PRW_P80	200000	37.42	
20		FEM_PRW_P160	201550.39	42.96	

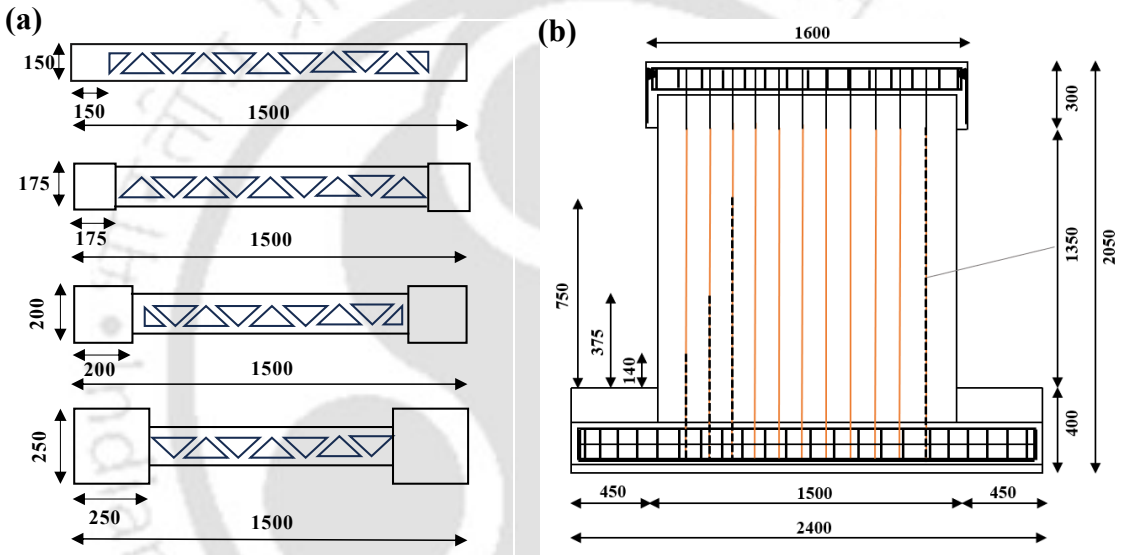

Fig. 4. 12. Details of geometric configuration used in parametric analysis; by varying (a) edge column cross-sectional area (mm^2) (i.e., 150×150, 175×175, 200×200, 250×250); (b) vertical GFRP bar length (mm) above the bottom beam surface (i.e., 140, 375, 750, 1350)

4.4.1. Effect of edge column size

Fig. 4.13 shows the envelope curve of the 3DPC wall (PRW) with varying edge column sizes as depicted in Fig. 4.12(a). In this setup, all aspects of the wall geometry, boundary and loading conditions, and material properties are remained constant, while the column size is adjusted up to the top beam width of 250 mm. The column sizes are ranging from 150 mm × 150 mm to 250 mm × 250 mm as per typical reinforced concrete columns [220]. This variation aims to explore the impact of column size on the cyclic in-plane load–displacement plot.

As anticipated the in-plane load capacity demonstrates an increase with the enlargement of column dimensions. The in-plane capacity of PRW with 175 mm × 175 mm, 200 mm × 200 mm, and 250 mm × 250 mm columns increased by 32.25%, 43.76%, and 56.26%, respectively

compared to the 150 mm × 150 mm column (as shown in Fig. 4.13). This trend is consistent with findings reported in [220,221]. In addition to the ultimate lateral load, the stiffness of wall also increases with the larger column size.

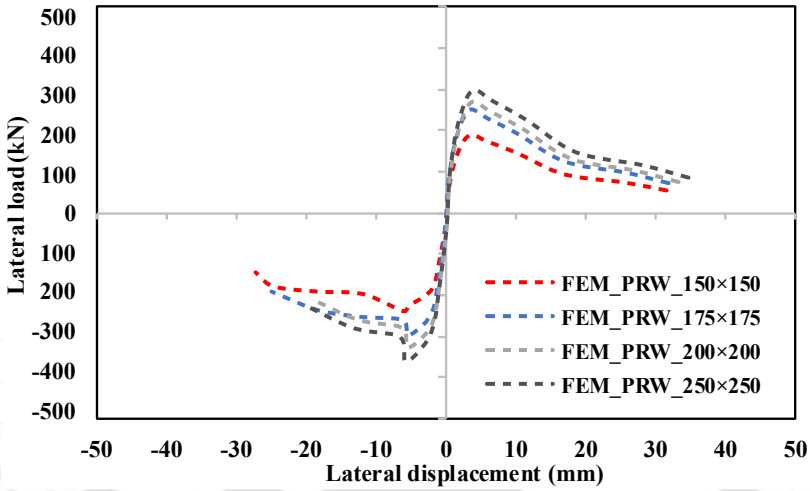

Fig. 4. 13. Effect of edge column size on loading capacity

The initial stiffness of PRW increased progressively with larger column sizes: specifically, PRW with 175 mm × 175 mm, 200 mm × 200 mm, and 250 mm × 250 mm columns exhibited increments of 5%, 11%, and 22%, respectively, compared to PRW with 150 mm × 150 mm columns. This rise in stiffness can be attributed to the greater cross-sectional area of the columns, resulting in enhanced resistance to lateral displacement.

Interestingly, despite the variation in column sizes, the peak in-plane load for PRW with 150 mm × 150 mm, 175 mm × 175 mm, 200 mm × 200 mm, and 250 mm × 250 mm columns are within the same displacement range of 3-3.5 mm. This phenomenon suggests that the structural behaviour of the walls approached a common limit irrespective of column size, likely due to the constraints imposed by other structural elements or material properties. Notably, sliding shear has been found to be the most common failure mode in all PRW cases. The shear capacity is found to be less than flexural capacity as no extra shear reinforcement was added when column dimensions are changed and this ultimately caused the failure of walls due to sliding shear.

4.4.2. Effect of GFRP bar length above the bottom beam surface

Fig. 4.14 shows the envelope curve of PRW 3DPC wall with varying GFRP bar lengths (as indicated in Fig. 4.12b). All other model parameters are remained constant except length of the GFRP bar is changed from 140 mm to 375 mm, 750 mm, and 1350 mm. Additionally,

concrete is casted at the GFRP bar's length level since in numerical modelling method, the GFRP bar cannot be embedded in a hollow zone.

The in-plane cyclic loading capacity increases with the extension of the GFRP bar length. With GFRP bar lengths of 375 mm, 750 mm, and 1350 mm, the ultimate lateral load is found to be 12.35%, 70.53%, and 113.16% higher, respectively compared to the PRW with 140 mm GFRP bar length. This increase in loading capacity is due to the enhanced reinforcement provided by longer GFRP bars. However, after increasing the GFRP bar length from 140 mm to 375 mm, the stiffness of the wall tends to decrease and this decrease is due to the ineffective material distribution that affects the moment of inertia and stiffness (Fig. 4.14). Despite decrease in stiffness, the ultimate loading capacity shows a slight improvement.

Furthermore, when the bar length is increased to 1350 mm, improvements in sliding behaviour are observed at the interface between the top beam and first (hollow) layer of the wall. This improvement may be attributed to the longer GFRP bar reinforcement, which stabilises the structure against toppling and sliding and efficiently resists lateral forces. The primary failure mode is also shifted from "sliding failure" to "bending failure." This shows that the suggested reinforcing technique successfully prevents crushing and enhances the structure's mechanical behaviour (Fig. 4.15).

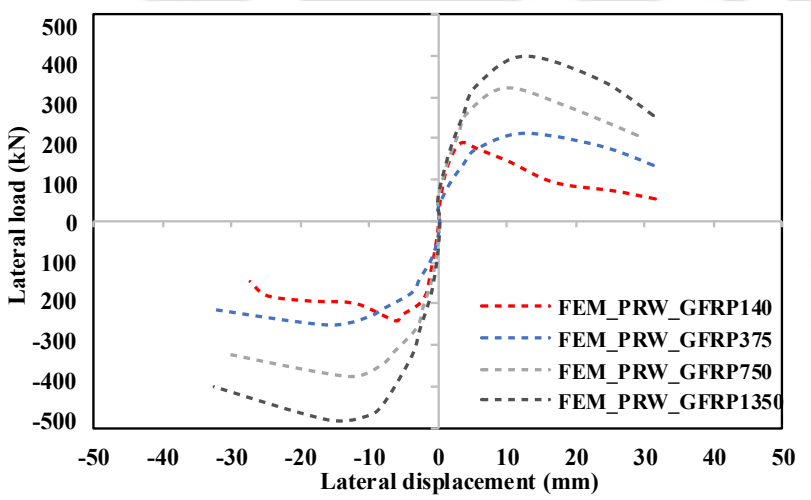

Fig. 4. 14. Effect of GFRP bar length above the bottom beam surface on loading capacity

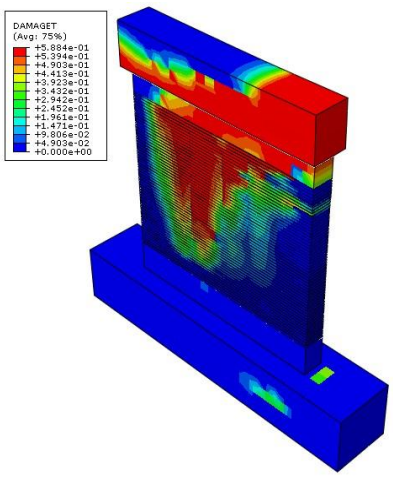

Fig. 4. 15. Effect of full GFRP bar length above the bottom beam surface on failure mode of the PRW_GFRP1350 wall

4.4.3. Effect of printed mortar compressive strength

The effect of mortar compressive strength of 40 MPa, 45 MPa, 50 MPa and 55 MPa on ultimate loading capacity and failure modes are analysed. Fig. 4.16 shows the computed envelope curve of the PRW 3DPC wall with varying printed mortar compressive strength. As expected, higher compressive strength resulted in increased loading capacity. For instance, compared to 40 MPa mortar, compressive strength of 45 MPa, 50 MPa, and 55 MPa led to 43.37%, 66.6%, and 122.14% increase in PRW's in-plane capacity respectively. Fig. 4.17 further clarifies that while the mortar strength affects ultimate loading capacity, it does not significantly alter the fundamental structural response of the wall.

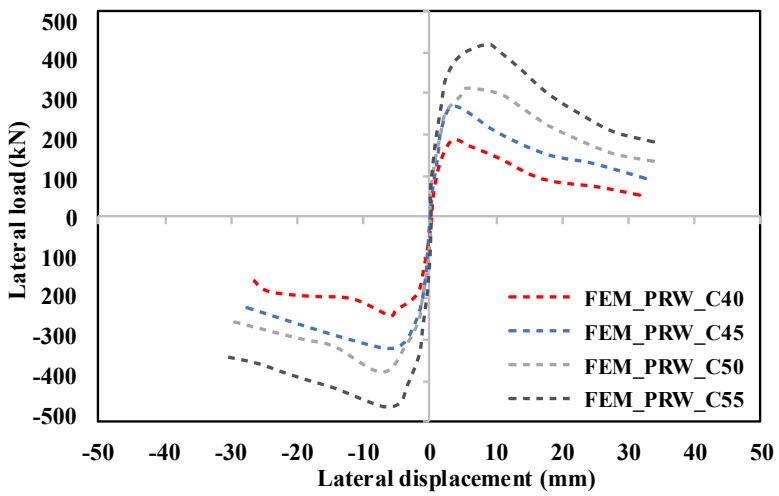

Fig. 4. 16. Effect of printed mortar compressive strength on loading capacity

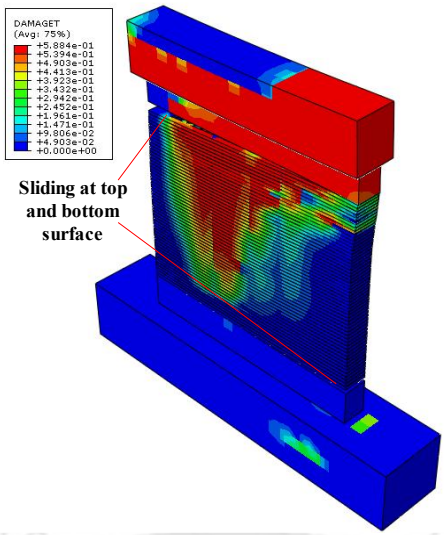

Fig. 4. 17. Effect of printed mortar compressive strength on failure mode of PRW_C55 wall

4.4.4. Effect of wall aspect ratio

The computed envelope curve of the 3DPC wall (PRW) with different aspect ratio (height/width) ranging from 1 to 2 is shown in Fig. 18. In this analysis, a constant wall height (1500 mm) is set for all the wall specimens, while different width such as 750 mm, 1000 mm, and 1200 mm are used to simulate the effect of aspect ratio considering their dominance on the cyclic in-plane structural performance.

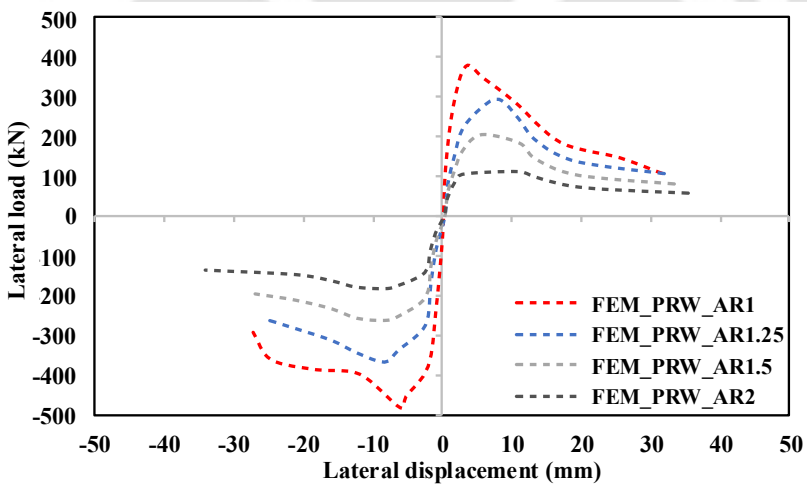

Fig. 4. 18. Effect of wall aspect ratio on cyclic in-plane loading capacity of 3DPC wall

When aspect ratio (AR) of the wall increases (or the width of the specimen decreases), a corresponding decrease in loading capacity is observed. For instance, compared to an AR of 1, increase in AR up to 1.25, 1.5, and 2 resulted in corresponding decreases of 23.18%, 46.6%, and 71.28% in PRW's in-plane capacity. This decrease in loading capacity is due to the

reduction in wall area with increase in AR. However, their ultimate lateral displacement capacity increased by 0.8%, 5.23%, and 11.54% respectively.

When considering failure mode and damage pattern (Fig. 4.18), it is observed that shear deformations mainly regulate the cyclic in-plane loading capacity. Additionally, Fig. 4.18 reveals that the lateral strength of the 3DPC wall increases with decrease in AR. This boost in lateral strength can be attributed to favourable distribution of material and load-bearing capacity at lower ARs. With reduction in AR, the wall's sectional area becomes more concentrated and it leads to increased stiffness and strength properties. Conversely, when the AR exceeds one, flexural deformation become more prominent as demonstrated in Fig. 4.19. This shift occurs because higher AR result leads to increased bending moment and greater susceptibility to flexural failure.

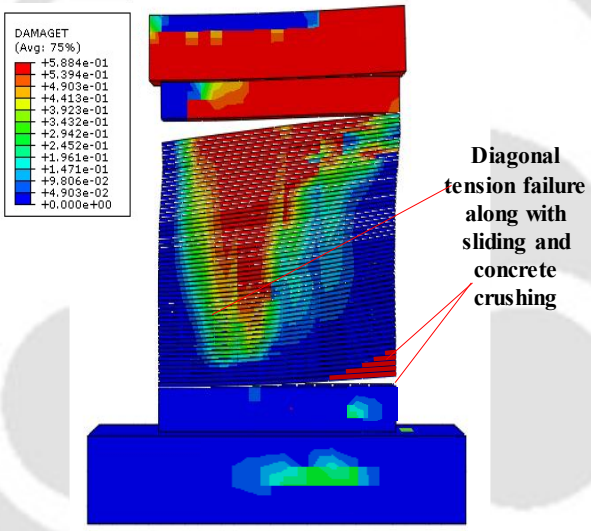

Fig. 4. 19. Effect of wall aspect ratio on failure mode of 3DPC wall (PRW_AR2)

4.4.5. Effect of pre-compression load

Fig. 2.20 shows the estimated envelope curve of the 3DPC wall (PRW) under different pre-compression load. The effect of pre-compression load of 20, 40, 80, and 160 kN are investigated on failure modes and ultimate loading capacity. Interestingly, there is no significant enhancement in the ultimate loading capacity when pre-compression loads are applied on the top beam surface. This lack of significant improvement can be attributed to the fact that pre-compression load primarily contributes to the stability of the wall rather than directly increasing its load-bearing capacity. For instance, increasing the pre-compression load to 40, 80, and 160 kN resulted in 3.24%, 6.38%, and 7.2% increase in PRW's in-plane capacity of respectively. However, the ultimate deformation capacity increases in the

magnitude of 10.19%, 18.11%, and 35.59%, respectively. This increase in ultimate deformation capacity occurs because the pre-compression load allows the wall to withstand greater deformation under the same load, thus enhancing its stability and overall resilience. This is particularly crucial in scenarios where external forces or environmental conditions may induce deformation in the wall.

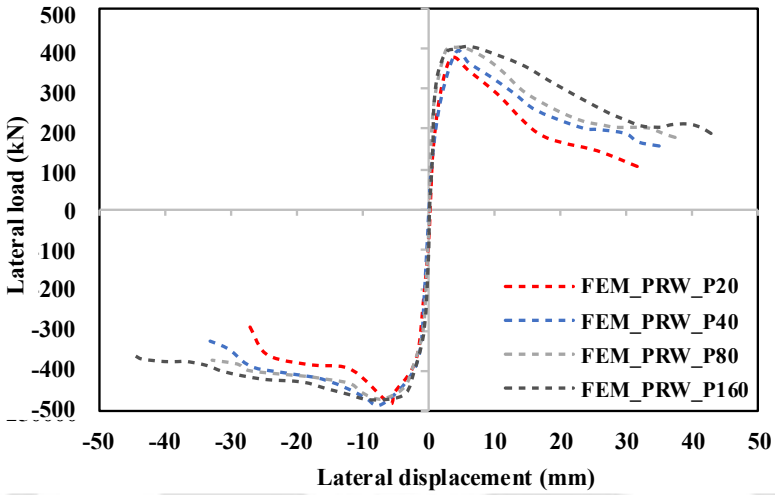

Fig. 4. 20. Effect of pre-compression load on cyclic in-plane loading capacity of 3DPC wall

4.5. Evaluation of the proposed modelling approach

To establish a performance-based seismic design strategy from parametric analysis results, it is essential to first evaluate the performance of walls under cyclic loading. The response of concrete members to cyclic lateral loading is significantly influenced by concrete cracking, which directly affects the energy dissipation capacity. Simple macro-modelling approaches, which often neglect stiffness degradation and pinching effect, tend to overestimate energy dissipation. The pinching effect, observed in the flexural response of walls causes the hysteresis curve to narrow progressively with each loading cycle due to the cyclic opening and closure of cracks. This leads to a notable reduction in stiffness during load inversion phases (see Fig. 4.21a,b). The following sections will discuss how the proposed composite interface micro-model approach better captures these factors, while providing a more accurate analysis of stiffness, energy dissipation capacity, and hysteresis curves for the PRW wall.

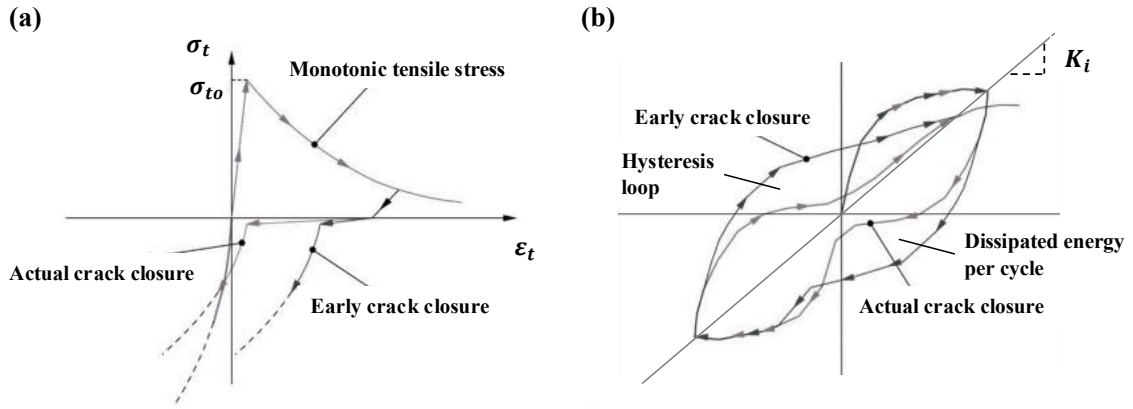

Fig. 4. 21. Effect of the pinching through cracking closure in simulation in the (a) mechanical model; (b) global response showing the pinching effect (reproduced from [222]

4.5.1. Hysteresis response

It can be observed from Fig. 4.22 that the predicted FE results are matching with experimental loading results shown in [6]. For the 3DPC wall (PRW) models shown in Fig. 4.22b, the pinching behaviour of the hysteresis curves is well predicted using the proposed model due to the fact that it integrates a number of phenomena including complex geometrical configurations, residual stress conditions, non-linear contact and slip, geometrical non-linearity (local instability), and material non-linearity (plasticity, strain-hardening) [223]. This behaviour is further exacerbated under cyclic loading by sequential static loading and unloading, where loading branches exhibit the typical pinching effect.

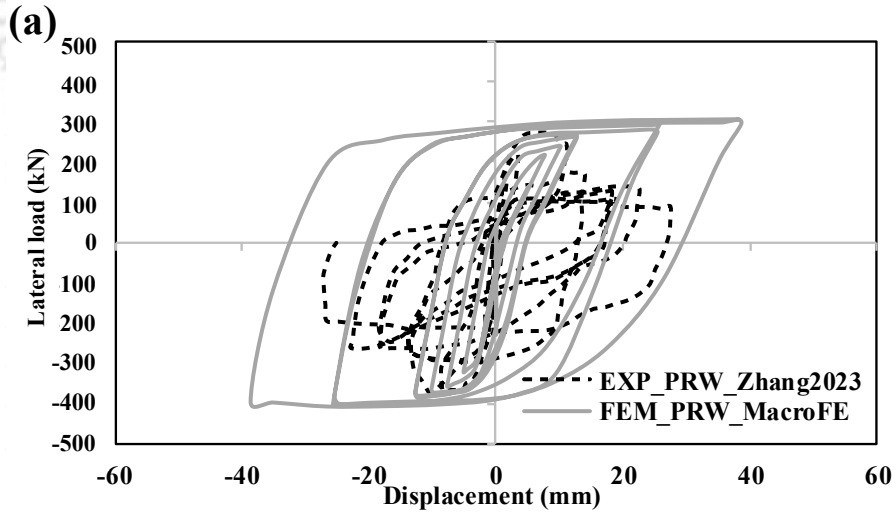

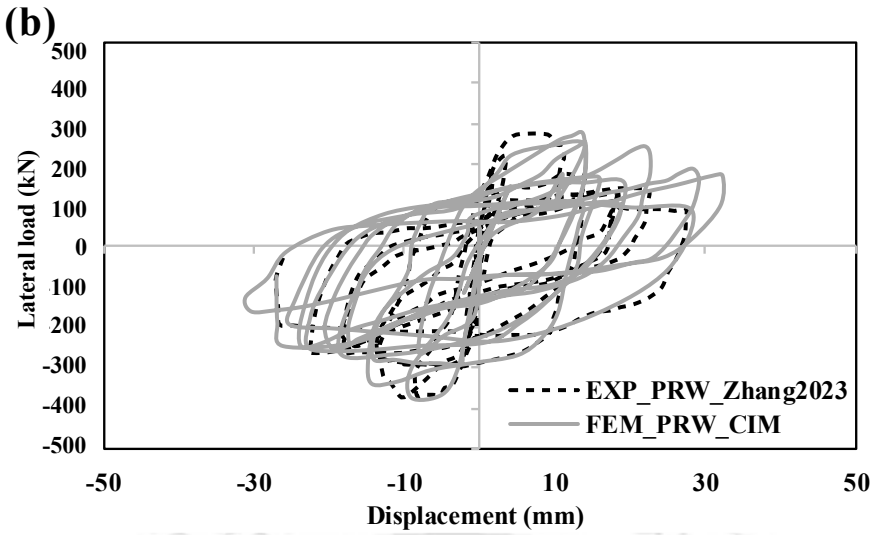

Fig. 4. 22. Comparison of hysteresis response in terms of pinching by using (a) simple macro-modelling; (b) composite interface micro-modelling approach

4.5.2. Secant stiffness and energy dissipation capacity

The inclination of the line connecting positive to the negative peak in a full cycle of the hysteresis curve defines secant stiffness of the specimens. By incorporating secant stiffness into the analysis, evolution of stiffness of the structure with increasing loads can be better understood, particularly in the presence of nonlinear behaviour or material degradation under cyclic loading. The macro model exhibits lower slope of the secant stiffness curve compared to the interface micro-model. Numerical findings show that the stiffness degradation is not considered in the macro modelling case. But micro-model-based stiffness degradation follows the common trend observed in [6] as depicted in Fig. 4.23a. Before 10 mm displacement, the stiffness degradation occurs at higher rate and the rate of crack development decreases at higher displacements due to redistribution of the stresses and reduced localized stress concentrations (see mild slope in the stiffness-displacement curve (Fig. 4.23a). Fig. 4.23b illustrates the accumulated energy dissipated by the walls as a function of displacement. This energy dissipation is represented by the area under the force-displacement curve, as shown in Fig. 4.21b. The numerical results indicate that the macro-modeling approach exhibits a significantly higher rate of energy dissipation. This is because stiffness degradation and pinching effects are not accounted for, resulting in a larger loop area and consequently greater energy dissipation compared to the interface micro modeling approach.

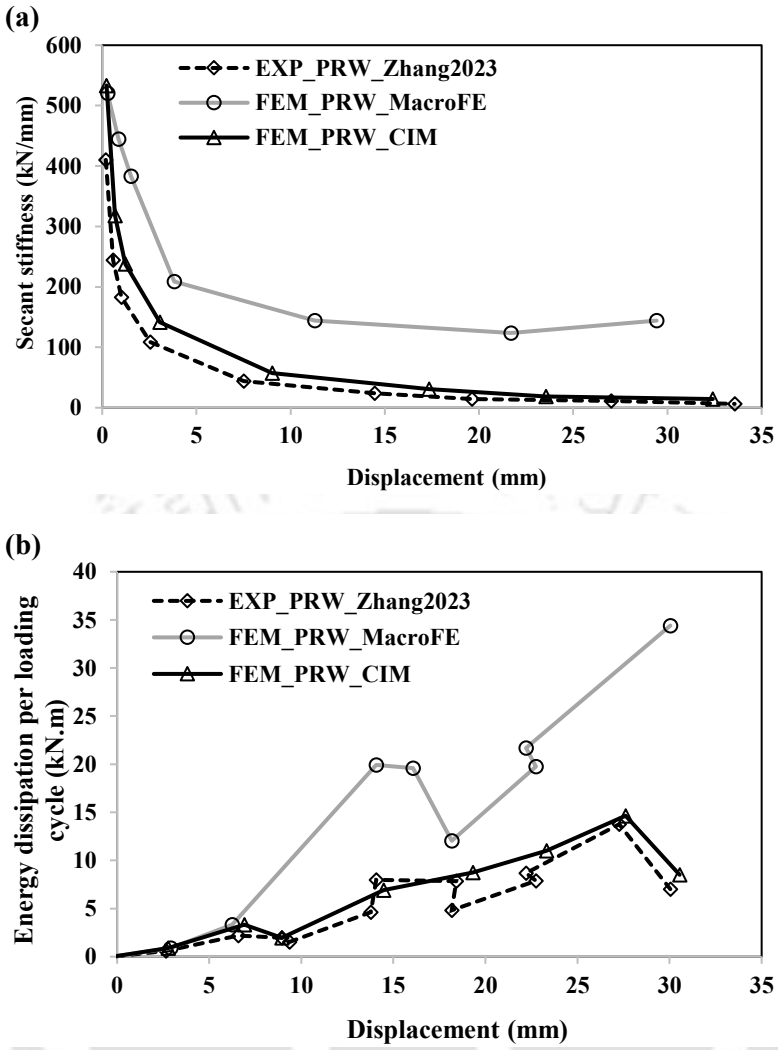

Fig. 4. 23. Comparison of different material model for computation of (a) secant stiffness; (b) energy dissipation capacity

It is clear from Fig. 4.23 that the anticipated secant stiffness and energy dissipation per loading cycle using the macro-modelling strategy are notably higher than the experimental values [6] at initial and final applied displacement amplitudes. However, both secant stiffness and energy dissipation capacity align well using the composite interface modelling (CIM) or micro modelling approach, thus highlighting the accurate prediction capability of the proposed model.

4.6. Effect of strain hardening material on seismic performance of 3DPC wall

The suggested cohesive model depends on a key parameter, i.e., the stiffness coefficient, which is calculated via experimentation to give as input in numerical model to predict the accurate response. The following section discusses an effective method for precisely

determining these cohesive model parameters. These interface elements allow disruptions in the displacement field and articulate their response through the correlation between tractions and relative displacements across the layer interface.

4.6.1. Description of the 3DPC lattice wall specimen and numerical model

In the proposed 3D finite element composite interface model, both the linear and non-linear behavior of the printed layers and interfaces are explicitly defined. Specifically, 3D hexahedral-shaped eight-node linear brick elements with reduced integration and hourglass control (type C3D8R) are employed to model the printed layers, top and bottom beam.

For the interfaces between printed layers, a surface-to-surface cohesive discretization approach is applied, utilizing finite sliding formulation. Whereas a surface-to-surface interaction is established to facilitate communication between the bottom and top layer of wall with bottom and top cast beam connected to the 3DPC lattice wall. For further information on cohesive discretization and the selected mesh size of 50 mm, see [5].

Encastre boundary condition was used to replicate the fixed-base conditions and loads on 3DPC lattice walls are applied in two steps (Fig. 4.24a): initially a pre-compression vertical stress of 0.5 MPa is applied which was kept constant during the test, and then the walls are subjected to horizontal in-plane cyclic loads under displacement control. The wall considered here, is subjected to 21 number of cycles [1] (Fig. 4.24c). Fig. 1b shows the cyclic load applied to the control node and the top surface of the top beam, respectively. All specimens underwent displacement-controlled cycle mode with 1 mm increment. A non-linear dynamic implicit procedure is followed, thus facilitating the pursuit of a quasi-static solution that iteratively resolves equilibrium at each increment.

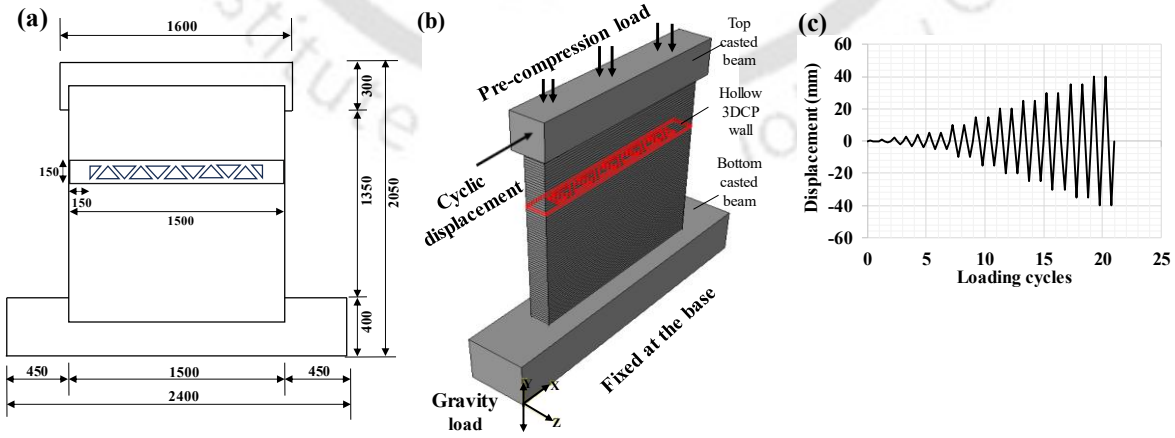

Fig. 4. 24. (a) Section detailing, (b) elevation and numerical loading setup of the 3DPC lattice wall, (c) cyclic loading protocol.

4.6.2. Material properties for modelling

The material properties of 3DPC are obtained from the testing of printed cubes of size 50 mm × 50 mm under uniaxial compression and split tensile. The compressive and split tensile strength were measured using a constant displacement control rate of 1 mm/min [6]. Total four type of materials are taken into consideration i.e., mortar (control, M), fiber reinforced mortar (FRM), concrete (mortar with aggregate, C) and fiber reinforced strain hardening concrete (FRSHC), where aggregate (5-9.5 mm) are added into the printing process between the printed layers by the weight % of mortar; as shown in Fig. 4.25. It was found out that by combination of 0.5% steel fiber with 15% dosage of aggregate (by weight % of printed mortar) specimen are showing strain hardening behavior with a strain hardening exponent of value 1.16 (Fig. 4.26).

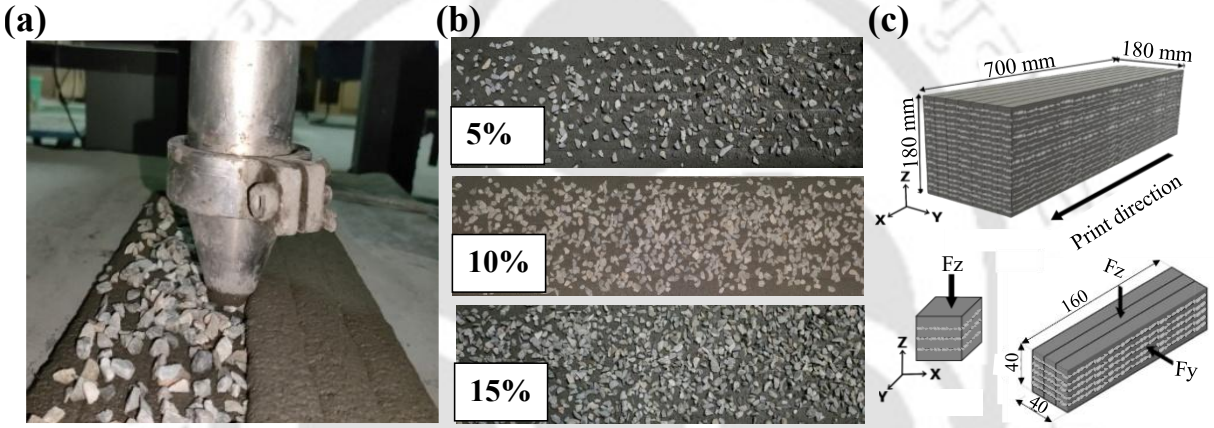

Fig. 4. 25. Process of adding aggregate during printing in 3D printable mortar (a) layer of 3D printable mortar after aggregate addition; (b) application of different dosage of aggregate on printed layer; (c) schematic of printed beams, extracted cubes and prisms

The material mix composition and average compressive, split tensile and direct tensile strength of all specimens normal to bed joint (which is the case of real loading scenario), is given in Table 4.5 and Fig. 4.26.

Table 4. 5. Mixture composition

Mix ID	Sand/ OPC Binder	Water/ binder	VMA (%)	SP (%)	Fiber (vol.%)	Coarse aggregate/ Sand
M	1	0.35	0.25	0.25	…	…
C	1	0.35	0.25	0.25	…	0.8
FRM	1	0.35	0.25	0.25	0.5	…
FRSHC	1	0.35	0.25	0.25	0.5	0.8

Abbreviation: VMA- Viscosity Modifying Admixture, SP- Superplasticizer, Sand: fine aggregates

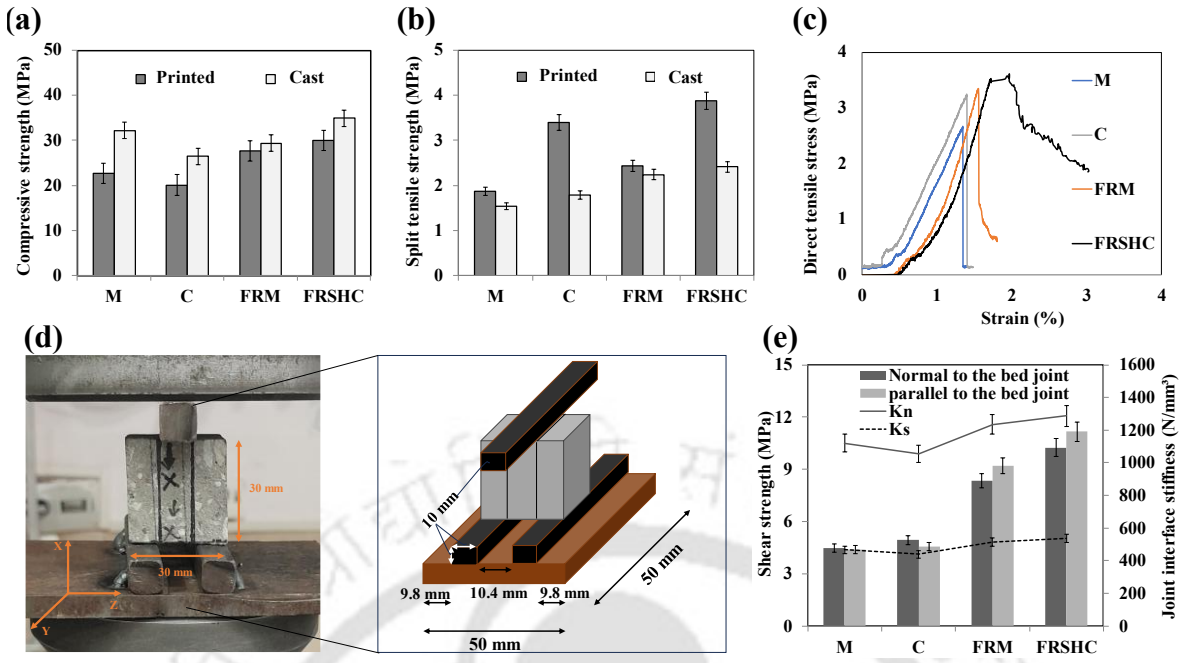

Fig. 4. 26. Mechanical strength of all specimens (a) compressive strength; (b) split tensile strength; (c) uniaxial direct tensile strength; (d) test set up for shear strength test of 3DPC layer triplet; (e) shear strength and stiffness of printed specimen

Experiment is also conducted on 3DPC shear triplets. 3DPC shear triplets are casted using three layers of printed mortar with 10 mm layer height and 30 mm layer width with 30 mm cube size as shown in Fig. 4.26. In plane shear strength was studied by applying compression along middle layer and supporting the two end layers (Fig. 4.26d). Testing of shear triplets help to estimate the shear strength of 3DPC layer joint. The strength and stiffness of the triplets are found significantly increased due to the presence of fibers and aggregate which enhances the bonding between the layers. All other parameters are detailed in Table 4.6, serves as input in ABAQUS to accurately capture the behavior of 3DPC lattice wall under quasi-static cyclic loading.

Table 4. 6. Material properties used in the numerical investigation of 3DPC lattice wall

Interface-based model		CDP model	
Young modulus, E_c (N/mm^2)	22404 (M), 21075 (C), 24716 (FRM), 25742 (FRSHC)	Ultimate compressive strength, f_{cm} (N/mm^2)	22.72 (M), 20.11 (C), 27.66 (FRM), 30 (FRSHC)
Poisson's ratio (ϑ)	0.2	Strain at peak stress, ε_{c1}	0.002 (M), 0.0022 (C), 0.0023 (FRM), 0.0028 (FRSHC)
Shear modulus, G_c (N/mm^2)	9335 (M), 8781 (C), 10298 (FRM), 10726 (FRSHC)	Yield stress (σ_{c0})	0.4 f_{cm}
Normal joint stiffness, K_n (N/mm^3)	Fig. 2e	Compression and tension damage parameter (d_c and d_t)	$0 < d_c < 0.98$; $0 < d_t < 0.59$
Shear and tangential joint stiffness, $K_s = K_t$ (N/mm^3)	Fig. 2e	Density (N/mm^3)	22404 (M), 21075 (C), 24716 (FRM), 25742 (FRSHC)
Layer thickness, t_c (mm)	10	Dilation angle (degree)	35^0
Coefficient of friction (μ)	0.75	Viscosity parameter Eccentricity	0.00001 0.1

4.6.3. Results and discussion

The performance of concrete walls hinges primarily on their aspect ratio (AR). Medium- to high-rise walls tend to flex, while low-rise walls are primarily influenced by shear deformations. Previous tests on shear walls have revealed that their nonlinear response varies due to factors like wall geometry, precompression load, boundary conditions, and interaction between connected elements. AR emerges as a pivotal parameter affecting wall behavior under cyclic loading. An effective analytical model should accurately predict both the monotonic capacity of the wall and its behavior under reversed cyclic loading. The micro model proposed in the beginning of this chapter excels in capturing specific phenomena such as concrete cracking, tension stiffening, and strength degradation with cyclic loading—factors typically overlooked in simpler macro models.

4.6.3.1. Flexure wall

The load bearing concrete walls which resist the applied loads primarily through flexure or bending are referred as flexure specimens. The specimens which have AR more than or equal to two can be termed as flexure specimens. Flexural specimens with a height of 1500 mm and width of 750 mm (h/w = 2) are considered under the current investigation. The loads are applied on the top of wall. In case of M, C, and FRM, the lateral load resistance linearly increases up to displacement of 10 mm with vertical compression of 0.55 MPa but after that there is noticeable decrease in ultimate strength can be observed beyond 10 mm displacement except FRSHC, due to its strain hardening properties. The ultimate lateral strength of FRSHC specimen is 88.83%, 59.02%, and 28.9% higher than M, C, and FRM, respectively (Fig. 4.27a).

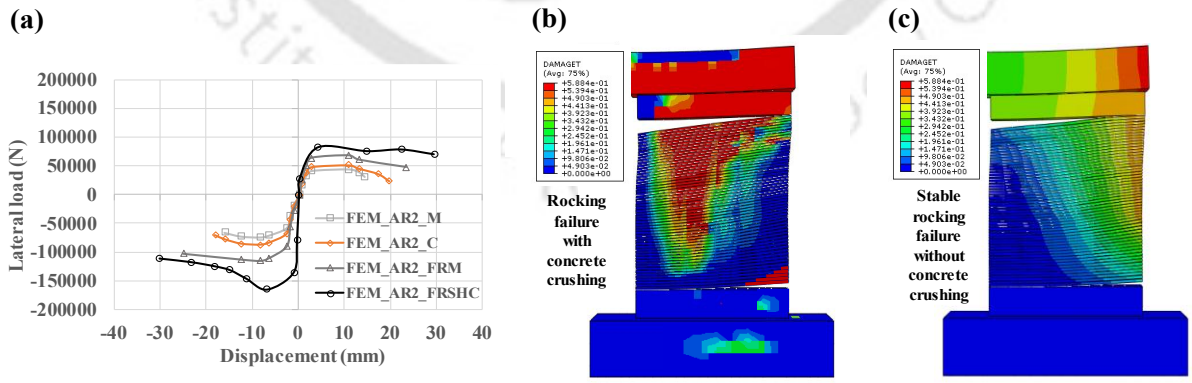

Fig. 4. 27. Effect of walls material property on 3DPC lattice flexure wall (a) cyclic in plane strength, and failure mode of 3DPC lattice wall; (b) M; (c) FRSHC

The flexural specimen except FRSHC, failed through crushing of the bottom layer when the compressive strength was attained at the toe portions of the specimen. The ultimate loading

capacity and deformation capability of FRSHC is found to be slightly improved (Fig. 4.27b) since the strain hardening concrete reduces the rigid body rotations around the wall's toe due to its higher stability and compressive strength, which ultimately neglects the crushing and experienced a more stable rocking failure making it stable to take further displacement.

4.6.3.2. Shear wall

In load bearing concrete shear specimen, the load transfer is primarily through shearing deformation and not by bending. Shear specimens have very low AR, normally lesser than or equal to one. The behavior of shear specimen with an AR (h/w = 0.75 i.e., with a height of 1500 mm and width of 2000 mm) under both vertical compression of 0.55 MPa and quasi-static cyclic loading is studied. The partial strut action along the compression diagonal is observed in both i.e., M and FRSHC the shear specimen. Significant improvement in the ultimate capacity with a strength increment of 127.27%, 108.33%, and 38.89% is observed when FRSHC compared with M, C, and FRM, as shown in Fig. 4.28. From Fig. 4.28b, it can be observed that specimen M experienced overturning with maximum displacement of 17 mm due to its lesser compressive strength and lesser interface stiffness. FRSHC specimen with strain hardening concrete has curtailed toppling and sliding at the interface, avoiding catastrophic failure, as depicted in Fig. 4.28c.

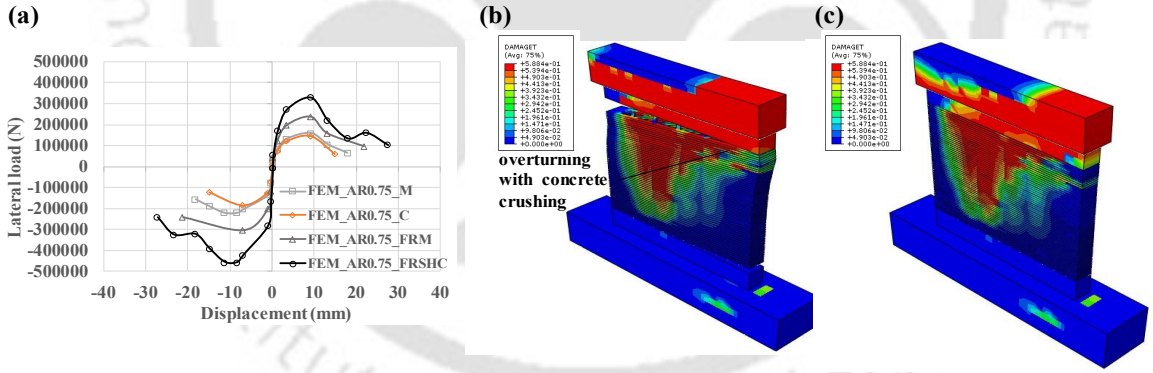

Fig. 4. 28. Effect of walls material property on 3DPC lattice shear wall (a) cyclic in plane strength, and failure mode of 3DPC lattice wall; (b) M; (c) FRSHC

In case of both the 3DPC lattice wall i.e., shear wall and flexure wall, with strain hardening concrete (FRSHC) the ultimate lateral displacement capacity has been increased with an increment of 53.42% and 105.33%, respectively, when compared to M specimen. In both the flexural and shear wall improvement from FRM to FRSHC is 28.9% and 38.89%, respectively, due to the agglomeration of aggregate and fibers.

4.7. Summary

This chapter focuses on the numerical investigation of 3DPC walls subjected to quasi-static cyclic loading through a validated composite interface micro-model. The key highlights and findings are summarized as follows:

i. **Development of a composite interface micro-model:** A robust finite element-based micro-model integrating CDP and CZM is developed to simulate the in-plane cyclic behavior of 3DPC walls, accounting for interlayer effects and localized failure mechanisms inherent to the printing process.

ii. **Model validation:** The proposed model accurately replicates experimental hysteresis loops, stiffness degradation, and energy dissipation trends for both 3D printed and cast concrete walls under cyclic loading, demonstrating its superiority over conventional macro-modeling approaches.

iii. **Parametric investigation:** Extensive numerical simulations are performed to analyze the influence of edge column dimensions, wall aspect ratio, reinforcement bar length, material strength, and pre-compression load on wall behavior.
    a. Increasing edge column size (150×150 mm to 250×250 mm) enhances lateral load capacity by 56% and deformation tolerance by 10%.
    b. Extending reinforcement bar length and increasing material strength significantly improve ultimate load capacity and structural performance.
    c. Increasing the aspect ratio reduces lateral strength by approximately 71%, indicating lower stiffness and stability.

iv. **Performance of strain-hardening concrete:** The strain-hardening concrete (FRSHC) enhanced the deformability and strength of the 3DPC lattice shear wall by 127.27%, 108.33%, and 38.89%, and the 3DPC flexure wall by 88.83%, 59.02%, and 28.9% compared to mortar (M), concrete (C), and fiber-reinforced mortar (FRM) under cyclic loading.

The developed composite micro-model provides a computationally efficient and realistic tool for predicting 3DPC wall behavior under cyclic loads. It effectively bridges the gap between material-scale advancements and structural-scale performance, enabling performance-based seismic design and optimization of 3D printed systems.

Chapter 5

Structural characterization and codal-based design framework for seismic-resistant 3D printed concrete walls

*This chapter focuses on the structural characterization and codal-based design of 3DPC walls subjected to cyclic in-plane loading. A preliminary framework based on ACI 318-19, Eurocode 8, IS 13920:2016 is assessed for applicability to 3DPC, while various reinforcement strategies—including single-layer, double-layer, self-centering, and confined boundary configurations—are evaluated. Numerical simulations capture the cyclic in-plane response of 3DPC walls, incorporating interlayer bonding, material anisotropy, and reinforcement interactions. The work builds upon the outcomes of the numerical validation studies (Chapter 4), extending them to component-level applications, and offering guidelines for future standardization in earthquake-resistant wall design.

*A portion of this chapter has been published in:

1. **Warsi SBF**, Panda B, Biswas P. Design of earthquake-resistant 3D printed concrete wall based on ACI 318–19: Analytical investigation and numerical modelling. Structures 2025, p. 109371. https://doi.org/10.1016/j.istruc.2025.109371.
2. **Warsi SBF**, Panda B, Biswas P. Numerical evaluation of the seismic performance of self-centering 3D printed concrete wall. **10th International Conference on Computational Methods in Structural Dynamics and Earthquake Engineering**, 2025 (Accepted).
3. **Warsi SBF**, Panda B, Biswas P. 3D Finite Element Analysis on the Effects of Boundary Elements Confinement on Cyclic Performance of 3D Printed Concrete Wall. **1st RILEM Youth Symposium**, 2025 (Accepted).

5.1. Introduction

With 3DPC technology extending to structurally critical applications, such as load-bearing walls [95,104,106] and earthquake-resistant systems [6,111], establishing design standards becomes essential for widespread and reliable implementation. Codal guidelines tailored to the unique behaviors and requirements of 3DPC walls hold immense potential to accurately assess lateral and vertical load capacities, advancing beyond reliance on testing-based validation alone. Salet et al. [224] have made remarkable contributions to the field through pioneering projects such as the world's first 3D-printed bridge, demonstrating the feasibility of the "Design by Testing" approach. However, such methods require significant resources and may not yet be practical for widespread application in mainstream construction. In this regard, adapting existing codal provisions for 3DPC walls is essential to simplify design and construction processes while maintaining safety, particularly under seismic loading. In the existing literature [143,225,226], it is often assumed that the structural responses of 3DPC walls are qualitatively aligned with those of traditional masonry walls. However, this assumption lacks justification in various scenarios. Key factors such as tensile cracking strength, dowel action in vertical reinforcement, and truss action in flexural and shear reinforcement exhibit distinctive behaviors in 3DPC walls that differ from those in masonry or pre-cast systems. Specifically, the unique material properties and construction techniques employed in 3DPC lead to variations in load distribution and failure mechanisms, which may not be adequately represented by conventional assumptions. Therefore, a detailed examination of these factors is essential to understand the actual performance characteristics of 3DPC walls under cyclic loading conditions to address both structural feasibility and practicality in earthquake-resistant 3DPC wall design.

This chapter focuses on the characterization of the cyclic in-plane response of 3DPC structural walls through analytical and numerical investigations, aligning the design approach with the American Concrete Institute ACI 318-19 [11], Eurocode 8 [12], and IS 13920-2016 [13] provisions. Preliminary design is carried out based on existing RC wall design guidelines, followed by an assessment of their applicability to 3DPC configurations. Reinforcement strategies, including single-layer and double-layer are evaluated to identify practical and structurally efficient solutions compatible with the 3D printing process. Comparative analysis of single- and double-layer reinforcement systems under quasi-static cyclic loading shows that the double-layer configuration achieves 30.6% higher lateral load capacity (465.72 kN vs. 356 kN), 9.8% greater failure displacement, a higher ductility factor (4.36 vs. 4.01), and superior energy dissipation. The single-layer reinforcement, while lower in strength, maintains

comparable stiffness, reduces strain concentrations, and offers easier integration in 3DPC construction. To further enhance seismic performance, self-centering reinforcement and confined boundary reinforcement (CBRF) are incorporated following codal guidelines, resulting in lateral strength gains of 54.08% and 46.89%, along with improved stability and damage tolerance. Overall, this chapter establishes a robust codal-based design framework for 3DPC walls and demonstrates that realistic simulation of their cyclic response is achievable through advanced finite element micro-modeling. This modeling approach successfully bridges material-scale behavior with structural-scale performance, enabling the development of practical, lightweight, and earthquake-resistant 3DPC systems suitable for large-scale construction.

5.2. Principles for structural wall design

The structural walls are designed according to ACI 318:19 [11] provisions to resist earthquake motions through ductile inelastic response of particular which vary with wall layout and aspect ratio. A good design anticipates the inelastic mechanism and provides proportions and details in the wall that will enable it to respond as intended. The following sections summarize the key principles for the design of structural walls. Detailed design of the structural 3DPC wall is presented in the upcoming section.

For example slender walls (Hight (h_w)/ length (l_w) $\geq$ 2.0)) tend to behave much like flexural cantilevers. The preferred inelastic behavior mode of slender walls is ductile flexural yielding, without shear failure. In contrast, walls with very low aspect ratios ($h_w/l_w \leq 0.5$) tend to resist lateral forces through a diagonal strut mechanism and basically three types of deformation (as shown in Fig. 5.1) can be seen in case of squat wall components: flexure, shear, and sliding. The wall behavior transitions between these extremes for intermediate aspect ratios. Shear yielding of very squat walls is often accepted [227] because such walls exhibit high inherent strength and low ductility demands (Fig. 5.1d), while shear yielding of slender walls is not acceptable because it reduces inelastic deformation capacity below expected values. Reinforcement for structural walls includes distributed web reinforcement and concentrated vertical reinforcement at the wall boundaries.

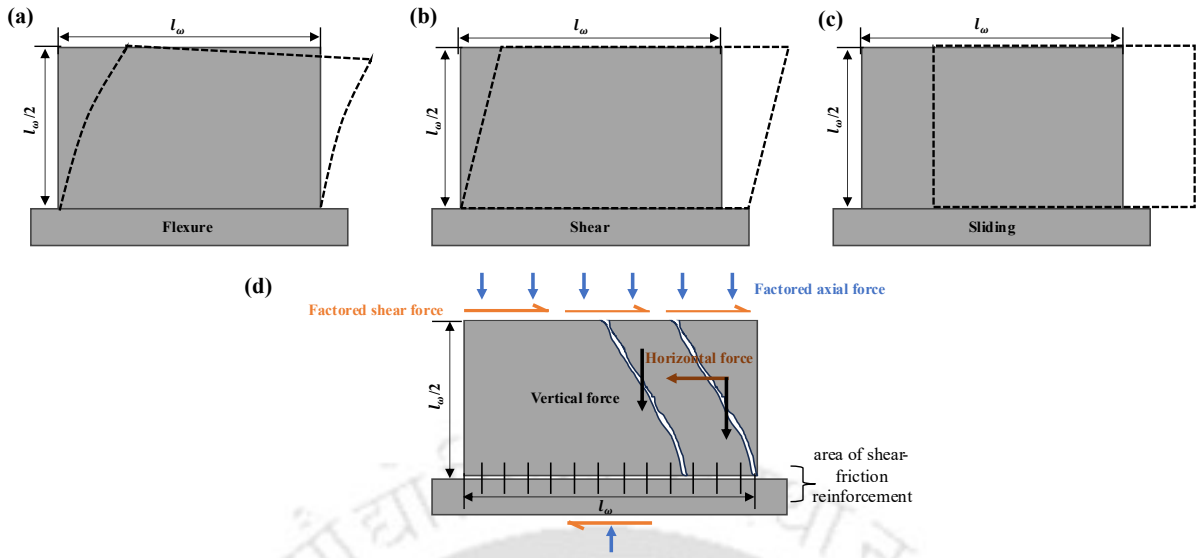

Fig. 5. 1. Mode of failure in squat wall ($h_w/l_w \leq 0.5$) (a) flexure; (b) shear; (c) sliding; (d) shear yielding and shear sliding in a RC squat wall [227]

ASCE 7 [228] mandates that the structural wall containing web reinforcement and concentrated vertical reinforcement at the wall boundaries should be designed to meet strength and drift requirements, as per the loading and the type of system used. Structural walls are designed alongside moment-resisting frames to enhance lateral strength and deformability. Depending on the system's characteristics, walls can be designed to respond either elastically or in a nonlinear manner. For scenarios requiring an elastic response, seismic design forces are amplified to account for the absence of inelastic energy dissipation. In other scenarios, non-linear design allows for economic solutions by reducing seismic forces and overturning moments.

5.3. 3DPC structural wall design based on codal provisions

The following section presents an structured approach for assessing the seismic performance of 3DPC walls by adapting ACI 318-19 [11] provisions, and relevant considerations from Eurocode 8 [12] for ductile detailing. While ACI 318 is traditionally applied to conventional RC structures, this chapter explores its applicability to 3DPC walls. To achieve this, relevant sections of ACI 318, particularly those governing reinforcement detailing, load-bearing capacity, and shear and flexural behavior, are carefully interpreted to align with 3DPC's distinctive structural responses. Specific adaptations are made to address 3DPC's unique load distribution patterns and reinforcement integration challenges, especially in hollow wall configurations.

The analytical framework considers various constant parameters—such as reinforcement ratio, concrete compressive strength, axial and lateral loads, and slenderness and aspect ratios—to construct models that reflect realistic loading and boundary conditions. This approach evaluates the extent to which traditional ACI provisions meet the demands of earthquake-resistant 3DPC structures and identifies areas requiring modification or supplementary design considerations, offering insights into potential adaptations of ACI 318 for future codification in 3DPC applications.

5.3.1. Design methodology for 3DPC walls with ACI 318:19, Eurocode 8, IS 13920-16

This adaptation process involves critical evaluations, including checks for minimum reinforcement, flexural strength, shear resistance, and axial capacity to ensure 3DPC structural wall can withstand applied loads and perform reliably under seismic and other complex loading conditions.

5.3.1.1. Comprehensive strategy for analyzing 3DPC walls

Two walls are designed and numerical performance is investigated subjected to cyclic in-plane loading with pre-axial compression. As shown in Table 5.1, the dimensions of the designed walls are presented. The aspect ratio (h_w/l_w) and slenderness ratio (h_w/t_w) of the designed walls are kept constant, as 1.0 and 8, respectively, in line with ACI 318-19 design guidelines [11]. Two types of reinforcement arrangements i.e., single layer or double layers are chosen. To investigate the effects of reinforcement detailing on 3DPC structural walls and to compare their in-plane cyclic behaviour, a constant reinforcement ratio of 0.25% (vertically and horizontally) is maintained in the designed walls. In addition, as part of simulation, the walls are subjected to a pre-compression stress of 1.3 MPa. This stress level is equivalent to approximately 5% of the axial section capacity, which is applied in conjunction with the specific concrete strength and cross-sectional area of the walls.

The design of 3DPC structural walls adheres to minimum vertical and horizontal reinforcement criteria, specified as 0.25% with spacing requirements of 250 mm and 200 mm, respectively, in accordance with ACI 318-19. The primary governing load combination applied is Load and Resistance Factor Design (LRFD) combination [11], and the analysis addresses the flexural (F_d), shear (S_d), and axial demands (P_d) on the walls, which can be found through Eq. (5.1):

$$F_d = S_d = P_d = 1.0D + 1.0E \tag{5.1}$$

where D is the dead load or self -weight of the wall, E is the seismic load.

Flexural capacity

The flexural capacity of the 3DPC wall, is measured by calculating the neutral axis (n.a.) depth, which depends on parameters: the beta (β), omega (ω), and alpha (α) factor. The value of these parameters can be derived using Eq. (5.2), Eq. (5.3), and Fig. 5.2.

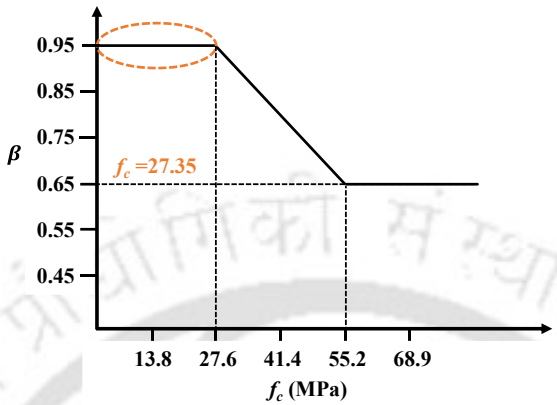

Fig. 5. 2. Beta value verses concrete characteristics strength [11]

Omega facor (ω) for n.a. determination [11]:

$$\omega = \rho_l \frac{f_y}{f_c} \tag{5.2}$$

$$c = \left(\frac{\alpha + \omega}{0.85\beta + 2\omega}\right).l_w \tag{5.3}$$

α factor value (for n.a. equation, when wall is under compression) = 0.02

According to the codal provision the effective flexural depth (d) is approximately equal to $0.8l_w$ (ACI 318-19 (11.5.4.2)).

The nominal flexural strength can be found through Eq. (5.4) and Fig. 5.3a.

$$M_n = T.\left[\frac{l_w}{2}\right] + P_d.\left[\frac{l_w - c}{l_w}\right] \tag{5.4}$$

where P_d is the design axial compressive strength, T is the total tensile component of force couple during bending (Eq. (5.5)) and A_{st} is the total area of vertical reinforcement (Eq. (5.6)):

$$T = A_{st} \times f_y \left[\frac{l_w - c}{l_w}\right] \tag{5.5}$$

$$A_{st} = A_{st,V} \frac{l_w}{s_{provided}} \tag{5.6}$$

The design flexural strength can be calculated according to the given Eq. (5.7):

$$M_d = \phi M_n \tag{5.7}$$

where ϕ is the factor which can be calculated according to the Fig. 3b. The strain denoted as ε_1 in Fig. 5.3(b) represents the tensile strain in the extreme tension reinforcement fiber at the section under consideration. This value is used in accordance with ACI 318 provisions to determine whether a section is compression-controlled, tension-controlled, or within the transition zone.

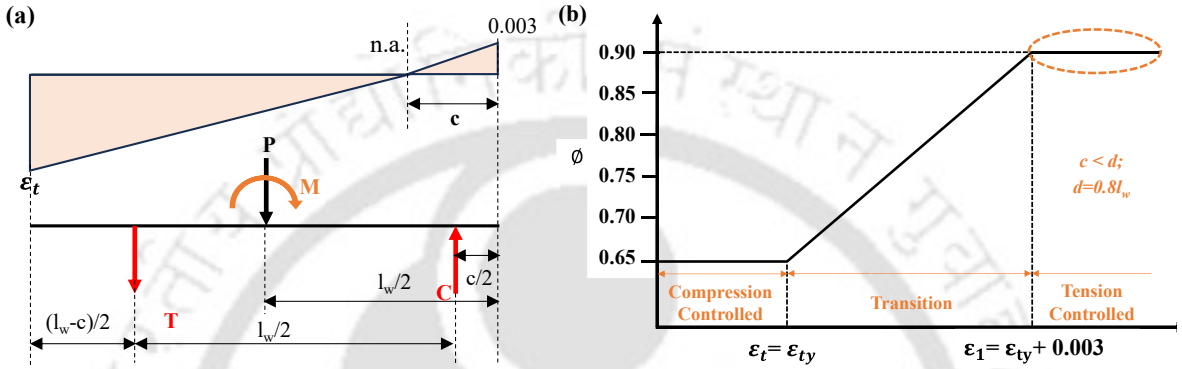

Fig. 5. 3. (a) Nominal flexural strength determination; (b) ϕ value to determine the controlled section [11]

While Eqs. (5.4) to (5.7) are conventionally derived for solid sections, their applicability to hollow sections remains valid in this investigation due to the dependence of the governing parameters—such as the neutral axis depth (c), total tensile force (T), and axial compressive strength (P_d), material properties (f_y, f_c), wall length (l_w), and reinforcement layout, rather than the presence of solid or void regions. The strain distribution and internal force equilibrium assumptions remain applicable, as illustrated in Fig. 5.3a. The critical factor ϕ, shown in Fig. 5.3b, is determined based on strain compatibility and section control (tension or compression), which are also unaffected by the presence of a hollow core when reinforcement is placed in the boundary elements. Thus, the equations retain their relevance and accuracy for the hollow wall sections considered in this investigation.

Shear capacity

Observations from previous studies [226] reveal that shear failure frequently occurs in boundary elements, largely because these elements are not always designed to address shear demands comprehensively. Consequently, it becomes essential to carefully define boundary elements, ensuring they meet shear requirements through appropriate detailing. As ACI 318-19 provides limited guidance on ductile detailing for boundary elements, Eurocode 8 is referenced to supplement these specifications. Eurocode 8 classifies ductility requirements based on seismic hazards into three categories:

a. *DCL (Low):* Recommended for regions with low seismic activity.

b. *DCM (Medium):* Suitable for areas with moderate seismic hazards.

c. *DCH (High):* Essential for high seismic risk areas.

In seismic-prone regions, DCM or DCH classifications are preferable for structural walls, enhancing energy dissipation and minimizing the risk of brittle failure. For ductile walls in seismic zones, Eurocode 8 stipulates that the maximum spacing of transverse reinforcement in confined zones be limited to the smallest of the following:

a. 0.25 times the wall thickness (t_w),

b. 8 times the longitudinal reinforcement diameter, or

c. 200 mm.

With boundary or confined zone elements defined in accordance with Eurocode 8, the analysis then reverts to ACI 318-19 to determine the nominal in-plane shear strength (ACI 318-19 Section 11.5.4.3), as calculated by Eq. (5.8):

$$V_n = (\alpha_c . \lambda \sqrt{f_c} + \rho_t f_y) A_{cv} \tag{5.8}$$

where α_c is the coefficient defining the relative contribution of concrete strength to nominal wall shear strength. Since $h_w/l_w = 1 \leq 1.5$; wall is in compression, therefore $\alpha_c = 3$ (ACI 318-19 (11.5.4.3)). A_{cv} is gross area of concrete section bounded by web thickness and length of section in the direction of shear force considered (given by Eq. (5.9)):

$$A_{cv} = t_w . l_w \tag{5.9}$$

The design shear strength can be calculated according the given Eq. (5.10):

$$V_d = \phi_v V_n \tag{5.10}$$

where ϕ_v is the strength reduction factor for shear:

$$\phi_v = 0.75 \; (ACI\ 318 - 19\ Table\ 21.2.1(b))$$

Axial capacity

Since 3DPC wall is non-prestressed conforming to ACI 318:19 (22.4.2.4), the nominal axial capacity of the wall can be calculated by Eq. (5.11):

$$P_n = 0.8 \times P_o \tag{5.11}$$

where P_o is the axial compressive strength (ACI 318-19 Eq. (22.4.2.2)), given by Eq. (5.12):

$$P_o = \left(0.85.f_{c\prime}.\left(A_g - A_{st}\right) + f_y.A_{st}\right) \quad (5.12)$$

The design axial compressive strength can be calculated according to the given Eq. (5.13):

$$P_d = \phi_c P_n \quad (5.13)$$

where ϕ_c is the strength reduction factor for compression-controlled member with ties conforming to 22.4.2.4:

$\phi_c = 0.65$ (as per ACI 318)

5.3.2. Reinforcement detailing of designed 3DPC walls

In this section, the reinforcement detailing of the designed structural 3DPC walls are presented in Fig. 5.4, which illustrates the structural reinforcement configurations as designed in accordance with ACI 318:19 and Eurocode 8. Following the design process, the reinforcement layout is finalized to analyze structural performance and load distribution. The reinforcement ratio, concrete strength, axial load, aspect ratio, and slenderness ratio of the both walls are kept constant to compare the effect of both the reinforcement strategy solely.

The selection of reinforcement spacing, infill pattern, and layer thickness in this chapter is based on established design codes and practical constraints of 3D concrete printing. Specifically, the transverse reinforcement spacing adheres to Eurocode 8 (EN 1998-1, Section 5.4.3.5.2) [12], which stipulates that the maximum horizontal reinforcement spacing in seismic zones should not exceed 300 mm or 0.75 times the wall thickness, whichever is smaller. For a wall thickness of 250 mm, this limit equates to 180 mm (also based on minimum reinforcement ratio of 0.25%). Transverse reinforcement spacings of 125 mm and 160 mm are used for single- and double-layer configurations, respectively (Fig. 5.4 and Table 5.1)—both well within the code-defined limits, thereby ensuring adequate confinement and ductility under cyclic loading. The chosen truss-type infill pattern is based on recent findings by Dey et al. [229], who demonstrated that this configuration enhances bending capacity while allowing for controlled deformation, making it well-suited for seismic applications. The layer thickness is selected in accordance with realistic 3D concrete printing constraints. Specifically, a minimum of 40 mm layer thickness is necessary in compliance with the new ISO/ASTM52939:2023 [230], to accommodate reinforcement placement and maintain interlayer bonding integrity. Consequently, the geometric and structural parameters of all wall configurations are designed to reflect practical construction feasibility while ensuring compliance with seismic design

standards, following a rational selection approach similar to that outlined by Forcellini et al. [231] in their seismic fragility assessment framework.

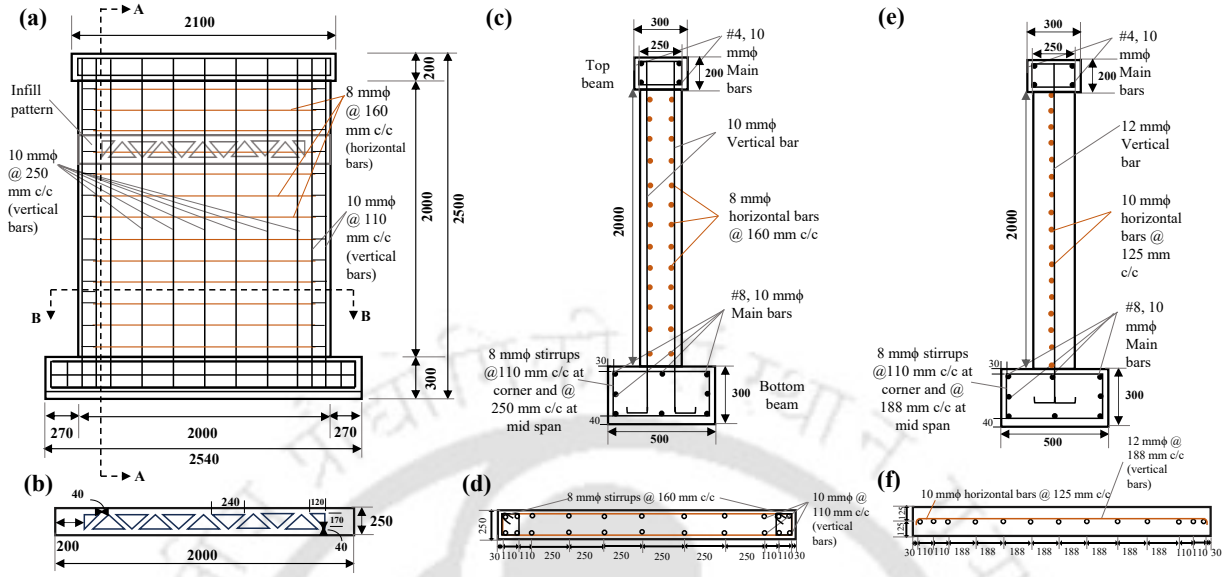

Fig. 5. 4. Reinforcement details of the structural 3DPC wall (a) elevation; (b) cross-sectional infill geometry; (c) cross-section detailing of double layer reinforced wall (c) along A-A; (d) along B-B; (e) cross-section detailing of single layer reinforced wall (e) along A-A; (f) along B-B (all dimensions are in mm)

Table 5.1 provides an overview of the geometric properties and reinforcement detailing of the 3DPC walls. Reinforcement detailing values outline bar diameters, spacing, and placement as determined by the combined ACI 318:19 and Eurocode 8 provisions.

Table 5. 1. Description of designed 3DPC walls

Wall properties	In M.K.S	In F.P.S
Wall thickness (t_w)	250 mm	9.84 in
Wall length (l_w)	2500 mm	98.43 in
Wall height (h_w)	2500 mm	98.43 in
For double reinforcement layer:		
Vertical reinforcement: 10 mm dia bars at 250 mm on centers in each face (As, vertical = 10 mmØ @ 250 c/c)		
Horizontal reinforcement: 8 mm dia bars at 160 mm on centers in each face (As, horizontal = 8 mmØ @ 160 c/c)		
For single reinforcement layer:		
Vertical reinforcement: 12 mm dia bars at 180 mm on centers in each face (As, vertical = 12 mmØ @ 180 c/c)		
Horizontal reinforcement: 10 mm dia bars at 125 mm on centers in each face (As, horizontal = 10 mmØ @ 125 c/c)		

5.4. Numerical modelling framework

The numerical modelling framework employed in this section follows the same material modelling approach as detailed in Chapter 4, Section 4.2, ensuring consistency in the

representation of the mechanical behavior of 3D printed concrete under cyclic loading conditions.

5.4.1. Calibration of material models

Considering that concrete in the 3DPC wall experiences both compressive and tensile stresses, the Concrete Damage Plasticity model is employed incorporating damage characteristics. The comprehensive stress-strain response of 3DPC under compression and tension, and reinforcements are depicted in Fig. 5.5. All other parameters are detailed in Table 5.2, serves as input in ABAQUS FEM package to accurately capture the behaviour of 3DPC wall reinforced with single and double layer of reinforcemnt with the provisions of ACI 318 [11] and Eurocode 8 [12] under quasi-static cyclic loading conditions.

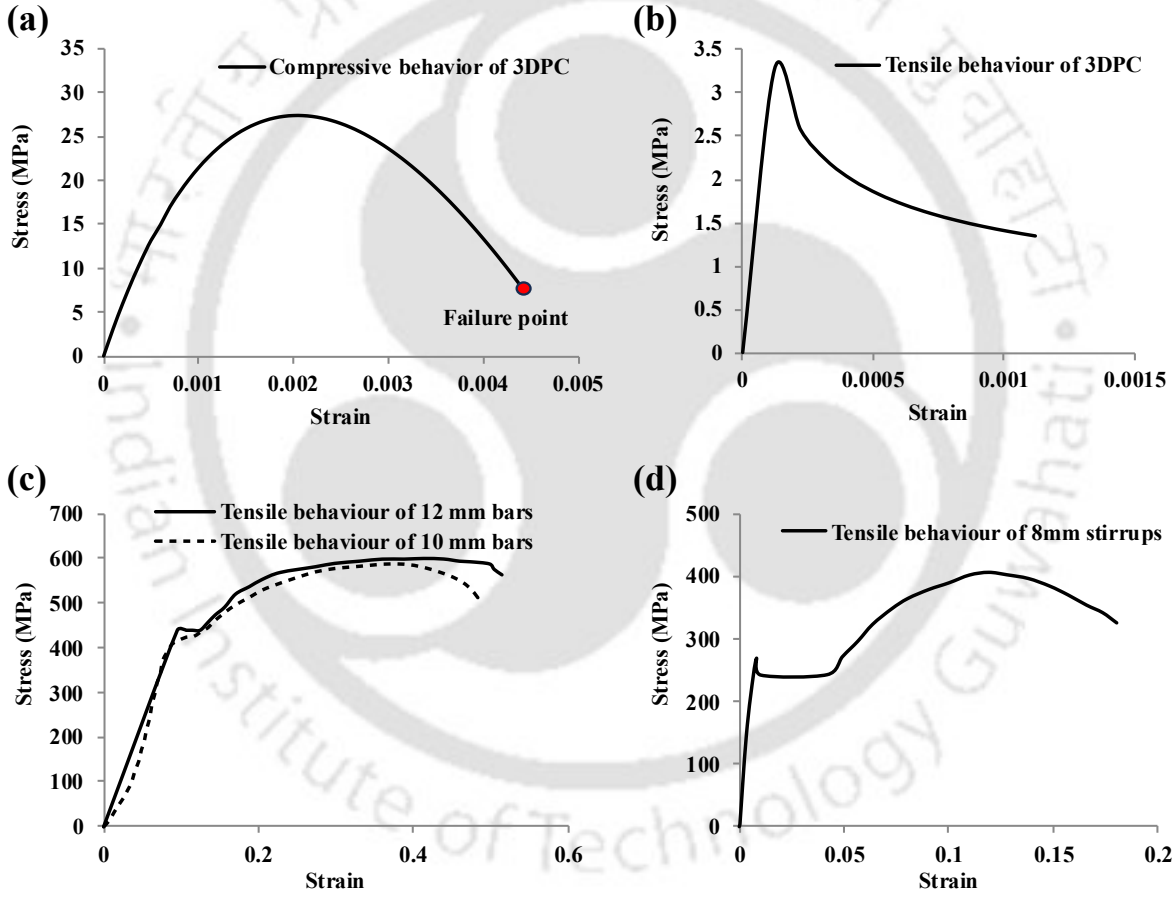

Fig. 5. 5. Stress-strain properties: (a) compressive behaviour of 3DPC; (b) tensile behaviour of 3DPC; (c) tensile behaviour of 12 mm and 10 mm main reinforcement bars; (d) tensile behaviour of 8 mm stirrups

The input for numerical models are partly obtained from experimental data, and a complete stress strain response have been produced and some values are assumed based on pertinent information available in the literature (Table 5.2). The average cubic compressive strength of 3DPC tested at 28 days was 34.19 MPa. However, design codes often rely on compressive

strength of the Φ150 cylinders and therefore, as per Eurocode 2 [213], a constant value of 0.8 has been adopted here to determine the cylindrical compressive strength of the material [216,217].

The complete stress-strain response of the reinforcemnet bars are given by Fig. 5.5c,d. The Poisson's ratio (ϑ) is presumed to be *0.2*, aligning with prior studies [107]. For the layer interface, the cohesion value (c) is established at 0.6 N/mm² in line with experimental findings [218]. The shear fracture energy is set at 0.6 N/mm, in accordance with the recommended range provided in [201]. The coefficient of friction is assumed to be 0.75, as mentioned in earlier studies [205]. The material parameters utilized in the simulation are detailed in Table 5.2.

Table 5. 2. Input parameters used for the numerial simulation

Interface-based model		Concrete Damage Plasticity model	
Young modulus of 3DPC, E_c (N/mm^2)	35670	Ultimate compressive stress of 3DPC, f_{cm} (N/mm^2)	27.35
Poisson ratio, ϑ	0.2 [107]	Strain at peak stress, ε_{c1}	0.0022
Shear modulus of 3DPC, G_c (N/mm^2) (Calculated by $E=2G(1+\vartheta)$)	10243.33	k (Calculated from Eq. 18)	2.32
layer thickness, t_c (mm) as per assumption	15	Compressive yield stress of 3DPC, σ_{c0} ($0.4f_{cm}$) (N/mm^2)	14.4
Normal interface elastic stiffness, K_n (N/mm^3) (Calculated from Eq. 4.5))	1639	Density (N/mm^3)	21000 [6]
Tangential interface elastic stiffness, $K_s = K_t$ (N/mm^3) (Calculated from Eq. 4.5))	683, 683	Dilation Angle (degree)	35^0 [211]
Specific fracture toughness for Mode I, G_{IC} (N/mm) (Calculated from Eq. 4.8))	0.29	Flow potential eccentricity	0.1 [204]
Specific fracture toughness for Mode II and III, G_{IIC}, G_{IIIC} (N/mm) (Calculated from Eq. 4.8))	0.6, 0.6	Ratio of biaxial compressive yield stress to uniaxial compressive yield stress (f_{b0}/f_{c0})	1.16 [211]
Friction coefficient	0.75 [205]	Ratio between second stress invarient on the tensile meridian and that on the compressive meridian, K	0.67 [204]
		Viscosity parameter	0.00001 [232]

5.4.2. Description of the numerical model: wall geometry, boundary conditions, meshing and loading protocol

In 3D finite element composite interface model, the linear and non-linear behaviors of the printed layers and interfaces are explicitly defined. The model employs 3D hexahedral-shaped eight-node linear brick elements with reduced integration and hourglass control (type C3D8R) to represent the cast beams and 3DPC layers. Enhanced hourglass control is activated to prevent zero-energy deformation of the linear hexahedral element under bending due to the selected reduced integration. Steel reinforcing bars are represented using the wire feature, associated with three-dimensional truss elements with two nodes (T3D2).

For the interfaces between printed layers, a surface-to-surface discretization method is applied, incorporating cohesive interaction in the interaction property manager and utilizing a finite sliding formulation (Fig. 5.6b). Embedded body constraints are employed to facilitate load

transfer and ensure proper bonding between the steel reinforcement and the 3DPC matrix. This constraint ensures that the reinforcement nodes exhibit identical displacement to the surrounding concrete nodes.

Based on the comprehensive sensitivity analysis in chapter 4, Section 4.3, a mesh size of 50 mm and a viscosity parameter of 0.00001 are selected for all subsequent simulations to strike a balance between numerical accuracy and computational efficiency. The analysis is conducted using the Abaqus dynamic-implicit solver in three steps: initial, gravity and pre-compression, and in-plane cyclic loading. The initial step initializes the boundary conditions with the bottom surface of the foundation beam fixed using the encastre boundary condition, which are mandatory and default for all analyses. In the subsequent step, gravity load and pre-compression load are applied (Fig. 5.6). Finally, in-plane cyclic displacement-controlled loading [6] is applied at the cross-sectional center of the top beam (Fig. 5.6a,c).

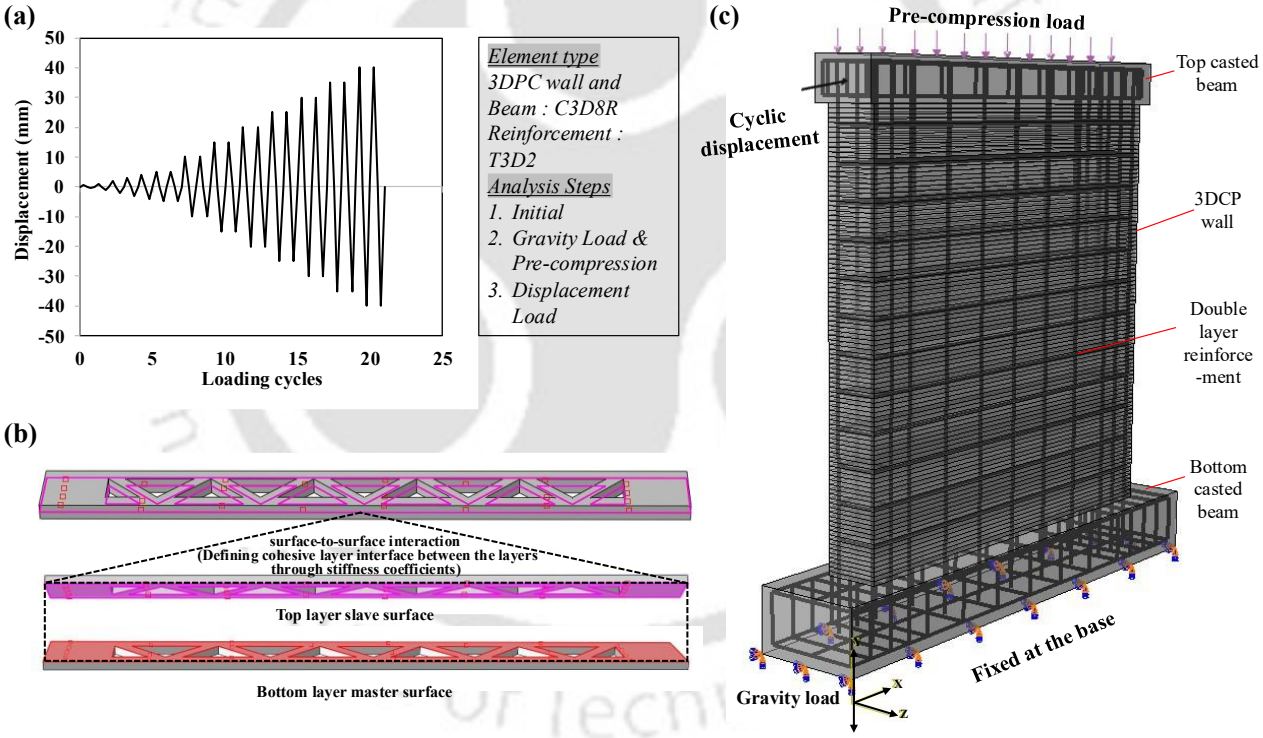

Fig. 5. 6. Cyclic loading protocol [6]; (b) interaction between the 3DPC layers (e) 3DPC wall configuration and numerical loading setup

5.5. Results and discussion

This chapter focuses on the characterization of the cyclic in-plane response of 3DPC structural walls through analytical and numerical investigations, aligning the design approach with the American Concrete Institute ACI 318-19 [11], Eurocode 8 [12], and IS 13920-2016 [13] provisions. Specifically, two types of reinforcement strategies are evaluated i.e., single-layer

and double-layer configurations; through analytical and numerical modeling, highlighting their distinct responses under cyclic loading. To further enhance seismic performance, self-centering reinforcement and confined boundary reinforcement are incorporated following codal guidelines. The discussion below explores the key findings, their implications for 3DPC wall design, and recommendations for future research.

5.5.1. Seismic performance analysis of single- and double-layer reinforcement configurations

The results demonstrate that the reinforcement strategy plays a crucial role in enhancing the seismic performance of 3DPC walls. While both the single-layer and double-layer reinforcement configurations exhibit favorable strength and ductility, the double-layer reinforcement outperforms the single-layer design in terms of both ultimate strength and energy dissipation. This is attributed to the increased load transfer capacity and better control over cracking behavior in the double-layer setup. Additionally, the increased redundancy in reinforcement provided by the double-layer design enhances the wall's resilience to seismic forces by improving its ability to resist localized failures, particularly in areas of high stress concentrations such as near openings or wall boundaries. In contrast, the single-layer wall exhibits lower strain, indicating better resistance to strain-induced damage

5.5.1.1. 3DPC wall with single-layer reinforcement

The single-layer reinforced 3DPC wall was designed with both vertical and horizontal reinforcement in a single layer. During simulation, it is observed that cracking initially initiated diagonally and extended towards the toe and heel regions at a displacement of 10 mm (Fig. 5.7, 5.8). As the displacement increases, the cracks propagated both horizontally and vertically. The failure progression of the single-layer reinforced 3DPC wall is illustrated in Fig. 5.8. The maximum lateral load capacity is reached at a displacement of 18.31 mm. In the post-peak loading stage, significant damge is evident on the concrete surface, particularly at the end regions (Fig. 5.8). The ultimate displacement is determined to be 31.95 mm, marking the failure point at a lateral load of 275 kN (Fig. 5.7).

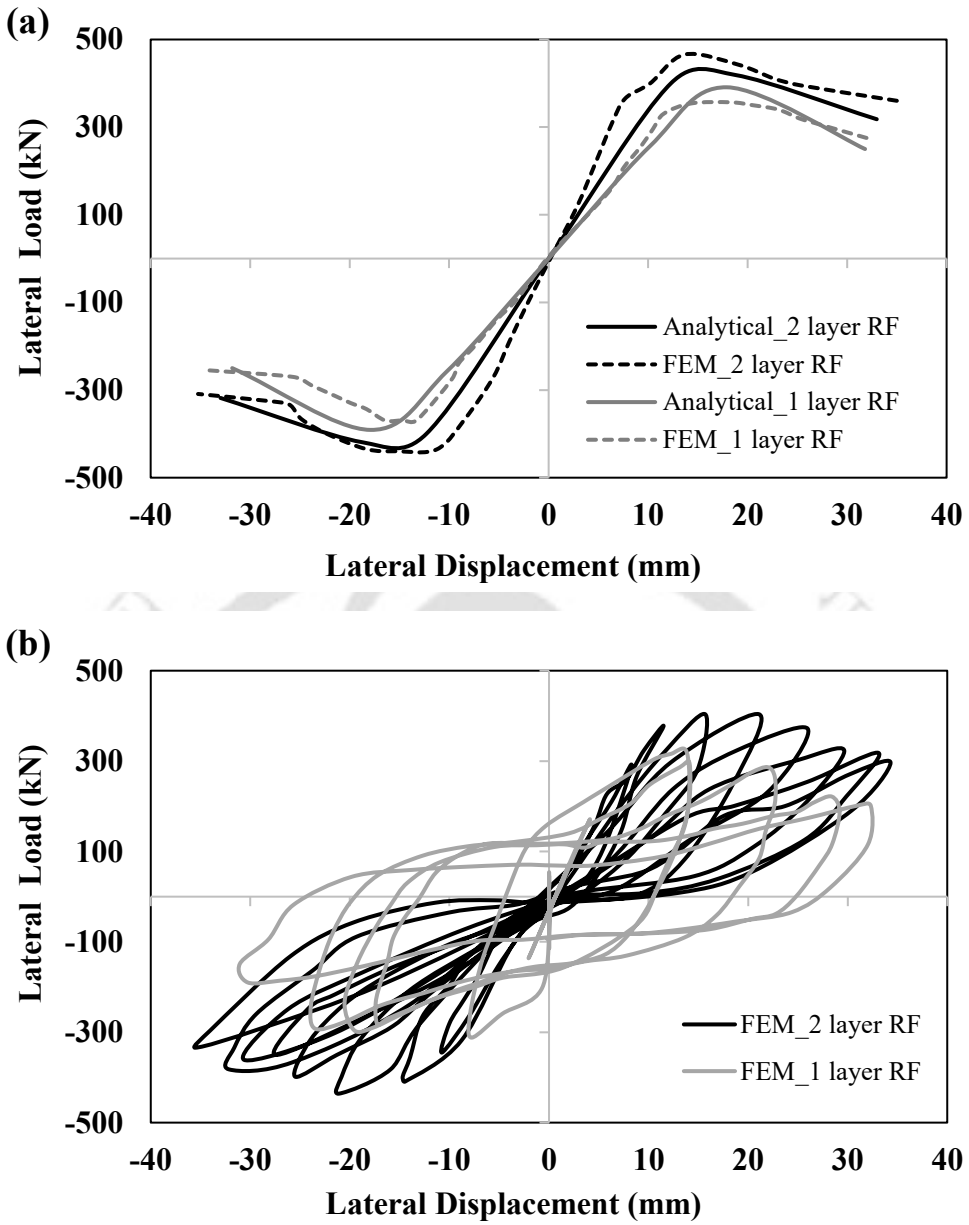

Fig. 5. 7. Cyclic behaviour of double and single layer reinforcement in 3DPC wall (a) Envelope curve; (b) hysteretic curve

Further analysis of the simulated single-layer reinforced 3DPC wall reveals that the vertical steel bars at the end regions (heel and toe) did not experience significant deformation during the final loading stages, and no buckling isobserved (Fig. 5.8). This observation suggests that the surrounding concrete, along with the horizontal reinforcement, provided sufficient lateral support, preventing local buckling of the vertical bars.

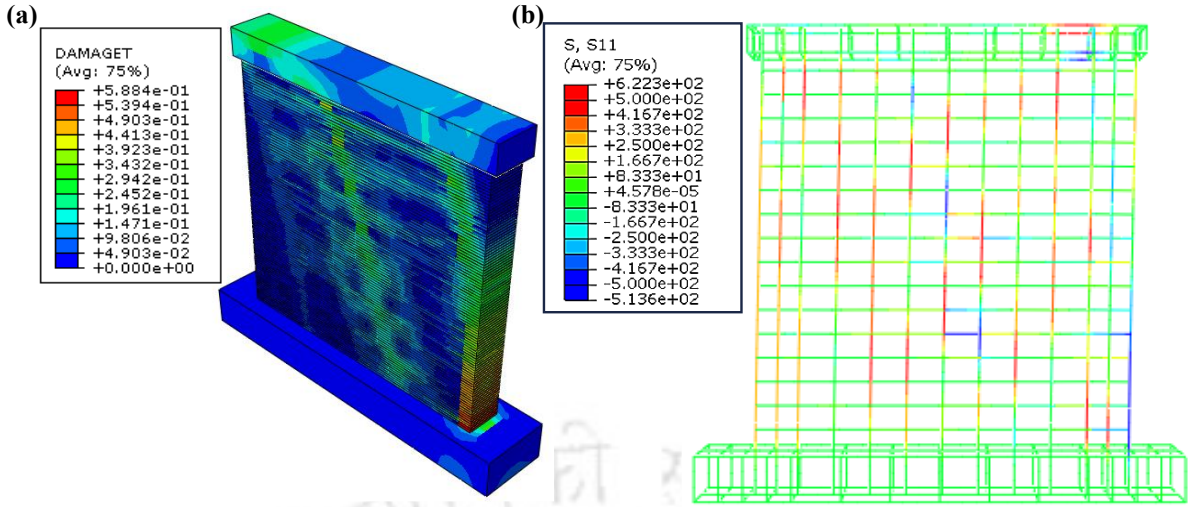

Fig. 5. 8. Failure mode of (a) 3DPC wall with (b) single layer reinforcement

5.5.1.2. 3DPC wall with double-layer reinforcement

The 3DPC wall with double-layer reinforcement is designed with two layers of reinforcement, both vertically and horizontally. In contrast to the single-layer reinforced 3DPC wall, no diagonal cracking is observed in the double-layer reinforced wall (Fig. 5.8 and Fig. 5.9). Instead, significant damage is noted at the toe region, particularly as the displacement increased (Fig. 5.9). This suggests that the additional reinforcement helps to distribute the stresses more evenly across the concrete layer, but does not prevent localized crushing at the toe, which resulted in substantial damage in this area. The enhanced confinement provided by the additional layer of reinforcement likely delayed the onset of cracking but contributed to a more pronounced compressive response, ultimately leading to the observed crushing.

The maximum lateral load capacity of the double-layer reinforced 3DPC wall is reached at a displacement of 13.66 mm, with an ultimate load capacity of 465.72 kN. This represents an increase of approximately 30.6% in lateral load capacity compared to the single-layer reinforced 3DPC wall, which reached a peak load of 356.65 kN at a displacement of 18.31 mm. The ultimate displacement at failure for the double-layer reinforced wall was found to be 35 mm, indicating a 9.8% increase in deformation capacity compared to the single-layer reinforced wall, which achieved failure at 31.95 mm (Fig. 5.7). Despite the increase in damage at the toe, no buckling of the vertical reinforcement was observed during the simulation (Fig. 5.9). It can be concluded that the concrete matrix, in conjunction with the reinforcement strategy, provided adequate lateral restraint to the vertical bars, preventing any buckling from occurring during the final stages of loading.

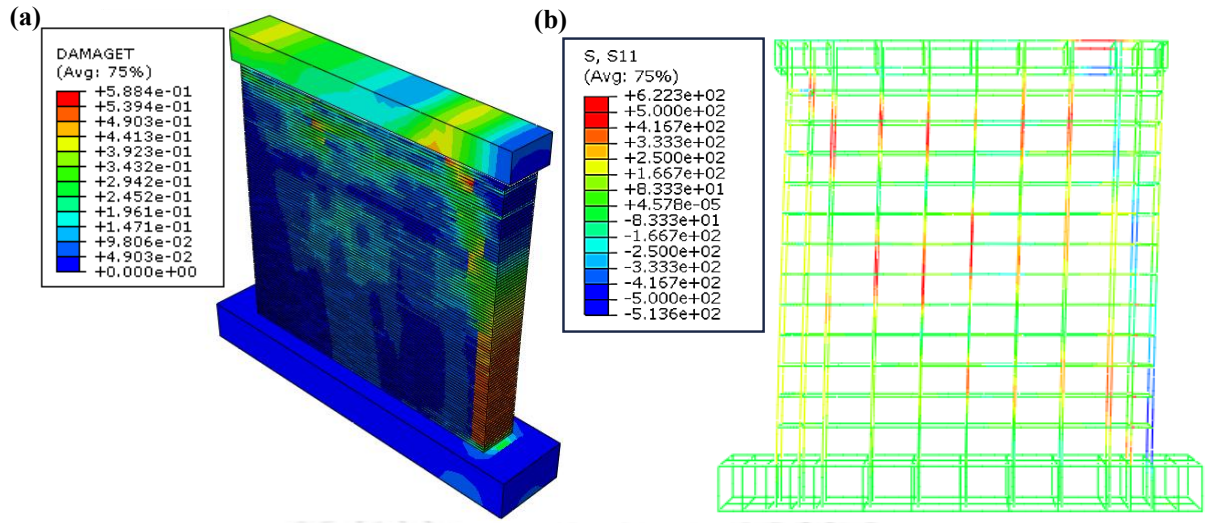

Fig. 5. 9. Failure mode of (a) 3DPC wall with (b) double layer reinforcement

5.5.1.3. Structural parameters analysis

This section delves into key structural properties, including ductility, stiffness, energy absorption, equivalent damping, and strain in concrete for both one-way and two-way reinforced 3DPC walls. These parameters are crucial for evaluating the seismic performance of walls, as they influence the structure's ability to withstand deformations, resist forces, and dissipate energy effectively during seismic events. Understanding these properties ensures the design of resilient and efficient 3DPC walls tailored to varying seismic demands.

Ductility assessment

The ductility of a structural wall refers to its capacity to sustain large deformations without collapsing. It is commonly measured as displacement ductility (μ), defined by the ratio of the ultimate displacement (d_{ult}) to the yield displacement (d_{yield}), as expressed in Eq. (5.14) and illustrated in Fig. 5.10:

$$\mu = \frac{d_{ult}}{d_{yield}} \tag{5.14}$$

Concrete's inherent brittleness, combined with the complexities of integrating reinforcement into 3DPC, necessitates the strategic placement of reinforcing steel bars in 3DPC structural walls. To ensures a ductile response, allowing the structure to withstand significant inelastic deformations under severe seismic loading a precise reinforcement detailing is crucial for achieving structural resilience and performance. The method employed to evaluate the ductility of the simulated 3DPC walls is illustrated in Fig. 5.10. The load–displacement curve is idealized as a bilinear representation (elastic-perfectly-plastic) [233]. The parameters required to calculate ductility are extracted based on the key points depicted in Fig. 5.10 and are

summarized for both wall configurations in Table 5.3. The idealized load–displacement curves for the simulated 3DPC walls are presented in Fig. 5.7.

The results indicate that the 3DPC wall reinforced with two layers of steel exhibits slightly higher ductility compared to the single-layer reinforced wall, even though both configurations use similar reinforcement percentages (Table 5.3). This improvement is attributed to the enhanced distribution of stresses and better confinement provided by the additional reinforcement layer. These findings confirm that double-layered reinforcement significantly improves the ductility characteristics of 3DPC walls, making them more resilient to seismic forces.

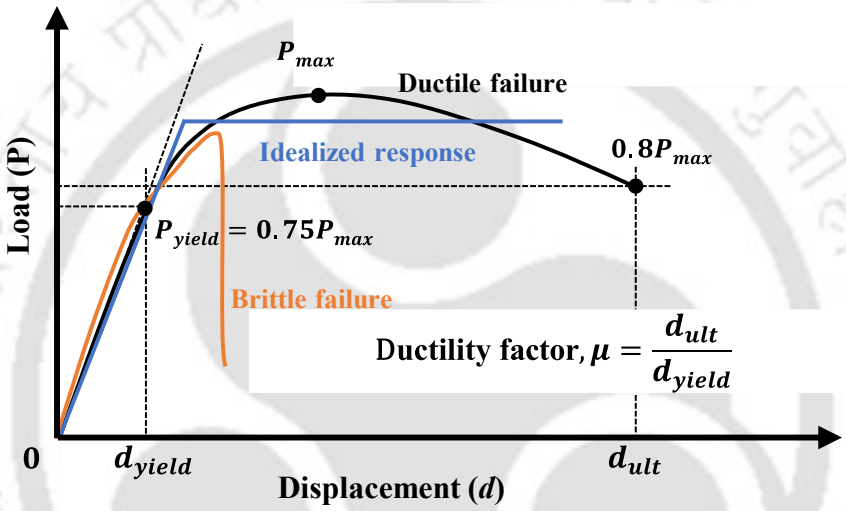

Fig. 5. 10. Ductility assessment through idealised load–displacement curve

Table 5. 3. In plane displacement derived from the load displacement response

Wall type	Loading direction	d_{dyield}	d_{ult}	μ
3DPC wall with 2 layer RF	Push (+)	+7.70	+35.00	4.36
	Pull (-)	-8.40	-35.24	
3DPC wall with 1 layer RF	Push (+)	+7.57	+31.95	4.01
	Pull (-)	-9.03	-34.60	

Energy dissipation capacity

The energy dissipation capacity of a structural member is a critical parameter in evaluating its seismic performance. It represents the ability of the structure to absorb and dissipate energy imposed during cyclic or dynamic loading, thereby reducing the seismic demands transferred to the superstructure [234]. A greater energy dissipation capacity corresponds to a higher additional damping ratio, enhancing the structure's seismic resistance and minimizing damage during earthquakes. In structural analysis, the area enclosed within the hysteresis load-

displacement response curve is commonly used to quantify the energy dissipated under sustained loading (Fig. 5.11a).

In this section, the energy dissipation capacity of single-layer and double-layer reinforced 3DPC walls is assessed. Up to a drift capacity of 0.5%, both wall types exhibited nearly identical energy dissipation behavior (Fig. 5.11b). However, beyond a drift capacity of 1%, a marked increase in the energy dissipation capacity was observed in the double-layer reinforced 3DPC wall compared to its single-layer counterpart. This significant improvement is attributed to the additional reinforcement layer in the double-layer configuration, as well as the influence of the infill pattern. Previous discussions in the chapter 4 have demonstrated that the energy dissipation capacity of 3DPC walls is higher than that of cast-in-place walls, which helps mitigate catastrophic failure by enhancing structural resilience. Notably, both reinforcement methods utilizes the same percentage of total reinforcement. Despite this, the double-layer arrangement demonstrated better energy dissipation, likely due to the more effective distribution and interaction of reinforcement layers, which delayed the onset of localized damage and allowed the structure to absorb more energy during repeated loading cycles. These findings emphasize the importance of reinforcement detailing in optimizing seismic performance, with double-layer reinforcement showing superior energy dissipation characteristics under larger deformation demands.

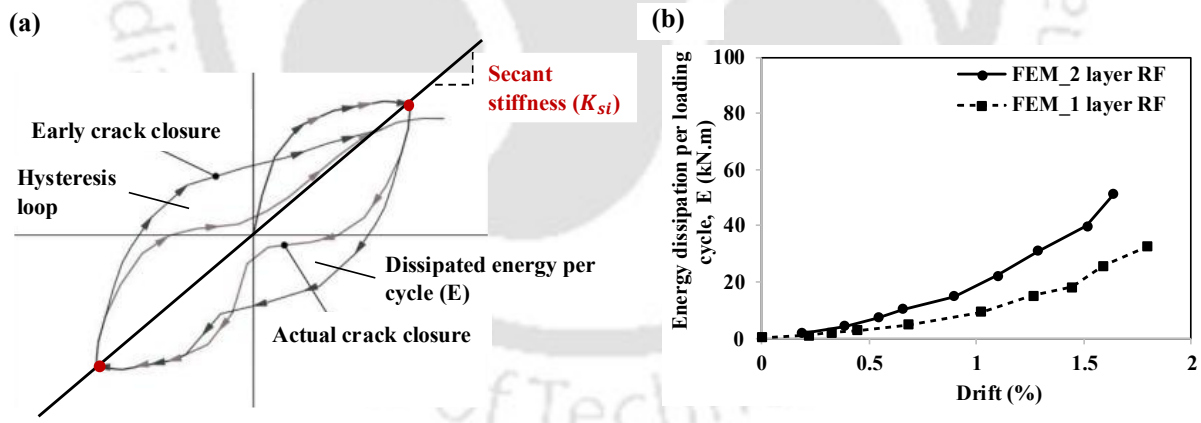

Fig. 5. 11. (a) Energy dissipation assessment through idealized curve; (b) energy dissipation capacity of double and single layer reinforcement in 3DPC wall

Stiffness degradation

Stiffness degradation refers to the rate at which the stiffness of structural elements diminishes during lateral cyclic or earthquake loading conditions. It is a key indicator of how a structure loses its ability to resist further deformation under repeated loading. The rate of stiffness degradation (K_R) can be quantified using Eq. (5.15):

$$K_R = \frac{K_{si}}{K_0} \tag{5.15}$$

where K_{si} is the secant stiffness i.e., stiffness at a specific secant location and K_o is the initial stiffness corresponds to the stiffness at first cycle step/increment.

For both the single-layer and double-layer reinforced 3DPC walls, stiffness degradation trends are nearly coincident up to a drift level of about 0.2%. Beyond this point, very minor variations are observed up to a drift level of approximately 1%, after which the stiffness degradation values again converge and remain nearly identical until a drift level of 1.6%, as illustrated in Fig. 5.12a. This behaviour suggests that, despite the variation in reinforcement strategy, both types of walls exhibited a similar stiffness to cyclic loading. The concrete matrix and reinforcement, while influencing the load-carrying capacity and deformation resistance, appear to have a comparable impact on stiffness reduction. Therefore, the similar stiffness degradation between the two reinforcement configurations indicates that the primary function of reinforcement in both cases is to improve the overall strength and deformation resistance, rather than significantly altering the stiffness degradation pattern.

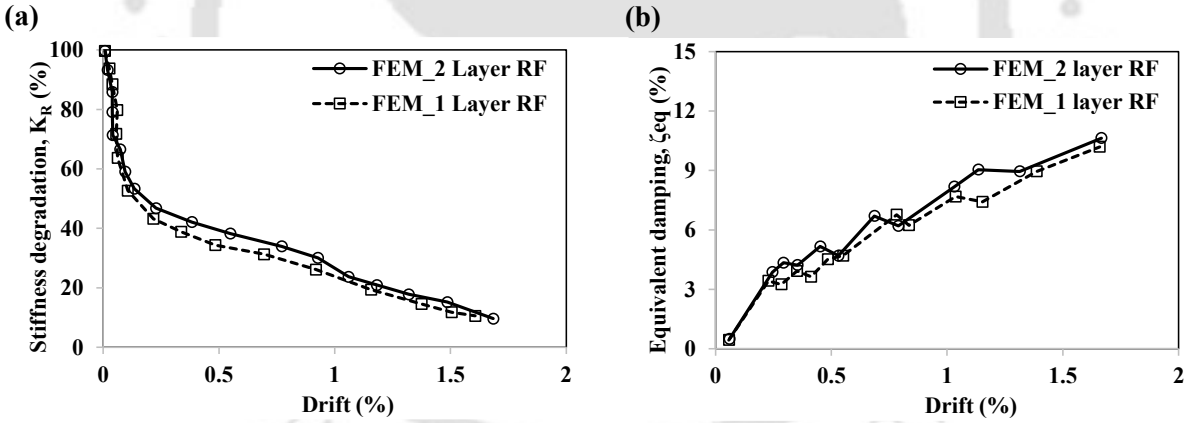

Fig. 5. 12. Response of double and single layer reinforced 3DPC wall (a) stiffness degradation; (b) equivalent viscous damping

Equivalent viscous damping

The relationship between energy dissipation and wall behavior is often complex to interpret, as narrow-loop hysteresis curves with high load resistance may dissipate more energy than wider-loop hysteresis curves with lower load resistance. To facilitate a meaningful comparison, the equivalent viscous damping ratio (ζ_{eq}) is calculated for both simulated wall. To evaluate ζ_{eq}, a method is employed that equates the energy dissipated in each hysteretic cycle to that of a linear viscous damping system, as described by Eq. (5.16):

$$\zeta_{eq} = \frac{E_i}{2\pi K_{si}\delta_{max,i}^2} \tag{5.16}$$

In this equation, E_i represents the energy dissipated during each cycle, K_{si} is the secant stiffness of the cycle, and $\delta_{max,i}$ is the maximum displacement during the i^{th} load cycle.

The variation of the equivalent viscous damping ratio with drift levels is illustrated in Fig. 5.12b. Initially, up to a drift level of approximately 0.23%, both single-layer and double-layer reinforced 3DPC walls exhibit nearly identical viscous damping behavior. However, slight variations are observed between drift levels of 0.4% and 1.15%. These differences can be attributed to the reinforcement strategy and the structural response to increasing lateral displacement. The double-layer reinforced wall exhibits a slightly higher damping ratio at specific drift levels, likely due to its enhanced ability to distribute stresses and maintain energy disspation and stiffness under cyclic loading. Conversely, the single-layer reinforced wall shows a slightly lower damping ratio in the same range, reflecting its comparatively limited capacity to dissipate energy effectively through hysteretic behavior.

The results highlight that the equivalent viscous damping ratio is sensitive to both the reinforcement configuration and the loading conditions, serving as a critical metric for assessing the seismic energy dissipation performance of reinforced 3DPC walls. This observation aligns with recent findings [235], where the importance of understanding mutual effects between energy dissipation mechanisms and structural interactions are emphasized, particularly in systems subjected to dynamic loading. Their work supports the interpretation of damping behavior as a function of both internal reinforcement detailing and external interaction effects in innovative structural systems such as 3DPC.

Concrete strain levels at the wall length

The variation in concrete strain along the wall length, as shown in Fig. 5.13, highlights a notable difference between single-layer and double-layer reinforced walls at 1% and 2% drift levels. The single-layer reinforced 3DPC wall exhibits lower concrete strain at the same drift level compared to the double-layer reinforced wall, consistent with the significant damage observed in the toe region of the double-layer wall (Fig. 5.13). Additionally, as the wall height increases, a decreasing trend in concrete strain values is observed for both reinforcement configurations.

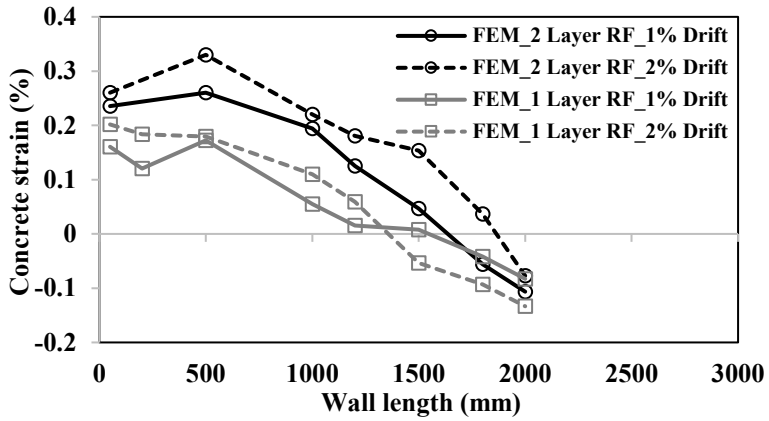

Fig. 5. 13. Concrete strain levels of double- and single-layer reinforcement in 3DPC wall

Despite the double-layer reinforcement strategy enhancing other structural performance parameters, such as load resistance and displacement capacity, the higher strain levels in the concrete suggest that this reinforcement strategy may amplify localized stress demands, particularly in the critical regions of the wall. The increased reinforcement density in the double-layer configuration contributes to a stiffer overall structure, which intensifies stress concentrations in areas like the toes, leading to significant damage and higher strain levels. Furthermore, the two-layer reinforcement design alters the internal load transfer mechanisms, resulting in greater localized stress and strain within the concrete. Conversely, the single-layer reinforced wall demonstrates comparatively lower strain levels, indicating a more favorable performance in terms of minimizing strain-induced damage. This highlights the importance of evaluating strain levels when optimizing reinforcement strategies for 3DPC walls, as improved performance in other parameters may not necessarily correlate with reduced strain or localized damage.

5.5.2. Effect of boundary elements confinement on cyclic performance of 3DPC wall

This section examines the influence of confined boundary reinforcement on the cyclic response of 3DPC structural walls through finite element micro-modelling. The incorporation of boundary confinement, following conventional reinforced concrete design principles, is intended to enhance lateral strength, ductility, and energy dissipation capacity. The analysis considers various boundary configurations and reinforcement detailing under quasi-static cyclic loading. The findings demonstrate that boundary confinement effectively delays the initiation of damage, mitigates stiffness degradation, and improves post-peak load stability.

5.5.2.1. Boundary element configurations

A total of four 3DPC wall configurations—Wall A, Wall B, Wall C, and Wall D—are numerically modeled and analyzed to investigate the influence of boundary element

confinement on cyclic structural performance of the 3DPC walls. Each configuration is subjected to lateral cyclic displacement loading as per the protocol illustrated in Fig. 5.6a, with the loading steps and boundary conditions as defined in Fig. 5.6c.

- **Wall A** is modeled without any solid boundary elements, serving as the control specimen to understand the baseline behavior of a plain 3DPC infill wall.
- **Wall B** incorporates solid boundary elements without reinforcement, simulating the effect of added mass and stiffness without reinforcement.
- **Wall C** introduces vertical reinforcement within the solid boundary columns, representing an unconfined reinforced boundary system.
- **Wall D** includes both vertical reinforcement and lateral confinement in the form of transverse ties (stirrups), simulating confined boundary elements as per seismic design recommendation.

In practical terms, such a configuration (Wall D) can be achieved through a hybrid approach, wherein an infill printing pattern can be designed to create cavities in the boundary zones. These cavities allow subsequent placement of column reinforcement along with stirrups, which can then be conventionally cast with concrete. This ensures structural feasibility of the reinforcement detailing while maintaining compatibility with 3D printing processes.

5.5.2.2. Reinforcement detailing of designed 3DPC walls

The reinforcement detailing of the structural 3DPC walls are illustrated in Fig. 5.14, which presents the configurations developed in accordance with the provisions outlined in ACI 318-19 [11], Eurocode 8 [12], and IS 13920-2016 [13]. The reinforcement layouts are finalized following a comprehensive design procedure aimed at evaluating the structural behavior under lateral cyclic loading. The detailed design procedure is described in Section 5.3.

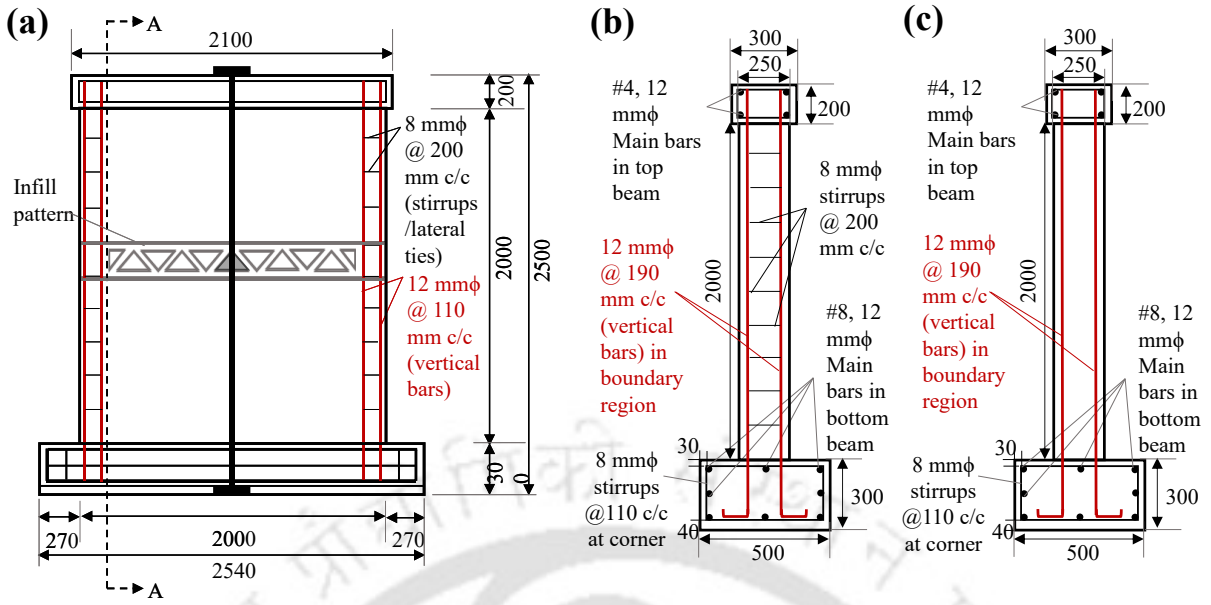

Fig. 5. 14. Reinforcement details of the structural 3DPC wall (a) elevation of Wall D; (b) cross-section detailing of (b) Wall D along A-A; (c) Wall C along A-A

To ensure a controlled comparison, key design parameters—concrete compressive strength, reinforcement bar strength and diameter, axial load, aspect ratio, slenderness ratio, and all other geometric parameters are kept constant across all wall models. This approach isolates the effect of boundary confinement detailing on the cyclic performance of the 3DPC walls.

5.5.2.3. Effect of boundary elements on lateral displacement capacity of 3DPC wall

The lateral displacement capacity increases progressively with enhancements in boundary element detailing. Wall A, which lacks any solid or reinforced boundary elements, records the lowest displacement (13.85 mm), indicating a limited ability to deform plastically (Fig. 5.15 and Fig. 5.16a). With the addition of solid boundary columns in Wall B, displacement capacity increases by 61.67%, as these columns provide improved anchorage and resistance to lateral forces. Wall C, which incorporates vertical reinforcement into the boundary elements, further increases displacement by 79.31% over Wall A. This improvement reflects the vertical bars' ability to resist tensile stresses and delay crack formation. Wall D, which combines vertical and transverse confinement reinforcement, exhibits the highest displacement (27.34 mm), marking a 97.35% increase from Wall A and a 10.06% improvement over Wall C. The additional confinement enhances crack control and post-yield deformation, promoting a highly ductile response.

These trends demonstrate that confined reinforcement improves strain compatibility and restrains lateral crack widening, thus facilitating enhanced lateral displacement without significant degradation in structural integrity.

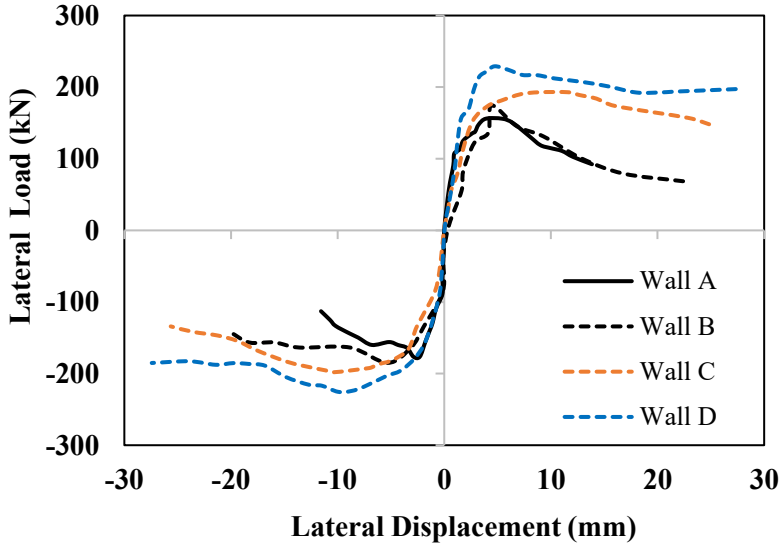

Fig. 5. 15. Effect of boundary element on cyclic in-plane loading capacity of 3DPC wall

5.5.2.4. Impact on load-carrying capacity

A similar trend appears in the peak lateral load capacity (Fig. 5.15). Wall A, exhibiting early brittle failure due to the absence of confinement, carries the lowest load (155.99 kN) (Fig. 5.16a). The introduction of solid boundary columns in Wall B improves load resistance by 11.85%, due to better load transfer and suppression of premature shear cracking, but showing almost similar failure profile (Fig. 5.16b). Wall C, with vertical reinforcement, sustains a further increase of 23.67% compared to Wall A, owing to enhanced flexural resistance and energy absorption capacity. Wall D achieves the highest peak load of 229.14 kN, which corresponds to a 46.89% increase from Wall A and a 31.33% gain over Wall B. The difference between Wall C and Wall D (18.78%) underscores the additional strength imparted by transverse confinement, which limits concrete spalling and bar buckling under cyclic loads which ultimately restricted wall topling and concrete crushing (Fig. 5.16d). Mechanically, these load enhancements result from improved confinement effectiveness, increased axial load capacity in boundary zones, and a delayed onset of material degradation.

5.5.2.5. Stress distribution and crack propagation

The stress contour plots reveal a clear correlation between boundary detailing and failure mode. Wall A shows localized stress concentration at the base, leading to premature shear cracking and rapid stiffness loss and resulted in overturning of the wall (Fig. 5.16a). Wall B redirects stress paths upward due to improved confinement at the edges, resulting in delayed overturning and minor concrete crushing (Fig. 5.16b). In Wall C, vertical reinforcement spreads stress along the wall height, promoting a more ductile flexural failure pattern without overturning (Fig. 5.16c). Wall D exhibits the most favorable distribution: cracks form in a stable and well-

distributed manner, with confinement reinforcement preventing excessive damage at critical regions such as toe crushing and also restricted overturning. This balanced stress path maintains structural performance even after yielding (Fig. 5.16d).

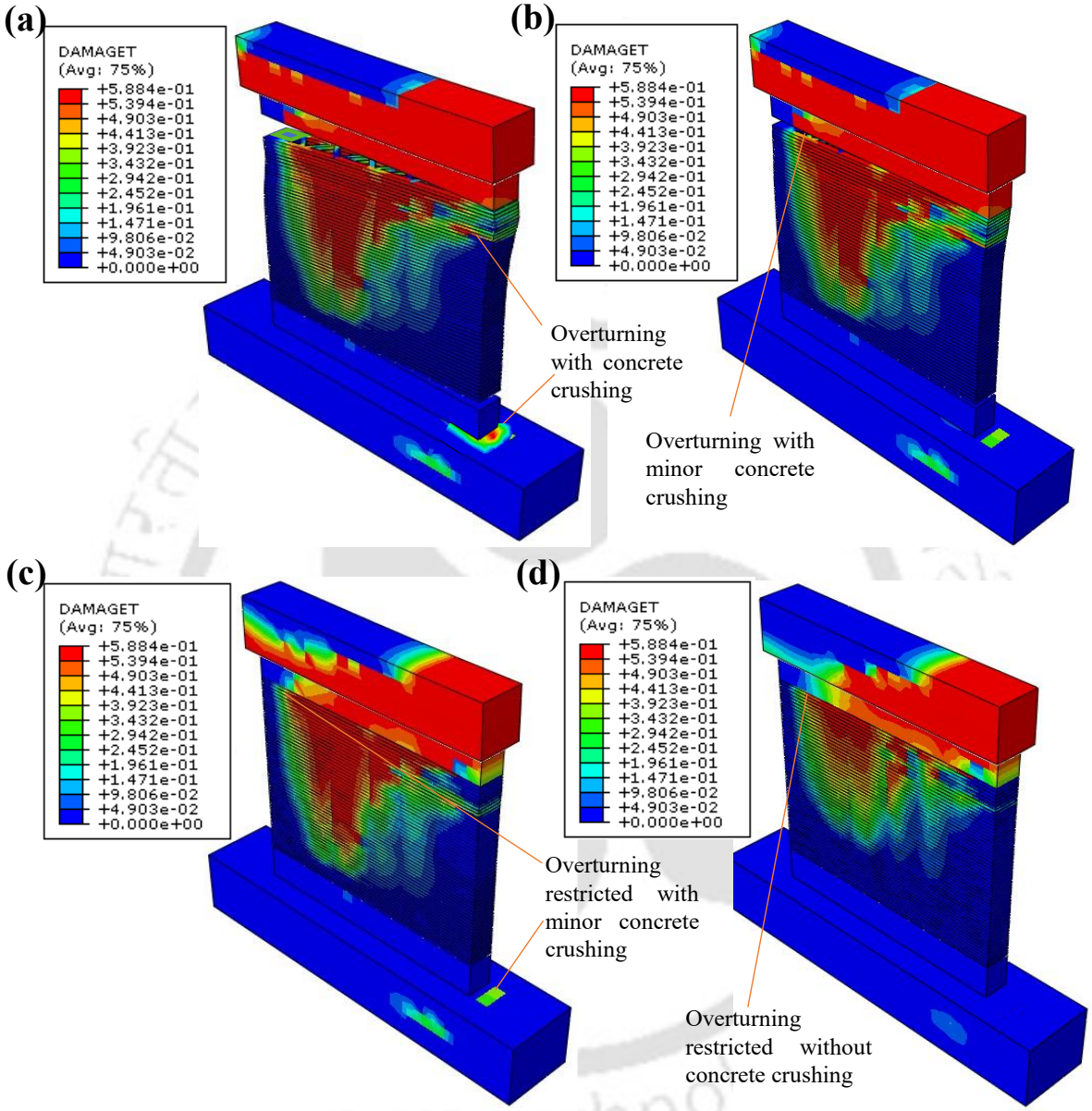

Fig. 5. 16. Failure mode of (a) Wall A; (c) Wall B; (c) Wall C; (d) Wall D

5.5.2.6. Ductility index

The ductility of the wall calculated in the same manner as described in Section 5.5.1.3. As shown in Table 5.4, Wall D exhibits the highest ductility index, reaching a value of 11.74, while Wall A displays the lowest index of 5.88, indicating a relatively brittle response. Wall B, with only solid boundary columns, achieves a ductility index of 8.66, indicating moderate improvement over Wall A. The presence of these solid elements allows the wall to sustain

larger displacements before failure, though without the additional reinforcement, its post-peak behavior remains less controlled.

Table 5. 4. In plane displacement derived from the load displacement response to calculate the ductility Index

Wall type	Loading direction	d_{yield}	d_{ult}	μ
Wall A	Push (+)	+2.63	+13.85	5.88
	Pull (-)	-1.78	-11.56	
Wall B	Push (+)	+2.69	+22.39	8.66
	Pull (-)	-2.23	-20.05	
Wall C	Push (+)	+2.72	+24.84	10.07
	Pull (-)	-2.33	-25.65	
Wall D	Push (+)	+2.63	+27.94	11.74
	Pull (-)	-2.14	-27.53	

Wall C, with vertical reinforcement in the boundary elements, demonstrates a significant improvement, achieving a ductility index of 10.07. This reflects the vertical bars' ability to engage more effectively after yielding and contribute to strain redistribution along the height of the wall. However, the highest ductility, again, is observed in Wall D, where both vertical and lateral reinforcement confine the boundary regions, promoting enhanced post-yield performance and stable hysteretic behavior under cyclic loading.

This supports the argument for codified design practices incorporating such confinement strategies for printed structures in seismic zones.

5.5.3. Effect of self-centering reinforcement on cyclic performance of 3DPC Wall

The numerical simulation results of the 3DPC and 3DPC-SC systems are presented in Fig. 5.17, illustrating the crack propagation patterns, failure mechanisms, and structural enhancement achieved through self-centering reinforcement under cyclic loading. As the applied displacement increased, the unreinforced 3DPC wall exhibits extensive horizontal vertical cracking, ultimately leading to wall toppling and concrete crushing, as shown in Fig. 5.17b. In contrast, the 3DPC-SC wall demonstrates a more controlled crack evolution. Initial cracking originated near the centrally positioned reinforcement bar and extended diagonally downward but does not propagate toward the toe and heel regions. This behavior can be attributed to the confining effect provided by the reinforcement, which effectively restricted crack propagation within the central region (Fig. 5.17b).

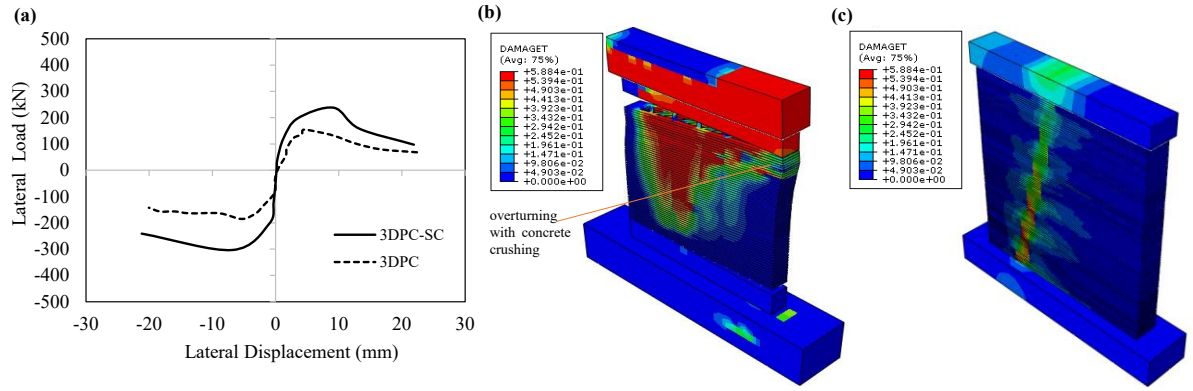

Fig. 5. 17. Numerical results (a) backbone curves of the hysteretic response; numerical failure mode of (b) 3DPC; (c) 3DPC-SC

The self-centering reinforcement strategy significantly improved the lateral load capacity, with the 3DPC-SC wall achieving a peak load of 238 kN at a displacement of 9.19 mm (Fig. 5.17a), representing a 54.08% enhancement compared to the unreinforced 3DPC wall. In the post-peak phase, substantial concrete damage is observed in the lower regions of the 3DPC-SC wall, particularly between the reinforcement bars and the edge column (Fig. 5.17c). This damage primarily resulted from localized stress concentrations and material degradation at the transition zone between reinforced and unreinforced regions, where shear and flexural stresses peaked, leading to crack widening and eventual concrete crushing. The findings underscore the critical role of strategically positioned reinforcement in enhancing the structural integrity and failure resistance of 3DPC walls under cyclic loading.

5.6. Compatibility of ACI 318 with 3DPC: challenges and recommendations

One of the significant contributions of this research is the adaptation of ACI 318-19 provisions to investigate the cyclic performance of 3DPC walls. The findings indicate that the analytical and numerical results are in good agreement, demonstrating the reliability of the proposed models in capturing the structural behavior of 3DPC walls (Fig. 9). This compatibility validates the potential for adapting conventional design guidelines, but it also highlights the need for adjustments to address specific challenges associated with 3DPC construction.

While the existing ACI 318 guidelines for conventional reinforced concrete walls provide a robust foundation, modifications are required to accommodate the unique characteristics of 3DPC. The anisotropic material properties, inter-layer bonding strength, and potential non-homogeneous reinforcement distribution are critical factors that must be considered. These parameters influence load transfer mechanisms, failure modes, and reinforcement detailing, necessitating additional guidelines for layer-by-layer construction. This investigation suggests

incorporating additional parameters into the design framework, such as inter-layer shear strength, anisotropy factors for material stiffness, and strain limits tailored for 3DPC construction. These enhancements would ensure that the provisions are compatible with the structural and material behavior observed in 3DPC walls, providing a safer and more reliable design basis for future applications.

5.7. Summary

This chapter focuses on establishing a codal-based analytical and numerical framework for designing earthquake-resistant 3DPC structural walls, addressing the absence of design standards specific to 3DPC systems. A preliminary design analysis is conducted using ACI 318-19 and Eurocode 8 provisions to assess their applicability to 3DPC, emphasizing lateral load resistance, ductility, and reinforcement detailing.

i. **Influence of reinforcement configuration:** Double-layer reinforcement configuration demonstrating 30.6% higher lateral load capacity (465.72 kN) compared to the single-layer design (356 kN), and exhibits 9.8% increase in failure displacement, a higher ductility factor (4.36 vs. 4.01), and improved energy dissipation capacity, particularly at larger drift levels. Whereas single layer reinforcement exhibits lower strain concentrations, indicating better resistance to strain-induced damage.

ii. **Effect of confined boundary reinforcement**: Boundary confinement plays a decisive role in improving the deformation capacity, load resistance, and damage control of 3DPC walls.

   a. **Progressive confinement enhancement (**Wall A to Wall D**):** incremental confinement—through solid boundary columns, vertical bars, and transverse reinforcement—led to an approximate 97% increase in lateral displacement and 47% improvement in load-carrying capacity, emphasizing the positive correlation between confinement intensity and ductile response.

   b. Role of transverse confinement: Transverse reinforcement within the boundary elements proved to be the most influential parameter, ensuring crack stability, restricting concrete spalling, and preventing bar buckling. This resulted in sustained post-yield deformation and improved ductile energy dissipation under cyclic loads.

iii. **Effectiveness of self-centering reinforcement:** The incorporation of a centrally positioned reinforcement bar significantly enhanced the cyclic performance of the 3DPC wall, improving its lateral load capacity by 54.08% compared to the unreinforced 3DPC wall.

a. **Controlled crack propagation:** In the 3DPC-SC system, cracks initiated near the reinforcement bar and remained confined within the central region, preventing extensive damage to the toe and heel areas, unlike the unreinforced wall, which exhibited widespread cracking and eventual toppling.
b. **Failure mechanism and damage distribution:** The post-peak phase of 3DPC-SC exhibited localized damage primarily in the lower wall regions between the reinforcement bars and edge column due to stress concentration and material degradation at the transition zone.

The findings collectively demonstrate that codal principles from ACI 318-19 and Eurocode 8 can be partially adapted to 3DPC, paving the way for a standardized design framework for printed structural walls. Overall, this chapter provides a validated numerical and codal-based design methodology that bridges the gap between material-level developments and full-scale structural applications, establishing the foundation for performance-based seismic design of 3DPC systems.

Chapter 6

Experimental response of earthquake resistant 3D printed concrete walls

*This chapter experimentally investigates the in-plane cyclic behavior of full-scale 3DPC structural walls to validate the material, design and numerical findings established in the preceding chapters. Three wall configurations are fabricated using extrusion-based 3D printing: (i) an unreinforced plain mortar wall (3DPM), (ii) a strain-hardening ductile mix wall combining coarse aggregates and critical fiber fraction (3DPC-CF), and (iii) a modularly reinforced wall (3DPC-CFR) integrating prefabricated steel cages within the 3DPC-CF matrix. The findings advance the feasibility of deploying 3DPC for earthquake-resistant applications, contributing critical insights toward safe, economical, and scalable adoption in large-scale constructions.

* A portion of this chapter has been published:
Warsi, S. B. F., Panda, B., & Biswas, P. (2026) Experimental investigation of the cyclic in- plane behavior of full-scale 3D printed concrete walls through quasi-static cyclic testing. *Journal of Building Engineering,* 115916. https://doi.org/10.1016/j.jobe.2026.115916.

6.1. Introduction

Despite rapid progress in 3DPC extrusion systems, and printable cementitious materials [5,6], the application of 3DPC to seismically resilient structural components remain in its infancy. As the main vertical structural component, walls deserve to be studied thoroughly in terms of their mechanical performance since they easily can be automatically constructed on site. Only a limited number of studies have experimentally investigated the seismic behavior of 3DPC walls [6–9] (see Table 2.2). However, these investigations are mostly confined to specific reinforcement systems or isolated wall configurations, while aspects such as material design, reinforcement detailing with standard design provisions, and failure mechanisms under realistic cyclic loading remain largely unexplored. This leaves significant gaps in developing a comprehensive understanding of the seismic performance of large-scale 3DPC walls. In 3DPC, steel reinforcement remains the most widely adopted approach, similar to conventional construction. However, its integration must be carefully managed to avoid disrupting the printing process, while ensuring adequate bond with the printed matrix, since this interface is critical to structural performance [10]. Another critical limitation is the lack of standard design provisions specific to 3DPC systems, particularly for reinforcement detailing, ductility, and energy dissipation—essential parameters in earthquake-resistant design.

Building upon the material development, numerical modelling, and design framework established in Chapters 3, 4, and 5, this chapter focuses on the experimental validation of earthquake-resistant 3DPC wall systems through large-scale cyclic testing. Based on the insights obtained from simulation and design analyses, it is observed that conventional infill geometries are incompatible with the proposed reinforcement configuration, necessitating modifications to achieve effective integration and structural compatibility. Hence, a modified infill pattern with hollow side regions is developed to facilitate reinforcement placement which also reduces material consumption by ~20%. Numerical simulations confirmed a ~20% increase in lateral load capacity and slower stiffness degradation. Subsequently, full-scale quasi-static cyclic tests are performed on three 3DPC wall systems: (i) a plain mortar reference wall (3DPM), (ii) a ductile wall containing coarse aggregates and critical fiber fraction (3DPC-CF), and (iii) a modularly reinforced wall incorporating prefabricated steel cages within the 3DPC-CF matrix (3DPC-CFR). The experimental results demonstrated a clear progression in seismic performance, with 3DPC-CFR exhibiting the highest lateral strength, delayed stiffness degradation, enhanced ductility, and stable post-peak load retention. This research presents the first integrated framework encompassing material-level innovation, codal design adaptation,

advanced numerical modeling, and full-scale experimental validation of 3DPC structural walls. Moreover, the findings underscore the importance of material heterogeneity, reinforcement detailing, and infill design in influencing the seismic behavior of 3D printed structures. The use of modular prefabricated reinforcement cages not only simplifies placement within printed geometries but also supports automation-compatible workflows—paving the way for future integration of fully automated reinforcement systems in 3D concrete printing. By validating these aspects through full-scale testing, the research advances the structural applicability of 3D concrete printing and supports its safe and efficient deployment in seismically active regions. The approach also aligns with sustainability objectives by enabling material-efficient designs and encouraging the adoption of coarse aggregates and fiber reinforcements in future iterations.

6.2. Materials and method

6.2.1. Materials and mix preparation

The mixture compositions of the 3D-printable mortar (3DPM) and 3D-printable concrete (3DPC) are formulated based on the material development framework established in chapter 3 (presented in Table 6.1). The mixing procedure, rheological characterization, and fresh-state assessments are maintained consistent with the methodology outlined therein. The 3DPC mix design follows the guidelines specified in IS 10262:2009 [155] and IS 456:2000 [156], targeting the mechanical characteristics of M30-grade concrete. The 3DPM mix serves as the reference benchmark to isolate and evaluate the individual contributions of coarse aggregates, critical fiber reinforcement, and modular steel reinforcement to the overall seismic performance of the 3DPC wall system. The 3DPC-CF mix includes corrugated steel fibers at the critical fiber volume fraction ($V_{f,cr}$), established based on prior material performance evaluations detailed in chapter 3. The geometrical and mechanical properties of these corrugated steel fibers are summarized in Table 6.2.

Table 6. 1. Mixture compositions

Mix ID	OPC	Sand	Water	VMA	SP	Steel Fiber	Coarse aggregate
3DPM	740	1209	296	1.9	3.7	…	…
3DPC-CF	541	851	220	2.2	9.9	**1.18**	625

Table 6. 2. Properties of corrugated steel fibers

Type	Density (g/cm^3)	Length (mm)	Diameter (mm)	Ultimate tensile strength (GPa)	Elastic modulus (GPa)	Aspect ratio
Corrugated (CF)	7.85	30±2	0.5	2.15	190	64

All mixtures are prepared using tap water, and locally available coarse aggregate (10 mm passing). This choice is made with an aim for sustainable, cost-effectiveness, and regional suitability, and their physical properties are measured in accordance with ASTM C125 [157] and ASTM C127 [158], as shown in Table 6.3.

Table 6. 3. Physical properties of coarse aggregate

Aggregate	Bulk specific gravity-Dry*	Bulk specific gravity-SSD*	Apparent specific gravity*	Water absorption (%) *	Fineness modulus**
Basalt	2.47	2.49	2.52	1.7	3.5

Abbreviations: SSD – Density at the saturated surface dry condition

*- ASTM C127[158]; **- ASTM C125[157]

6.2.2. Rheological and mechanical properties of 3DPC constituents

To evaluate the workability of the 3DPC mixtures, a mini slump cone with an inside diameter of 70 mm at the top, 100 mm at the bottom, and a height of 60 mm is used to test the slump and flowability of the mix designs (Table 6.4). The spread diameter of fresh mortar mixtures is measured after 25 drops of the flow table according to ASTM C1437-20 [161]. A 3D printed cylindrical mold is employed to measure the slump and diameter of the sample after demolding to estimate the density and yield stress [162]. It is important to emphasize that the slump value of the selected mix is within the range for smooth extrusion and desired buildability [163].

Table 6. 4. Fresh state properties of the printable mixes

Mix	Slump (mm)	Flowability (mm)	Density (kg/m^3)	Yield stress (Pa)
3DPM	11	138	2200	1381
3DPC-CF	6	112	2352	1491
3DPC-CFR	6	112	2352	1491

In addition to the mix design, steel reinforcement bars are incorporated to enhance the lateral load resistance, deformation capacity, and to increase energy dissipation and delay stiffness degradation under cyclic loading of the 3D printed wall system. The evaluation of material properties of reinforcement bars are performed through Universal Testing Machine (UTM Detailed mechanical properties of the reinforcing steel bars are presented in Table 6.5. The mechanical properties of the 3DPC, including compressive strength, tensile strength, flexural strength, and elastic modulus, are characterized to ensure consistency with structural performance requirements and are summarized in Table 6.6.

Table 6. 5. Mechanical properties of reinforcement bars

Diameter (mm)	Section area (mm^2)	Ultimate tensile strength (MPa)	Elastic modulus (GPa)	Elongation (%)
8	50	426	200	14
10	78	585	206	16
12	113	600	210	16

Table 6. 6. Mechanical properties of the printable mixes

Mix	Compressive strength (MPa)	Split tensile strength (MPa)	Flexural strength (MPa)	Direct tensile strength (MPa)	Ultimate strain (%)
3DPM	28.11	2.11	4.93	2.48	1.15
3DPC-CF	42.96	5.88	11.25	5.62	6.95
3DP-CFR	42.96	5.88	11.25	5.62	6.95

6.2.3. 3D printing process

A customized gantry-based 3D concrete printing system, constructed with a steel frame and offering a build volume of 4.0 × 4.0 × 3.0 meters, is used. The printing system integrates an auger-driven extrusion mechanism specifically developed to accommodate coarse aggregates (10 mm passing) and steel fibers exceeding 30 mm in length. A circular nozzle with a diameter of 30 mm is used for the 3D printing process, producing filament cross-sections measuring approximately 35 mm in width and 10 mm in height.

To support the transport of such complex mixtures (3DPC-CF), a critical enhancement is made to the auger extruder—an intentional clearance between the auger shaft and the internal wall of the extrusion chamber. This adjustment significantly reduces clogging risks and ensures a steady, uninterrupted flow of material through the system (see Fig. 6.1). The advanced extrusion setup enables the seamless incorporation of coarse aggregates and long fibers within the deposited layers, resulting in a consistent and well-bonded matrix, as illustrated in Fig. 6.2. Additionally, the auger's rotation speed is finely tunable, allowing real-time control of the output rate and ensuring compatibility with varied particle sizes. These system-level modifications, coupled with a tailored mix formulation strategy, contribute to improved homogeneity, print continuity, and mechanical performance of the printed elements. A visual overview of the printing infrastructure is provided in Fig. 6.1.

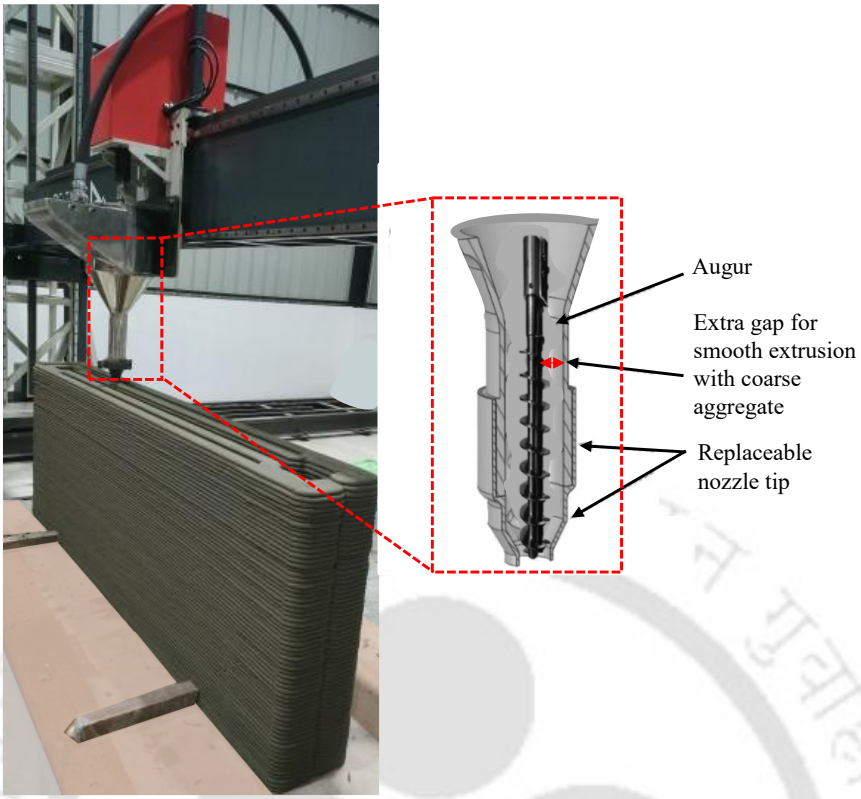

Fig. 6. 1. 3D printing system with mortar wall (3DPM) printing and enlarged view of the nozzle

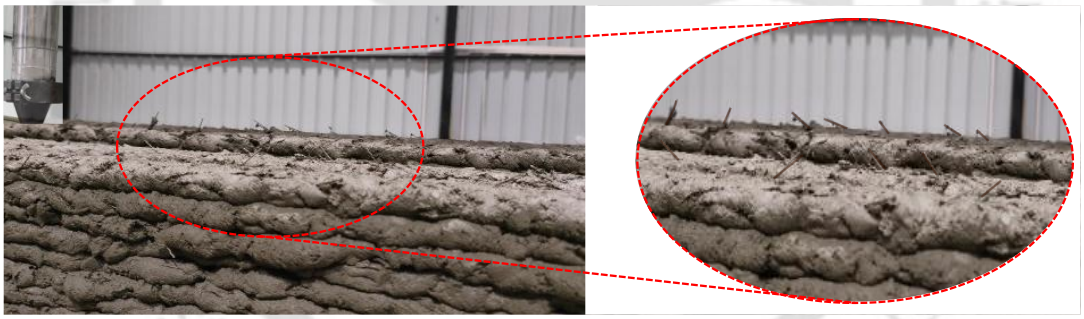

Fig. 6. 2. Macro-view of 3D-printed wall layers illustrating stable incorporation of long fibers and coarse aggregates (3DPC-CF)

6.3. Experimental program

6.3.1. Printing of large-scale 3D printed concrete wall

To evaluate the seismic performance of reinforced 3DPC walls, three full-scale wall specimens are optimized (Fig. 6.3 and Fig. 6.4), designed, and fabricated, as illustrated in Fig. 6.5 and Fig. 6.6. Among these, the 3DPC-CFR wall incorporates modular reinforcement cages, which, although manually inserted due to equipment limitations, are designed to be compatible with automation systems owing to their prefabricated and modular feature. All wall specimens have dimensions of 2000 mm in height, 2000 mm in width, and 250 mm in thickness. These dimensions are selected based on relevant codal provisions [11,12], balancing the structural

requirements of seismic testing with practical considerations for large-scale printing and testing. To ensure proper load transfer and structural continuity, each wall is embedded 200 mm into a bottom beam (400 mm width × 350 mm hight). Unlike the bottom beam, which is cast separately, the top beam (250 mm width × 200 mm height) is printed integrally as part of the wall immediately after the wall printing is completed (Fig. 6.4). This approach is adopted to simplify the construction process, avoid additional casting of the top beam, and does not compromise structural performance while significantly easing fabrication.

A critical challenge encountered during reinforcement design was selecting an infill pattern that could accommodate the reinforcement layout—comprising centrally aligned vertical bars and confined boundary reinforcement—without disrupting the 3D printing process. Several previously studied infill geometries [229,236], including truss (Fig. 6.3b), rhombus (Fig. 6.3c), and rectangular (Fig. 6.3d) configurations, are evaluated.

However, these conventional infill geometries are found to be incompatible with the chosen reinforcement design due to practical constraints during reinforcement placement. Consequently, a new infill configuration (Fig. 6.3e) is developed, specifically tailored to allow unobstructed reinforcement integration while preserving structural performance. This proposed infill demonstrated superior load resistance in simulation studies and offered approximately 20% material savings. This efficiency is achieved by strategically introducing hollow side regions, requiring concrete casting only in the central and boundary zones—unlike other infills that necessitate full-volume casting after reinforcement placement. The seismic performance of different infill patterns (Fig. 6.3) is evaluated through numerical simulations under quasi-static cyclic loading (Fig. 6.4), with each configuration examined in combination with the proposed reinforcement layout. The results indicate that the proposed infill pattern enhances lateral load capacity by approximately 20% and exhibits a slower rate of stiffness degradation compared to alternative patterns (Fig. 6.4). This improvement reflects superior energy dissipation and structural integrity, primarily attributed to the continuous reinforcement and the incorporation of a double-layered arrangement at the corner regions, which represent the most critical zones under seismic loading. Additionally, the proposed infill achieves these benefits while requiring a reduced material volume, thereby improving both structural efficiency and resource utilization.

Based on its structural viability, reinforcement compatibility, and material efficiency, the proposed infill pattern (Fig. 6.3e) is selected for final implementation in the experimental program, forming the basis for the subsequent quasi-static cyclic loading tests.

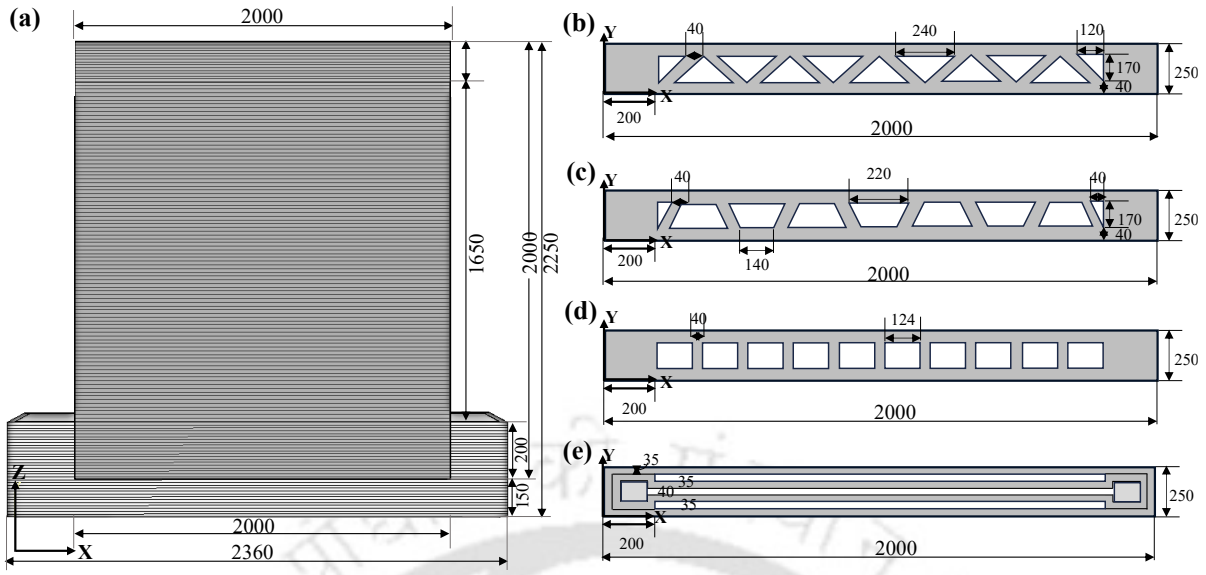

Fig. 6. 3. (a) 3DPC wall configuration (All dimensions are in mm); various infill patterns selected for final reinforcement layout and cyclic testing of the 3DPC wall: (b) truss infill; (c) rhombus infill; (d) rectangular infill; (e) proposed infill

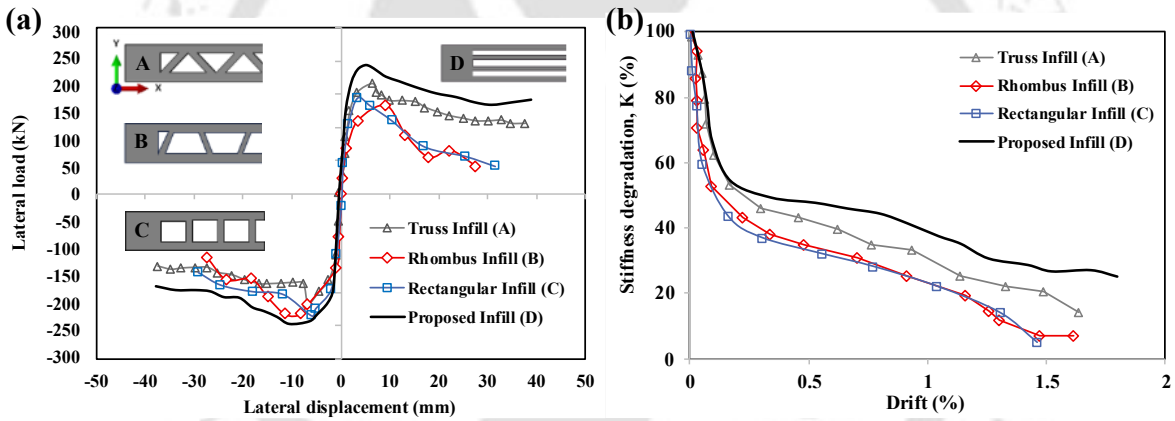

Fig. 6. 4. Comparison of different infill patterns under simulated quasi-static cyclic loading (a) envelope curve; (b) stiffness degradation

The complete fabrication sequence of the 3DPC walls is schematically illustrated in Fig. 6.5, and the actual experiment figures are included in Appendix (A1). First, the bottom mould is cast, followed by the casting of reinforced beams up to a height of 150 mm within the mould. For the 3DPC-CFR wall, a hollow arrangement is created by inserting foam during casting to accommodate the column reinforcement and the vertical bars of the central grid. The wall printing process is then initiated, and after the wall reaches a height of 2 m, continuous printing of the top beam mould is carried out to an additional height of 200 mm. Reinforcement cages, along with strain gauges, are subsequently placed in the longitudinal direction of the columns at 16 critical locations (Fig. 6.7). Thereafter, the walls are cast in the column regions and the central portion only, where the reinforcements are provided. To maintain equivalent boundary

conditions and ensure uniform load transfer during testing, the other two walls without reinforcement (3DPM and 3DPC-CF) are also cast in the same regions. This approach minimizes variations in structural response that could arise due to differences in support conditions, thereby allowing a more accurate comparison of the seismic performance among all wall specimens. Finally, the walls are cast using the same material employed during printing: mortar for the mortar wall and a mixture containing coarse aggregates and the critical fiber volume fraction for the 3DPC-CF wall.

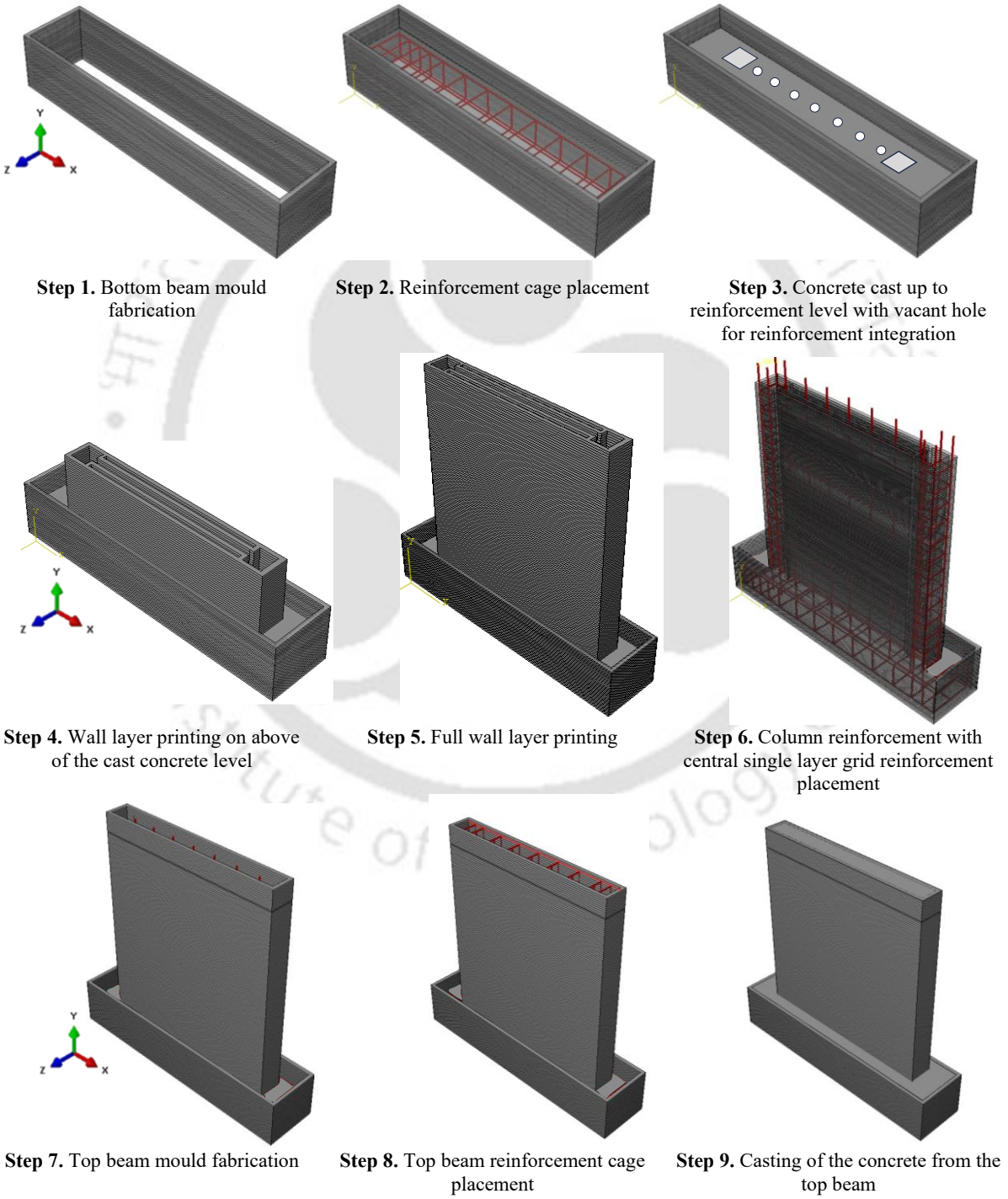

Step 1. Bottom beam mould fabrication

Step 2. Reinforcement cage placement

Step 3. Concrete cast up to reinforcement level with vacant hole for reinforcement integration

Step 4. Wall layer printing on above of the cast concrete level

Step 5. Full wall layer printing

Step 6. Column reinforcement with central single layer grid reinforcement placement

Step 7. Top beam mould fabrication

Step 8. Top beam reinforcement cage placement

Step 9. Casting of the concrete from the top beam

Fig. 6. 5. Illustration of the fabrication process of 3DPC-CFR wall

6.3.2. Reinforcement detailing of designed 3DPC walls

The reinforcement configuration adopted for the structural 3DPC walls are illustrated in Fig. 6.6, where detailing is carried out in accordance with the design recommendations of ACI 318-19 [11], Eurocode 8 [12], and IS 13920-2016 [13]. The reinforcement strategy is developed to ensure ductile response under seismic loading while remaining compatible with the constraints of 3D printing. The reinforcement layout, including both central grid and boundary zones, is finalized based on structural design calculations, with a focus on achieving consistent axial load, wall geometry, and aspect ratio of all specimens. This ensures that the influence of material type and reinforcement arrangement can be studied in isolation, eliminating other confounding parameters.

To ensure printability, structural compliance, and ease of reinforcement integration, the infill pattern is selected through a comparative evaluation of various configurations under simulated cyclic loading (Fig. 6.4). Reinforcement spacing and layer deposition are determined in accordance with relevant design standards [11,12] and practical printing constraints. Furthermore, all design parameters and fabrication strategies for the 3DPC walls are developed not only to meet established codal guidelines but also to ensure direct applicability in real-world construction scenarios—thereby advancing the practical deployment of 3DPC and pushing the boundaries of its structural use in seismic applications globally. The transverse reinforcement spacing follows Eurocode 8 (EN 1998-1, Section 5.4.3.5.2), which limits horizontal bar spacing to the lesser of 300 mm or 0.75 times the wall thickness. For a wall thickness of 250 mm, this translates to a maximum spacing of 187.5 mm. In this analysis, a transverse spacing of 140 mm is adopted for both the central reinforcement grid and the stirrups in the confined boundary columns (as per ductility-based design provisions of Eurocode 8). For vertical reinforcement, a spacing of 250 mm is maintained in the central zone, aligning with the minimum vertical reinforcement ratio of 0.25% (IS 13920: 2016, Clause 10.1.6 [13]). The overall reinforcement layout meets and exceeds the minimum vertical and horizontal reinforcement thresholds, providing reliable confinement and enhanced ductility under cyclic loading conditions. All walls maintain a constant aspect ratio (h_w/l_w) of 1.0 and a slenderness ratio (h_w/t_w) of 8.0, accordance with established design standards [11], ensuring consistent and codal-compliant geometrical parameters across all test specimens. The central region is reinforced using a modular steel grid, designed for integration without interrupting the printing process, while the end columns feature confined boundary reinforcement (CBRF) to enhance edge confinement and energy dissipation. Importantly, the modular nature of the reinforcement

cage facilitates future potential for automation in reinforcement placement, making it well-suited for scalable additive construction workflows.

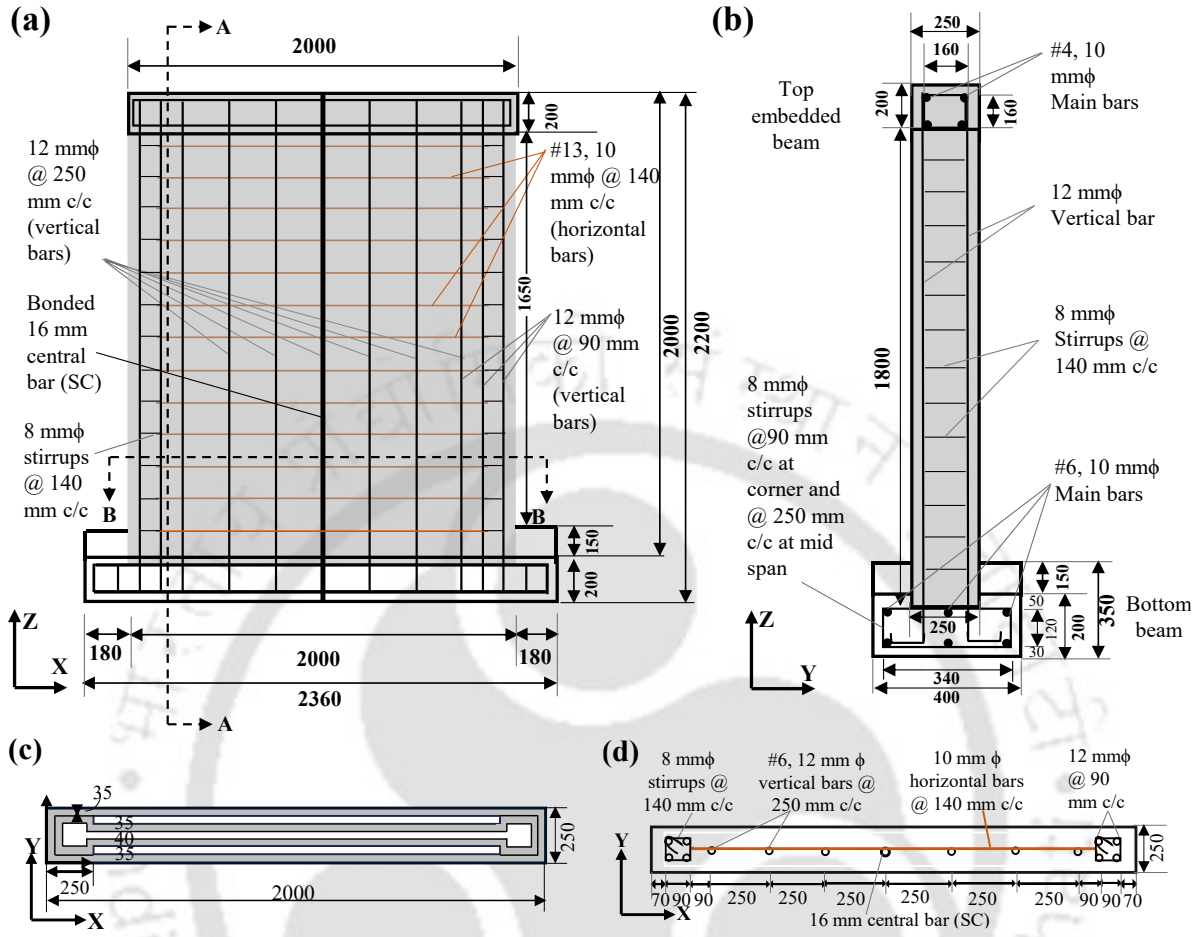

Fig. 6. 6. Reinforcement details of the structural 3DPC wall (a) elevation of 3DPC-CFR; (b) infill pattern; (c) cross-section detailing along A-A; (d) detailing along B-B process

6.3.3. Test procedure, instrumentation and loading protocol

All wall specimens are tested under a standardized setup to ensure consistent evaluation of their seismic performance (Fig. 6.8). The foundation beams are firmly anchored to the laboratory strong floor to eliminate any risk of sliding or overturning during cyclic loading. To prevent out-of-plane movement, steel buttress frames with roller bearings are positioned at slab level, ensuring in-plane deformation is captured accurately. The deformation response of the specimens is monitored using linear variable differential transformers (LVDTs) placed at different heights along the tie-columns. Critical strain development in the reinforcement is captured by strain gauges bonded at predetermined locations along the longitudinal bars, particularly in regions susceptible to plastic hinge formation (Fig. 6.7). A complete step wise procedure to attach the strain gauges are described in Appendix (A2). Additionally, a uniform pre-compression load of 18 kN, equivalent to approximately 2.5% of the axial load capacity,

is applied to all walls. This simulates the influence of vertical gravity loads and reproduces realistic boundary conditions during seismic action.

Fig. 6. 7. (a) Modular reinforcement cage showing the complete 3D configuration with strain gauges with cross-sectional infill pattern; (b) 3DPC–CFR wall with visible strain gauge wires

Quasi-static lateral loading is applied through a servo-controlled hydraulic actuator with a load capacity of 250 kN and a stroke length of ±500 mm, attached at the center of the top beam (Fig. 6.8). The loading history consists of displacement-controlled cycles, where lateral drifts are progressively increased to capture post-yield and failure behavior (Fig. 6.8b), as per ACI 374.1–05 [237]. Each cycle is repeated thrice for all specimens. Loading is applied alternately in push and pull directions, corresponding to positive and negative displacement histories. A preload of 20 kN is introduced in all specimens to stabilize the wall and the actuator–specimen interaction before formal testing. Displacement-controlled loading is quantified using the lateral drift ratio (θ), defined as $\theta = \Delta/H$, where Δ denotes the lateral displacement at the loading point and H is the wall height to the actuator level. In addition, the specific distributions of linear variable differential transformers (LVDTs) and strain gauges are provided and illustrated in Fig. 6.7 and Fig. 6.8a, respectively. Alongside global displacements, shear deformations and foundation beam movements are measured to obtain a comprehensive response profile. All measurements are integrated into a computer-controlled data acquisition system, developed

and operated using LabVIEW, ensuring synchronized recording and high-resolution analysis of the structural response of all the walls.

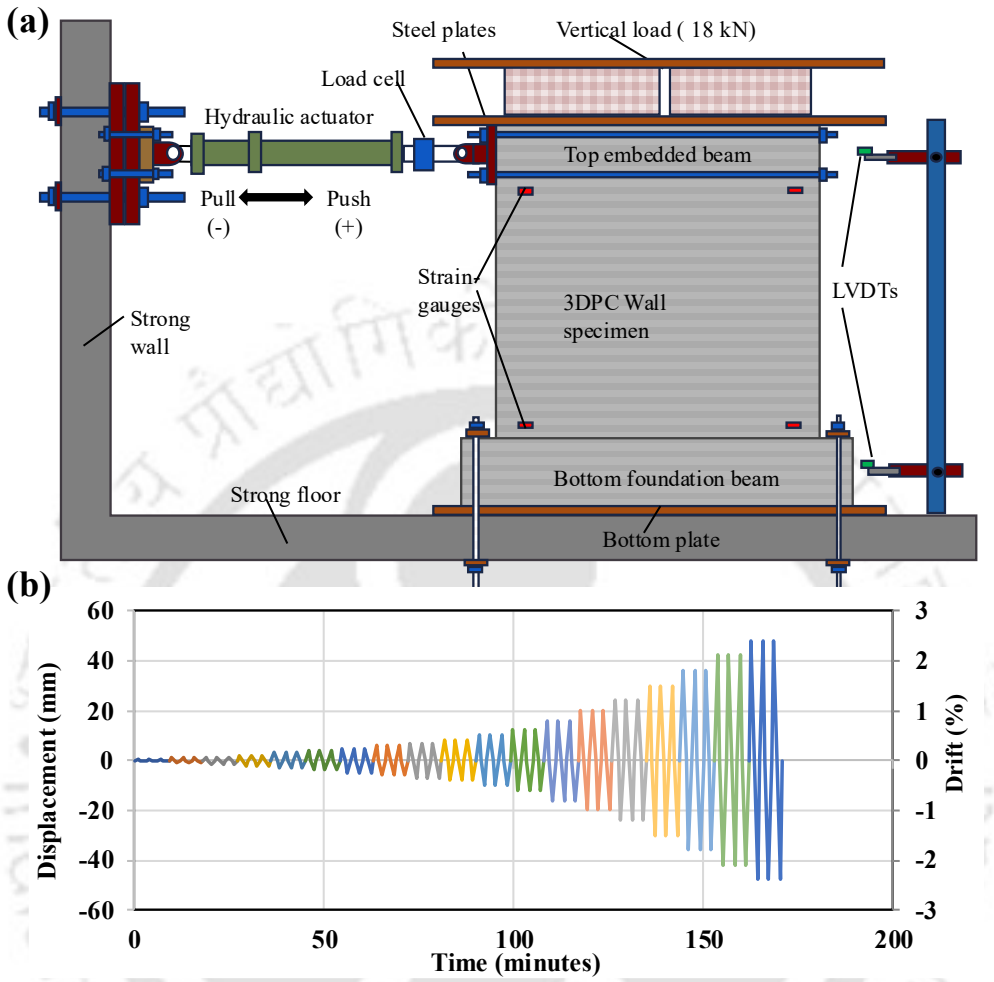

Fig. 6. 8. Schematic representation of the experimental setup and instrumentation; (b) loading protocol

Table 6.7 shows the details of all the specimens. The selected wall parameters are consistent with the provisions of IS 13920:2016 [13], thereby ensuring codal compliance and reliable seismic performance. The adopted wall thickness of 250 mm exceeds the minimum requirement of 150 mm specified for special shear walls (Clause 10.1.2). The ratio of wall length to thickness (L_w/t_w = *8*) is greater than the prescribed minimum of *4* (Clause 10.1.3), confirming adequate in-plane stiffness. The height-to-length ratio (h_w/l_w = 1.0) classifies the wall as intermediate, in line with Clause 10.1.4. Boundary elements with dimensions of 250 × 250 mm have been provided at the edges, satisfying the requirements of Clause 10.4.1.

Furthermore, for the quasi-static cyclic loading tests, the constant axial precompression equal to 2.5% of the sectional axial capacity is applied during the cyclic loading protocol. This level

of axial load is intentionally selected to reproduce the behaviour of structural wall elements operating under light-to-moderate gravity effects, which is characteristic of many wall-type systems, 3D-printed structural elements, and emerging low-density or optimized construction typologies [6]. Previous experimental programs on RC and composite walls have also employed low axial load ratios in the range of 1–3% to isolate the lateral–flexural deformation mechanisms and to limit the artificial confinement that higher axial loads tend to induce [238]. Lower axial ratios are known to promote a more pronounced flexural cracking pattern, wider hysteresis loops, and clearer identification of strain-hardening or ductility-enhancing mechanisms—responses that cannot be observed clearly when the element is tested under high axial compression. Since the objective of this study is to quantify the intrinsic lateral load-resisting behaviour, ductility development, and energy dissipation characteristics of the material/system without the overshadowing influence of high axial confinement, the adopted axial load level of 2.5% aligns well with established experimental practices and provides a conservative yet realistic representation of lightly loaded structural elements. Additionally, recent recommendations for some precast interfaces identify 0.025 as a practical lower bound to avoid shear-slip problems [239], making the chosen precompression scientifically consistent with the behavioural regime being investigated. For the 3DPC walls with an average nominal axial capacity of 700 kN, this corresponds to an applied axial load of 18 kN, equivalent to an average compressive stress of approximately 0.045 MPa over the gross wall cross-section. This level of precompression is sufficient to represent realistic gravity effects while avoiding excessive constraint on lateral deformation, thereby allowing a focused evaluation of the wall's cyclic behavior and ductility characteristics.

Table 6. 7. Details of all the specimens

Specimen	Height × Width × Thickness (mm)	Aspect ratio (Height / Width)	Slenderness ratio (Height/ Thickness)	Edge column (mm)	Axial force ratio
3DPM	2000×2000×250	1	8	200×250	0.025
3DPC-CF	2000×2000×250	1	8	200×250	0.025
3DPC-CFR	2000×2000×250	1	8	200×250	0.025

This restriction ensures adequate ductility and prevents brittle compression failure in reinforced concrete walls under seismic actions. This consideration is particularly important for reinforced 3DPC walls due to their layer-by-layer construction and potential anisotropy in material behaviour. Collectively, these chosen parameters reflect compliance with the codal guidelines and support the structural effectiveness of reinforced 3DPC walls under seismic actions.

6.4. Results and discussion

This Section investigates the seismic performance of 3DPC walls, focusing on the earthquake-resistant design by integrating the codal provisions and strain hardening ductile material. Specifically, three types of full-scale 3DPC walls (3DPM, 3DPC-CF, and 3DPC-CFR) are designed with internal infill geometry for seamless integration with the printing process. The reinforcement strategy, consisting of centrally aligned vertical bar and confined boundary reinforcement (CBRF), follows the provision of IS 13920-16 [13], ACI 318-19 [11], and Eurocode 8 [12] and is implemented using modular prefabricated grid cages. The discussion below explores the key findings, their implications for 3DPC wall design, and recommendations for future research.

6.4.1. Response of the specimen

6.4.1.1. Hysteresis curve: cyclic force-displacement plots

The ability of a structural wall to dissipate energy under cyclic loading is governed by its load-carrying capacity, deformation tolerance, and stability of hysteretic response. A comparative evaluation of the three wall configurations—3DPM, 3DPC-CF, and 3DPC-CFR—clearly demonstrates the progressive enhancement in lateral resistance and deformation capacity as material (with ductile strain hardening behaviour) and optimized reinforcement are introduced.

The reference plain wall (3DPM) reached a maximum lateral load of 76.94 kN and a peak deformation of 12.52 mm, producing slender, pinched hysteresis loops characteristic of limited energy dissipation and rapid stiffness degradation (Fig. 6.9). This response is indicative of brittle behavior (Fig. 6.10a), where cracking initiates early at the wall–beam interface and damage localizes due to insufficient tensile bridging and low interlayer cohesion. The sharp post-peak strength reduction confirms minimal reserve strength beyond first cracking. In contrast, the 3DPC-CF wall achieved a significantly higher peak load of 175.51 kN, representing an approximate 128% increase in lateral load capacity relative to 3DPM (Fig. 6.9b). Similarly, the deformation capacity improved to 26.28 mm, which is an 110% enhancement over the 3DPM. The hysteresis loops for this wall configuration are noticeably broader, with reduced pinching, demonstrating that the corrugated steel fiber facilitates distributed cracking with fibre bridging phenomenon (Fig. 6.10d), increases the effective tensile capacity of the matrix, and delays damage localization. Although strength degradation becomes apparent at larger drift demands, the wall maintains stable cycling without sudden drops, reflecting improved ductility derived from the strain-hardening composite.

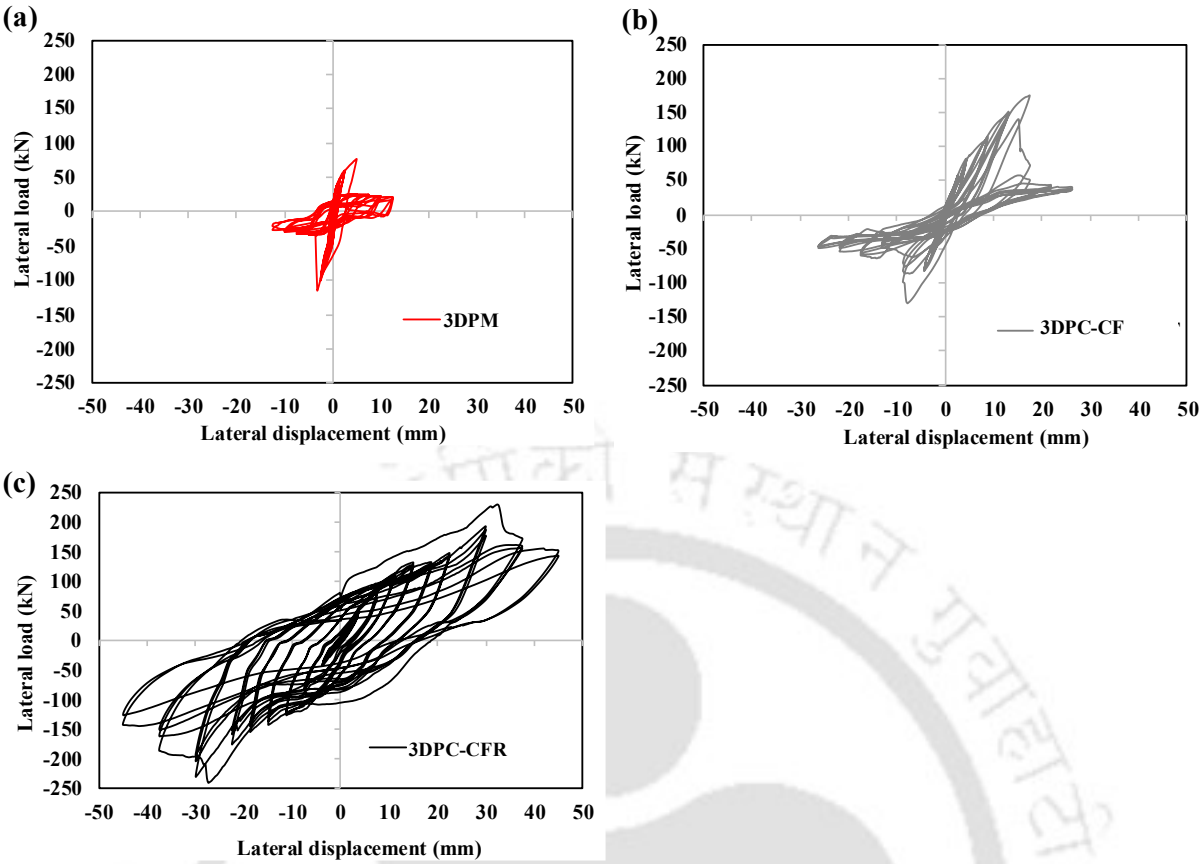

Fig. 6. 9. Hysteretic response (a) 3DPM; (b) 3DPC-CF; (c) 3DPC-CFR

The most pronounced improvement is observed in the 3DPC-CFR wall, which exhibited a peak lateral load of 228.84 kN, equal to a 197% increase compared to 3DPM and a 30% increase over the 3DPC-CF wall (Fig. 6.9). The deformation capacity also increased to 45.02 mm, which corresponds to a 260% increase relative to 3DPM and a 71% improvement relative to 3DPC-CF. The hysteresis loops for 3DPC-CFR wall are substantially larger with minimal pinching, indicating superior energy dissipation capacity. The integration of vertical reinforcement and boundary confinement significantly enhances the tensile stress redistribution capabilities, improves interlayer shear transfer, and stabilizes the post-peak response. This leads to symmetric load–displacement behavior across cycles and prevents abrupt strength degradation even at higher drift levels. The confined reinforcement region effectively restrains crack propagation and enhances the composite action between the printed layers and concrete, resulting in a stable and ductile cyclic response.

6.4.1.2. Crack pattern and failure mechanism

The observed failure modes and crack patterns of the three full-scale 3DPC walls indicate that material composition and reinforcement strategy significantly influence structural response under cyclic in-plane loading. 3DPM exhibited predominantly brittle behavior, with horizontal

cracking and completely separated after peak load. Sliding shear deformations are evident without flexural failures, highlighting a shear-dominated response with rapid strength degradation (Fig. 6.10a). In contrast, 3DPC-CF displayed a flexural-dominated response, characterized by minor diagonal cracks near toe region without premature shear failure. Crack initiation occurred at approximately 0.52–0.66% top drift, with the first cracks developing at 38–39% of the experimental yield load (Fig. 6.10b). Post-cracking, the 3DPC-CF exhibited gradual strength reduction and distributed cracking, with concrete spalling observed near the compression zones at higher drifts (1.0–1.5%). Notably, the strain-hardening composite exhibited sustained crack-control capability, with fibers effectively maintaining load transfer across crack openings up to 15 mm. The persistence of this bridging mechanism (Fig. 6.10b) under large-amplitude cyclic deformations highlights the material's exceptional tensile strain capacity and its ability to delay loss of structural integrity even at substantial damage states.

The 3DPC-CFR wall exhibits the highest structural resilience among the tested specimens (Fig. 6.10c). Yielding of the outer longitudinal reinforcement is observed at approximately 0.52% drift, while initial cracking in the wall panel occurred later, at about 1.2% drift (22 mm displacement), indicating delayed tensile distress due to the improved composite action. The peak lateral resistance is recorded at approximately 1.8–2.0 d_y displacement levels, after which the specimen experiences-controlled damage concentrated primarily in the bottom beam on both the compression and tension sides, with no significant cracking or degradation observed in the central wall region and no evidence of longitudinal bar buckling (Fig. 6.10c). The ultimate failure mode is governed by localized concrete crushing in the bottom beam, while the longitudinal steel bars remained structurally intact, demonstrating enhanced ductility and sustained energy dissipation capacity with considerable post-peak load retention. This enhanced performance can be attributed to the synergistic effect of the strain-hardening ductile concrete matrix and the prefabricated reinforcement cage. The 3DPC-CF matrix facilitates distributed micro-cracking, delaying the formation of localized failure planes and allowing progressive energy absorption. Simultaneously, the CBRF ensures effective confinement of the concrete core, improves bond between reinforcement and the matrix, delays bar buckling, and stabilizes post-peak deformation. Together, these mechanisms enable the wall to sustain higher drifts, achieve greater cumulative energy dissipation, and resist brittle failure, consistent with principles of reinforced concrete seismic design where confinement and ductile matrix behavior are critical for enhanced structural resilience.

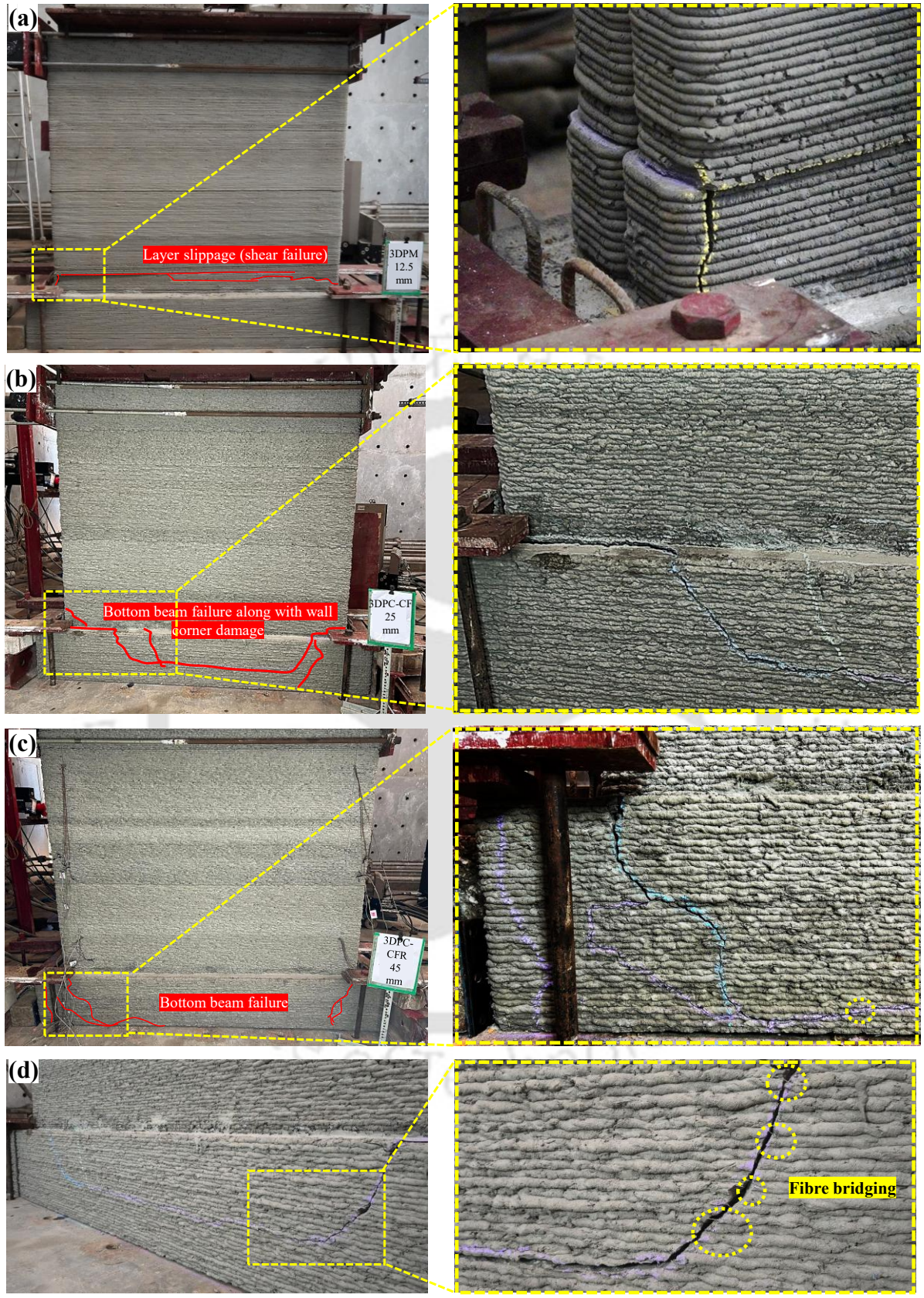

Fig. 6. 10. Ultimate failure modes of the 3DPC walls (a) 3DPM; (b) 3DPC-CF; (c) 3DPC-CFR; (d) fibre-bridging in 3DPC-CF during cyclic testing

6.4.1.3. Strain in longitudinal bars (CBRF)

The strain development in CBRF of the 3DPC-CFR wall is evaluated through strain gauges installed on the longitudinal bars at four critical regions where plastic hinges are expected to form (Fig. 6.7). The recorded strain responses across locations 1–4 demonstrate consistent and stable bond transfer between the reinforcement and the 3DPC matrix, confirming effective composite interaction under cyclic in-plane loading. Across all measurement locations, the reinforcement exhibits a tension-dominated response, with tensile strains increasing significantly with drift while compressive strains remain comparatively small. Strains remain negligible in the pre-cracking regime but begin to rise sharply once flexural cracking initiates. Among the four monitored regions, location 3 consistently develops the highest tensile strain, reaching peak values of 0.0028, which is 30% higher than the peak strains observed at locations 1 and 2 (0.0020–0.0022) and nearly 50% higher than those at location 4 (0.0016) (Fig. 6.11).

This elevated response at location 3 reflects its position within the primary plastic hinge zone at the wall–foundation interface, where maximum curvature demand is concentrated. The reinforcement at location 3 also shows the earliest and most rapid strain escalation after cracking, indicating that it experiences higher flexural tension demand relative to the other locations. Despite these elevated strain levels, the response remains smooth and stable, with no indication of bar instability or sudden strain reversal. The maximum recorded strains represent a substantial portion of the reinforcement's yield strain capacity (0.002–0.0025), demonstrating efficient mobilization of boundary reinforcement without exceeding safe deformation limits. The combined effect of centrally aligned grid reinforcement and CBRF effectively enhanced the ductility, deformation capacity, and seismic resistance of the 3DPC-CFR wall, thereby validating the proposed modular reinforcement strategy for 3D-printed structural applications. Overall, the strain profiles confirm that the CBRF is most active at the lower boundary region (location 3), where flexural demands are greatest, while locations 1, 2, and 4 exhibit progressively lower strain amplitudes consistent with reduced curvature demand. This behaviour aligns with the expected flexure-controlled response of RC and composite shear walls, where longitudinal boundary bars at the base experience the highest tensile demand and govern post-yield deformation capacity.

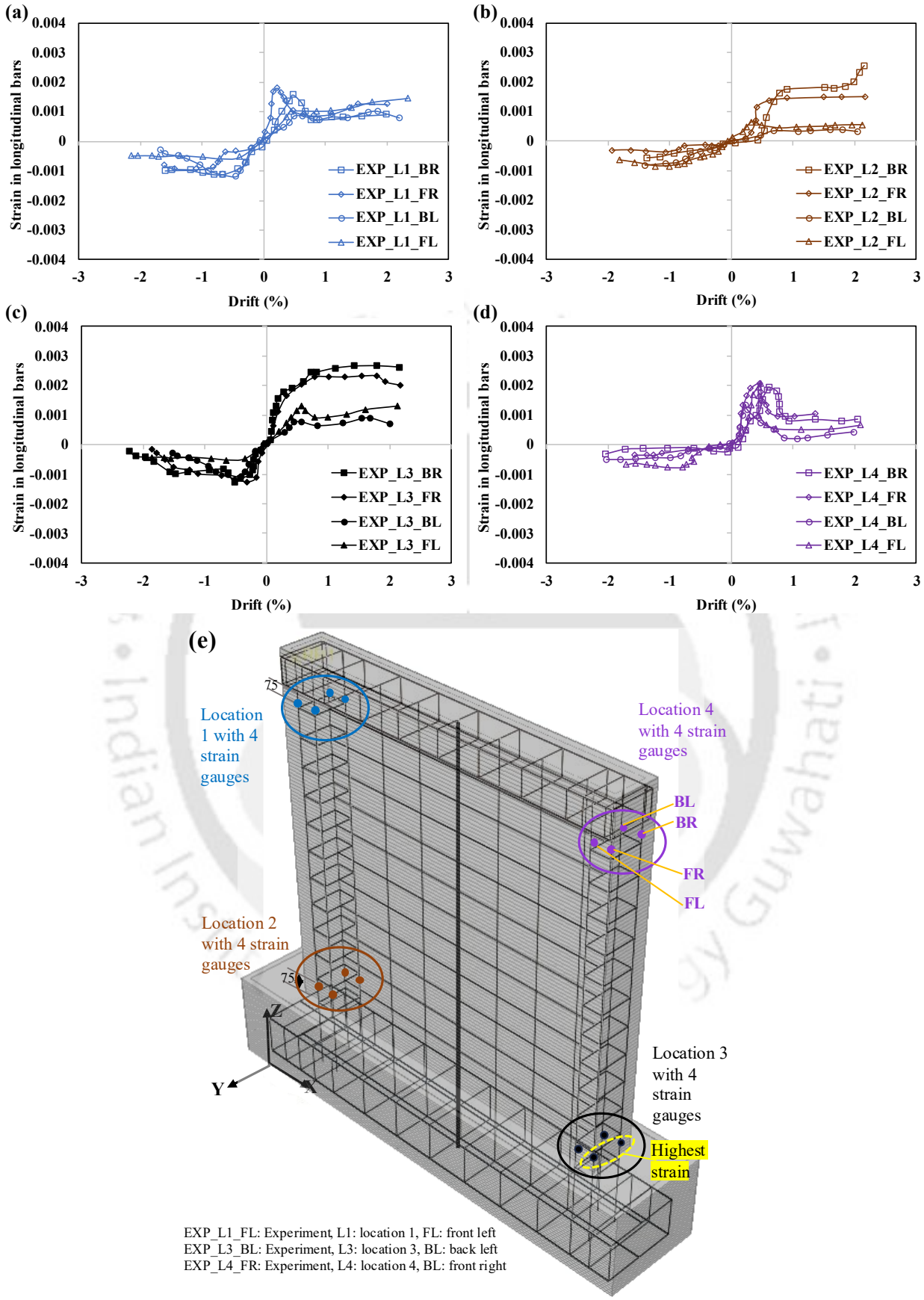

Fig. 6. 11. Strain in the longitudinal bars in CBRF (a) at location 1; (b) at location 2; (c) at location 3; (d) at location 3; (e) strain gauge locations in 3DPC-CFR

6.4.2. Influencing seismic parameters analysis

This section delves into key structural properties, including energy absorption, equivalent damping, strength degradation, stiffness degradation, damage index, ductility, structural behaviour factor, and strain in concrete for all 3DPC walls. These parameters are crucial for evaluating the seismic performance of walls, as they influence the structure's ability to withstand deformations, resist forces, and dissipate energy effectively during seismic events. Understanding these properties ensures the design of resilient and efficient 3DPC walls tailored to varying seismic demands.

6.4.2.1. Envelope curve

The envelope curve, obtained by connecting the peak force points of successive loading cycles from the hysteretic response, represents the equivalent monotonic behavior of the wall specimens. The envelope curves extracted from the hysteretic responses of the three wall specimens provide a clear representation of their monotonic strength development, peak resistance, and post-peak degradation characteristics (Fig. 6.12a). The 3DPM wall exhibits a steep initial stiffness followed by an early strength plateau, reaching a maximum lateral load of 76.94 kN, after which a rapid drop in capacity reflects its brittle, shear-governed failure. In contrast, the 3DPC-CF wall shows a significantly larger and smoother envelope, with peak strength increasing to 175.51 kN, indicating a 128% enhancement relative to 3DPM. This improvement corresponds to the strain-hardening behavior of the ductile matrix, which enables gradual micro-crack propagation and delays stiffness deterioration.

The 3DPC-CFR wall presents the most robust envelope among the three, achieving a peak lateral load of 228.84 kN, representing a 197% increase over the reference wall (3DPM) and a 30% gain over the 3DPC-CF configuration. Its envelope curve displays pronounced post-peak load retention and a well-distributed degradation slope, confirming the stabilizing influence of modular boundary reinforcement and efficient stress redistribution under increasing drift. The progressive widening of the envelope—from 3DPM to 3DPC-CF and ultimately to 3DPC-CFR—demonstrates the collective effects of strain hardening material, controlled crack formation, and reinforcement confinement on the in-plane cyclic resistance of large-scale 3DPC walls.

6.4.2.2. Energy dissipation capacity

The ability of a structural element to dissipate energy is a key indicator of its seismic performance, as it represents the portion of input energy absorbed through inelastic deformation during cyclic loading. This dissipated energy directly contributes to an increased

equivalent damping ratio, thereby enhancing the element's capacity to withstand repeated lateral reversals without experiencing severe strength degradation. In experimental studies, the cumulative area enclosed by the load–displacement hysteresis loops is widely accepted as the principal metric for quantifying this behavior.

In the present research, the evolution of energy dissipation for the three wall specimens is assessed as a function of increasing lateral displacement. At low displacement levels (up to approximately 5 mm), the energy dissipation capacities of all three walls remained comparable, with differences within around **5–10%**, reflecting predominantly elastic response and limited crack development. As the lateral displacement increased beyond 10 mm, pronounced performance differences emerged. The 3DPC-CF wall exhibited a noticeable rise in cumulative energy dissipation i.e., 99% higher than the 3DPM wall at comparable displacement levels, and showing almost the same enhancement as 3DPC-CFR. This improvement is attributed to the strain-hardening response of the ductile matrix, which facilitated the formation of multiple micro-cracks, enabling the specimen to sustain higher inelastic deformation without localized damage concentration (Fig. 6.12b). The 3DPC-CFR wall demonstrated the most pronounced improvement. Relative to the 3DPM specimen, the energy dissipation increment reached as high as 614% at larger displacements, indicating a more than sixfold improvement in seismic energy absorption at larger displacement stages. When compared to the 3DPC-CF wall, the 3DPC-CFR specimen further exhibited 83% higher energy dissipation across the displacement range. This significant enhancement is attributed to the synergistic action between the strain-hardening matrix and the optimized reinforcement with CBRF, which together improved load redistribution, delayed localized cracking, and enabled sustained inelastic deformation. These results clearly indicating that the reinforcement strategy effectively engaged after matrix cracking, sustained tensile resistance, and stabilized post-peak behavior. These findings emphasize that while material composition (as in 3DPC-CF) improves ductility and energy absorption, the integration of optimized reinforcement (3DPC-CFR) further amplifies seismic performance by maximizing cumulative energy dissipation and mitigating stiffness degradation under repeated cyclic loading.

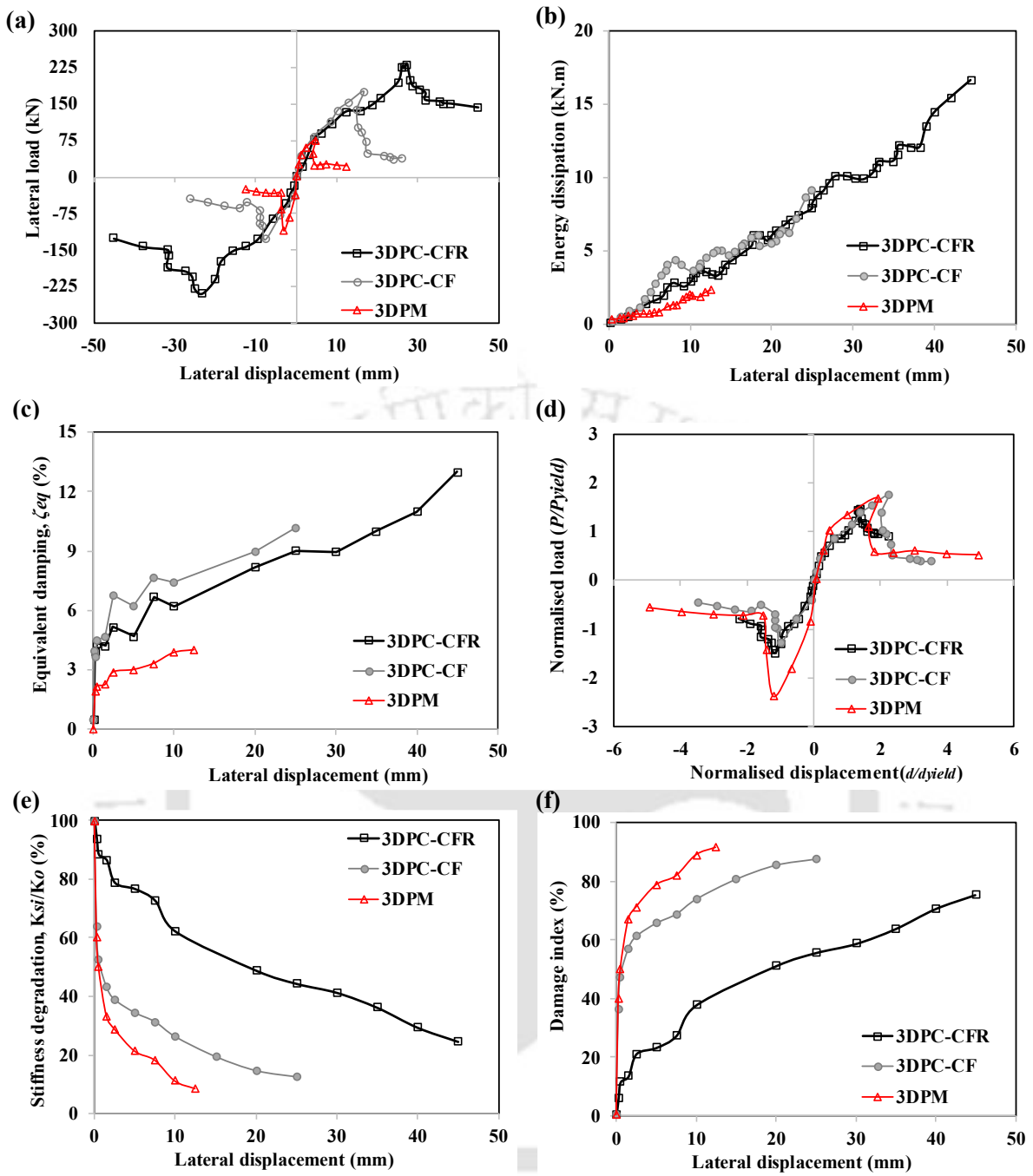

Fig. 6. 12. Comparison of key influencing seismic parameters (a) envelope curves of the hysteretic response; (b) energy dissipation per loading cycle; (c) equivalent viscous damping; (d) strength degradation; (e) stiffness degradation; (f) damage index

6.4.2.3. Effect on viscous damping

The correlation between energy dissipation and wall response is not always straightforward; in some cases, narrow hysteresis loops with higher load resistance can dissipate more energy than wider loops with lower resistance. To enable consistent comparison, the equivalent viscous damping ratio (ζ_{eq}) is also determined for the 3DPC walls. This parameter is calculated by

equating the energy released in each hysteretic cycle to that of an equivalent linear viscous system, as expressed in Eq. (6.1):

$$\zeta_{eq} = \frac{E_i}{2\pi K_{si}\delta_{max,i}^2} \tag{6.1}$$

In this equation, E_i represents the energy dissipated during each cycle, K_{si} is the secant stiffness of the cycle, and $\delta_{max,i}$ is the maximum displacement during the i^{th} load cycle.

Fig. 6.12c illustrates the evolution of ζ_{eq} with increasing displacement for all three wall specimens. At small displacement levels (≤ 2.5 mm), both the 3DPC-CFR and 3DPC-CF walls exhibited nearly identical damping ratios (≈3.8–5.16%), indicating that the initial damping behavior is dominated by matrix cracking and elastic–inelastic transition rather than reinforcement effects. Within this range, the 3DPM wall exhibited substantially lower damping (≈1.9–2.9%), reflecting its limited micro-crack distribution and higher tendency toward localized cracking. Between intermdiate displacement levels of approximately 7.5 mm and 25 mm, the influence of strain hardeneing ductile matrix became progressively evident. The 3DPC-CF wall consistently exhibited higher damping (≈7.7–10.2%) compared with the 3DPC-CFR specimen (≈6.7–9.01%), with the 3DPC-CF wall showing up to 15–20% greater ζ_{eq} in this intermediate drift region. This enhancement is linked to the distributed micro-cracking and stable inelastic deformation associated with the strain-hardening matrix, which contributes to greater equivalent damping as cyclic degradation progresses.

At larger displacement demands (≥ 25 mm), the response trends shifted. The 3DPC-CFR wall demonstrated a steady increase in ζ_{eq}, reaching 9–13%, whereas the damping capacity of the 3DPC-CF wall plateaued around 10.2% near 25 mm displacement. The continued rise in the CFR wall's damping ratio is attributed to the combined action of boundary confinement and centrally aligned grid reinforcement, which delays stiffness degradation and maintains higher lateral resistance at large deformation amplitudes. This sustained strength retention magnifies the damping contribution, particularly as energy dissipation grows with each cycle. Across all drift levels, the 3DPM wall consistently exhibited the lowest ζ_{eq} (≈1–4%), confirming its limited capacity to dissipate energy due to reduced ductility and early stiffness degradation. This behavior underscores the crucial role of both fiber reinforcement and boundary steel confinement in enhancing damping characteristics and overall cyclic stability.

6.4.2.4. Strength degradation

Post-peak strength degradation is a critical parameter for assessing the residual load-carrying capacity, deformation tolerance, and overall seismic stability of structural walls. To quantify

this response, the lateral load in each cycle is normalized with respect to the corresponding yield strength (P_{yield}), and the displacement is normalized by the yield displacement (d_{yield}). The resulting strength degradation curves, expressed as P/P_{yield} versus d/d_{yield}, are presented in Fig. 6.12d. Across the cyclic history, 3DPM and 3DPC-CF exhibited broadly similar degradation trends, characterized by a monotonic reduction in normalized lateral resistance as displacement demands increased. For the 3DPM wall, this degradation occurred rapidly due to early localization of cracking and brittle post-peak softening, causing a steep drop in strength for both positive and negative excursions. The 3DPC-CF wall displayed a comparatively slower decay, attributed to the distributed micro-cracking and gradual stiffness reduction typical of strain-hardening ductile matrix. Nevertheless, in the absence of boundary reinforcement, its normalized strength eventually stabilized at moderate residual levels once the matrix cracking saturated. A distinct behavior is observed in the 3DPC-CFR wall. Following the initial post-peak drop in normalized strength, a noticeable increase in P/P_{yield} occurred, producing a mild "re-hardening" response before the curve resumed its degrading trend. This secondary rise in strength aligns with the confining action provided by the centrally aligned grid reinforcement and prefabricated boundary cage, which prevented premature spalling, enhanced lateral restraint, and mobilized additional resistance at larger drift demands, confirming the role of well-anchored reinforcement in delaying instability.

A direct comparison at a common drift level highlights these trends quantitatively. At a normalized displacement of approximately 1.75%, the residual strength ratios for 3DPC-CFR, 3DPC-CF, and 3DPM are 0.88, 0.69, and 0.48, respectively. These results demonstrate that the 3DPC-CFR wall retained ~80% more residual strength than the 3DPM wall and approximately 28% greater residual strength than the 3DPC-CF wall at the same drift. This superior performance arises from the coordinated action of a strain-hardening ductile matrix and boundary reinforcement, enabling progressive crack distribution, delayed localization, and improved confinement.

6.4.2.5. Stiffness degradation and damage index

Stiffness degradation describes the progressive reduction in the lateral stiffness of structural members when subjected to cyclic or seismic loading. It reflects how the structure gradually loses its capacity to resist deformation under repeated lateral actions. The degradation rate (K_R) is expressed through Eq. (2) as:

$$K_R = \frac{K_{si}}{K_0} \tag{6.2}$$

where K_{si} is the secant stiffness i.e., stiffness at a specific secant location and K_o is initial stiffness measured during the first loading cycle.

Fig. 6.12e illustrates the stiffness–displacement response of all three wall systems. A clear trend emerges: the 3DPM wall undergoes the most rapid degradation, losing nearly 50% of its initial stiffness within the first 2.5 mm of lateral displacement. This steep reduction aligns with the inherently brittle behavior of plain 3D-printed material (mortar), where cracking initiates early and propagates rapidly under cyclic loading. The 3DPC-CF wall shows a noticeably slower degradation pattern. At 5 mm displacement, it retains approximately 34% of its initial stiffness, compared to only 21% for the 3DPM wall at the same displacement. This improved stability is attributed to the strain-hardening ductile matrix, which delays crack localization and distributes deformation more uniformly. The most favorable performance, however, is demonstrated by the 3DPC-CFR wall. This wall maintains a significantly higher stiffness across the entire displacement range. At the largest displacement tested (45 mm), the wall still maintains 24.5% stiffness, highlighting superior residual capacity. These observations confirm that although the ductile matrix plays a major role in controlling stiffness loss, the combined effect of the material and reinforcement yields the most stable stiffness profile. The continuous and uniform force transfer provided by long fibers suppresses crack widening (Fig. 6.10d), delays stiffness deterioration, and enhances the wall's tolerance to repeated lateral deformations. A summary of stiffness values corresponding to different displacement levels is presented in Table 6.8.

In addition to stiffness degradation, the damage index (*DI*) is used to quantify the extent of structural damage and assess wall performance under applied loading. The index is defined through Eq. (6.3) as [240]:

$$DI = 1 - \frac{K_{si}}{K_0} = 1 - K_R \tag{6.3}$$

As shown in Fig. 6.12f, the 3DPC-CFR wall exhibits the slowest and most controlled increase in *DI* with increasing displacement. At 5 mm displacement, the *DI* for the 3DPC-CFR wall is only 0.23, compared with 0.66 for the 3DPC-CF and 0.79 for the 3DPM. At 15–25 mm, while the 3DPC-CF and 3DPM walls exceed 0.80–0.90, the CFR wall remains around 0.50. More importantly, despite this measured *DI* in 3DPC-CF, its physical damage was limited to minor

flexural cracks near the base, without any signs of instability, sudden unloading, or brittle fracture (Fig. 6.10b). This behavior is highly noteworthy because the 3DPC-CF wall contains no passive reinforcement, meaning its stability arises purely from the inherent strain-hardening and crack-distribution capabilities of the fiber-rich ductile matrix (Fig. 6.12b,d). At the ultimate displacement level (45 mm) corresponds to a *DI* of approximately 0.75 for the 3DPC-CFR wall, which is consistent with major flexural cracking and localized concrete crushing near the base (Fig. 6.10c). However, despite this elevated *DI*, the wall maintained structural stability and did not exhibit signs of global instability or impending collapse (Fig. 6.10c). This satisfies the collapse-prevention criteria proposed by Carrillo [240], reaffirming the superior deformation and damage resistance of 3DPC-CFR systems.

6.4.2.6. Ductility assessment and structural behavior factor

The deformation response of the tested wall is examined through parameters such as drift, ductility, and the structural behavior factor. Ductility in structural walls describes their ability to undergo significant deformations without experiencing collapse. It is generally expressed in terms of displacement ductility (μ), calculated as the ratio of ultimate displacement (d_{ult}) to the yield displacement (d_{yield}), as shown in Eq. (6.4) and illustrated in Table 6.8:

$$\mu = \frac{d_{ult}}{d_{yield}} \tag{6.4}$$

Based on the experimental results, the 3DPM wall exhibited the lowest deformation capacity, with an ultimate displacement of 12.5 mm and a yield displacement of 5.0 mm, resulting in a displacement ductility of μ = 2.5. This limited ductility reflects the brittle nature of the unreinforced printed matrix and its tendency to develop localized cracking at relatively small deformations. The 3DPC-CF wall demonstrated a markedly improved ductile response, achieving an ultimate displacement of 25 mm against a yield displacement of 7.5 mm, resulting in μ = 3.5. Despite the absence of passive reinforcement, the strain-hardening cementitious matrix enabled stable crack distribution and delayed stiffness degradation, allowing the wall to undergo significantly larger inelastic deformation without instability. The highest ductility is observed in the 3DPC-CFR wall, which reached an ultimate displacement of 45 mm with a corresponding yield displacement of 10 mm, yielding μ = 4.5. The incorporation of modular reinforcement provided sustained tensile resistance after yielding and ensured effective confinement at the wall–foundation interface, which enabled the wall to accommodate large nonlinear deformations while maintaining stable hysteretic response. According to ASCE 41-17 [241], structural components exhibiting a displacement ductility $\mu \geq 4$ fall into the category

of high-ductility systems. Based on this criterion, the 3DPC-CFR wall clearly qualifies as a high-ductility element, while the 3DPC-CF wall approaches this threshold. The enhanced ductility recorded in both fiber-reinforced configurations underscores the synergistic effect of strain-hardening material behavior and controlled cracking in improving the deformation capacity of 3D-printed structural walls.

The response reduction or structural behavior factor reflects the system's capacity to dissipate seismic energy through nonlinear mechanisms. It is used to normalize the elastic seismic force ($P_{e,max} = K_o . d_{ult}$) to an equivalent design force or ultimate lateral capacity. The factor (q) is calculated as per Eq. (6.5) [242]:

$$q = \frac{P_{e,max}}{P_{ult}} \tag{6.5}$$

The experimental values of the structural behavior factor is found to be 4.86, in case of 3DPC-CFR. For comparison, EN 1998 (Part 1): 2004 [12] specifies structural behavior factors of 3.0 for medium-ductility RC walls and 4.0 for high-ductility walls. The experimentally observed values therefore place the 3DPC-CFR wall within the medium-to-high ductility range, confirming its favorable seismic energy-dissipation capability. In contrast, the 3DPC-CF and 3DPM walls exhibited lower behavior factors of approximately 3 and 2, respectively, reflecting their comparatively reduced capacity for nonlinear deformation and energy dissipation under seismic loading. Hence, the proposed 3DPC-CFR wall demonstrates ductility characteristics falling within the medium-to-high range. A summary of the key influencing parameters of the tested walls are presented in Table 6.8.

Table 6. 8. Influencing seismic parameters

Seismic parameter	Limit	3DPM			3DPC-CF			3DPC-CFR		
		Push (+)	Pull (-)	Average (CoV)	Push (+)	Pull (-)	Average (CoV)	Push (+)	Pull (-)	Average (CoV)
Lateral peak strength (kN)	Yield	26.77	33.12	29.95 (0.11)	101.45	115.65	108.55 (0.09)	210.12	196.22	203.17 (0.05)
	Ultimate	77.68	75.95	76.82 (0.01)	175.82	175.21	175.51 (0.01)	231.55	226.17	228.86 (0.01)
Deformation (mm)	Yield	4.57	5.33	4.95 (0.10)	7.56	7.45	7.51 (0.01)	10.52	10.54	10.03 (0.01)
	Ultimate	12.37	12.63	12.5 (0.01)	26.27	24.01	25.14 (0.06)	45.07	45.18	45.13 (0.01)
Drift (%)	Yield	0.23	0.27	0.25 (0.11)	0.37	0.37	0.37 (0.00)	1.23	1.27	1.25 (0.02)
	Ultimate	0.62	0.63	0.63 (0.01)	1.31	1.20	1.25 (0.06)	2.25	2.25	2.25 (0.00)
Energy Absorption (kNmm)	Yield	0.68	0.65	0.67 (0.03)	4.12	4.95	4.54 (0.12)	8.26	8.54	8.41 (0.02)
	Ultimate	2.34	2.22	2.28 (0.03)	9.12	9.15	9.14 (0.02)	16.67	15.61	16.14 (0.04)
Viscous damping (%)	Yield	3.05	2.99	3.02 (0.01)	7.68	7.66	7.67 (0.01)	9.03	9.14	9.09 (0.01)

	Ultimate	4.02	4.21	4.12 (0.03)	10.19	10.02	10.11 (0.01)	13.05	12.99	13.02 (0.01)
Strength degradation (%)	Yield	0.58	0.72	0.65 (0.11)	1.14	1.01	1.08 (0.08)	1.30	1.02	1.16 (0.17)
	Ultimate	0.92	0.56	0.74 (0.31)	0.4	0.44	0.42 (0.06)	0.78	0.89	0.84 (0.09)
Stiffness degradation (%)	Yield	20.33	21.98	21.35 (0.05)	32.15	30.28	31.26 (0.04)	43.59	45.09	44.34 (0.02)
	Ultimate	8.19	8.98	8.57 (0.06)	12.33	12.57	12.45 (0.01)	24.04	25.06	24.54 (0.02)
Damage index (%)	Yield	78.66	77.87	78.27 (0.01)	68.74	69.15	68.95 (0.01)	55.65	56.12	55.89 (0.01)
	Ultimate	91.43	90.45	90.94 (0.01)	87.55	86.51	87.03 (0.01)	75.46	74.89	75.18 (0.01)
Ductility factor	Ult/yield	2.70	2.36	2.52 (0.09)	3.47	3.22	3.34 (0.05)	4.28	4.28	4.49 (0.01)
Structural behaviour factor	Ultimate	1.99	2.05	2.02 (0.02)	3.01	2.98	3.00 (0.01)	4.74	4.98	4.86 (0.03)

Abbreviations: **CoV-** Coefficient of Variation (defined as the ratio of the standard deviation to the mean of a dataset)

Overall, the progression from 3DPM → 3DPC-CF → 3DPC-CFR demonstrates a systematic enhancement in lateral load resistance, drift capacity, and energy dissipation. The results highlight that fibers alone substantially improve ductility and distributed damage, while the addition of reinforcement and confinement provides the structural continuity and post-peak stability necessary for seismic applications.

6.4.3. Idealization with multi-linear backbone curve

An idealized multi-linear backbone curve is formulated following the Guidelines for Cyclic Response (GCR 14-917-25 [243]), as illustrated in Fig. 6.13. The backbone response is expressed in terms of shear capacity, defined through Eq. (6.6):

$$V = A_{cv}\tau \tag{6.6}$$

where A_{cv} represents the nominal shear area of the wall and τ denotes the shear stress. The proposed model adopts a modified shear modulus, ($G_{eff} = 0.8G_c$), up to a shear strength corresponding to $1.5\sqrt{f_{ck}}$,, identified as the cracking threshold. Beyond this point, a secondary slope of ($0.4G_c$) is used, extending from the first yield until 60% of the nominal shear strength ($0.6V_n$). The effective secant stiffness across these initial branches corresponds to approximately ($0.52G_c$), considering the compressive strength of the concrete. The final branch of the curve is assigned a reduced slope of ($0.1G_c$), continuing up to the nominal shear strength (V_n).

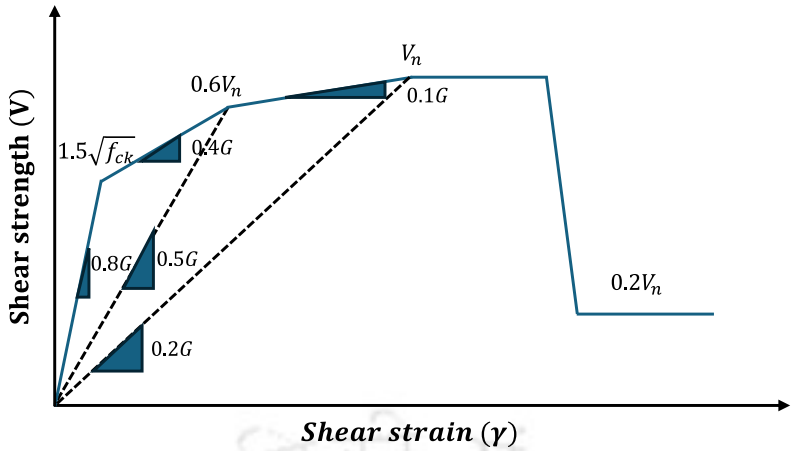

Fig. 6. 13. Multilinear idealized curve based on PEER/ATC-72-1, ASCE/SEI 41-06, and GCR 14-917-25 [243]

The experimentally obtained hysteretic responses for all three wall configurations are further idealized into multilinear backbone curves, as presented in Fig. 6.14. These curves provide a simplified yet structurally representative envelope that captures the essential strength, stiffness, and deformation characteristics required for performance-based seismic assessment. The idealization process, aligned with GCR 14-917-25 and ATC/PEER modeling guidelines [243], enables a direct interpretation of the nonlinear behavior by clearly defining the elastic, cracking, yielding, and post-peak degradation branches. For the 3DPM wall, the multilinear backbone highlights its limited deformation capacity and rapid post-cracking stiffness loss, consistent with the brittle shear-dominated response observed experimentally (Fig. 6.14a). In contrast, the 3DPC-CF wall exhibits a noticeably longer inelastic branch with a smoother transition from cracking to peak strength (Fig. 6.14b), confirming the efficacy of the strain-hardening cementitious matrix in mobilizing distributed micro-cracking and delaying stiffness degradation.

The idealized curve for the 3DPC-CFR wall demonstrates a substantially broader and more stable backbone shape, characterized by a steeper initial stiffness, higher yield strength, and a prolonged post-yield plateau (Fig. 6.14c). This reflects the combined contribution of the strain hardening ductile matrix and the optimized reinforcement, which together provide enhanced confinement, improved shear transfer, and effective stress redistribution under large cyclic deformations. The comparison plot (Fig. 6.14d) further illustrates the progressive improvement across the three systems, with the envelope of the 3DPC-CFR wall showing superior strength retention and the largest deformation capacity. Integrating these idealized backbones into numerical models can allow more accurate prediction of global seismic performance metrics,

such as ductility factors, energy dissipation capacity, and structural behavior coefficients. Moreover, the multilinear idealization facilitates compatibility with existing nonlinear analysis platforms and performance-based design procedures, enabling future development of code-compatible models for 3D-printed concrete shear walls.

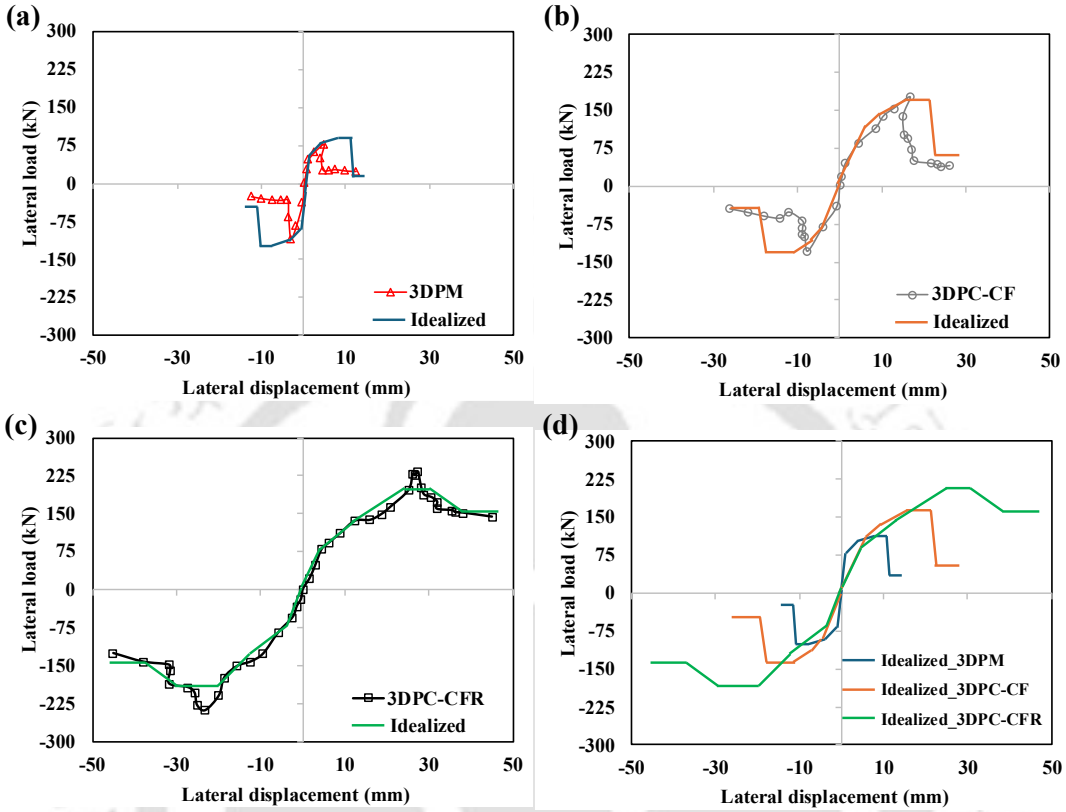

Fig. 6. 14. Development of multilinear idealized curve for (a) 3DPM; (b) 3DPC-CF; (c) 3DPC-CFR; (d) comparison of the idealized curve

6.5. Challenges and recommendations

The findings of this study highlight several important challenges associated with the seismic performance and practical implementation of 3DPC wall systems. A key challenge arises from the use of large-sized coarse aggregates, which, although economically beneficial, introduce heterogeneity in the printed layers. This affects interlayer bonding, fiber dispersion, and the consistency of strain-hardening behavior. X-CT observations and experimental responses indicate that fiber misalignment and localized matrix discontinuities can influence crack initiation and propagation, ultimately affecting the stability of load transfer during cyclic loading.

Furthermore, the absence of passive reinforcement in the 3DPC-CF wall, despite its promising performance, limits its applicability in seismic zones requiring enhanced shear resistance and boundary confinement. While the strain-hardening matrix demonstrated the ability to sustain

distributed cracking, its capacity to fully substitute for reinforcement remains limited under high seismic demand. In contrast, the plain 3DPM wall exhibited brittle shear failure with rapid stiffness degradation, confirming the vulnerability of unreinforced printed walls and underscoring the importance of integrated reinforcement in structural 3DPC applications. Finally, the absence of codified design provisions for 3D-printed structural elements, strain-hardening matrices, or modular prefabricated reinforcement systems presents a broader challenge, as existing seismic design codes (EN 1998, ACI, ASCE 41) do not directly address the unique behavior of 3DPC walls, leaving designers without standardized equations for deformation limits, shear capacity, or behavior factors.

To address these challenges, several recommendations emerge from the experimental evidence. Improving aggregate grading and fiber integration is essential to minimize material heterogeneity and ensure consistent mechanical performance; optimized grading curves and controlled fiber alignment strategies can help in achieving stabilized matrix behavior across printed layers. Future experimental programs should consider applying axial loads in the range of 5–10% of axial capacity to better simulate real structural conditions and capture the influence of axial compression on stiffness retention and crack development. The results also demonstrate clear advantages of incorporating modular prefabricated reinforcement—specifically the continuous boundary reinforcement—which significantly enhances ductility, energy dissipation, and post-peak stability. Therefore, such reinforcement systems should be prioritized in seismic applications where conventional rebar placement within printed geometries is challenging.

Given the pronounced brittleness of plain printed walls, their use should be limited to non-structural or low-demand applications, as they cannot reliably serve as primary lateral-force-resisting elements. The development of calibrated analytical and numerical models based on the full-scale hysteretic response is recommended to support future design guidelines, particularly for estimating stiffness degradation, peak-to-residual strength ratios, and appropriate q-factors for different 3DPC wall configurations. Standardizing printing parameters—such as layer time gaps, extrusion rates, and nozzle control—will further enhance the uniformity and structural reliability of printed walls. Finally, broader testing across varying wall geometries, aspect ratios, boundary reinforcement layouts, and height-to-thickness ratios is necessary to build comprehensive design methodologies suitable for mid- and high-rise 3D-printed systems. While the use of coarse aggregates improves economic feasibility, continued

optimization of mix design and printing processes is essential to fully realize the cost-efficiency and structural performance potential of large-scale 3D concrete printing.

6.6. Summary

The experimental evaluation of three full-scale 3DPC walls—3DPM, 3DPC-CF, and 3DPC-CFR—under cyclic in-plane loading demonstrates the significant influence of material composition and reinforcement strategy on seismic performance. The results indicate that integrating a strain-hardening ductile matrix with prefabricated modular reinforcement substantially enhances ductility, energy dissipation, and post-peak load-carrying capacity. Key conclusions drawn from the study are summarized as follows:

i. Seismic response and energy dissipation

- The 3DPM wall exhibited brittle behavior with pinched hysteresis loops, limited strength (76.94 kN), and low deformation capacity (12.52 mm).
- The strain-hardening 3DPC-CF wall showed flexure-dominated response with enhanced energy dissipation, achieving 175.51 kN peak load (128% increase) and 26.28 mm displacement (110% increase) due to distributed micro-cracking.
- The 3DPC-CFR wall achieved the highest performance, reaching 228.84 kN peak load (197% increase) and 45.02 mm displacement (260% increase), with stable post-peak behavior and peak energy absorption of 16.67 kN·mm.

ii. Crack pattern and failure mechanism

- 3DPM failed in a shear-dominated mode with rapid stiffness degradation.
- 3DPC-CF exhibited flexure-controlled cracking with limited spalling at higher drift levels (1.0–1.6%).
- 3DPC-CFR showed controlled flexural cracking, minimal spalling, and delayed failure without bar buckling.

iii. Reinforcement strain and utilization

- Longitudinal bars in 3DPC-CFR reached ~0.34% strain (~50% of ultimate capacity), indicating efficient reinforcement engagement.
- Prefabricated boundary reinforcement delayed bar buckling and stabilized post-peak response.

iv. Strength and stiffness degradation

- Normalized strength at 1.75% drift increased from 0.48 (3DPM) to 0.69 (3DPC-CF) and 0.88 (3DPC-CFR).

- Stiffness degradation was severe in 3DPM, moderate in 3DPC-CF, and minimal in 3DPC-CFR.

v. Ductility and structural behavior factor

- Displacement ductility factors are: 3DPM = 2.5, 3DPC-CF = 3.5 (40% increase over 3DPM), 3DPC-CFR = 4.5 (80% increase over 3DPM, 29% over 3DPC-CF).
- Structural behavior factors (q) are: 3DPM ≈ 2, 3DPC-CF ≈ 3 (50% higher than 3DPM), 3DPC-CFR ≈ 4.86 (143% higher than 3DPM, 62% higher than 3DPC-CF), demonstrating high ductility and substantial energy dissipation in accordance with ASCE 41-17 standards.

vi. Design implications

- The combined use of a strain-hardening matrix and modular reinforcement significantly improves seismic performance by promoting distributed cracking and sustained post-peak capacity.
- 3DPC-CFR walls are thus well-suited for earthquake-resistant applications requiring high ductility and energy absorption.
- Multilinear backbone curves effectively capture nonlinear behaviour and enable direct integration into performance-based design and numerical modelling frameworks.

The present study highlights the seismic performance potential of 3DPC walls for large-scale applications, demonstrating a cost-efficient approach through the integration of coarse aggregates—the first study to utilize such large aggregates in large-scale 3D printing. Future research should extend the evaluation to walls with varying slenderness and aspect ratios to validate performance in high-rise or complex structural systems. Although this approach reduces material cost, further optimization is required to enhance the economic feasibility of the entire 3D concrete printing system. In addition, the outcomes of this research provide a critical foundation for technology transfer from laboratory-scale investigations to field-level implementation, facilitating the transition of 3D concrete printing from a research-driven innovation to a practical construction technology. Advancements in process standardization, material optimization, and code-aligned design methodologies are expected to play a key role in accelerating the adoption of 3DPC over conventional construction practices, particularly in applications requiring rapid, automated, and performance-driven construction solutions.

Chapter 7

Conclusions and future scope

7.1. Conclusions

7.1.1. Development of strain hardening ultra-ductile 3DPC Composite

- This chapter establishes the feasibility of achieving ultra-ductile strain-hardening behavior in 3D-printed concrete through the controlled incorporation of coarse aggregates and steel fibers at critical volume fractions.
- The optimized 3DPC-CF composite exhibited a tensile ductility factor (μ) of 10.86, a strain-hardening factor (φ) of 1.62, and a fracture energy (G_{pc}) of 105 kJ/m³, confirming stable multiple micro-cracking and sustained post-cracking load transfer.
- Comparative evaluation demonstrated that the 3DPC-CF mixture outperformed when compared to 3DPC-SF and 3DPM, achieving increases of 193% in ductility, 15% in strain-hardening capacity, and 114% in energy absorption.
- The results further confirmed that strain-hardening response and energy dissipation are governed primarily by fiber type and critical fiber dosage, whereas first-crack tensile strength is predominantly controlled by the presence of coarse aggregates.
- The synergistic interaction between aggregates and fibers enhanced fiber–matrix bonding, crack bridging efficiency, and interfacial stress transfer, enabling the development of Level VI ultra-ductile 3DPC composites suitable for reinforced and seismic-resistant applications.

7.1.2. Composite micro-modelling and seismic performance evaluation of 3DPC walls

- This chapter presents a validated composite interface micro-model integrating continuum damage plasticity and cohesive zone modelling for simulating the in-plane cyclic behavior of 3DPC walls.
- The numerical framework accurately reproduced experimental hysteresis loops, stiffness degradation, and energy dissipation trends, demonstrating superior predictive capability compared to conventional macro-modelling approaches.
- Parametric investigations revealed that increasing edge column dimensions from 150×150 mm to 250×250 mm enhanced lateral load capacity by 56% and deformation capacity by approximately 10%.

- Increasing reinforcement bar length and material compressive strength resulted in substantial improvements in ultimate load resistance, whereas increasing wall aspect ratio led to an approximately 71% reduction in lateral strength due to reduced stiffness and stability.
- The incorporation of strain-hardening concrete improved the lateral load resistance, deformation capacity, and energy dissipation of lattice shear walls by 127.27%, 108.33%, and 38.89%, respectively, and of flexural walls by 88.83%, 59.02%, and 28.9%, compared to mortar- and concrete-based systems.
- These results confirm the capability of the developed micro-model to link material-level ductility with structural-scale seismic performance.

7.1.3. Structural characterization and codal-based design framework for seismic-resistant 3DPC walls

- This chapter demonstrates the applicability of ACI 318-19 and Eurocode 8 provisions to 3DPC structural walls through analytical and numerical evaluation.
- A double-layer reinforcement configuration increased lateral load capacity by 30.6% and improved failure displacement by 9.8% compared to a single-layer system, accompanied by higher ductility and energy dissipation at elevated drift levels.
- Progressive enhancement of boundary confinement resulted in an approximate 47% increase in load-carrying capacity and a 97% improvement in lateral deformation capacity.
- Among confinement parameters, transverse reinforcement within boundary elements exerted the most pronounced influence by limiting concrete spalling, stabilizing crack propagation, and preventing longitudinal bar buckling, thereby sustaining post-yield deformation.
- The introduction of a centrally placed self-centering reinforcement bar improved lateral load capacity by 54.08% relative to the unreinforced wall, while localizing crack development and mitigating toe crushing.
- These findings establish a quantitative basis for adapting existing seismic design provisions to 3DPC walls with appropriate reinforcement detailing.

7.1.4. Experimental response of earthquake resistant 3D printed concrete walls

- This chapter provides full-scale experimental validation of the seismic performance enhancement achieved through material ductility and modular reinforcement in 3DPC walls.

- The plain mortar wall exhibited brittle shear-dominated behavior with an ultimate lateral strength of 76.94 kN and a maximum displacement of 12.52 mm. In contrast, the strain-hardening 3DPC-CF wall achieved a peak lateral strength of 175.51 kN, representing a 128% increase, and a displacement capacity of 26.28 mm, corresponding to a 110% improvement over the mortar reference.
- The modularly reinforced 3DPC-CFR wall demonstrated the highest performance, reaching a peak lateral load of 228.84 kN (197% increase over 3DPM) and a maximum displacement of 45.02 mm (260% increase).
- Normalized strength at 1.75% drift increased from 0.48 (3DPM) to 0.88 (3DPC-CFR), while displacement ductility improved from 2.5 to 4.5, corresponding to an 80% increase.
- Minimal stiffness degradation and stable post-peak response confirmed effective stress redistribution and reinforcement engagement, with longitudinal bars reaching approximately 50% of their tensile capacity.
- The experimental results validate the proposed design and modelling frameworks and confirm the viability of 3DPC-CFR walls for earthquake-resistant structural applications.

7.2. Future scope and recommendations

- **Advanced material characterization and durability performance:** The present study incorporated essential fresh-state assessments and experimental validation to ensure printability and structural feasibility of the developed ECC-based 3DPC system. However, detailed rheological characterization—such as static and dynamic yield stress evolution, thixotropic behaviour, structural build-up rate, and extrusion pressure monitoring—was beyond the primary scope of this thesis. Future research may undertake comprehensive rheological investigations to further quantify pumpability, filament stability, and interlayer buildability beyond conventional slump and flow-based evaluation.
- **Durability performance:** Additionally, long-term durability aspects such as permeability, shrinkage cracking, interlayer durability, freeze–thaw resistance, and environmental exposure performance should be investigated to assess service life and sustainability of layered ECC-based 3DPC systems.
- **Refinement of the proposed model under seismic loading:** Furthermore, the proposed numerical framework can be refined by incorporating an effective Young's modulus to better represent the reduced stiffness of 3D printed concrete arising from microcracking, interlayer discontinuities, and inherent material heterogeneity. Instead of adopting the nominal elastic modulus, the use of an effective modulus aligned with codal provisions—

such as the recommendations in **ACI 318**and **ACI 209**, which account for stiffness reduction due to cracking and long-term effects—can improve the accuracy of stiffness prediction and global response. This modification is expected to enhance the reliability of simulations, particularly in capturing initial stiffness, stiffness degradation, and overall structural response under cyclic loading.

- **Structural system expansion and numerical advancements:** Future investigations may extend the present work to varied wall geometries, slenderness ratios, and boundary conditions, as well as multi-storey structural systems to evaluate global seismic performance. Refinement of constitutive and interface modelling strategies is also necessary to efficiently capture construction-induced heterogeneity and anisotropic response.
- **Reinforcement integration and automation**: Future work can focus on automated or semi-automated reinforcement placement techniques, including embedded reinforcement, hybrid printing–assembly approaches, and robotic integration, to improve construction efficiency and quality control.
- **Design standardization and codal development**: The validated numerical models and experimental backbone curves may be extended to develop simplified design expressions, constitutive models, and detailing guidelines tailored for 3DPC walls. These outcomes can contribute toward the formulation of dedicated design provisions within existing seismic codes.
- **Performance-based seismic design applications**: The experimentally derived backbone curves and behavior factors should be employed in nonlinear performance-based design frameworks, fragility analysis, and resilience assessment of 3DPC structures at the building scale.

Overall, continued research integrating material innovation, structural design, automation, and codal standardization will accelerate the safe, economical, and large-scale adoption of 3D concrete printing for earthquake-resistant construction.

References

[1] A.H. Alami, A.G. Olabi, M. Ayoub, H. Aljaghoub, S. Alasad, M.A. Abdelkareem, 3D Concrete Printing: Recent Progress, Applications, Challenges, and Role in Achieving Sustainable Development Goals, Buildings 13 (2023). https://doi.org/10.3390/buildings13040924.

[2] Y. Chen, Y. Zhang, B. Pang, Z. Liu, G. Liu, Extrusion-based 3D printing concrete with coarse aggregate: Printability and direction-dependent mechanical performance, Constr Build Mater 296 (2021) 123624. https://doi.org/10.1016/j.conbuildmat.2021.123624.

[3] L. Hass, F. Bos, Bending and Pull-Out Tests on a Novel Screw Type Reinforcement for Extrusion-Based 3D Printed Concrete BT - Second RILEM International Conference on Concrete and Digital Fabrication, in: F.P. Bos, S.S. Lucas, R.J.M. Wolfs, T.A.M. Salet (Eds.), Springer International Publishing, Cham, 2020: pp. 632–645.

[4] R.A. Buswell, W.R. Leal de Silva, S.Z. Jones, J. Dirrenberger, 3D printing using concrete extrusion: A roadmap for research, Cem Concr Res 112 (2018) 37–49. https://doi.org/https://doi.org/10.1016/j.cemconres.2018.05.006.

[5] B. García de Soto, I. Agustí-Juan, J. Hunhevicz, S. Joss, K. Graser, G. Habert, B.T. Adey, Productivity of digital fabrication in construction: Cost and time analysis of a robotically built wall, Autom Constr 92 (2018) 297–311. https://doi.org/https://doi.org/10.1016/j.autcon.2018.04.004.

[6] D. Zhang, P. Feng, P. Zhou, W. Xu, G. Ma, 3D printed concrete walls reinforced with flexible FRP textile: Automatic construction, digital rebuilding, and seismic performance, Eng Struct 291 (2023) 116488. https://doi.org/https://doi.org/10.1016/j.engstruct.2023.116488.

[7] M. Giulivo, C. Menna, EXPERIMENTAL BEHAVIOR OF A 3D PRINTED CONCRETE WALL WITH FIXED BASE ANCHORAGE SUBJECTED TO IN-PLANE CYCLIC LOADS, (n.d.). https://doi.org/10.24355/dbbs.084-202408190801-0.

[8] C. Liu, Z. Liang, H. Liu, Y. Wu, Y. Zhang, G. Bai, Seismic performance of 3D printed reinforced concrete walls: Experimental study and numerical simulation, Eng Struct 333 (2025). https://doi.org/10.1016/j.engstruct.2025.120176.

[9] Ö. Mercimek, O. Şahin, A. Çelik, M. Özkan Ekinci, E. Teksin, K. Bıçakçıoğlu, S.T. Akkaya, H. İlcan, H. Ulugöl, Ö. Anıl, M. Şahmaran, Structural performance of pre-fabricated 3D printed concrete walls: Effect of cold joint, axial load and load type, Journal of Building Engineering 112 (2025). https://doi.org/10.1016/j.jobe.2025.113788.

[10] M.T. Mollah, R. Comminal, W.R. Leal Da Silva, B. Šeta, J. Spangenberg, Integration of reinforcement bars in 3D concrete printing, n.d. https://ssrn.com/abstract=4363612.

[11] ACI Committee, Building code requirements for structural concrete, 318, American Concrete Institute (2019).

[12] Eurocode 8, Design of structures for earthquake resistance. Part 1, General rules, seismic actions and rules for buildings, British Standards Institution, 2005.

[13] IS 13920-2016: Ductile Design and Detailing of Reinforced Concrete Structures Subjected to Seismic Forces-Code of Practice, 2016. www.bis.org.inwww.standardsbis.in.

[14] D. Lowke, E. Dini, A. Perrot, D. Weger, C. Gehlen, B. Dillenburger, Particle-bed 3D printing in concrete construction – Possibilities and challenges, Cem Concr Res 112 (2018) 50–65. https://doi.org/10.1016/j.cemconres.2018.05.018.

[15] R.A. Buswell, W.R. Leal de Silva, S.Z. Jones, J. Dirrenberger, 3D printing using concrete extrusion: A roadmap for research, Cem Concr Res 112 (2018) 37–49. https://doi.org/10.1016/j.cemconres.2018.05.006.

[16] E. Dini, D-SHAPE - The 21st century revolution in building technology has a name, 2009.

[17] S. Lim, R.A. Buswell, T.T. Le, S.A. Austin, A.G.F. Gibb, T. Thorpe, Developments in construction-scale additive manufacturing processes, Autom Constr 21 (2012) 262–268. https://doi.org/10.1016/j.autcon.2011.06.010.

[18] A. Paolini, S. Kollmannsberger, E. Rank, Additive manufacturing in construction: A review on processes, applications, and digital planning methods, Addit Manuf 30 (2019) 100894. https://doi.org/10.1016/j.addma.2019.100894.

[19] F.P. Bos, E. Bosco, T.A.M. Salet, Ductility of 3D printed concrete reinforced with short straight steel fibers, Virtual Phys Prototyp 14 (2019) 160–174. https://doi.org/10.1080/17452759.2018.1548069.

[20] J. Li, Y. Durandet, X. Huang, G. Sun, D. Ruan, Additively manufactured fiber-reinforced composites: A review of mechanical behavior and opportunities, J Mater Sci Technol 119 (2022) 219–244. https://doi.org/https://doi.org/10.1016/j.jmst.2021.11.063.

[21] C. Menna, J. Mata-falcón, F.P. Bos, G. Vantyghem, L. Ferrara, D. Asprone, T. Salet, W. Kaufmann, Opportunities and challenges for structural engineering of digitally fabricated concrete, Cem Concr Res 133 (2020) 106079. https://doi.org/10.1016/j.cemconres.2020.106079.
[22] G. Ma, Z. Li, L. Wang, F. Wang, J. Sanjayan, Mechanical anisotropy of aligned fiber reinforced composite for extrusion-based 3D printing, Constr Build Mater 202 (2019) 770–783. https://doi.org/10.1016/j.conbuildmat.2019.01.008.
[23] M. Liu, Y. Huang, F. Wang, J. Sun, G. Ma, Tensile and flexural properties of 3D-printed jackets-reinforced mortar, Constr Build Mater 296 (2021) 123639. https://doi.org/10.1016/j.conbuildmat.2021.123639.
[24] K. Korniejenko, M. Łach, S.-Y. Chou, W.-T. Lin, A. Cheng, M. Hebdowska-Krupa, S. Gądek, J. Mikuła, Mechanical Properties of Short Fiber-Reinforced Geopolymers Made by Casted and 3D Printing Methods: A Comparative Study, Materials 13 (2020). https://doi.org/10.3390/ma13030579.
[25] S.H. Chu, L.G. Li, A.K.H. Kwan, Development of extrudable high strength fiber reinforced concrete incorporating nano calcium carbonate, Addit Manuf 37 (2021). https://doi.org/10.1016/j.addma.2020.101617.
[26] W. Zhou, Y. Zhang, L. Ma, V.C. Li, Influence of printing parameters on 3D printing engineered cementitious composites (3DP-ECC), Cem Concr Compos 130 (2022) 104562. https://doi.org/10.1016/j.cemconcomp.2022.104562.
[27] S. Al-Qutaifi, A. Nazari, A. Bagheri, Mechanical properties of layered geopolymer structures applicable in concrete 3D-printing, Constr Build Mater 176 (2018) 690–699. https://doi.org/10.1016/j.conbuildmat.2018.04.195.
[28] C. Vlachakis, M. Perry, J. McAlorum, 3D printed self-sensing alkali-activated coatings for civil infrastructure, Conference Record - IEEE Instrumentation and Measurement Technology Conference 2021-May (2021) 1–5. https://doi.org/10.1109/I2MTC50364.2021.9459899.
[29] C. Vlachakis, J. McAlorum, M. Perry, 3D printed cement-based repairs and strain sensors, Autom Constr 137 (2022) 104202. https://doi.org/10.1016/j.autcon.2022.104202.
[30] S.A.O. Nair, A. Tripati, N. Neithalath, Examining layer height effects on the flexural and fracture response of plain and fiber-reinforced 3D-printed beams, Cem Concr Compos 124 (2021) 104254. https://doi.org/10.1016/j.cemconcomp.2021.104254.
[31] L. Pham, P. Tran, J. Sanjayan, Steel fibres reinforced 3D printed concrete: Influence of fibre sizes on mechanical performance, Constr Build Mater 250 (2020) 118785. https://doi.org/10.1016/j.conbuildmat.2020.118785.
[32] S.H. Bong, B. Nematollahi, M. Xia, S.H. Ghaffar, J. Pan, J.-G. Dai, Properties of additively manufactured geopolymer incorporating mineral wollastonite microfibers, Constr Build Mater 331 (2022) 127282. https://doi.org/10.1016/j.conbuildmat.2022.127282.
[33] L. Gebhard, J. Mata-Falcón, A. Anton, B. Dillenburger, W. Kaufmann, Structural behaviour of 3D printed concrete beams with various reinforcement strategies, Eng Struct 240 (2021). https://doi.org/10.1016/j.engstruct.2021.112380.
[34] L. Demont, N. Ducoulombier, R. Mesnil, J.F. Caron, Flow-based pultrusion of continuous fibers for cement-based composite material and additive manufacturing: rheological and technological requirements, Compos Struct 262 (2021) 113564. https://doi.org/10.1016/j.compstruct.2021.113564.
[35] J.H. Lim, B. Panda, Q. Pham, Improving flexural characteristics of 3D printed geopolymer composites with in-process steel cable reinforcement, Constr Build Mater 178 (2018) 32–41. https://doi.org/10.1016/j.conbuildmat.2018.05.010.
[36] Z. Wu, A.M. Memari, J.P. Duarte, State of the Art Review of Reinforcement Strategies and Technologies for 3D Printing of Concrete, Energies (Basel) 15 (2022) 360. https://doi.org/10.3390/en15010360 (accessed July 16, 2023).
[37] M. Hambach, D. Volkmer, Properties of 3D-printed fiber-reinforced Portland cement paste, Cem Concr Compos 79 (2017) 62–70. https://doi.org/10.1016/j.cemconcomp.2017.02.001.
[38] B. Panda, S. Chandra Paul, M. Jen Tan, Anisotropic mechanical performance of 3D printed fiber reinforced sustainable construction material, Mater Lett 209 (2017) 146–149. https://doi.org/10.1016/j.matlet.2017.07.123.
[39] B. Zhu, J. Pan, B. Nematollahi, Z. Zhou, Y. Zhang, J. Sanjayan, Development of 3D printable engineered cementitious composites with ultra-high tensile ductility for digital construction, Mater Des 181 (2019) 108088. https://doi.org/10.1016/j.matdes.2019.108088.
[40] B. Zhu, J. Pan, Z. Zhou, J. Cai, Mechanical properties of engineered cementitious composites beams fabricated by extrusion-based 3D printing, Eng Struct 238 (2021) 112201. https://doi.org/10.1016/j.engstruct.2021.112201.

[41] H. Ogura, V.N. Nerella, V. Mechtcherine, Developing and testing of Strain-Hardening Cement-Based Composites (SHCC) in the context of 3D-printing, Materials 11 (2018) 1–18. https://doi.org/10.3390/ma11081375.
[42] Y. Chen, Y. Zhang, B. Pang, D. Wang, Z. Liu, G. Liu, Steel fiber orientational distribution and effects on 3D printed concrete with coarse aggregate, Mater Struct 55 (2022) 1–19. https://doi.org/10.1617/s11527-022-01943-7.
[43] L.G. Li, B.F. Xiao, Z.Q. Fang, Z. Xiong, S.H. Chu, A.K.H. Kwan, Feasibility of glass/basalt fiber reinforced seawater coral sand mortar for 3D printing, Addit Manuf 37 (2021). https://doi.org/10.1016/j.addma.2020.101684.
[44] Y. Zhang, F. Aslani, Development of fibre reinforced engineered cementitious composite using polyvinyl alcohol fibre and activated carbon powder for 3D concrete printing, Constr Build Mater 303 (2021) 124453. https://doi.org/10.1016/j.conbuildmat.2021.124453.
[45] B. Nematollahi, P. Vijay, J. Sanjayan, A. Nazari, M. Xia, V.N. Nerella, V. Mechtcherine, Effect of polypropylene fibre addition on properties of geopolymers made by 3D printing for digital construction, Materials 11 (2018). https://doi.org/10.3390/ma11122352.
[46] T. Ding, J. Xiao, S. Zou, J. Yu, Flexural properties of 3D printed fibre-reinforced concrete with recycled sand, Constr Build Mater 288 (2021) 123077. https://doi.org/10.1016/j.conbuildmat.2021.123077.
[47] J. Liu, S. Li, K. Fox, P. Tran, 3D concrete printing of bioinspired Bouligand structure: A study on impact resistance, Addit Manuf 50 (2022) 102544. https://doi.org/10.1016/j.addma.2021.102544.
[48] T. Ding, J. Xiao, S. Zou, X. Zhou, Anisotropic behavior in bending of 3D printed concrete reinforced with fibers, Compos Struct 254 (2020) 112808. https://doi.org/10.1016/j.compstruct.2020.112808.
[49] V. Mechtcherine, A. Michel, M. Liebscher, T. Schmeier, Extrusion-based additive manufacturing with carbon reinforced concrete: Concept and feasibility study, Materials 13 (2020). https://doi.org/10.3390/ma13112568.
[50] J.F. Caron, L. Demont, N. Ducoulombier, R. Mesnil, 3D printing of mortar with continuous fibres: Principle, properties and potential for application, Autom Constr 129 (2021). https://doi.org/10.1016/j.autcon.2021.103806.
[51] Z.Y. Ahmed, F.P. Bos, M.C.A.J. van Brunschot, T.A.M. Salet, On-demand additive manufacturing of functionally graded concrete, Virtual Phys Prototyp 15 (2020) 194–210. https://doi.org/10.1080/17452759.2019.1709009.
[52] R.J.M. Wolfs, F.P. Bos, T.A.M. Salet, Cement and Concrete Research Hardened properties of 3D printed concrete : The influence of process parameters on interlayer adhesion, Cem Concr Res 119 (2019) 132–140. https://doi.org/10.1016/j.cemconres.2019.02.017.
[53] L. Wang, G. Ma, T. Liu, R. Buswell, Z. Li, Interlayer reinforcement of 3D printed concrete by the in-process deposition of U-nails, Cem Concr Res 148 (2021) 106535. https://doi.org/10.1016/j.cemconres.2021.106535.
[54] L. Gebhard, J. Mata-Falcón, A. Anton, B. Dillenburger, W. Kaufmann, Structural behaviour of 3D printed concrete beams with various reinforcement strategies, Eng Struct 240 (2021). https://doi.org/10.1016/j.engstruct.2021.112380.
[55] M.P. Tinoco, É.M. de Mendonça, L.I.C. Fernandez, L.R. Caldas, O.A.M. Reales, R.D. Toledo Filho, Life cycle assessment (LCA) and environmental sustainability of cementitious materials for 3D concrete printing: A systematic literature review, Journal of Building Engineering 52 (2022) 104456. https://doi.org/10.1016/j.jobe.2022.104456.
[56] Y. Jin, X. Zhou, M. Chen, Z. Zhao, Y. Huang, P. Zhao, L. Lu, High toughness 3D printed white Portland cement-based materials with glass fiber textile, Mater Lett 309 (2022) 131381. https://doi.org/10.1016/j.matlet.2021.131381.
[57] C. Liu, Y. Xiong, Y. Chen, L. Jia, L. Ma, Z. Deng, Z. Wang, C. Chen, N. Banthia, Y. Zhang, Effect of sulphoaluminate cement on fresh and hardened properties of 3D printing foamed concrete, Compos B Eng 232 (2022) 109619. https://doi.org/10.1016/j.compositesb.2022.109619.
[58] M. Nodehi, T. Ozbakkaloglu, A. Gholampour, Effect of supplementary cementitious materials on properties of 3D printed conventional and alkali-activated concrete: A review, Autom Constr 138 (2022) 104215. https://doi.org/10.1016/j.autcon.2022.104215.
[59] H. Liu, C. Liu, Y. Wu, G. Bai, C. He, R. Zhang, Y. Wang, Hardened properties of 3D printed concrete with recycled coarse aggregate, Cem Concr Res 159 (2022) 106868. https://doi.org/10.1016/j.cemconres.2022.106868.
[60] Z. Deng, Z. Jia, C. Zhang, Z. Wang, L. Jia, L. Ma, X. Wang, Y. Zhang, 3D printing lightweight aggregate concrete prepared with shell-packing-aggregate method - Printability, mechanical properties and pore structure, Journal of Building Engineering 62 (2022) 105404. https://doi.org/10.1016/j.jobe.2022.105404.

[61] Y. Chen, Y. Zhang, B. Pang, Z. Liu, G. Liu, Extrusion-based 3D printing concrete with coarse aggregate: Printability and direction-dependent mechanical performance, Constr Build Mater 296 (2021) 123624. https://doi.org/10.1016/j.conbuildmat.2021.123624.
[62] W.R.L. da Silva, M. Kaasgaard, T.J. Andersen, Sustainable 3D Concrete Printing with Large Aggregates, in: A. and C.S. and K.P. Buswell Richard and Blanco (Ed.), Third RILEM International Conference on Concrete and Digital Fabrication, Springer International Publishing, Cham, 2022: pp. 71–77. doi.org/10.1007/978-3-031-06116-5_11 (accessed July 13, 2023).
[63] S. Yu, H. Du, J. Sanjayan, Aggregate-bed 3D concrete printing with cement paste binder, Cem Concr Res 136 (2020) 106169. https://doi.org/10.1016/j.cemconres.2020.106169.
[64] T. Wangler, E. Lloret, L. Reiter, N. Hack, F. Gramazio, M. Kohler, M. Bernhard, B. Dillenburger, J. Buchli, N. Roussel, R. Flatt, Digital Concrete: Opportunities and Challenges, RILEM Technical Letters 1 (2016) 67. https://doi.org/10.21809/rilemtechlett.2016.16.
[65] I. Hager, A. Golonka, R. Putanowicz, 3D Printing of Buildings and Building Components as the Future of Sustainable Construction?, in: Procedia Eng, Elsevier Ltd, 2016: pp. 292–299. https://doi.org/10.1016/j.proeng.2016.07.357.
[66] W. Ferdous, Y. Bai, T.D. Ngo, A. Manalo, P. Mendis, New advancements, challenges and opportunities of multi-storey modular buildings – A state-of-the-art review, Eng Struct 183 (2019) 883–893. https://doi.org/10.1016/j.engstruct.2019.01.061.
[67] D. Avrutis, A. Nazari, J.G. Sanjayan, Chapter 19 - Industrial Adoption of 3D Concrete Printing in the Australian Market: Potentials and Challenges, in: J.G. Sanjayan, A. Nazari, B. Nematollahi (Eds.), 3D Concrete Printing Technology, Butterworth-Heinemann, 2019: pp. 389–409. https://doi.org/https://doi.org/10.1016/B978-0-12-815481-6.00019-1.
[68] A. Siddika, M.A. Al Mamun, W. Ferdous, A.K. Saha, R. Alyousef, 3D-printed concrete: applications, performance, and challenges, J Sustain Cem Based Mater 9 (2020) 127–164. https://doi.org/10.1080/21650373.2019.1705199.
[69] I. Perkins, M. Skitmore, Three-dimensional printing in the construction industry: A review, International Journal of Construction Management 15 (2015) 1–9. https://doi.org/10.1080/15623599.2015.1012136.
[70] S. Lim, R.A. Buswell, T.T. Le, S.A. Austin, A.G.F. Gibb, T. Thorpe, Developments in construction-scale additive manufacturing processes, Autom Constr 21 (2012) 262–268. https://doi.org/10.1016/j.autcon.2011.06.010.
[71] A. Moncaster, T. Malmqvist, T. Forman, F. Pomponi, J. Anderson, Embodied carbon of concrete in buildings, Part 2: are the messages accurate?, Buildings and Cities 3 (2022) 334–355. https://doi.org/10.5334/bc.199.
[72] X. Wang, L. Jia, Z. Jia, C. Zhang, Y. Chen, L. Ma, Z. Wang, Z. Deng, N. Banthia, Y. Zhang, Optimization of 3D printing concrete with coarse aggregate via proper mix design and printing process, Journal of Building Engineering 56 (2022). https://doi.org/10.1016/j.jobe.2022.104745.
[73] H. Liu, C. Liu, Y. Wu, G. Bai, C. He, Y. Yao, R. Zhang, Y. Wang, 3D printing concrete with recycled coarse aggregates: The influence of pore structure on interlayer adhesion, Cem Concr Compos 134 (2022). https://doi.org/10.1016/j.cemconcomp.2022.104742.
[74] Y. Liu, L. Wang, Q. Yuan, J. Peng, Effect of coarse aggregate on printability and mechanical properties of 3D printed concrete, Constr Build Mater 405 (2023) 133338. https://doi.org/https://doi.org/10.1016/j.conbuildmat.2023.133338.
[75] H. Liu, C. Liu, Y. Wu, G. Bai, C. He, R. Zhang, Y. Wang, Hardened properties of 3D printed concrete with recycled coarse aggregate, Cem Concr Res 159 (2022) 106868. https://doi.org/10.1016/j.cemconres.2022.106868.
[76] M. Fernand, Y. Li, Q. Qian, Y. Chi, Z. Yang, Effects of coarse aggregates on 3D printability and mechanical properties of ultra high performance fiber reinforced concrete, Journal of Building Engineering 96 (2024) 110516. https://doi.org/https://doi.org/10.1016/j.jobe.2024.110516.
[77] J.I. Guangchao, X. Jianzhuang, Mechanical Properties of 3D Printed Concrete with Coarse Aggregates, Journal of Tongji University (Natural Science Edition) 51 (2023) 1711–1718. jtunsen/article/abstract/202311009.
[78] S. Paritala, S. Raj, P.R. Singh, K.V.L. Subramaniam, Designing 3D printable concrete by integrating the influence of aggregate characteristics, Mater Struct 58 (2025) 267. https://doi.org/10.1617/s11527-025-02782-y.
[79] V.C. Li, F.P. Bos, K. Yu, W. McGee, T.Y. Ng, S.C. Figueiredo, K. Nefs, V. Mechtcherine, V.N. Nerella, J. Pan, G.P.A.G. van Zijl, P.J. Kruger, On the emergence of 3D printable Engineered, Strain Hardening Cementitious Composites (ECC/SHCC), Cem Concr Res 132 (2020) 106038. https://doi.org/https://doi.org/10.1016/j.cemconres.2020.106038.

[80] A.L. van Overmeir, B. Šavija, F.P. Bos, E. Schlangen, 3D printable strain hardening cementitious composites (3DP-SHCC), tailoring fresh and hardened state properties, Constr Build Mater 403 (2023). https://doi.org/10.1016/j.conbuildmat.2023.132924.
[81] W. Chen, J. Ye, F. Jiang, R. Fediuk, J. Yu, V.C. Li, K. Yu, Printability region for 3D-printable engineered cementitious composites (3DP-ECC), Cem Concr Compos 151 (2024) 105599. https://doi.org/https://doi.org/10.1016/j.cemconcomp.2024.105599.
[82] S. Chaves Figueiredo, C. Romero Rodríguez, Z.Y. Ahmed, D.H. Bos, Y. Xu, T.M. Salet, O. Çopuroğlu, E. Schlangen, F.P. Bos, An approach to develop printable strain hardening cementitious composites, Mater Des 169 (2019) 107651. https://doi.org/https://doi.org/10.1016/j.matdes.2019.107651.
[83] J. Yu, C.K.Y. Leung, Impact of 3D Printing Direction on Mechanical Performance of Strain-Hardening Cementitious Composite (SHCC), in: T. Wangler, R.J. Flatt (Eds.), First RILEM International Conference on Concrete and Digital Fabrication – Digital Concrete 2018, Springer International Publishing, Cham, 2019: pp. 255–265.
[84] Y. Bao, M. Xu, D. Soltan, T. Xia, A. Shih, H.L. Clack, V.C. Li, Three-Dimensional Printing Multifunctional Engineered Cementitious Composites (ECC) for Structural Elements, in: T. Wangler, R.J. Flatt (Eds.), First RILEM International Conference on Concrete and Digital Fabrication – Digital Concrete 2018, Springer International Publishing, Cham, 2019: pp. 115–128.
[85] Y. Chen, Y. Zhang, B. Pang, D. Wang, Z. Liu, G. Liu, Steel fiber orientational distribution and effects on 3D printed concrete with coarse aggregate, Materials and Structures/Materiaux et Constructions 55 (2022). https://doi.org/10.1617/s11527-022-01943-7.
[86] B. Zhu, J. Pan, J. Li, P. Wang, M. Zhang, Relationship between microstructure and strain-hardening behaviour of 3D printed engineered cementitious composites, Cem Concr Compos 133 (2022) 104677. https://doi.org/https://doi.org/10.1016/j.cemconcomp.2022.104677.
[87] L. Pham, P. Tran, J. Sanjayan, Steel fibres reinforced 3D printed concrete: Influence of fibre sizes on mechanical performance, Constr Build Mater 250 (2020) 118785. https://doi.org/https://doi.org/10.1016/j.conbuildmat.2020.118785.
[88] Y. Yang, C. Wu, Z. Liu, H. Wang, Q. Ren, Mechanical anisotropy of ultra-high performance fibre-reinforced concrete for 3D printing, Cem Concr Compos 125 (2022) 104310. https://doi.org/https://doi.org/10.1016/j.cemconcomp.2021.104310.
[89] N. Xu, Y. Qian, J. Yu, C.K.Y. Leung, Tensile performance of 3D-printed Strain-Hardening Cementitious Composites (SHCC) considering material parameters, nozzle size and printing pattern, Cem Concr Compos 132 (2022). https://doi.org/10.1016/j.cemconcomp.2022.104601.
[90] M. Qiu, Y. Sun, Y. Qian, Interfacial bonding performance of 3D-printed Ultra-High Performance Strain-Hardening Cementitious Composites (UHP-SHCC) and cast normal concrete, Journal of Building Engineering 82 (2024) 108268. https://doi.org/https://doi.org/10.1016/j.jobe.2023.108268.
[91] J. Liu, P. Tran, V. Nguyen Van, C. Gunasekara, S. Setunge, 3D printing of cementitious mortar with milled recycled carbon fibres: Influences of filament offset on mechanical properties, Cem Concr Compos 142 (2023) 105169. https://doi.org/https://doi.org/10.1016/j.cemconcomp.2023.105169.
[92] Virginia Launches World's Biggest 3D-Printed Housing Project. One Home Was Printed in 28 Hours. Now, Alquist 3D Is Building 200 More, (2022). https://www.freethink.com/hard-tech/3d-printing-houses (accessed February 15, 2024).
[93] L. Hass, K. Nefs, F.P. Bos, T.A.M. Salet, Application potential of combining strain hardening cementitious composites and helical reinforcement for 3D concrete printed structures: Case study of a spiral staircase, Journal of Building Engineering 80 (2023) 107926. https://doi.org/https://doi.org/10.1016/j.jobe.2023.107926.
[94] G. Beersaerts, J. Soete, M. Giels, L. Eykens, S. Lucas, Y. Pontikes, 3D printing of an iron-rich slag based hybrid mortar. A durable, sustainable and cost-competitive product?, Cem Concr Compos 144 (2023). https://doi.org/10.1016/j.cemconcomp.2023.105304.
[95] X. Han, J. Yan, M. Liu, L. Huo, J. Li, Experimental study on large-scale 3D printed concrete walls under axial compression, Autom Constr 133 (2022) 103993. https://doi.org/https://doi.org/10.1016/j.autcon.2021.103993.
[96] J. Zhang, J. Wang, S. Dong, X. Yu, B. Han, A review of the current progress and application of 3D printed concrete, Compos Part A Appl Sci Manuf 125 (2019). https://doi.org/10.1016/j.compositesa.2019.105533.
[97] S. Huang, W. Xu, Y. Li, The impacts of fabrication systems on 3D concrete printing building forms, Frontiers of Architectural Research 11 (2022) 653–669. https://doi.org/https://doi.org/10.1016/j.foar.2022.03.004.
[98] M.T. Souza, I.M. Ferreira, E. Guzi de Moraes, L. Senff, A.P. Novaes de Oliveira, 3D printed concrete for large-scale buildings: An overview of rheology, printing parameters, chemical admixtures,

reinforcements, and economic and environmental prospects, Journal of Building Engineering 32 (2020) 101833. https://doi.org/https://doi.org/10.1016/j.jobe.2020.101833.
[99] D. Srinivas, D. Dey, B. Panda, T.G. Sitharam, Printability, Thermal and Compressive Strength Properties of Cementitious Materials: A Comparative Study with Silica Fume and Limestone, Materials 15 (2022). https://doi.org/10.3390/ma15238607.
[100] F. Bos, R. Wolfs, T. Salet, CCR Digital Concrete 2020 SI: Editorial, Cem Concr Res 135 (2020) 106157. https://doi.org/https://doi.org/10.1016/j.cemconres.2020.106157.
[101] R.L. Truby, J.A. Lewis, Printing soft matter in three dimensions, Nature 540 (2016) 371–378. https://doi.org/10.1038/nature21003.
[102] L. Yang, S.M.E. Sepasgozar, S. Shirowzhan, A. Kashani, D. Edwards, Nozzle criteria for enhancing extrudability, buildability and interlayer bonding in 3D printing concrete, Autom Constr 146 (2023). https://doi.org/10.1016/j.autcon.2022.104671.
[103] P. Jiramarootapong, L. Prasittisopin, C. Snguanyat, G. Tanapornraweekit, S. Tangtermsirikul, Load Carrying Capacity and Failure Mode of 3D Printing Mortar Wall Panel Under Axial Compression Loading, in: F.P. Bos, S.S. Lucas, R.J.M. Wolfs, T.A.M. Salet (Eds.), Second RILEM International Conference on Concrete and Digital Fabrication, Springer International Publishing, Cham, 2020: pp. 646–657.
[104] Y. Zhang, Z. Wan, L. Wu, Study on mechanical properties of in-situ printed reinforced concrete wall with core column, in: SPIE-Intl Soc Optical Eng, 2022: p. 12. https://doi.org/10.1117/12.2628445.
[105] T. Daungwilailuk, P. Pheinsusom, W. Pansuk, Uniaxial load testing of large-scale 3D-printed concrete wall and finite-element model analysis, Constr Build Mater 275 (2021). https://doi.org/10.1016/j.conbuildmat.2020.122039.
[106] G. Tanapornraweekit, P. Jiramarootapong, S. Paudel, S. Tangtermsirikul, C. Snguanyat, Experimental and numerical investigation of 3D-printed mortar walls under uniform axial compression, Constr Build Mater 360 (2022) 129552. https://doi.org/https://doi.org/10.1016/j.conbuildmat.2022.129552.
[107] M. van den Heever, F. Bester, J. Kruger, G. van Zijl, Numerical modelling strategies for reinforced 3D concrete printed elements, Addit Manuf 50 (2022) 102569. https://doi.org/https://doi.org/10.1016/j.addma.2021.102569.
[108] S. Paudel, Investigation of modelling approaches to study the structural performance of 3D printed plain wall under uniform axial compression, Advances in Structural Engineering 26 (2023) 1911–1928. https://doi.org/10.1177/13694332231166566.
[109] V. Nguyen-Van, P. Tran, J. Liu, M. Van Tran, Y.M. Xie, Extended finite element multiscale modelling for crack propagation in 3D-printed fibre-reinforced concrete, Addit Manuf 81 (2024) 104019. https://doi.org/https://doi.org/10.1016/j.addma.2024.104019.
[110] M. Aghajani Delavar, H. Chen, P. Sideris, Analysis and design of 3D printed reinforced concrete walls under in-plane quasi-static loading, Eng Struct 303 (2024) 117535. https://doi.org/https://doi.org/10.1016/j.engstruct.2024.117535.
[111] D. Zhang, G. Ma, J. Guan, L. Wang, Q. Wang, Cyclic behavior of unbonded post-tensioned precast segmental concrete columns fabricated by 3D printed concrete permanent formwork, Eng Struct 292 (2023) 116436. https://doi.org/https://doi.org/10.1016/j.engstruct.2023.116436.
[112] N. Hack, C. Hühne, T. Rothe, Reinforcement Strategies for Additive Manufacturing in Construction Based on Dynamic Fibre Winding: Concepts and Initial Case Studies, in: Vision and Strategies for Reinforcing Additively Manufactured Concrete Structures, 2022: pp. 45–59.
[113] Y. Jacquet, A. Perrot, Sewing Concrete Device—Combining In-Line Rheology Control and Reinforcement System for 3D Concrete Printing, Materials 16 (2023). https://doi.org/10.3390/ma16145110.
[114] N. Xu, Y. Qian, J. Yu, C.K.Y. Leung, Tensile performance of 3D-printed Strain-Hardening Cementitious Composites (SHCC) considering material parameters , nozzle size and printing pattern, Cem Concr Compos 132 (2022) 104601. https://doi.org/10.1016/j.cemconcomp.2022.104601.
[115] P. Shakor, S. Nejadi, G. Paul, A study into the effect of different nozzles shapes and fibre-reinforcement in 3D printed mortar, Materials 12 (2019). https://doi.org/10.3390/MA12101708.
[116] D.G. Soltan, V.C. Li, A self-reinforced cementitious composite for building-scale 3D printing, Cem Concr Compos 90 (2018) 1–13. https://doi.org/10.1016/j.cemconcomp.2018.03.017.
[117] L. Pham, G. Lu, P. Tran, Influences of Printing Pattern on Mechanical Performance of Three-Dimensional-Printed Fiber-Reinforced Concrete, 3D Print Addit Manuf 9 (2022) 46–63. https://doi.org/10.1089/3dp.2020.0172.
[118] F.P. Bos, E. Bosco, T.A.M. Salet, Ductility of 3D printed concrete reinforced with short straight steel fibers, Virtual Phys Prototyp 14 (2019) 160–174. https://doi.org/10.1080/17452759.2018.1548069.
[119] X. Sun, C. Gao, H. Wang, Bond performance between BFRP bars and 3D printed concrete, Constr Build Mater 269 (2021) 121325. https://doi.org/10.1016/j.conbuildmat.2020.121325.

[120] L. Gebhard, J. Mata-Falcón, A. Anton, J. Burger, E. Lloret, L. Reiter, B. Dillenburger, F. Gramazio, M. Kohler, R. Flatt, W. Kaufmann, Aligned Interlayer Fibre Reinforcement and Post-tensioning as a Reinforcement Strategy for Digital Fabrication, in: RILEM Bookseries, 2020: pp. 622–631. https://doi.org/10.1007/978-3-030-49916-7_63.
[121] L. Gebhard, J. Mata-Falcón, A. Anton, B. Dillenburger, W. Kaufmann, Experimental investigation of reinforcement strategies for concrete extrusion 3D printed beams, in: 13th Fib International PhD Symposium in Civil Engineering, 2020: pp. 40–47. https://doi.org/10.3929/ethz-b-000444960.
[122] T. Marchment, J. Sanjayan, Lap Joint Reinforcement for 3D Concrete Printing, Journal of Structural Engineering 148 (2022) 04022063. https://doi.org/10.1061/(ASCE)ST.1943-541X.0003361.
[123] M.T. Mollah, R. Comminal, W.R. Leal da Silva, B. Šeta, J. Spangenberg, Computational fluid dynamics modelling and experimental analysis of reinforcement bar integration in 3D concrete printing, Cem Concr Res 173 (2023) 107263. https://doi.org/https://doi.org/10.1016/j.cemconres.2023.107263.
[124] J. Kruger, G. van Zijl, A compendious review on lack-of-fusion in digital concrete fabrication, Addit Manuf 37 (2021) 101654. https://doi.org/https://doi.org/10.1016/j.addma.2020.101654.
[125] F.P. Bos, E. Bosco, T.A.M. Salet, Ductility of 3D printed concrete reinforced with short straight steel fibers, Virtual Phys Prototyp 14 (2019) 160–174. https://doi.org/10.1080/17452759.2018.1548069.
[126] J. Lubliner, J. Oliver, S. Oller, E. Oñate, A plastic-damage model for concrete, Int J Solids Struct 25 (1989) 299–326. https://doi.org/https://doi.org/10.1016/0020-7683(89)90050-4.
[127] Y. Wang, M. Li, Finite Element Analysis of 3D Printed Steel-fiber RC Beam for Mechanical Performance, IOP Conf Ser Earth Environ Sci 643 (2021). https://doi.org/10.1088/1755-1315/643/1/012009.
[128] M. van den Heever, F. Bester, M. Pourbehi, J. Kruger, S. Cho, G. van Zijl, Characterizing the Fissility of 3D Concrete Printed Elements via the Cohesive Zone Method BT - Second RILEM International Conference on Concrete and Digital Fabrication, in: F.P. Bos, S.S. Lucas, R.J.M. Wolfs, T.A.M. Salet (Eds.), Springer International Publishing, Cham, 2020: pp. 489–499.
[129] M. van den Heever, F. Bester, J. Kruger, G. van Zijl, Numerical modelling strategies for reinforced 3D concrete printed elements, Addit Manuf 50 (2022) 102569. https://doi.org/10.1016/j.addma.2021.102569.
[130] J. Kruger, G. van Zijl, A compendious review on lack-of-fusion in digital concrete fabrication, Addit Manuf 37 (2021) 101654. https://doi.org/10.1016/j.addma.2020.101654.
[131] M. van den Heever, F. Bester, J. Kruger, G. van Zijl, Mechanical characterisation for numerical simulation of extrusion-based 3D concrete printing, Journal of Building Engineering 44 (2021) 102944. https://doi.org/https://doi.org/10.1016/j.jobe.2021.102944.
[132] L.P. B., R.J. G., B. Johan, Continuum Model for Masonry: Parameter Estimation and Validation, Journal of Structural Engineering 124 (1998) 642–652. https://doi.org/10.1061/(ASCE)0733-9445(1998)124:6(642).
[133] L.P. B., R.J. G., Multisurface Interface Model for Analysis of Masonry Structures, J Eng Mech 123 (1997) 660–668. https://doi.org/10.1061/(ASCE)0733-9399(1997)123:7(660).
[134] S. Govindjee, G.J. Kay, J.C. Simo, Anisotropic modelling and numerical simulation of brittle damage in concrete, Int J Numer Methods Eng 38 (1995) 3611–3633. https://doi.org/https://doi.org/10.1002/nme.1620382105.
[135] T.N.O. Building, Delft University of Technology University of Minho A USER / PROGRAMMER GUIDE FOR THE MICRO-MODELING OF MASONRY STRUCTURES TNO Building and Construction Research, (1996).
[136] E. Thorenfeldt, Mechanical properties of high-strength concrete and applications in design, in: 1987.
[137] Ceg_Hordijk_19911029.Pdf, (n.d.).
[138] J.G. Rots, P. Nauta, G.M.A. Kusters, J. Blaauwendraad, Smeared Crack Approach and Fracture Localization in Concrete., Heron 30 (1985).
[139] B.Z. P., C. Luigi, Blunt Crack Band Propagation in Finite Element Analysis, Journal of the Engineering Mechanics Division 105 (1979) 297–315. https://doi.org/10.1061/JMCEA3.0002467.
[140] H. Liu, K.I. Egbe, H. Wang, A.M. Nazar, P. Jiao, R. Zhu, A Numerical Study on 3D Printed Cementitious Composites Mixes Subjected to Axial Compression, (2021).
[141] V. Mechtcherine, S. Muthukrishnan, A. Robens-Radermacher, R. Wolfs, J. Versteege, C. Menna, O. Ozturk, N. Ozyurt, J. Roupec, C. Richter, J. Jungwirth, L. Miranda, R. Ammann, J.-F. Caron, V. de Bono, R. Monte, I. Navarrete, C. Eugenin, H. Lombois-Burger, B. Baz, M. Sinka, A. Sapata, I. Harbouz, Y. Zhang, Z. Jia, J. Kruger, J.-P. Mostert, M. Štefančič, L. Hanžič, A. Kaci, S. Rahal, M. Santhanam, S. Bhattacherjee, C. Snguanyat, A. Arunothayan, Z. Zhao, I. Mai, I.J. Rasehorn, D. Böhler, N. Freund, D. Lowke, T. Neef, M. Taubert, D. Auer, C.M. Hechtl, M. Dahlenburg, L. Esposito, R. Buswell, J. Kolawole, M.N. Isa, X. Liu, Z. Wang, K. Subramaniam, F. Bos, Mechanical properties of 3D printed concrete: a RILEM 304-ADC interlaboratory study – compressive strength and modulus of elasticity, Mater Struct 58 (2025) 181. https://doi.org/10.1617/s11527-025-02688-9.
[142] ICC 1500-202X, Standard for Automated Construction Technology for 3D Printing Walls, n.d.

[143] M.A. Delavar, H. Chen, P. Sideris, Design of 3D Printed Concrete Walls under In-Plane Seismic Loading, 12th National Conference on Earthquake Engineering 77840 (2022) 2–6.
[144] V. Mechtcherine, S. Muthukrishnan, A. Robens-Radermacher, R. Wolfs, J. Versteege, C. Menna, O. Ozturk, N. Ozyurt, J. Roupec, C. Richter, J. Jungwirth, L. Miranda, R. Ammann, J.-F. Caron, V. de Bono, R. Monte, I. Navarrete, C. Eugenin, H. Lombois-Burger, B. Baz, M. Sinka, A. Sapata, I. Harbouz, Y. Zhang, Z. Jia, J. Kruger, J.-P. Mostert, M. Štefančič, L. Hanžič, A. Kaci, S. Rahal, M. Santhanam, S. Bhattacherjee, C. Snguanyat, A. Arunothayan, Z. Zhao, I. Mai, I.J. Rasehorn, D. Böhler, N. Freund, D. Lowke, T. Neef, M. Taubert, D. Auer, C.M. Hechtl, M. Dahlenburg, L. Esposito, R. Buswell, J. Kolawole, M.N. Isa, X. Liu, Z. Wang, K. Subramaniam, F. Bos, Mechanical properties of 3D printed concrete: a RILEM 304-ADC interlaboratory study – compressive strength and modulus of elasticity, Mater Struct 58 (2025) 181. https://doi.org/10.1617/s11527-025-02688-9.
[145] L. Gebhard, L. Esposito, C. Menna, J. Mata-Falcón, Inter-laboratory study on the influence of 3D concrete printing set-ups on the bond behaviour of various reinforcements, Cem Concr Compos 133 (2022) 104660. https://doi.org/https://doi.org/10.1016/j.cemconcomp.2022.104660.
[146] Y.W.D. Tay, B. Panda, S.C. Paul, N.A. Noor Mohamed, M.J. Tan, K.F. Leong, 3D printing trends in building and construction industry: a review, Virtual Phys Prototyp 12 (2017) 261–276. https://doi.org/10.1080/17452759.2017.1326724.
[147] S. Lim, R.A. Buswell, T.T. Le, S.A. Austin, A.G.F. Gibb, T. Thorpe, Developments in construction-scale additive manufacturing processes, Autom Constr 21 (2012) 262–268. https://doi.org/https://doi.org/10.1016/j.autcon.2011.06.010.
[148] P. Wu, J. Wang, X. Wang, A critical review of the use of 3-D printing in the construction industry, Autom Constr 68 (2016) 21–31. https://doi.org/https://doi.org/10.1016/j.autcon.2016.04.005.
[149] Md.A. Hossain, A. Zhumabekova, S.C. Paul, J.R. Kim, A review of 3D printing in construction and its impact on the labor market, Sustainability 12 (2020). https://doi.org/10.3390/su12208492.
[150] R. Dörrie, V. Laghi, L. Arrè, G. Kienbaum, N. Babovic, N. Hack, H. Kloft, Combined Additive Manufacturing Techniques for Adaptive Coastline Protection Structures, Buildings 12 (2022) 1–12. https://doi.org/10.3390/buildings12111806.
[151] L.-Y. Xu, B.-T. Huang, V.C. Li, J.-G. Dai, High-strength high-ductility Engineered/Strain-Hardening Cementitious Composites (ECC/SHCC) incorporating geopolymer fine aggregates, Cem Concr Compos 125 (2022) 104296. https://doi.org/https://doi.org/10.1016/j.cemconcomp.2021.104296.
[152] M.-X. Xiong, J.Y.R. Liew, Y.-B. Wang, D.-X. Xiong, B.-L. Lai, Effects of coarse aggregates on physical and mechanical properties of C170/185 ultra-high strength concrete and compressive behaviour of CFST columns, Constr Build Mater 240 (2020) 117967. https://doi.org/https://doi.org/10.1016/j.conbuildmat.2019.117967.
[153] IS 269, Requirements of Ordinary Portland Cement, Bureau of Indian Standards, New Delhi, India (2015).
[154] IS 383-2016: Coarse and Fine Aggregate for Concrete - Specification (Third Revision), Bureau of Indian Standards (2016).
[155] IS 10262-2009: Concrete Mix Proportioning - Guidelines (Third Revision)., Bureau of Indian Standards (2009).
[156] IS 456-2000: Plain and Reinforced Concrete- Code of Practice (Fourth Edition), Bureau of Indian Standards (2000).
[157] ASTM C 125 - 13a, Standard Terminology Relating to Concrete and Concrete Aggregates, ASTM International, West Conshohocken, PA 04.02 (2013) 1–5. https://doi.org/10.1520/C0125-15A.2.
[158] American Society for Testing and Materials, ASTM C127-15: Standard Test Method for Density , Relative Density (Specific Gravity), and Absorption of Coarse Aggregate, ASTM Standard Book (2013) 1–6.
[159] K. Wille, A.E. Naaman, G.J. Parra-montesinos, Ultra-High Performance Concrete with Compressive Strength Exceeding 150 MPa (22 ksi): A Simpler Way, ACI Mater J 108 (2011) 46–54. 10.14359/51664215 (accessed July 25, 2023).
[160] A.R. Arunothayan, B. Nematollahi, R. Ranade, S.H. Bong, J. Sanjayan, Development of 3D-printable ultra-high performance fiber-reinforced concrete for digital construction, Constr Build Mater 257 (2020) 119546. https://doi.org/https://doi.org/10.1016/j.conbuildmat.2020.119546.
[161] ASTM, Standard Test Method for Flow of Hydraulic Cement Mortar: C1437-01, Standard (2001) 7–8.
[162] M. Sonebi, M. Dedenis, S. Amziane, A. Abdalqader, A. Perrot, Effect of Red Mud, Nanoclay, and Natural Fiber on Fresh and Rheological Properties of Three-Dimensional Concrete Printing, ACI Mater J 118 (2021) 97–110. https://doi.org/10.14359/51733108.
[163] D. Dey, D. Srinivas, U. Boddepalli, B. Panda, I.S.R. Gandhi, T.G. Sitharam, 3D printability of ternary Portland cement mixes containing fly ash and limestone, Mater Today Proc 70 (2022) 195–200. https://doi.org/10.1016/j.matpr.2022.09.020.

[164] J. Liu, F. Han, G. Cui, Q. Zhang, J. Lv, L. Zhang, Z. Yang, Combined effect of coarse aggregate and fiber on tensile behavior of ultra-high performance concrete, Constr Build Mater 121 (2016) 310–318. https://doi.org/https://doi.org/10.1016/j.conbuildmat.2016.05.039.
[165] J.J. Kim, Y.S. Jang, D.Y. Yoo, Enhancing the tensile performance of ultra-high-performance concrete through novel curvilinear steel fibers, Journal of Materials Research and Technology 9 (2020) 7570–7582. https://doi.org/10.1016/j.jmrt.2020.05.072.
[166] Z. Wu, C. Shi, K.H. Khayat, Multi-scale investigation of microstructure, fiber pullout behavior, and mechanical properties of ultra-high performance concrete with nano-CaCO3 particles, Cem Concr Compos 86 (2018) 255–265. https://doi.org/10.1016/j.cemconcomp.2017.11.014.
[167] D. Zhang, J. Jiang, Y. Weng, D. Wang, X. Wu, S. Fan, Pull-out behaviour of steel fibres embedded in ultra-high-performance concrete after exposure to high temperatures, Constr Build Mater 408 (2023) 133630. https://doi.org/https://doi.org/10.1016/j.conbuildmat.2023.133630.
[168] F. Han, H. Chen, K. Jiang, W. Zhang, T. Lv, Y. Yang, Influences of geometric patterns of 3D spacer fabric on tensile behavior of concrete canvas, Constr Build Mater 65 (2014) 620–629. https://doi.org/10.1016/j.conbuildmat.2014.05.041.
[169] D. Aveston, A. Kelly, Theory of multiple fracture of fibrous composites, 1973.
[170] P.K. Mallick, Fiber-Reinforced Composites Materials, Manufacturing, and Design, Third Edition, 3rd ed., CRC Press., Boca Raton, 2007.
[171] M.R. Mansor, S. Sapuan, E.S. Zainudin, N. A.A., H. A, Stiffness Prediction of Hybrid Kenaf/Glass Fiber Reinforced Polypropylene Composites using Rule of Mixtures (ROM) and Rule of Hybrid Mixtures (RoHM), Journal of Polymer Materials 30 (2013) 321–334.
[172] C. Cui, S. Sheikh, Experimental Study of Normal and High Strength Concrete Confined with Fiber Reinforced Polymers, Journal of Composites for Construction - J COMPOS CONSTR 14 (2010). https://doi.org/10.1061/(ASCE)CC.1943-5614.0000116.
[173] K. Wille, S. El-Tawil, A.E. Naaman, Properties of strain hardening ultra high performance fiber reinforced concrete (UHP-FRC) under direct tensile loading, Cem Concr Compos 48 (2014) 53–66. https://doi.org/10.1016/j.cemconcomp.2013.12.015.
[174] A.E.N. and H. Najm, Bond-Slip Mechanisms of Steel Fibers in Concrete, ACI Mater J 88 (n.d.). https://doi.org/10.14359/1896.
[175] E. Poveda, R.C. Yu, M. Tarifa, G. Ruiz, V.M.C.F. Cunha, J.A.O. Barros, Rate effect in inclined fibre pull-out for smooth and hooked-end fibres: a numerical study, Int J Fract 223 (2020) 135–149. https://doi.org/10.1007/s10704-019-00404-7.
[176] S. Zhandarov, E. Pisanova, E. Mäder, J.A. Nairn, Investigation of load transfer between the fiber and the matrix in pull-out tests with fibers having different diameters, J Adhes Sci Technol 15 (2001) 205–222. https://doi.org/10.1163/156856101743418.
[177] I. Löfgren, Fibre-reinforced Concrete for Industrial Construction - a fracture mechanics approach to material testing and structural analysis, 2005.
[178] P.P. Li, Y.Y.Y. Cao, M.J.C. Sluijsmans, H.J.H. Brouwers, Q. Yu, Synergistic effect of steel fibres and coarse aggregates on impact properties of ultra-high performance fibre reinforced concrete, Cem Concr Compos 115 (2021) 103866. https://doi.org/https://doi.org/10.1016/j.cemconcomp.2020.103866.
[179] A. Naaman, H.W. Reinhardt, Setting the stage: Toward performance based classification of FRC composites, High Performance Fiber Reinforced Cement Composites (HPFRCC-4) (2003) 1–4.
[180] S.H. Park, D.J. Kim, G.S. Ryu, K.T. Koh, Tensile behavior of Ultra High Performance Hybrid Fiber Reinforced Concrete, Cem Concr Compos 34 (2012) 172–184. https://doi.org/https://doi.org/10.1016/j.cemconcomp.2011.09.009.
[181] D. Srinivas, B. Panda, T.G. Sitharam, Comparative Study into the Interlayer Bond Strength of 3D Printed Mortar: Underwater vs. Air Environments, in: 4th RILEM International Conference on Concrete and Digital Fabrication, 2024: pp. 1–9. https://doi.org/10.24355/dbbs.084-202408020838-0.
[182] A.J.B. Johnston, Récollets of Brittany, in: McGill-Queen's University Press, 1996: pp. 155–157. https://doi.org/doi:10.1515/9780773566385-012.
[183] J. Han, M. Zhao, J. Chen, X. Lan, Effects of steel fiber length and coarse aggregate maximum size on mechanical properties of steel fiber reinforced concrete, Constr Build Mater 209 (2019) 577–591. https://doi.org/10.1016/j.conbuildmat.2019.03.086.
[184] D.-Y. Yoo, S.-T. Kang, Y.-S. Yoon, Effect of fiber length and placement method on flexural behavior, tension-softening curve, and fiber distribution characteristics of UHPFRC, Constr Build Mater 64 (2014) 67–81. https://doi.org/10.1016/j.conbuildmat.2014.04.007.
[185] J.P. Charron, E. Denarié, E. Brühwiler, Transport properties of water and glycol in an ultra high performance fiber reinforced concrete (UHPFRC) under high tensile deformation, Cem Concr Res 38 (2008) 689–698. https://doi.org/10.1016/j.cemconres.2007.12.006.
[186] B.A. Graybeal, J.L. Hartmann, Strength and durability of ultra-high performance concrete, 2003.

[187] B.A. Graybeal, F. Baby, Development of Direct Tension Test Method for Ultra-High-Performance Fiber-Reinforced Concrete, ACI Mater J 110 (2013) 177–186.
[188] K. Wille, D.J. Kim, A.E. Naaman, Strain-hardening UHP-FRC with low fiber contents, Mater Struct 44 (2011) 583–598. https://doi.org/10.1617/s11527-010-9650-4.
[189] A. Kamal, M. Kunieda, N. Ueda, H. Nakamura, Evaluation of crack opening performance of a repair material with strain hardening behavior, Cem Concr Compos 30 (2008) 863–871. https://doi.org/10.1016/j.cemconcomp.2008.08.003.
[190] A. Muttoni, Structural Behavior of Tension Members in UHPC, 2003.
[191] A.R. Arunothayan, B. Nematollahi, R. Ranade, S.H. Bong, J.G. Sanjayan, K.H. Khayat, Fiber orientation effects on ultra-high performance concrete formed by 3D printing, Cem Concr Res 143 (2021) 106384. https://doi.org/10.1016/j.cemconres.2021.106384.
[192] R. Zhong, K. Wille, R. Viegas, Material efficiency in the design of UHPC paste from a life cycle point of view, Constr Build Mater 160 (2018) 505–513. https://doi.org/10.1016/j.conbuildmat.2017.11.049.
[193] K. Wille, A.E. Naaman, G.J. Parra-Montesinos, Ultra-high performance Concrete with compressive strength exceeding 150 MPa (22 ksi): A simpler way, ACI Mater J 108 (2011) 46–54. https://www.scopus.com/inward/record.uri?eid=2-s2.0-79951736352&partnerID=40&md5=3366b5399db9393565bb3726edc7cbff.
[194] K. Yu, W. McGee, T.Y. Ng, H. Zhu, V.C. Li, 3D-printable engineered cementitious composites (3DP-ECC): Fresh and hardened properties, Cem Concr Res 143 (2021) 106388. https://doi.org/https://doi.org/10.1016/j.cemconres.2021.106388.
[195] S.C. Figueiredo, C.R. Rodríguez, Z.Y. Ahmed, D.H. Bos, Y. Xu, T.M. Salet, O. Çopuroglu, E. Schlangen, F.P. Bos, Mechanical behavior of printed strain hardening cementitious composites, Materials 13 (2020). https://doi.org/10.3390/ma13102253.
[196] H. Ogura, V.N. Nerella, V. Mechtcherine, Developing and testing of Strain-Hardening Cement-Based Composites (SHCC) in the context of 3D-printing, Materials 11 (2018). https://doi.org/10.3390/ma11081375.
[197] A. Naaman, H.W. Reinhardt, Setting the stage: Toward performance based classification of FRC composites, High Performance Fiber Reinforced Cement Composites (HPFRCC-4) (2003) 1–4.
[198] Recommendations for Design and Construction of High Performance Fiber Reinforced Cement Composites with Multiple Fine Cracks (HPFRCC), 2008.
[199] E.L. Kreiger, M.A. Kreiger, M.P. Case, Development of the construction processes for reinforced additively constructed concrete, Addit Manuf 28 (2019) 39–49. https://doi.org/10.1016/j.addma.2019.02.015.
[200] B.B. Paulo Lourenc, J.G. Rots, Multisurface interface model for analysis of masonry structures cap model for masonry, J Eng Mech 123 (1997) 660–668.
[201] P.B. Lourenco, Computational Strategy for Masonry Structures, n.d. https://www.researchgate.net/publication/27344834.
[202] L. De Lorenzis, B. Miller, A. Nanni, Bond of fiber-reinforced polymer laminates to concrete, ACI Mater J 98 (2001) 256–264. 10.14359/10281 (accessed February 11, 2024).
[203] M. Jirásek, T. Zimmermann, Embedded crack model: I. basic formulation, Int J Numer Methods Eng 50 (2001) 1269–1290. https://doi.org/10.1002/1097-0207(20010228)50:6.
[204] Y. Nie, T.Y. Xie, G.M. Chen, X.Y. Zhao, J.B. Lv, A 2D generic multi-surface cohesive zone model for simulating FRP-to-concrete mixed-mode debonding failure, Compos Struct 296 (2022). https://doi.org/10.1016/j.compstruct.2022.115890.
[205] K.F. Abdulla, L.S. Cunningham, M. Gillie, Simulating masonry wall behaviour using a simplified micro-model approach, Eng Struct 151 (2017) 349–365. https://doi.org/10.1016/j.engstruct.2017.08.021.
[206] R.D.S.G. Campilho, M.F.S.F. de Moura, J.J.M.S. Domingues, Using a cohesive damage model to predict the tensile behaviour of CFRP single-strap repairs, Int J Solids Struct 45 (2008) 1497–1512. https://doi.org/https://doi.org/10.1016/j.ijsolstr.2007.10.003.
[207] P.P. Camanho, Mixed-Mode Decohesion Finite Elements for the Simulation of Delamination in Composite Materials, 2002. https://ntrs.nasa.gov/api/citations/20020053651/downloads/20020053651/ (accessed August 24, 2024).
[208] M.L. Benzeggagh, M. Kenane, Measurement of mixed-mode delamination fracture toughness of unidirectional glass/epoxy composites with mixed-mode bending apparatus, Compos Sci Technol 56 (1996) 439–449. https://doi.org/https://doi.org/10.1016/0266-3538(96)00005-X.
[209] J. Lubliner, J. Oliver, S. Oller, E. Oñate, A plastic-damage model for concrete, Int J Solids Struct 25 (1989) 299–326. https://doi.org/https://doi.org/10.1016/0020-7683(89)90050-4.
[210] J. Lee, G.L. Fenves, Plastic-damage model for cyclic loading of concrete structures, J Eng Mech 124 (1998) 892–900. https://doi.org/10.1061/(ASCE)0733-9399(1998)124:8(892).

[211] E.O. Momoh, A.I. Osofero, O. Menshykov, Behaviour of clamp-enhanced palm tendons reinforced concrete, Constr Build Mater 341 (2022). https://doi.org/10.1016/j.conbuildmat.2022.127824.
[212] B.L. Wahalathantri, T.H.T. Chan, & Fawzia, A material model for flexural crack simulation in reinforced concrete elements using Abaqus, 2011.
[213] EN 1992-1-1: Eurocode 2: Design of concrete structures - Part 1-1: General rules and rules for buildings, 2004.
[214] T. Wang, T.T.C. Hsu, Nonlinear finite element analysis of concrete structures using new constitutive models, Comput Struct 79 (2001) 2781–2791. https://doi.org/https://doi.org/10.1016/S0045-7949(01)00157-2.
[215] A.S. Genikomsou, M.A. Polak, Finite element analysis of punching shear of concrete slabs using damaged plasticity model in ABAQUS, Eng Struct 98 (2015) 38–48. https://doi.org/https://doi.org/10.1016/j.engstruct.2015.04.016.
[216] C.T. Ozkan Sengul and Mehmet Ali Tasdemir, Influence of Aggregate Type on Mechanical Behavior of Normal- and High-Strength Concretes, ACI Mater J 99 (n.d.). https://doi.org/10.14359/12361.
[217] J.N. Pacheco, J. de Brito, C. Chastre, L. Evangelista, Probabilistic conversion of the compressive strength of cubes to cylinders of natural and recycled aggregate concrete specimens, Materials 12 (2019). https://doi.org/10.3390/ma12020280.
[218] N.; Mojsilović, G.; Simundic, A. Page, Static-cyclic shear tests on masonry wallettes with a damp-proof course membrane, (n.d.). https://doi.org/10.3929/ethz-a-006068632.
[219] A. Mukherjee, H.B. Kaushik, Numerical assessment of role of ferrocement overlay in strengthening of unreinforced masonry walls, Mater Today Proc (2023). https://doi.org/10.1016/j.matpr.2023.03.196.
[220] M.T. Islam, S. Noor-E-Khuda, T. Saito, A simple infill frame with macro element masonry model for the in-plane performance of infill walls, Structures 42 (2022) 386–404. https://doi.org/10.1016/j.istruc.2022.06.014.
[221] A.B. Mehrabi, P.B. Shing, M.P. Schuller, J.L. Noland, Experimental evaluation of masonry-infilled RC frames, Journal of Structural Engineering 122 (1996) 228–237. https://doi.org/10.1061/(ASCE)0733-9445(1996)122:3(228).
[222] G. Blasi, F. De Luca, M.A. Aiello, Hybrid micro-modeling approach for the analysis of the cyclic behavior of RC frames, Front Built Environ 4 (2018). https://doi.org/10.3389/fbuil.2018.00075.
[223] P. Nogueiro, L. Simões Da Silva, R. Bento, R. Simões, Numerical implementation and calibration of a hysteretic model with pinching for the cyclic response of steel joints, 2007.
[224] T.A.M. Salet, Z.Y. Ahmed, F.P. Bos, H.L.M. Laagland, Design of a 3D printed concrete bridge by testing, Virtual Phys Prototyp 13 (2018) 222–236. https://doi.org/10.1080/17452759.2018.1476064.
[225] M.A. Delavar, H. Chen, P. Sideris, Analytical and Numerical Investigation of Out-of-Plane Behavior of 3D Printed Concrete Walls, 12th National Conference on Earthquake Engineering 77840 (2022) 3–7.
[226] M. Aghajani Delavar, H. Chen, P. Sideris, Analysis and design of 3D printed reinforced concrete walls under in-plane quasi-static loading, Eng Struct 303 (2024) 117535. https://doi.org/https://doi.org/10.1016/j.engstruct.2024.117535.
[227] J.P. Moehle, T. Ghodsi, J.D. Hooper, D.C. Fields, R. Gedhada, Seismic Design of Cast-in-Place Concrete Special Structural Walls and Coupling Beams A Guide for Practicing Engineers, 2012. www.curee.org.
[228] Minimum design loads and associated criteria for buildings and other structures, American Society of Civil Engineers (ASCE), 2017. https://doi.org/10.1061/9780784414248.
[229] D. Dey, V.N. Van, H.N. Xuan, D. Srinivas, B. Panda, P. Tran, Flexural performance of 3D printed concrete structure with lattice infills, Developments in the Built Environment 16 (2023) 100297. https://doi.org/https://doi.org/10.1016/j.dibe.2023.100297.
[230] ISO/ASTM 52939:2023 Additive manufacturing for construction — Qualification principles — Structural and infrastructure elements, 2023.
[231] D. Forcellini, S. Alzabeebee, Seismic fragility assessment of geotechnical seismic isolation (GSI) for bridge configuration, Bulletin of Earthquake Engineering 21 (2023) 3969–3990. https://doi.org/10.1007/s10518-022-01356-5.
[232] B. Borah, H.B. Kaushik, V. Singhal, Finite Element Modelling of Confined Masonry Wall under In-plane Cyclic Load, in: IOP Conf Ser Mater Sci Eng, IOP Publishing Ltd, 2020. https://doi.org/10.1088/1757-899X/936/1/012020.
[233] S. Meghdad Ghaseminia, T. Zahra, D.P. Thambiratnam, J. Thamboo, Response of RC shear walls with single and double layers of reinforcements subjected to in-plane cyclic loading, Structures 56 (2023) 105005. https://doi.org/https://doi.org/10.1016/j.istruc.2023.105005.
[234] Y.-M. Zhang, Q.-X. Shi, L. Xin, B. Wang, Y. Liu, P. Wu, X.-W. Liang, Seismic behavior of prefabricated fiber reinforced concrete energy-dissipation wall under cyclic loading, Structures 70 (2024) 107635. https://doi.org/https://doi.org/10.1016/j.istruc.2024.107635.

[235] D. Forcellini, Key Parameters to Model the Mutual Effects Between Base Isolation (BI) and Soil–Structure Interaction (SSI), Applied Sciences (Switzerland) 14 (2024). https://doi.org/10.3390/app142411703.
[236] D. Dey, B. Panda, Y. Shukla, R. Rawal, A comprehensive assessment of thermal performance of 3D printed concrete lattice walls, Progress in Additive Manufacturing (2025). https://doi.org/10.1007/s40964-025-01042-3.
[237] A.C.I.C. 374, 374.1-05: Acceptance Criteria for Moment Frames Based on Structural Testing and Commentary, Technical Documents (n.d.).
[238] H. Zhang, K. Yuan, R. Zou, G. Zhang, J. Guo, Experimental study on seismic performance of squat precast concrete sandwich shear walls under low axial load ratio, Structures 63 (2024) 106483. https://doi.org/10.1016/j.istruc.2024.106483.
[239] L. Wang, Y. Song, Q. Han, X. Liu, B. Geng, X. Du, Dynamic direct shear strength of the assembled interface of precast bridge piers under impact loading, Eng Struct 333 (2025) 120150. https://doi.org/https://doi.org/10.1016/j.engstruct.2025.120150.
[240] J. Carrillo, Damage index based on stiffness degradation of low-rise RC walls, Earthq Eng Struct Dyn 44 (2015) 831–848. https://doi.org/10.1002/eqe.2488.
[241] ASCE. 2014. Seismic evaluation and retrofit of existing buildings (ASCE/SEI standard 41-13). ASCE 41. Reston, VA: ASCE., n.d.
[242] S. Singhal, A. Chourasia, S.K. Panigrahi, Y. Kajale, Seismic response of precast reinforced concrete wall subjected to cyclic in-plane and constant out-of-plane loading, Frontiers of Structural and Civil Engineering 15 (2021) 1128–1143. https://doi.org/10.1007/s11709-021-0753-5.
[243] Recommendations for Seismic Design of Reinforced Concrete Wall Buildings Based on Studies of the 2010 Maule, Chile Earthquake NEHRP Consultants Joint Venture A partnership of the Applied Technology Council and the Consortium of Universities for Research in Earthquake Engineering, n.d.

Appendix A1: 3DPC-CFR wall fabrication steps

Step 1. Bottom beam mould fabrication and reinforcement cage placement

Step 2. Concrete cast up to reinforcement level

Step 3. Wall layer printing on above of the cast concrete level

Step 4. Full wall layer printing (top view of the wall)

Step 5. Reinforcement cage insertion in the wall (Column reinforcement with central single layer grid reinforcement placement)

Step 6. Packing of the side hollow region

Step 7. Casting till wall level

Step 8. Top beam reinforcement cage placement

Step 9. Casting of the concrete from the top beam

Step 10. Casting of the bottom beam

Step 11. Full wall (with strain gauges wire coming out)

Appendix A2: Strain gauges attachment steps

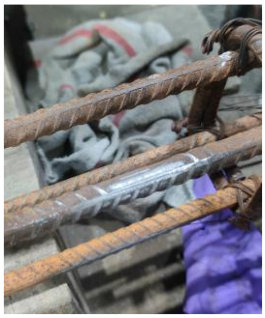

Step 1. Surface grinding of the bar (through ribbed bars and then sand paper to further smoothening)

Step 2. Clearing the surface through Isopropyl spray to clear out the dust

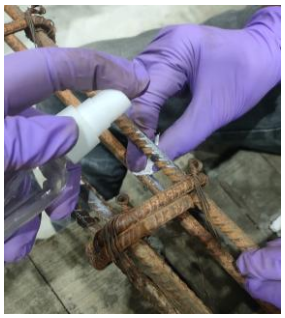

Step 3. Wiping off the surface through tissue

Step 4. Attaching the strain gauges (without any disturbance on the surface of gauges)

Step 5. Epoxy hardener and resin in 1:1 ratio

Step 6. Applying the epoxy on the surface of strain gauges

Step 7. Rest for 30 minutes, then applying 2nd layer of epoxy till wire rapping

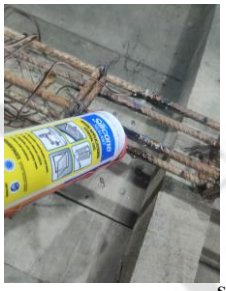

Step 8. Next day another layer of silicon

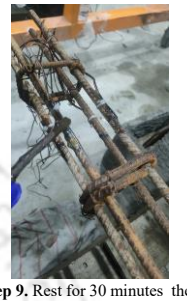

Step 9. Rest for 30 minutes then another layer of silicon (Now its ready for the operation)

Step 10. Drilling in the wall (at desired location as shown in Fig. 7b)

Step 11. A long wire (yellow) attached to strain gauges

Step 11. Column insertion with attached strain gauges

Publications from PhD thesis

International Journals

1. **Warsi SBF**, Panda B, Biswas P. Exploring fibre addition methods and mechanical properties of fibre-reinforced 3D printed concrete: A review. Developments in the Built Environment **2023**;16:100295. https://doi.org/https://doi.org/10.1016/j.dibe.2023.100295. **(IF=8.2)**
2. **Warsi SBF**, Srinivas D, Panda B, Biswas P. Investigating the impact of coarse aggregate dosage on the mechanical performance of 3D printable concrete. Innovative Infrastructure Solutions **2023**;9:5. https://doi.org/10.1007/s41062-023-01317-0. **(IF=2.4)**
3. **Warsi SBF**, Panda B, Biswas P. Development of ultra-ductile strain hardening 3D printed concrete composite utilizing critical fiber volume and coarse aggregate. Additive Manufacturing **2024**, p. 104541. https://doi.org/10.1016/j.addma.2024.104541. **(IF=11.1)**
4. **Warsi SBF**, Panda B, Biswas P. Structural analysis of 3D printed concrete wall under quasi-static cyclic loading using composite micro model. Progress in Additive Manufacturing **2024,** p. 1-21. https://doi.org/10.1007/s40964-024-00874-9. **(IF=5.4)**
5. **Warsi SBF**, Panda B, Biswas P. Design of earthquake-resistant 3D printed concrete wall based on ACI 318–19: Analytical investigation and numerical modelling. Structures **2025,** p. 109371**.** https://doi.org/10.1016/j.istruc.2025.109371. **(IF=4.3)**
6. **Warsi, S. B. F.**, Panda, B., & Biswas, P. (2026) Experimental investigation of the cyclic in- plane behavior of full-scale 3D printed concrete walls through quasi-static cyclic testing. *Journal of Building Engineering,* 115916. https://doi.org/10.1016/j.jobe.2026.115916. (**IF 7.4**)

Conference Papers

1. **Warsi SBF**, Panda B, Biswas P. Effect of strain hardening material on seismic performance of 3D printed concrete wall: a numerical study. **4th RILEM International Conference on Concrete and Digital Fabrication**, **2024**, p. 1–8. https://doi.org/10.24355/dbbs.084-202408191226-0.
2. **Warsi SBF**, Panda B, Biswas P. Numerical evaluation of the seismic performance of self-centering 3D printed concrete wall. **10th International Conference on Computational Methods in Structural Dynamics and Earthquake Engineering**, **2025. (Accepted)**
3. **Warsi SBF**, Panda B, Biswas P. A numerical study on the effects of boundary elements confinement on cyclic performance of 3D printed concrete wall. **1st RILEM Youth Symposium, 2025 (Accepted)**
4. **Warsi S B F**, Panda, B., & Biswas, P. (2026). Lean and low-carbon 3D printed concrete mixtures with strain-hardening ductile behavior for seismic applications. **4th Young Researchers' Symposium 2026**. **(Accepted)**

Patents

1. **S.B.F. Warsi**, B. Panda B, P. Biswas. 2024. ULTRA-DUCTILE STRAIN HARDENING 3D PRINTED CEMENTITIOUS COMPOSITES. Indian Patent, filed September 30, **2024**. Provisional patent. Patent Application No.: 202431073679, 2024.

Poster presentations and achievements

Poster Presentations

1. **Syed Bustan Fatima Warsi**, Biranchi Panda, and Pankaj Biswas, "Effect of strain hardening material on seismic performance of 3D printed concrete wall: a numerical study" Digital Concrete Conference (DCC 2024) held at Munich, Germany, Sep 3-5, 2024.
2. **Syed Bustan Fatima Warsi**, Biranchi Panda, and Pankaj Biswas, "Design and development of

earthquake resistant 3D printed concrete structure" IC-IMPACTS held at Indian Habitat Center, Delhi, India, Dec 9-11, 2024.

3. **Syed Bustan Fatima Warsi**, Uday Boddepalli, Dodda Srinivas, Dhrutiman Dey, Bhavesh Choaudhary, Biranchi Panda, T. G. Sitharam, and Indu Siva Ranjani Gandhi, "Development of outdoor furniture using 3D concrete printing" North East Research Conclave held at Indian Institute of Technology, Guwahati, India, May 20-22, 2022.
4. Dodda Srinivas, Uday Boddepalli, **Syed Bustan Fatima Warsi**, Dhrutiman Dey, Biranchi Panda, T.G. Sitharam, and Indu Siva Ranjani Gandhi., "Development of 3D Printed Structures at IIT Guwahati" presented among the selected projects at G20 summit in February, 2023. Organized by IIT Guwahati.

Achievements

1. Received the "**Best Departmental Idea Innovation Award**" under **oral thesis presentation** in **October 2025**.
2. **Prime Minister's Research Fellowship** in the lateral entry category for the **10th cycle** in **December 2022**.
3. Best exhibitors award in the "**Innovation for the future**" category in the **North-East Research Conclave (NERC)** held at **IIT Guwahati** on **May 20-22, 2022**.
4. Pre-finalists in **TATA Steel "Material Next 4.0"** competition held in **April 2023**.
5. Successfully completed and handover **3D printed sentry post to Indian Army** on **6th October 2022** under **Indigenous Research & Development Programme.**